



T.C.  
MANİSA CELAL BAYAR ÜNİVERSİTESİ  
FEN BİLİMLERİ ENSTİTÜSÜ

MANİSA CELAL BAYAR UNIVERSITY  
INSTITUTE OF NATURAL&APPLIED  
SCIENCE

CİLT:17 SAYI :4 YIL:2021  
VOLUME:17 ISSUE:4 YEAR:2021

ISSN: 1305-130X  
e-ISSN: 1305-1385

**CELAL BAYAR ÜNİVERSİTESİ  
FEN BİLİMLERİ DERGİSİ**

**CELAL BAYAR UNIVERSITY  
JOURNAL OF SCIENCE**

**CELAL BAYAR  
ÜNİVERSİTESİ**



# Journal of Science

Volume: 17, Issue: 4, Year: 2021

## Contact

Manisa Celal Bayar University  
Institute of Natural and Applied Sciences  
Campus of Şehit Prof Dr İlhan Varank 45140 Yunusmre – MANİSA, TURKEY  
Tel: (00 90) 236 201 27 05  
Fax: (00 90) 236 241 21 49  
e-mail: cbujos@gmail.com  
Web: <https://dergipark.org.tr/tr/pub/cbayarfbe>

“CBU Journal of Science is indexed by ULAKBIM-TUBITAK TR-DIZIN”



ISSN 1305-130X

E-ISSN 1305-1385

CBUJOS is published quarterly at Manisa Celal Bayar University Printing House

“CBU Journal of Science is a refereed scientific journal”



## Celal Bayar University Journal of Science

### Owner

Manisa Celal Bayar University,

**Editors :** Assoc. Prof. Dr. Kamil ŞİRİN

Assoc. Prof. Dr.. Emine KEMİKLİOĞLU

**Assistant Editor:** Assoc. Prof. Dr. Mustafa AKYOL

### Layout Editor & Secretary

Dr. İlker Çetin KESKİN

### International Scientific Advisory Board

Prof. Dr. Arianit REKA; State University of Tetova, Macedonia

Prof. Dr. Tomasz NIEMIEC; Warsaw University of Life Sciences, Poland

Prof. Dr. Alyani ISMAIL; Universiti Putra, Malaysia

Prof. Dr. Iuliana APRODU; Dunarea de Jos University, Romania

Assoc. Prof. Dr. Johanan Christian PRASANNA; Madras Christian College, South India

Assoc. Prof. Dr. Noureddine ISSAOUI; Université de Monastir, Tunisie.

Assoc. Dr. Edward Albert UECKERMANN; North-West University, South Africa

Assoc. Dr. Zhi-Qiang ZHANG; The University of Auckland, Holland

Assist. Prof. Dr. Young Ki KIM; Pohang University of Science and Technology, South Korea

Assist. Prof. Can BAYRAM; University of Illinois, USA

Assist. Prof. Dr. Mona MIRHEydARI; Rutgers University, USA

Assist. Prof. Dr. Donatella ALBANESE; Università Degli Studi Di Salerno, Italy

Assist. Prof. Dr. Jinghua JIANG; The University of Memphis, USA

Assist. Prof. Dr. Jens OLDELAND; University of Hamburg, Germany

Dr. Cheng CHENG; Apple Inc., USA

Dr. Sajedah AFGHAH; Microsoft Corporation, USA

Dr. Jinghua JIANG; The University of Memphis

### National Scientific Advisory Board

Prof. Dr. Mustafa Ersöz; Selçuk University

Prof. Dr. Oğuz Gürsoy; Mehmet Akif University

Prof. Dr. Mehmet Çevik; İzmir Katip Çelebi University

Prof. Dr. Sezgin Çelik; Yıldız Teknik University

Prof. Dr. Osman Dayan; Çanakkale Onsekiz Mart University

Prof. Dr. Serdar İplikçi; Pamukkale University

Prof. Dr. Yasin Üst; Yıldız Teknik University

Prof. Dr. Mahmut Kuş; Konya Teknik University

Prof. Dr. Ertuğ Gundüz; Hacettepe University

Prof. Dr. Tülin Aydemir; Manisa Celal Bayar University

Prof. Dr. Sezai Taşkın; Manisa Celal Bayar University

Prof. Dr. Fatma Şaşmaz Ören; Manisa Celal Bayar University

Assoc. Prof. Dr. Fatih Doğan; Çanakkale Onsekiz Mart University

Assoc. Prof. Dr. Erol Akpınar; Abant İzzet Baysal University

Assoc. Prof. Dr. Yeliz Yıldırım; Ege University

Assoc. Prof. Dr. Serap Derman; Yıldız Teknik University

Assoc. Prof. Dr. Hayati Mamur; Manisa Celal Bayar University

Assoc. Prof. Dr. Fatih Selimefendigil; Manisa Celal Bayar University

Assoc. Prof. Dr. Özlem Çağındı; Manisa Celal Bayar University

Assoc. Prof. Dr. Osman Çulha; Manisa Celal Bayar University

Assoc. Prof. Dr. Ali Demir; Manisa Celal Bayar University

Assoc. Prof. Dr. Ali Konuralp; Manisa Celal Bayar University

Assist. Prof. Dr. Nil Mansuroğlu; Ahi Evran University

Assist. Prof. Dr. Zeynep Çipiloğlu Yıldız; Manisa Celal Bayar University



## **CBU Journal of Science**

Celal Bayar University Journal of Science (CBUJOS) covers scientific studies in the fields of Engineering and Science and publishes accounts of original research articles concerned with all aspects of experimental and theoretical studies. CBU Journal of Science is a refereed scientific journal published four times annually (March, June, September and December) by Institute of Natural and Applied Sciences of Manisa Celal Bayar University. CBU Journal of Science considers the original research articles written in English for evaluation.

CBU Journal of Science is indexed by TUBİTAK ULAKBİM TR-DİZİN, and also is included in DOAJ, Cite Factor, Journal TOCS, Advanced Science Index and OAJI databases. Digital Object Identifier (DOI) number will be assigned for all the articles being published in CBU Journal of Science.

Instructions for Authors and Article Template can be found on the main page of MCBU Institute of Natural and Applied Sciences (<http://fbe.cbu.edu.tr>)





**Vol: 17, Issue: 4, Year: 2021**

**Contents**

**Research Article**


**Pages**

- Assessment of Asphaltene Production on Fracture Aperture During Heavy Oil Recovery  
DOI: 10.18466/cbayarfbe.857178  
Serhat Canbolat 337-345
- A New Hybrid Scatter Search Method for Solving the Flexible Job Shop Scheduling Problems  
DOI: 10.18466/cbayarfbe.926756  
Safa Klahlı, Orhan Engin, İsmail Koç 347-359
- Analysis of Factors Affecting Coronaphobia by Analytical Network Process  
DOI: 10.18466/cbayarfbe.898038  
Edanur Sonel, Şeyda Gr, Tamer Eren 361-367
- Stability Analysis of Discretized Model of Glucose–Insulin Homeostasis  
DOI: 10.18466/cbayarfbe.838451  
İlkem Turhan Çetinkaya, Mehmet Kocabıyık, Mevlde Yakıt Ongun 369-377
- Response Surface Methodology for Radioactive Strontium Adsorption on Molecular Sieves  
DOI: 10.18466/cbayarfbe.807377  
Ekrem Çiçek 379-382
- Decolorization Potential of *Pleurotus ostreatus*, *Lentinula edodes* and *Ganoderma lucidum* against Solvaderm Brown MF-GO Textile Dye  
DOI: 10.780314/cbayarfbe.887824  
Fatih Kalyoncu, Yurdanur Akyol 383-385
- Spectroscopic analyses on the binding interaction of thiosemicarbazone-derived Cu(II) complex with DNA/BSA  
DOI: 10.18466/cbayarfbe.902377  
Mkerrem Fındık, Asuman Uçar, Emine Gler Akgemci 387-395
- Adsorptive Removal of Tartrazine Dye by Poly(N-vinylimidazole-ethylene glycol dimethacrylate) And Poly(2-hydroxyethyl methacrylate-ethylene glycol dimethacrylate) Polymers  
DOI: 10.801544/cbayarfbe.869963  
Ayşe Dinçer, Tlin Aydemir 397-404
- A Mixed N-Heterocyclic Carbene/Triphenylphosphine Palladium(II) Complex for Suzuki-Miyaura Cross-Coupling Reactions  
DOI: 10.18466/cbayarfbe.941916  
Deniz Demir Atlı 405-415



- The Study on The Cooling of The Hot Side of The Thermoelectric Modules Utilized For High Cooling Requirements  
DOI: 10.18466/cbayarfbe.899975 417-427  
Anıl Başaran, Uğur Pehlivanoglu
- Comparative Performance Analysis of Surface Mounted Permanent Magnet Synchronous Generators  
DOI: 10.18466/cbayarfbe.959474 429-436  
Tuğberk Özmen, Nevzat Onat
- Regenerative Braking of Hub Type Brushless Direct Current Machine Used on Electric Bicycle  
DOI: 10.18466/cbayarfbe.866972 437-445  
Alper Kağan Candan, Hayati Mamur
- AES Encrypted Real-Time Video Stream and Image Transmission from ESP32-CAM  
DOI: 10.18466/cbayarfbe.835945 447-452  
Pınar Savaştürk, Ömer Aydın, Gökhan Dalkılıç

# Assessment of Asphaltene Production on Fracture Aperture During Heavy Oil Recovery

Serhat Canbolat<sup>1\*</sup> 

<sup>1</sup> Petroleum and Natural Gas Engineering, Engineering Faculty, Near East University, Nicosia / TRNC, Mersin 10 – Turkey

\*[serhat.canbolat@neu.edu.tr](mailto:serhat.canbolat@neu.edu.tr)

\*Orcid: 0000-0002-7591-8276

Received: 9 January 2021

Accepted: 6 December 2021

DOI: 10.18466/cbayarfbe.857178

## Abstract

During reservoir engineering analysis, the assessment of the possibility of asphaltene precipitation and corresponding heavy oil recovery with economic losses is carried out before any thermal operation. To investigate this phenomenon, three steam injection experiments using only steam, steam-CO<sub>2</sub>, and steam-n-C<sub>4</sub>H<sub>10</sub> at 1:1.29 volumetric ratios were carried out in naturally fractured limestone cores saturated with a 12.4° API heavy crude oil. After each experiment, the produced oil's asphaltene content was measured. Further, to determine the asphaltene effect on the fracture apertures and permeability, an improved cubic law (ICL) equation was used to determine the equivalent fracture aperture (EFA) change during the experiments. EFAs were calculated analytically. An initial observation made for only the steam injection experiment was a decline in asphaltene levels present in the producing oil. Asphaltene levels gradually increased as the effects of steam progressed. When CO<sub>2</sub> was added to the steam, the asphaltene content of the produced oil increased. Nevertheless, the asphaltene content increased in the produced oil did not change the fracture permeability and EFA considerably. In contrast, when n-C<sub>4</sub>H<sub>10</sub> was injected with steam concurrently, the asphaltene levels gradually increased above the starting value. However, in the further injection period, the asphaltene content in the produced oil was lower than the starting value as the injection progressed. This indicated that a partial upgrading of the asphaltene in the rock matrix caused an improvement in the EFA.

**Keywords:** asphaltene content, EFA, hydrocarbon gas, ICL, steam injection, upgrading.

## 1. Introduction

Heavy crude oils contain significant quantities of asphaltene. Because these oils are extremely viscous and nearly immobile, it is critical to have a reservoir recovery mechanism in place to reduce the viscosity of the oil and allow it to flow into the well for production. Cyclic steam and steam-assisted gravity drainage (SAGD) types of thermal processes are based on viscosity reduction. The cyclic steam also includes an oil thermal expansion drive for growth. Alternatively, SAGD is mainly a gravity-based method of draining oil into horizontal production wells [1]. In this process, using the horizontal injector, a steam chamber is produced and the steam continuously flows around the chamber where the surrounding oil is condensed and heated. Heat is transferred by the latent heat of steam, conduction, and convection. Under the force of gravity, the heated oil drains to a horizontal production well situated at the reservoir's base. Steam can lead to

changes in the behavior of the oil phase and the conditions of equilibrium that favor asphaltene deposition [1].

Asphaltene is generally described as crude oil fractions that are insoluble in n-heptane and soluble in benzene. Moreover, asphaltene is an amorphous form of hydrocarbon that is thought to be colloiddally dispersed fine particles and partially soluble compounds found in crude oil [2]. Due to the size of the asphaltene, it is difficult to grasp the cycle of asphalt precipitation and agglomeration. Asphaltene can be dissolved in the oil reservoir and stored in crude oil as micelles or colloidal suspensions. When both resins and asphaltene are present, as in oil, on their incorporation, the asphaltene tends to associate preferentially with the resins [3].

When applying thermal EOR (enhanced oil recovery) methods to undersaturated reservoirs, the possibility of asphaltene precipitation and oil-wet inducement, among

other potential issues, has become unavoidable and must be properly examined. In the case of saturated oil-wet reservoirs, on the other hand, wettability changes to water-wet can enable greater oil production than other mechanisms of thermal EOR methods [4].

The deposition of asphaltene from reservoir fluids is a serious problem during the production of oil as it may lead to plugging into the producer formation. In primary depletion of highly undersaturated reservoirs, either with hydrocarbon gas or injection of CO<sub>2</sub>, asphaltene precipitation can occur [5].

The analysis of Batu Raman crude oil demonstrated an important and novel insight: increasing the concentration of saturates-fraction in the deasphalted oil resulted in greater asphaltene precipitation. This tendency is thought to be caused by impurities in crude oil's saturates fraction [6].

Ghahfarokhi et al. (2017) discovered that the two most significant factors influencing the rate of asphaltene deposition are flow rate and asphaltene concentration. The attachment of asphaltene particles to the surface reduces as the flow rate increases, resulting in more asphaltene particles in the solution. However, as more of an agent is applied, the concentration of asphaltene in the mixture rises, accelerating the deposition process [7].

While physical characterization studies revealed only moderate correlations between bulk sample density/viscosity and asphaltene content, it was discovered that the ratio of heavy fractions (resins + asphaltene) to light fractions (saturates + aromatics) has the greatest influence on crude oil viscosity and °API value. As this ratio increases, crude oil becomes more viscous and denser. The asphaltene/resin ratio was also found to be significant by zeta-potential tests due to its effect on asphaltene stability. The high asphaltene/resin ratios cause reduced asphaltene stability; however, this effect is compensated by the higher aromatics fraction in the bulk oil [8].

The effects of the asphaltene precipitation have been studied as part of a solvent-based recovery process such as Vapor Extraction (VAPEX). One of the advantages of asphaltene precipitation is the in-situ upgrading of the bitumen. This result suggests that asphaltene precipitation occurs when the injected solvent condenses and aggregates near the edge of the chamber, which potentially contributes to the in-situ upgrading of the bitumen [9].

To characterize the permeability damage caused by asphaltene deposition during a gas injection EOR process, a unique systematic technique was developed. Based on the fluid analysis conducted in this study, the tendency for asphaltene flocculation to occur under the

expected operating conditions of gas injection in GOM Miocene reservoirs could be important. As the miscible front advances in the reservoir, the effect of decreased permeability is considered minor on the overall sweep performance [10].

All the aforementioned studies in the literature show that the precipitation of the asphaltene affects permeability, oil production, saturation, and thus, the equivalent fracture aperture of the reservoir. From this point of view, a new approach has gained importance for the analysis of the flow of heavy oil in the fractured medium during thermal methods. To investigate and analyze this phenomenon, an analytical approach has been used to evaluate the asphaltene production and precipitation when applying thermal EOR.

### 1.1 Assessment of Fracture Aperture

Typically, the cubic law (CL) has been improved and updated through testing on glass plates or concrete slabs rather than actual rock fractures. Nonetheless, some basic fluid flow problems in fractures, such as small-scale roughness, large-scale aperture variability, and high nonlinearity Reynolds number, have been established [11]. It assisted efforts to simulate the behavior of a single-phase flow in rough fractures. The flow tortuosity generated by fracture roughness has resulted in the development of pore-scale approaches such as channel models or the local cubic law (LCL), which better model local flow behavior by accounting for both aperture variance and, more recently, fracture layer ripple. The classical LCL, also known as the Reynolds equation, has been commonly implemented in fluid flow studies and convective and reactive solvent transport via a single fracture [12].

Early breakthroughs in the injection of water or aquifers can result in high-fluid transmission by fractures inside the reservoir. As a result, such analysis necessitates the understanding of the variation in the opening or aperture along the fracture [13]. Knowing the basics of fluid flow and the processes of transportation across related fractures is important. Comprehensive analysis of flow and transport processes inside complex networks of fractures continues to be a problem, as evidenced by studies based on isolated single rough-walled fractures [14, 15].

A modified cubic law (MCL) was first proposed by introducing a friction factor to account for the fracture roughness and tortuosity. Exact analysis of the flow system through rough and tortuous fractures helps to understand the problems of transportation in broken media. This can then provide a method for estimating efficient transport parameters based on the geometrical properties of the fracture [16].



In 2019, Canbolat and Parlaktuna developed the improved cubic law equation (ICL) for analyzing a flow system as;

$$Q = C \frac{b^3}{12\mu} \left( \frac{\Delta p}{L} \right) \quad (1.1)$$

where  $Q$ , flow rate (ml/min),  $C$ , coefficient,  $b$ , the equivalent fracture aperture (mm),  $\mu$ , the viscosity of flowing fluids (cp),  $\Delta p$ , the pressure difference between the inlet and outlet of the core holder (psi), and  $L$  is the length of the fracture, which is the length of the core plug (mm). For fractured core flow analysis, the  $C$  coefficient for the ICL equation was assumed to be 0.60 [13].

In reservoir engineering research, experimental and/or modeling studies are needed to determine when, where, and how much asphaltene will precipitate. Steam injection experiments using only steam, steam-CO<sub>2</sub>, and steam-n-C<sub>4</sub>H<sub>10</sub> at 1:1.29 volumetric ratios are carried out in naturally fractured limestone cores saturated with a 12.4° API Batu Raman heavy oil. Asphaltene content is measured in the extracted oil during the study. The effect of in-situ upgrading or flocculation of the heavy oil using the asphaltene content is investigated. Hence, analytical calculations using the ICL equation are used to determine the asphaltene effect on the equivalent fracture apertures and the fracture permeability.

## 2. Materials and Methods

### 2.1. Experimental Set-up

The experimental set-up has four main parts. These are; 1. Fluid Injection System, 2. Core Holder, 3. Fluid Production System, 4. Data Recording and Controlling System. A schematic view of the experimental set-up is illustrated in Figure 1.

### 2.1.1. Fluid Injection System

The fluid injection system consisted of a steam generator, CO<sub>2</sub>, and n-C<sub>4</sub>H<sub>10</sub> bottles. The steam generator used in the experiments is an electric steam boiler type that is suitable for laboratories. The generator was used to continuously produce steam at 40 psi and 140–150 °C during the experiments. The amount of noncondensable gas added to the steam was controlled and adjusted by a flowmeter. It was connected to the injection line, which was wrapped with a line heater and covered with an insulator to minimize heat loss during steam injection. Steam injection experiments were carried out with the presence of CO<sub>2</sub> and n-C<sub>4</sub>H<sub>10</sub> in the steam at a volumetric ratio of 1:1.29.

### 2.1.2. Core Holder

A schematic drawing of the core holder and experimental set-up is given in Figure 1. The properties of the core plugs and Batu Raman oil are given in Table 1. The viscosity alteration of crude oil as a function of temperature is given in Figure 2 accordingly.

**Table 1.** Naturally fractured core plug and heavy oil properties.

<b>Rock Type</b>	Limestone
<b>Density (gr/cc)</b>	2.61
<b>*Porosity (%)</b>	34-37
<b>*Permeability (darcy)</b>	0.1516 - 0.2424
<b>Length (cm)</b>	20.5
<b>Diameter (cm)</b>	5.08
<b>API gravity (°API)</b>	12.4
<b>Asphaltene Content (weight %)</b>	30 ± 5 (approximately)

\* Measured experimentally.

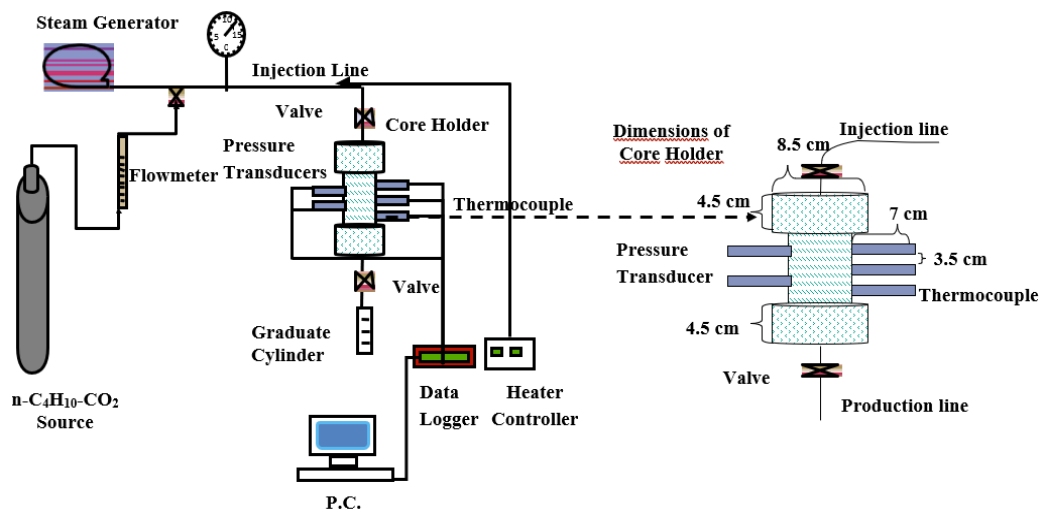


**Figure 1.** Experimental set-up & core holder.

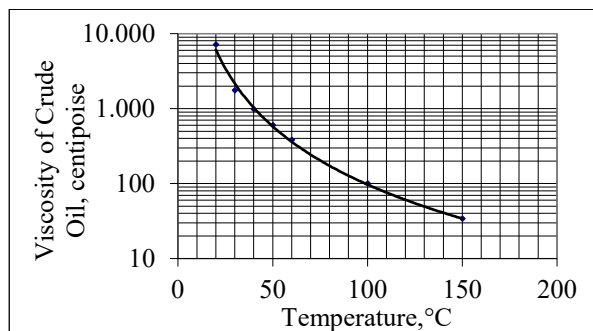


**Figure 2.** Viscosity alteration of the crude oil.

### 2.1.3. Fluid-Production System

During the experiments, the injection and production pressures were recorded at both ends using pressure gauges and pressure transducers. The input and output lines were covered with heaters and insulation material to reduce heat losses. The graduate cylinder collected the fluids produced and was placed below the core holder exit.

### 2.1.4. Data Recording and Controlling System

Data recording and the controlling system consist of thermocouples, a personal computer, and data loggers. Temperature distributions during the experiments were measured by 3 thermocouples connected to the core cell and then recorded in a data logger. The data records were continuously monitored by a personal computer using an excel spreadsheet.

## 2.2. Experimental Procedure

Before the experiments, the core plugs were completely saturated with the 12.4° API Batı Raman heavy oil. The core holder's temperature was raised to 50 °C. The heated and insulated injection line pumped superheated steam into the core holder at 40–55 psia and 140–150 °C. The production end of the core holder has been opened to the atmosphere. Both experiments were conducted until a preset steam-oil ratio and the recovery of oil were established. Besides, the temperature of the flow line and the temperature profile in the center were continuously measured and reported during each experiment. Following the experiments, core plugs were taken out of the core holder and put in the toluene extraction apparatus (SOXHLET) to determine saturation distribution after each experiment.

## 2.3. Asphaltene Measurements

The asphaltene measurement of the produced oil showed us the deposition, production, and sweep efficiency of the process applied to the system. Asphaltene measurements were carried out using toluene and hexane following the ASTM method. Toluene provided a dissolving effect for oil and hexane used for precipitation while measuring the asphaltene content of both produced oils [17].

Akmaz et al. (2011) reported the chemical analysis of Batı Raman crude oil and its asphaltene percent, respectively [6]. Batı Raman's heavy crude oil has high amounts of asphalt (28%), resin (27%), and aromatic fractions (26%). The amount of produced asphaltene in the oil was measured using samples taken from the produced fluids. The ratio of crude oil to hexane for the calculation of asphaltene content was taken at 1:10. One gram of oil was taken and mixed with 10 cc of hexane. Asphaltene particles were precipitated in the produced samples, and the weight percent of asphaltene was calculated in the oil. In this study, the measured asphaltene weight (Asp.W.) in Batı Raman heavy crude oil was 30%.

## 2.4. Porosity Measurement of Core Plugs

A mercury porosimeter was used to measure the porosity of the core plugs. The measured values of the porosity are given in Table 1.

## 2.5. Permeability Measurement of Core Plugs

The limestone core plugs' permeability ranges between 0.1516 and 0.2424 darcy, respectively. The permeability measurements of Core#1, 0.2424 darcy, Core#2, 0.1516 darcy, and Core#3, 0.2424 darcy were found respectively.

## 3. Results of the Steam Experiments

Oil wet limestone core plug experiments were performed. Three experiments were carried out in such a way that the system resembles a vertical cross-section of a reservoir of gravity drainage. The temperature of the process gradually increased for steam alone (Figure 3). For other systems, the ratio of the injected volume of steam was lower than the CO<sub>2</sub> and n-C<sub>4</sub>H<sub>10</sub> injection volumes (1:1.29). Therefore, the temperature fluctuated around the temperature of the original core plug. (Figures 4, 5).

As a result, the steam could not be supplied at high temperatures and/or near high temperatures enough to reach the core plugs as it was generated in all experiments. It became hot water because of the decrease in permeability and the addition of CO<sub>2</sub> and n-C<sub>4</sub>H<sub>10</sub> at room temperature. In the further production period, only in the steam case experiment, a steady temperature rise was observed. The steam-only oil recovery and steam-n-C<sub>4</sub>H<sub>10</sub> cases are comparable (Figure 6). This may be due to the heterogeneity of the core plugs and fractures. However, the recovery of oil for adding CO<sub>2</sub> was lower than the other two. This may be due to the lower core plug permeability, although it took the longest time for the experiment. For both cases, the steam condensed at the core's entrance. In the steam-only case experiment, the early stages of steam chamber formation, described as the rising steam chamber, were seen [1].

**Table 2.** Improved cubic law analysis of the steam only experiment for equivalent fracture aperture and fracture permeability.

Time	Pump Rate	Pressure Difference, $\Delta P$	ICL Rate	Equivalent Fracture Aperture	Fracture Permeability, kf	Fracture Permeability, kf
hours	ml/min	bar	ml/min	mm	cm <sup>2</sup>	md
0	0	0	0	0	0	0
00:58	0.370	0.180	0.370	0.235	2.17 E-09	217
01:58	0.370	0.180	0.370	0.235	2.17 E-09	217
02:43	0.370	0.200	0.370	0.227	1.95 E-09	195
03:22	0.370	0.220	0.370	0.219	1.77 E-09	177
03:55	0.370	0.200	0.370	0.227	1.95 E-09	195
04:24	0.370	0.180	0.370	0.235	2.17 E-09	217
04:49	0.370	0.160	0.370	0.244	2.44 E-09	244
05:15	0.370	0.220	0.370	0.219	1.77 E-09	177
05:36	0.370	0.210	0.370	0.223	1.85 E-09	185
05:57	0.370	0.200	0.370	0.227	1.95 E-09	195
06:14	0.370	0.180	0.370	0.235	2.17 E-09	217
06:34	0.370	0.160	0.370	0.244	2.44 E-09	244
06:50	0.370	0.200	0.370	0.227	1.95 E-09	195
07:05	0.370	0.192	0.370	0.230	2.03 E-09	203
07:18	0.370	0.192	0.370	0.230	2.03 E-09	203
07:28	0.370	0.180	0.370	0.235	2.17 E-09	217
07:34	0.370	0.160	0.370	0.244	2.44 E-09	244

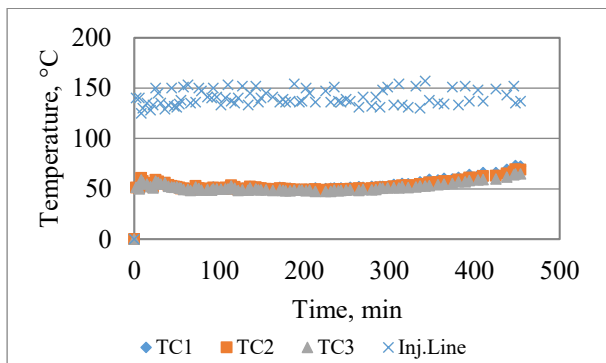


**Figure 3.** Temperature variation of core#2 during the steam-only experiment.

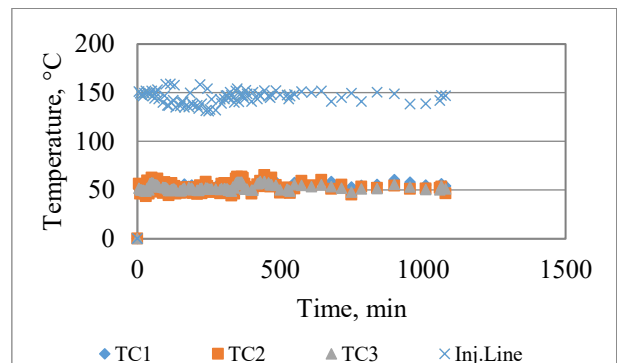


**Figure 5.** Temperature variation of core#4 during the steam+n-C<sub>4</sub>H<sub>10</sub> experiment.

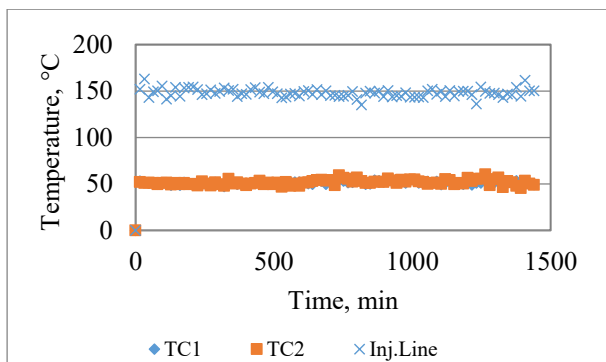


**Figure 4.** Temperature variation of core#3 during the steam+CO<sub>2</sub> experiment.

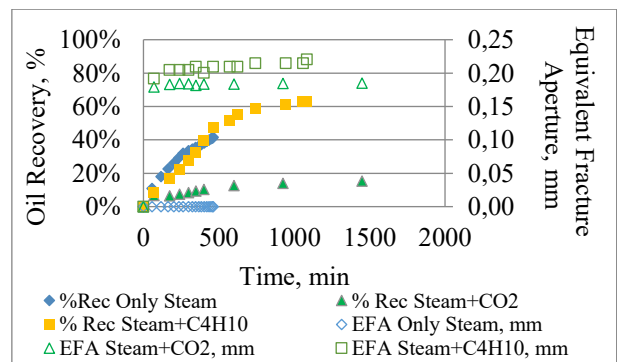


**Figure 6.** Effect of equivalent fracture aperture on % oil recovery.

Equivalent fracture aperture calculations showed that the variations due to flocculation affected the total recovery in the only steam case. However, CO<sub>2</sub> and n-C<sub>4</sub>H<sub>10</sub> additions did not change the fracture aperture. However, the n-C<sub>4</sub>H<sub>10</sub> addition case provided the highest recovery. Equivalent fracture aperture variations also changed the fracture permeability calculations of the core plugs. The steam-only case varied more with respect to CO<sub>2</sub> and n-C<sub>4</sub>H<sub>10</sub> addition cases due to flocculation (Figures 7, 8) [13].

The influence of aperture on flow is often characterized by the steady-state solution to the Navier-Stokes equations for laminar viscous flow, which was improved as ICL and aforementioned in equation 1.1 [13]. Darcy's law and the ICL equation show that there is a direct relation between fracture permeability and equivalent fracture aperture. Higher EFA increased the fracture permeability (Figures 7, 8) [13].

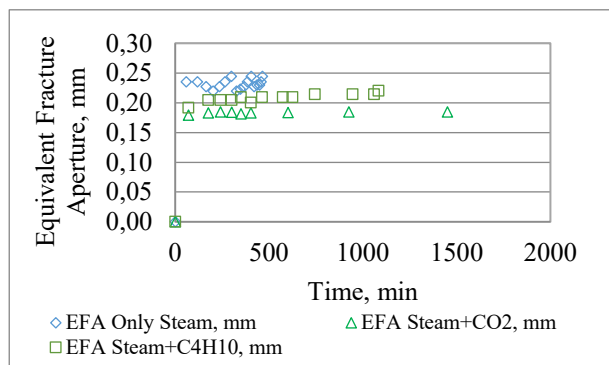


Figure 7. EFA variations.

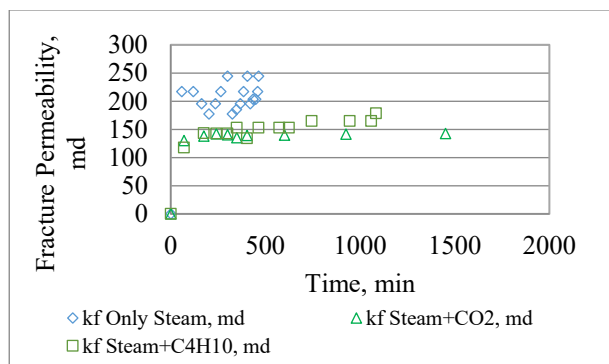


Figure 8. Fracture permeability variations.

To follow the variation during production, the initial asphaltene content of the heavy oil is shown with a dashed line on the graphs (Figures 9, 10). Measurements of asphaltene weight percent showed an increase in the asphaltene content of the oil originally produced in both cases (Figures 9, 10). Thus, partial upgrading was observed in core plug experiments. However, CO<sub>2</sub> addition to steam stabilized or decreased produced asphaltene content, showing adsorption of asphaltene at sites created by the injected steam with or without CO<sub>2</sub>

gas. Nevertheless, the produced oil asphaltene content was decreased for the n-C<sub>4</sub>H<sub>10</sub> addition below the initial value as the injection continued. This indicated partial upgrading of the asphaltene by the n-C<sub>4</sub>H<sub>10</sub> addition [9].

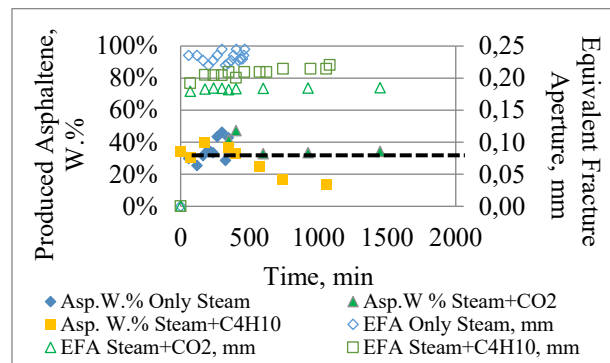


Figure 9. Effect of produced asphaltene on equivalent fracture aperture.

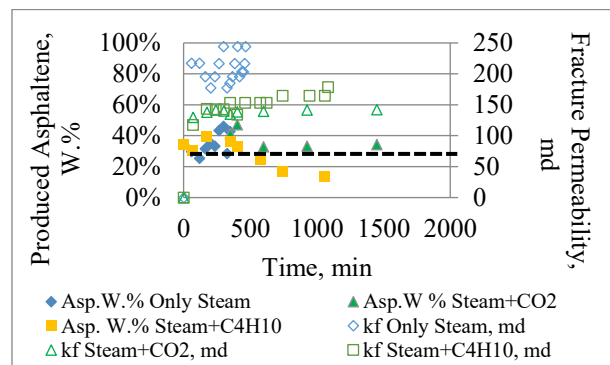


Figure 10. Effect of produced asphaltene on fracture permeability.

#### 4. Discussions

Analytically, the equivalent fracture apertures were calculated for both core experiments using the ICL equation to observe the asphaltene effect on the equivalent fracture apertures and permeability. In the only steam injection case, an initial decrease in the asphaltene content of the extracted oil was observed (Table 2, Figure 9).

As the influence of steam progressed, the asphaltene content gradually increased. Therefore, the oil produced in situ was improved. Fracture permeability and equivalent fracture aperture were increased accordingly. The asphaltene content of the extracted oil indicates asphaltene remobilization (Figure 10) [9].

The addition of CO<sub>2</sub> to the steam increased the amount of produced oil with asphaltene content. The content of asphaltene has changed around the initial value (Table 3, Figure 9). The size of the non-uniform asphaltene deposition was comparable to that of the only steam case, but there was no significant impact on fracture

permeability and equivalent fracture aperture due to the increased asphaltene content in developed oil (Figures 9, 10) [8].

In comparison, injecting  $n\text{-C}_4\text{H}_{10}$  concurrently with steam raised the asphaltene content gradually above the initial value. Then the asphaltene content in the extracted

oil was lowered below the initial value as the injection progressed in the further injection phase. This indicated a partial upgrading of the asphaltene in the rock matrix (Figures 9, 10). Moreover,  $n\text{-C}_4\text{H}_{10}$  addition to steam also increased the equivalent fracture aperture and fracture permeability of the core, which verified the upgrading of oil (Table 4) [10].

**Table 3.** Improved cubic law analysis of the steam+CO<sub>2</sub> experiment for equivalent fracture aperture and fracture permeability.

Time	Pump Rate	Pressure Difference, ΔP	ICL Rate	Equivalent Fracture Aperture	Fracture Permeability, kf	Fracture Permeability, kf
hours	ml/min	bar	ml/min	mm	cm <sup>2</sup>	md
0	0	0	0	0	0	0
01:10	0.184	0.206	0.184	0.179	1.30 E-09	130
02:55	0.184	0.190	0.184	0.183	1.38 E-09	138
04:00	0.184	0.186	0.184	0.185	1.42 E-09	142
05:00	0.184	0.187	0.184	0.184	1.40 E-09	140
05:49	0.184	0.194	0.184	0.182	1.35 E-09	135
06:42	0.184	0.183	0.184	0.183	1.39 E-09	139
10:00	0.184	0.188	0.184	0.184	1.40 E-09	140
15:25	0.184	0.185	0.184	0.185	1.42 E-09	142
18:25	0.184	0.185	0.184	0.185	1.42 E-09	142
21:10	0.184	0.183	0.184	0.186	1.43 E-09	143
23:55	0.184	0.182	0.184	0.186	1.44 E-09	144

**Table 4.** Improved cubic law analysis of the steam+n-C<sub>4</sub>H<sub>10</sub> experiment for equivalent fracture aperture and fracture permeability.

Time	Pump Rate	Pressure Difference, ΔP	ICL Rate	Equivalent Fracture Aperture	Fracture Permeability, kf	Fracture Permeability, kf
hours	ml/min	bar	ml/min	mm	cm <sup>2</sup>	md
0	0	0	0	0	0	0
01:10	0.203	0.183	0.203	0.192	1.17 E-09	117
02:55	0.203	0.185	0.203	0.203	1.43 E-09	143
04:00	0.203	0.186	0.203	0.205	1.43 E-09	143
05:00	0.203	0.188	0.203	0.205	1.43 E-09	143
05:49	0.203	0.181	0.203	0.209	1.53 E-09	153
06:42	0.203	0.197	0.203	0.200	1.34 E-09	134
07:43	0.203	0.183	0.203	0.209	1.53 E-09	153
09:34	0.203	0.179	0.203	0.209	1.53 E-09	153
10:24	0.203	0.177	0.203	0.209	1.53 E-09	153
12:22	0.203	0.170	0.203	0.214	1.65 E-09	165
15:45	0.203	0.167	0.203	0.215	1.65 E-09	165
17:39	0.203	0.170	0.203	0.215	1.65 E-09	165
18:04	0.203	0.160	0.203	0.220	1.78 E-09	178

#### 4.1. Estimated Asphaltene Deposition after Steam Experiments

The asphaltene deposition of the experiments originated from the effective heating of the steam that was caused to produce all light fractions of the oil, sweeping through the core. This decreased the viscosity of the oil and increased the adsorption of asphaltene particles on limestone (Figures 9 and 10). % Recovery graphs of the

only steam experiment have also supported this conclusion [4]. This can be explained by the fact that before reaching the injection line, the injected gas is at room temperature, so it takes a while to heat up. However, at the inlet of the core, the steam condenses, and the core temperature does not rise as non-condensing gas is added. The inlet temperature was still above the lower levels.

Precipitation of asphaltene from reservoir fluids during oil withdrawal is a serious issue, as the deposition of asphaltene can cause the blockage of wells and production facilities. Asphaltene precipitation occurs for better oil recovery during primary depletion of highly unsaturated reservoirs that have a very low bubble point pressure or during hydrocarbon gas or CO<sub>2</sub> injection. This can also occur in heavy oil reservoirs during solvent injection. By changing the pH or solubility properties of the crude oil, asphaltene can be destabilized [18].

It was known that, from the analysis of Batı Raman crude, an increase in saturates-fraction concentration in the deasphalted oil resulted in more asphaltene precipitation. This trend is seen in the addition of n-C<sub>4</sub>H<sub>10</sub> to steam, both by increased equivalent fracture aperture and fracture permeability of the core during the upgrading of oil [6].

The addition of n-C<sub>4</sub>H<sub>10</sub> to steam also increased the destabilization of the asphaltene, making the residual oil more viscous and denser as the heavy fractions (resins + asphaltene) to light (saturates + aromatics) ratio increases. Since the heavier fractions were produced by the addition of n-C<sub>4</sub>H<sub>10</sub> to steam, the residual water saturation increased [8].

Unbelievably, in the naturally fractured limestone core plug experiment, the steam-CO<sub>2</sub> case, due to the major chemical component of the core sample, which was CaCO<sub>3</sub>, might have reacted with formed carbonic acid to cause the dissolution of calcite [19]. This might cause the dissolution of calcite after the interaction of CO<sub>2</sub>-water-rock, which leads to the formation of a new texture in the core, plugging the pathway. That's why the recovery performance of the experiment cannot be realized as intended.

## 5. Conclusions

Precipitation and flocculation of asphaltene are considered problems of formation damage, which can reduce the recovery of oil. To analyze this phenomenon using a new approach, the asphaltene content of the produced oil was measured. The effect of asphaltene content on fracture apertures and permeability was investigated using the ICL equation. EFA change was calculated for the steam-only and CO<sub>2</sub>/C<sub>4</sub>H<sub>10</sub>-addition cases.

1. For both core plug experiments, the EFAs were analytically calculated using the ICL equation to observe the asphaltene effect on the fracture aperture and permeability. Asphaltene levels slowly increased as the effects of steam progressed. Therefore, the produced oil was noted to improve in-situ. The fracture permeability and equivalent fracture aperture increased.

2. Comprising CO<sub>2</sub> in steam increased the asphaltene content of the produced oil. However, the asphaltene levels increased in produced oil did not change the fracture permeability and equivalent fracture aperture considerably.
3. On the contrary, when hydrocarbon gas n-C<sub>4</sub>H<sub>10</sub> was introduced concurrently with steam, the levels of asphaltene increased slowly, and the content of asphaltene in produced oil decreased as the injection progressed, indicating a partial upgrade of asphaltene in the rock matrix.
4. The asphaltene deposition of the experiments originated from the effective heating of the steam that caused it to produce all the light fractions of the oil. Asphaltene flocculation was detected in only steam injection experiments by changing the equivalent fracture aperture and permeability.

## Future Work

This study provides an understanding of the asphaltene flocculation/alteration during steam with/without CO<sub>2</sub>/n-C<sub>4</sub>H<sub>10</sub> injection cases in an oil-wet reservoir. The equivalent fracture aperture variation was analyzed according to the precipitated and produced asphaltene. More investigation should be done to analyze the water-wet and mixed-wet reservoirs to see how the solvents and steam alter the asphaltene effect on the equivalent fracture aperture.

## Nomenclature

A	: Cross-Sectional Area, ft <sup>2</sup>
b	: Fracture Aperture, mm
C	: Constant, (0.6)
CL	: Cubic Law
EFA	: Equivalent Fracture Aperture
ICL	: Improved Cubic Law
kf	: Fracture Permeability, md
L	: Length, cm
MCL	: Modified Cubic Law
Q	: Total Flow Rate, ml/min
ΔP	: Drawdown, psi
TC	: Thermocouple

## Symbols

μ	: Fluid Viscosity, cP
φ	: Porosity, percent

## Author's Contributions

Serhat CANBOLAT: Drafted and wrote the manuscript, performed the experiments, interpretations, and result in analysis with conclusions.



## Ethics

There are no ethical issues after the publication of this manuscript.

## References

1. Canbolat, S., Akin, S., and Kovscek, A. R., 2004, Non-condensable gas steam-assisted gravity drainage, *Journal of Petroleum Science and Engineering*, 45(1-2), 83-96.
2. Lee, K. S., Cho, J., Lee, J.H., 2020. CO<sub>2</sub> Storage Coupled with Enhanced Oil Recovery, ISBN 978-3-030-41901-1, 1st edn. Springer Nature eBook, Switzerland AG, 2020, pp 51-71.
3. Canbolat, S., Akin, S., Kovscek, A.R., 2006. Asphaltene Deposition During Steam-Assisted Gravity Drainage: Effect of Non-Condensable Gases, *Journal of Petroleum Science and Technology*; 24:1, 69-92.
4. Canbolat, S., Ozturk, H., Akin, S., 2021. Exploitation of Bati Raman field using advanced thermal methods: MAHOP VS. CSHP, *Journal of Petroleum Science and Engineering*; 208, (2022), 109802.
5. Oskui, G.P., Jurma, M.A., Abuhaimeid, W.A., 2009. Laboratory Investigation of Asphaltene Precipitation Problems during CO<sub>2</sub>/Hydrocarbon Injection Project for EOR Application in Kuwaiti Reservoirs, SPE 126267, SPE Kuwait International Petroleum Conference and Exhibition held in Kuwait City, 14-16 December.
6. Akmaz, S., Iscan, O., Gurkaynak, M. A., Yasar M., 2011. The Structural Characterization of Saturate, Aromatic, Resin, and Asphaltene Fractions of Batu Raman Crude Oil, *Petroleum Science, and Technology*; 29:2, 160-171.
7. Ghahfarokhi, A.K., Kor, P., Kharrat, R., Soulgani, B.S., 2017. Characterization of the asphaltene deposition process in flow loop apparatus; An experimental investigation and modeling approach, *Journal of Petroleum Science and Engineering*; 151, 330-340 January 2017.
8. Prakoso, A. A., Punase, A. D., Hascakir, B., 2017. A Mechanistic Understanding of Asphaltenes Precipitation From Varying-Saturate-Concentration Perspectives, *SPE Production & Operations*; pp 86-98, February 2017.
9. Kaito, Y., Kiriakhehata, S., Nakagawa, K., Nakashima, H., Izumi, T., Yamada, T., 2020. Determination of Asphaltene Precipitation Amount under the Condition of the Solvent Assisted SAGD Process by the Application of PVT Apparatus SPE-199950-MS, e SPE Canada Heavy Oil Technical Conference originally scheduled to be held in Calgary, Alberta, Canada, 18 – 19 March.
10. Fassih, M.R. Turek, E. and Honarpour, M.M., Fyfe, R., 2020. Investigation of Permeability Impairment Due to Asphaltene Precipitation During Gas Injection EOR in a Major GoM Field, SPE-200429-MS, SPE Improved Oil Recovery Conference held in Tulsa, OK, USA, 18 – 22 April.
11. Renshaw, C.E., Dadakis, J.S., Brown, S. R., 2000. Measuring Fracture Apertures: A Comparison of Methods. *Geophysical Research. Letters*, 27 (2), 289-292.
12. Brush, D.J., Thomson, N.R., 2003. Fluid Flow in Synthetic Rough- Walled Fractures: Navier-Stokes, Stokes and Local Cubic Law Simulations. *Water Resources Research*. 39 (4), 1085.
13. Canbolat, S., Parlaktuna, M., 2019. Analytical and Visual Assessment of Fluid Flow in Fractured Medium. *Journal of Petroleum Science and Engineering*; 173, 77-94 February 2019.
14. Zimmerman, R.W., Al-Yaarubi, A., Pain, C.C., Grattoni, C.A., 2004. Non-linear Regimes of Fluid Flow in Rock Fractures. *International Journal of Rock Mechanics and Mining Sciences*; 41 (1), 163-169.
15. Cardenas, M.B., Slottke, D.T., Ketcham, R.A., Sharp Jr., J.M., 2007. Navier-Stokes Flow and Transport Simulations Using Real Fractures Shows Heavy Tailing Due to Eddies. *Geophysical Research. Letters*; 34, L14404.
16. Wang, L., Cardenas, M.B., 2014. Non-Fickian Transport Through Two-Dimensional Rough Fractures, Assessment and Prediction. *Water Resources Research*; 50, 871-884.
17. Srivastava, R.K., Huang, S.S., Dong M., 1999. Asphaltene Deposition During CO<sub>2</sub> Flooding. *SPE Production & Facilities*; (November), 14 (4): 235-245.
18. Nghiem, L. X., Kohse, B. F., Farouq Ali, S.M., Doan, Q., 2000. Asphaltene Precipitation: Phase Behavior Modelling and Compositional Simulation, SPE-59432-MS, SPE Asia Pacific Conference on Integrated Modelling for Asset Management, Yokohama, Japan, 25-26 April.
19. Xiao, N., Li, S., Lin, M., 2017. An Investigation of CO<sub>2</sub>-Water-Rock Interactions During CO<sub>2</sub> Flooding, *Electronic Journal of Geotechnical Engineering*; 2017 (22.05), pp 1629-1642.





# A New Hybrid Scatter Search Method for Solving the Flexible Job Shop Scheduling Problems

Safa K ulahlı<sup>1</sup>, Orhan Engin<sup>2\*</sup>, İsmail Koç<sup>3</sup>

<sup>1</sup> Management and Organization Department, Vocational School, Selçuk University, Konya, Turkey  
<sup>2</sup> Industrial Engineering Department, Engineering and Natural Science Faculty, Konya Technical University, Konya, Turkey  
<sup>3</sup> Software Engineering Department, Engineering and Natural Science Faculty, Konya Technical University, Konya, Turkey

\* [orhanengin@yahoo.com](mailto:orhanengin@yahoo.com)

\* Orcid: 0000-0002-7250-0317

Received: 23 April 2021

Accepted: 11 November 2021

DOI: 10.18466/cbayarfbe.926756

## Abstract

Flexible job shop scheduling (FJSS) is derived by inheriting the features of the job-shop scheduling problem. It has an extra routing sub-problem of the job-shop scheduling. FJSS is well known as an NP-hard problem in the literature. A new hybrid scatter search method is proposed to solve the FJSS problem. The objective function of the proposed hybrid scatter search method is minimizing the maximum completion time ( $C_{max}$ ) for FJSS problems. The proposed hybrid scatter search method is integrating a local and global search for generating an initial population. The performance of the proposed new hybrid scatter search method is dependent on the selected parameters. These parameters are the size of the initial population and reference set; the number of subsets, reference set updating and population sub updating; reproduction, crossover, and mutation operators, and their ratio. A full factorial experimental design is made to determine the best values of control parameters and operators for the proposed new hybrid scatter search to solve the FJSS problems. The proposed new hybrid scatter search method is tested on a set of the well-known benchmark flexible job shop scheduling instances from the literature. The computational results indicated that the proposed new hybrid scatter search is an effective method for solving the FJSS problems.

**Keywords:** Flexible job shop scheduling problem, Full factorial experimental design, Hybrid scatter search method, Makespan.

## 1. Introduction

Job shop scheduling (JSS) is the hardest problem in this domain [1]. The flexible job shop scheduling is a much more complicated version of the JSS. In the FJSS problem, processes are permitted to be committed on any machine chosen from inside a set of available machines. The FJSS is an extremely NP-hard problem [2]. FJSS can be solved via two main approaches called integrated and hierarchical. While in the integrated approach allocating and ordering of problems are concurrently considered, in hierarchical approaches, these two operations are processed one by one [3]. Though designing integrated approaches are more difficult, their results are better than the other in general [4,5]. Brucker and Schlie [6] studied first on the FJSS problems. They developed a polynomial algorithm for FJSS problems. Kacem et al. proposed an evolutionary

optimization method for solving the FJSS problem [7]. Tay and Wibowo studied the representation of the four different chromosomes for the evolutionary algorithms to solve the FJSS [8]. They indicated that the representation of the chromosome also plays an important role in the solution success of FJSS problems. Ong et al. developed an algorithm with an integrated approach attempting based on the clonal selection mechanism for solving the FJSS problems with the repetition processing [9]. Ho et al. generated a genetic architecture method for FJSS problems [10]. Gao et al. presented a hybrid genetic algorithm for FJSS problems [11]. Fattahi et al. developed a heuristic approach for solving the FJSS problems [12]. They also presented the mathematical model of the problems. Gholami and Zandieh integrated the simulated annealing and genetic algorithm approaches for the dynamic FJSS problems [13]. Xing et al. developed a search method for the

multi-objective FJSS problem [14]. Zhang et al. presented a particle swarm optimization method for multi-objective FJSS problems [15]. Bagheri et al. developed an artificial immune algorithm based on an integrated approach for FJSS problems [16]. Guohui et al. hybridized a tabu search and genetic algorithm approaches for the FJSS [17]. Wang and Yu considered an FJSS with constraints of the machine [18]. Zhang et al. proposed a genetic algorithm to solve the FJSS problems with minimizing the makespan value [1]. They determined global and local selection to produce a high-grade starting population in the stage of initialization in their method. Birgin et al. presented a MILP model for the FJSS [19]. Demir and İşleyen compiled four of the most used formulations of the FJSS and proposed a time-indexed model for FJSS [20]. Yuan and Xu proposed a hybrid differential evolution algorithm to solve FJSS with the makespan minimization criterion [21]. Demir and İşleyen considered the FJSS with overlapping in operations [22]. Abdelmaguid dealt with the makespan minimization problem in scheduling FJSS whenever there exist distinguishable sequence-dependent setup times [23]. He presented a randomized neighborhood searching function, and he experimentally specified its best parameters using modified FJSS benchmark samples. Gao et al. developed an artificial bee colony algorithm (ABCA) to schedule and reschedule with a new job(s) to minimize makespan for FJSS [24]. Besides, they proposed a new rule for initializing the bee colony populations. González et al. developed influential neighborhood structures for the FJSS containing feasibility and non-improvement circumstances, as well as procedures for fast prediction of the quality of neighbors [25]. They included these neighborhoods in a scatter search (SS) algorithm that employs tabu search and path relinking. They determined a new dissimilarity measurement to construct these meta-heuristics. Ishikawa et al. proposed a novel optimization mechanism for distributing genetic algorithms to solve FJSS problems [26]. Singh and Mahapatra developed a particle swarm optimization for solving FJSS [27]. They introduced mutation operators used commonly in genetic algorithms. Zabihzadeh and Rezaeian presented the integer linear programming model for the FJSS [28]. Li et al. proposed a hybrid ABCA for solving FJSS problems [29]. They integrated tabu search and bee colony algorithm. Shen et al. considered the FJSS problem with sequence-dependent setup times [30]. Min et al. proposed a genetic algorithm for solving the multi-objective FJSS problem with transportation constraints [31]. Li et al. generated a java algorithm for solving the FJSS problem [32]. Currently, there is no reported paper on the hybrid scatter search (HSS) method for solving the FJSS problems. The main contributions of this paper are summarized as follows:

- In this paper, the basic scatter search method is hybridized first by new strategies and new methods to obtain a good balance between exploration and exploitation in SS.
- At the proposed HSS, local and global search methods are used to determine the initial populations.
- Also, at the proposed HSS, the crossover and mutation operators and ratios are used first.
- The proposed new HSS method is the first used to solve the FJSS problems. The objective of the proposed HSS is to minimize the  $C_{max}$ .
- The proposed HSS method found the new best  $C_{max}$  values for four benchmark problems from the literature.
- A full experimental design is done for determining the best parameter sets of the new HSS method for solving the FJSS problems.
- The proposed new HSS method is tested on a set of benchmark FJSS problems.

The proposed new hybrid scatter search method (HSS) is analyzed. The results of HSS are compared to the Fattahi et al. [12], Özgüven et al. [33], Bagheri et al. [16], and Birgin et al. [19] from the literature.

The paper is organized as follows. Section 2 gives the FJSS formulation. Section 3 provides the proposed HSS method. Section 4 gives the computational results. Finally, the conclusion and future research are presented in Section 5.

## 2. Flexible job shop scheduling

This paper considers FJSS problems. The problem can be denoted as  $FJc // C_{max}$ , where  $FJc$  denotes the flexible job shop with  $c$  work center. Each work center has several identical machines in parallel.  $C_{max}$  indicates the performance measure, makespan. The objective is to minimize the  $C_{max}$  values for FJSS problems. The FJSS problem has  $m$  machine and  $n$  job. Each job consists of a sequence of operations. The assumptions in the FJSS problems are given as follow:

- The jobs and machines numbers are known at the beginning of the schedule,
- All processors, machines, and jobs are available,
- The processing time of each job on the machine is given before,
- The processing time are including the setup time of the jobs,
- The processing sequence of each job on the machine is known previously,
- The objective function is minimizing the makespan values.

The FJSS problem is formulated as a mixed integer linear programming model as follow [12, 33, 19].

*Parameters;*

$n$  : Jobs number ( $j = 1, \dots, n$ )  
 $m$  : Machines number ( $i = 1, \dots, m$ )  
 $k$  : Number of operations ( $k = 1, \dots, k_j$ )  
 $M_{j,k}$  : Job  $j$  requires operation  $k$  on Machine  
 $O_{j,k}$  :  $k$  th operation of the  $j$  th job  
 $Z_{i,j,k}$  : Capable machines set  $M_{j,k}$  assigned to operation  $O_{j,k}$   
 $t_{i,j,k}$  : Processing time of operation  $O_{j,k}$  if performed on machine  $i$  ( $t_{i,j,k} > 0$ )  
 $LN$  : Large number  
 $C_{max}$  : Makespan  
 $S_{j,k}$  : Start time of operation  $O_{j,k}$   
 $p_i$  : The assigned operations number on machine  $i$ ; ( $p = 1, \dots, p_i$ )  
 $SWT_{i,p}$  : Start of working time for machine  $i$  in priority  $p$  ( $p = 1, \dots, p_i$ )  
 $T_{j,k}$  : Processing time of operation  $O_{j,k}$  after select a machine

*Decision variables;*

$$X_{i,j,k,p} = \begin{cases} 1 & \text{if } O_{j,k} \text{ is performed on machine } i \text{ in priority } p \\ 0 & \text{otherwise} \end{cases}$$

$$Y_{i,j,k} = \begin{cases} 1 & \text{if machine } i \text{ is selected for operation } O_{j,k} \\ 0 & \text{otherwise} \end{cases}$$

$$Z_{i,j,k} = \begin{cases} 1 & \text{if } O_{j,k} \text{ can be performed on machine } i \\ 0 & \text{otherwise} \end{cases}$$

*The mixed integer linear programming model;*

The objective function is to minimize the makespan.

Min  $C_{max}$

Subject to

$$C_{max} \geq S_{j,k_j} + T_{j,k_j} \quad ; (j=1, \dots, n) \quad (2.1)$$

$$\sum_i (Y_{i,j,k}) (t_{i,j,k}) = T_{j,k} \quad ; (j=1, \dots, n); (k = 1, \dots, k_j) \quad (2.2)$$

$$S_{j,k} + T_{j,k} \leq S_{j,k+1} \quad ; (j=1, \dots, n); (k = 1, \dots, k_j-1) \quad (2.3)$$

$$SWT_{i,p} + (T_{j,k})(X_{i,j,k,p}) \leq SWT_{i,p+1} \quad ; (i = 1, \dots, m) \quad (j=1, \dots, n); (k = 1, \dots, k_j); (p = 1, \dots, p_i-1) \quad (2.4)$$

$$SWT_{i,p} \leq S_{j,k} + (1 - X_{i,j,k,p}) \cdot LN \quad ; (i = 1, \dots, m) \quad (j=1, \dots, n); (k = 1, \dots, k_j); (p = 1, \dots, p_i) \quad (2.5)$$

$$SWT_{i,p} + (1 - X_{i,j,k,p}) LN \geq S_{j,k} \quad ; (i = 1, \dots, m) \quad (j=1, \dots, n); (k = 1, \dots, k_j); (p = 1, \dots, p_i) \quad (2.6)$$

$$Y_{i,j,k} \leq Z_{i,j,k} \quad ; (i = 1, \dots, m); (j=1, \dots, n); (k = 1, \dots, k_j) \quad (2.7)$$

$$\sum_j \sum_k X_{i,j,k,p} = 1 \quad ; (i = 1, \dots, m); (p = 1, \dots, p_i) \quad (2.8)$$

$$\sum_i Y_{i,j,k} = 1 \quad ; (j=1, \dots, n); (k = 1, \dots, k_j) \quad (2.9)$$

$$\sum_p X_{i,j,k,p} = Y_{i,j,k} \quad ; (i = 1, \dots, m) \quad (j=1, \dots, n); (k = 1, \dots, k_j) \quad (2.10)$$

$$S_{j,k} \geq 0 \quad ; (j=1, \dots, n); (k = 1, \dots, k_j) \quad (2.11)$$

$$T_{j,k} \geq 0 \quad ; (j=1, \dots, n); (k = 1, \dots, k_j) \quad (2.12)$$

$$SWT_{i,p} \geq 0 \quad ; (i = 1, \dots, m); (p = 1, \dots, p_i) \quad (2.13)$$

$$X_{i,j,k,p} \in \{0, 1\} \quad ; (i = 1, \dots, m); (j=1, \dots, n); (k = 1, \dots, k_j); (p = 1, \dots, p_i) \quad (2.14)$$

$$Y_{i,j,k} \in \{0, 1\} \quad ; (i = 1, \dots, m); (j=1, \dots, n); (k = 1, \dots, k_j) \quad (2.15)$$

$$Z_{i,j,k} \in \{0, 1\} \quad ; (i = 1, \dots, m); (j=1, \dots, n); (k = 1, \dots, k_j) \quad (2.16)$$

Constraint (2.1) determines the makespan ( $C_{max}$ ). Constraint (2.2) provides the processing time of operation  $O_{j,k}$ . Constraint (2.3) determines each job to follow a specified operation sequence. Constraint (2.4) defines each machine to process one operation at a time. Constraints (2.5) and (2.6) denote each operation  $O_{j,k}$  can be started after its assigned machine is idle. Constraint (2.7) defines the capable machines for each operation. Constraint (2.8) determines the operations to a machine and sequences assigned operations on all machines. Constraints (2.9) and (2.10) define each operation can be performed only on one machine at one priority. Constraints (2.11); (2.12) and (2.13) denote the non-negative parameters. Constraints (2.14); (2.15) and (2.16) permitted the variables  $X_{i,j,k,p}$ ;  $Y_{i,j,k}$ ;  $Z_{i,j,k} \in \{0, 1\}$  or equivalently are binary.

### 3. Proposed hybrid scatter search method

#### 3.1. Scatter search method

Scatter search (SS) is one of the evolutionary methods [34]. The SS method was proposed in the 1970s [35]. Contrary to other evolutionary methods, SS is established on the premise which systematic designs and methods to generate new solutions afford significant benefits. It utilizes strategies for search diversification and concentration that have verified efficiency in various optimization problems [36].

SS is based on an approach to solution generation and recombination [37]. The fundamental characteristic of

SS is the diversification of optimization solutions. The steps of the SS method are given in Fig. 1.

1. An initial population is created,
2. A reference set is generated from the population,
3. A subset is selected from the reference set,
4. A combination procedure is applied to the subset,
5. An improvement procedure is applied to the combinations,
6. The reference set is updated,
7. Step 3 to Step 6 are repeated until a new reference set is needed,
8. Step 2 to Step 7 are repeated until a population is needed,
9. Step 1 to Step 8 are repeated until the stopping criterion is met.

**Figure 1.** The steps of the SS method. [38, 39]

The SS strategy is implemented by utilizing six procedures and three stopping criteria for solving an optimization problem. These six procedures are based on five components. SS has five main methods namely diversification generator, improvement, reference set update, subset generation, and solution combination method [40, 41, 42, 43]. A diversification generator is a means to start the search procedure. Improvement method is the procedure where local search procedure is defined. The reference set update method is the procedure by which the elements of the *RefSet* are selected. The Subset generation method declares the orders to choose the pairs of parents which will be combined later to constitute new solutions combination method. The method aims to generate new solutions by using the existing solutions.

### 3.2. The Hybrid scatter search method

In this study, we hybridized the basic SS by new strategies and new methods to obtain a good balance between exploration and exploitation in SS. These strategies are local and global search methods to determine the initial population. This global search method is used to escape from local optimum traps in the solution space. These strategies are good for exploration. Also, the new methods for basic SS are crossover and mutation operator and ratios. These new methods are good at exploitation.

The outline of the proposed HSS is given as follows:

- Step 1. Setting initial parameters of HSS*  
Number of the initial population,  
Number of reference set,  
Number of subsets,  
Number of updating initial population,  
Number of updating subset,  
Method of crossover,  
Method of mutation,  
The ratio of crossover,  
The ratio of mutation,  
Set CPU time.
- Step 2. Solving problem,*

- Determining initial population by the local and global search,*  
*Generate reference set,*  
*Select subset,*  
*Choose two job sequences for crossover from the subset,*  
*Do crossover*  
*If new job sequences are feasible and the objective function is better than before;*  
*Add they subset*  
*Else*  
*Eliminate they*  
*Until crossover ratio*  
*Choose a job sequence for mutation from the subset,*  
*Do mutation*  
*If the new job sequences are feasible and the objective function is better than before*  
*Add it subset*  
*Else*  
*Eliminate it*  
*Until mutation ratio*  
*Until the number of subsets*  
*Update the reference set*  
*Until the number of references set*  
*Until the stopping criterion met*  
*Step 3. Output the minimum makespan ( $C_{max}$ )*

#### 3.2.1. Initial population

The initial population is a crucial task in the scatter search algorithm [44]. In this study, two methods are presented to solve the first sub-problem by assigning each operation to a suitable machine.

The steps of the first method are given as follows [1]:

- Step 1:* A new array is created and starts each member to 0.  
*Step 2:* Choose a job randomly.  
*Step 3:* Add the processing time and the time of the corresponding machine.  
*Step 4:* Compare the added time to determine the shortest time.  
*Step 5:* Set the allele which corresponds with the current process in the machine selection part to  $k$ .  
*Step 6:* Add the processing time of the current chosen machine.  
*Step 7:* Select the next process of the current job and execute Step 3 to Step 6 until all operations of the current job are chosen, then go to Step 8.  
*Step 8:* Until all jobs are selected once, go to step 2.

A local search is used as a second method.

#### 3.2.2. Generating reference set and subset selection

The individual in the reference set comprises selecting the best individuals in the initial population. The individuals in the reference set rank from the worst to the best according to the determinate objective function. The objective function of this study is to minimize the makespan ( $C_{max}$ ). The sorted individuals are selected by starting from the best ones according to the predefined

reference set generation rate and the reference set is generated. The subsets are constituted by choosing the best individuals from individuals in the reference set because the combination and improvement procedures will be implemented over the best ones.

### 3.2.3. Crossover

Crossover is described as new individuals' generation from between two individuals selected from within the whole population according to the given rules [45]. The objective of the crossover method is to facilitate achieving the optimal result by providing the formation of better individuals. There exist different methods used in the solution of several problems. In addition to these, some methods are privately developed according to the characteristic structure of the problems. In this study, the four crossover operators are considered, namely priority-based sequential, single point, operation sequence change, and alternative machine change crossover. In the priority-based sequential crossover method, two jobs are randomly selected from the first parent individual and all the processes which belong to those jobs are selected. However, the other jobs are transferred into the child individual by selecting from the second parent individual. In the example below, 1<sup>st</sup> and 3<sup>rd</sup> jobs are randomly selected from the first parent individual (p1); the other jobs (2<sup>nd</sup> and 4<sup>th</sup> jobs) are selected from the first parent individual (p2). Then, a new child individual (c1) is generated by using p1 and p2 as shown in Fig. 2.

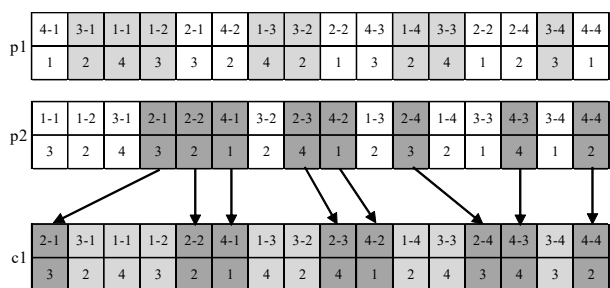


Figure 2. An example of priority-based sequential crossover operator.

Single point crossover, a point that is randomly determined on any selected individual.

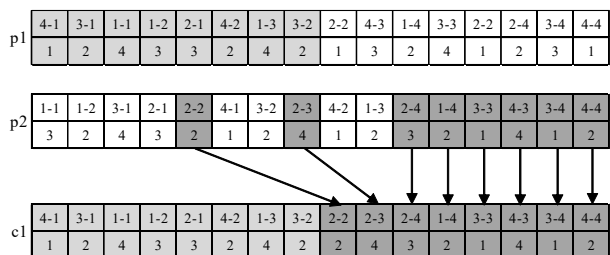


Figure 3. An example of a single-point crossover operator.

It is replaced by splitting the chromosome into two parts from that selected point. This method is used by modifying in this study.

The part of the first chromosome until the predefined cut point is transferred into the new chromosome from the first one. However, after the genes transferred from the first chromosome are extracted from the second individual, the others are transferred into the new chromosome in order. A sample of single-point crossover is shown in Fig. 3.

In the operation sequence change crossover method, it is operated on any single chromosome. Two jobs together with their whole processes are randomly selected over a single chromosome. Selected jobs are implemented by replacing over the same chromosome. An example of operation sequence change crossover is presented in Fig. 4.

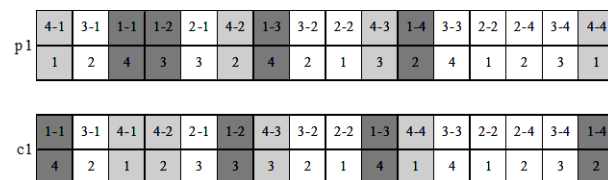


Figure 4. An example of operation sequence change crossover operator.

In the alternative machine change crossover method, the genes are randomly selected from the first chromosome. The same selected genes are chosen from the second chromosome, too. The machines of the selected genes over the second chromosome are assigned to the selected genes over the first chromosome. In sort, the method is applied by changing the machine assignment components of the same genes. An example an alternative machine change crossover is presented in Fig. 5.

### 3.2.4. Mutation

The mutation operator is implemented after crossover. Mutation used to provide diversity in the population is generally employed in small proportions because that mutation rate is great can destroy the good individuals.

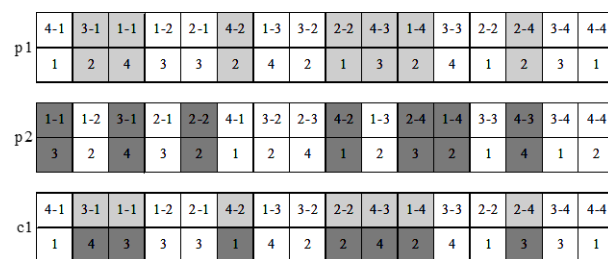


Figure 5. An example of an alternative machine change crossover operator.

In mutation, it is altered over the genes of only one individual. It is decided whether mutation will be implemented over the individual according to a defined possibility value. In this study, the four mutation operators are considered, namely random assignment machine, operation relocation, best machine change, and last operation relocation.

The random assignment machine method, a machine where a process randomly selected from the chromosome would be operated is randomly changed. This operation is performed regardless of the processing time on the machine. For example, while the machine, where the process 2-3 would be operated, is the 1<sup>st</sup> machine before mutation, the machine is changed as the 4<sup>th</sup> machine at the end of the mutation. An example of a random assignment machine is presented in Fig. 6.

Before	1-1	2-1	1-2	2-2	3-1	3-2	1-3	2-3
Mutation	2	1	3	4	3	2	3	1
After	1-1	2-1	1-2	2-2	3-1	3-2	1-3	2-3
Mutation	2	1	3	4	3	2	3	4

**Figure 6.** An example of a random assignment machine mutation operator.

In Operation Relocation Method, a process is randomly selected on the chromosome. The position of this process is changed by considering its predecessor and subsequent processes of this selected process. In the example below, the randomly selected process 1-2 is replaced with a position that is determined randomly between the process 1-1 and 1-3. A sample of operation relocation is shown in Fig. 7.

Before	1-1	2-1	1-2	2-2	3-1	3-2	1-3	2-3
Mutation	2	1	3	4	3	2	3	1
After	1-1	2-1	2-2	3-1	1-2	3-2	1-3	2-3
Mutation	2	1	4	3	3	2	3	4

**Figure 7.** An example of operation relocation mutation operator.

In the best machine change method, a machine where a randomly selected process would be operated is changed by considering the processing time. In Fig. 8, the machine where process 2-3 would be operated is changed by detecting which machine process 2-3 is operated in the shortest time on.

Before	1-1	2-1	1-2	2-2	3-1	3-2	1-3	2-3
Mutation	2	1	3	4	3	2	3	1
After	1-1	2-1	1-2	2-2	3-1	3-2	1-3	2-3
Mutation	2	1	3	4	3	2	3	3

**Figure 8.** An example of the best machine change mutation operator.

While the present machine where this process is operating in the 1<sup>st</sup> machine, the 3<sup>rd</sup> machine was assigned to operate this process after mutation. A sample of the best machine change is presented in Fig. 8. The last process on the chromosome which is randomly selected and will be mutated is determined. The position of the determined last process is randomly replaced by considering the position of the predecessor process. A sample of the last operation relocation is given in Fig. 9.

Before	1-1	2-1	1-2	2-2	3-1	3-2	1-3	2-3
Mutation	2	1	3	4	3	2	3	1
After	1-1	2-1	1-2	2-2	3-1	2-3	1-3	3-2
Mutation	2	1	3	4	3	4	3	2

**Figure 9.** An example of last operation relocation mutation operator.

### 3.2.5. Local search and reference set updating procedure

In the local search procedure, before two chromosomes which would be crossover are subjected to the crossover method, the value  $C_{max}$  is calculated according to the available machine assignment and recorded, to perform the assignment of the machine where the processes would be operated in the shortest time according to the determined process array. Then, indices of all the machines are reset. By considering the process sequences of the chromosomes in which the index of the machine has been reset, these chromosomes are subjected to crossover.

New chromosomes generated at the end of the crossover are assigned to the machine which has the earliest completion time, by starting from the beginning of the chromosome via the local search procedure. In this procedure, for the process which would assign, the algorithm assigns the machine that has the earliest completion time by scanning all the alternative machines.

The steps of the local search procedure are given as follows:

- Step 1: Reset the indices of machines in the chromosome.
- Step 2: Select operations from the chromosome depending on the order of the processes.
- Step 3: Determine the processing times on the alternative machines where the selected operation can be processed.
- Step 4: Find the completion time of the previous operation from the selected operation.
- Step 5: Find enough time spans according to the empty time span and the processing time on the alternative machine.

*Step 6:* Assign the machine which has the earliest completion time and enough time spans as the machine where the operation will be processed.

*Step 7:* Go to Step 2 until all the processes are selected.

The main objective of the local search procedure is to determine the span where the operations at the chromosome with the process sequence which occurs in the end of the crossover and mutation are earliest processed. Therefore, by assuming that the end of the previous operation is the lower limit, the whole alternative machines should be scanned for finding the machine where the operation would be earliest processed when assigning.

The solutions occurring at the end of the local search are compared to the solutions in the reference set and after new solutions are included in the reference set, the worst solutions in the reference set are removed.

### 3.2.6. Reference set population updating and stopping criteria

The values  $C_{max}$  obtained in the result of mutation are compared to the values in the reference set, if the new value is the better solution, by including it in the reference set the worst result is removed from the set and therefore the reference set is updated. This loop is executed until a new reference set is needed.

The generation and updating procedure of both population and the reference set included in the SS method contains 3 stopping criteria. These are given as follows [38]:

1. *New Reference Set Criterion*; contains the decision about when a new reference set should be created from the population.
2. *New Population Criterion*; contains the decision about when a new initial population should be generated.

**Table 2.** Parameter ratios.

Parameter	Ratio (Level)									
Initial population size	20	30	40	50	60	70	80	90	100	
Size of reference set (%)	20	30	40	50	60	70	80	90	100	
Number of subsets	2	4	6							
Number of reference set updating	50	100	150	200	250					
Number of population set updating	50	100	150	200	250					

**Table 3.** Parameter ratios for crossover methods.

Crossover Methods	Ratio									
Priority-based sequential	0.1	0.2	0.3	0.4	0.5	0.6	0.7	0.8	0.9	
Single point	0.1	0.2	0.3	0.4	0.5	0.6	0.7	0.8	0.9	
Operation sequence change	0.1	0.2	0.3	0.4	0.5	0.6	0.7	0.8	0.9	
Alternative machine change	0.1	0.2	0.3	0.4	0.5	0.6	0.7	0.8	0.9	

3. *Stopping Criterion*; contains the decision about when the whole searching operations set should be stopped.

## 4. Computational results

### 4.1. Parameter test

A full factorial experimental design is made to determine the best values of control parameters and operators for the proposed new HSS to solve the FJSS problems.

The developed new HSS algorithm is examined on the benchmark instances. First studies are conducted on the problem group that belongs to Fattahi et al. [46]. Besides, the algorithm is also carried out for the problem groups formed by Kacem et al. [7,47] and Fattahi et al. [12].

The parameters used in the HSS method are utilized as fixed in all the problems. The optimization where all the levels are examined is carried out by dividing 20 parts which have Intel Xenon CPU E5-1650 3Ghz and 8GB RAM. The parameters and the ratio (levels) are given in Tables 1, 2, 3, and 4.

**Table 1.** The ratios of the global, local, and random methods.

Method	Ratio			
Global search	0.6	0.5	0.4	0.3
Local search	0.3	0.4	0.5	0.6
Random	0.1	0.1	0.1	0.1

The best values of global, local, and random search methods ratios are found as follows:

- Global search method : 0.6
- Local search method : 0.3
- Random method : 0.1

**Table 4.** Parameter ratios for mutations methods.

Mutation methods	Ratio		
Random assignment machine	0.05	0.1	0.15
Operation relocation	0.05	0.1	0.15
Best machine change	0.05	0.1	0.15
Last operation relocation	0.05	0.1	0.15

The best parameter values are found by the full factorial experimental design. These parameters are given in Tables 5, 6, and 7.

**Table 5.** Initial parameter values.

Initial parameters of proposed HSS	
Size of the initial population	40
Size of reference set (%)	30
Number of subsets	6
Number of reference set updating	200
Number of population set updating	40

**Table 6.** The best ratios for crossover methods.

Crossover methods	Ratio
Priority-based sequential	0.6
Single point	0.2
Operation sequence change	0.2
Alternative machine change	0.7

**Table 7.** The best ratios for mutation methods.

Mutation methods	Ratio
Random assignment machine	0.05
Operation relocation	0.1
Best machine change	0.1
Last operation relocation	0.05

#### 4.1.1. Performance comparison of HSS

The objective function of the proposed HSS is minimizing the maximum completion time ( $C_{max}$ ). The algorithm is examined on two different benchmark sets of problems.

The first test set of the problem is SFJS and MFJS group containing 20 problems and developed by Fattahi et al. [12]. While 10 of the problems in this group consist of small jobs; the remaining 10 problems consist of major jobs. To solve these problems, Fattahi et al. [12] proposed a mathematical model and heuristic approach. For small jobs (SFJS1,..., SFJS10) their mathematical model achieved optimal solution but for major jobs did not find any optimal solutions in a reasonable time by mathematical model since FJSS problem is NP-hard. Then, Özgüven et al. [33] developed a mixed-integer linear programming model for solving FJSS problems. They used the same benchmark problems with Fattahi et al. [12]. They obtained optimal solutions for small jobs (SFJS1,...,

SFJS10) like Fattahi et al. [12]. They also found for only five of major jobs problems optimal solutions in a reasonable time. Later, Birgin et al. [19] proposed a new a mixed-integer linear programming model for solving FJSS problems. They used the same benchmark problems with Fattahi et al. [12]. They obtained optimal solutions for small jobs (SFJS1,..., SFJS10) like Fattahi et al. [12] and Özgüven et al. [33]. They also found for only seven of major jobs problems optimal solutions in a reasonable time. For this reason, we proposed a new HSS method for solving the FJSS problems.

The results, in Table 8, acquired by running the algorithm are compared to the studies which are conducted for this set of problems in the literature. For all benchmark problems relative percentage deviation is calculated. The performance of the heuristic is calculated as the relative percentage deviation (RPD) with Equation 4.1 [12, 33, 16, 19].

$$RPD = \frac{\text{Heuristic Algorithm}(C_{max}) - \text{Lower Bound}}{\text{Lower Bound}} \times 100 \quad (4.1)$$

In Equation 4.1, *Lower Bound (LB)* states the known lower bound of  $C_{max}$  obtained from the literature for benchmark problems. In Table 8, the proposed HSS method found the known best  $C_{max}$  value for eighteen problems. Only two benchmark problems, the proposed HSS couldn't find the best  $C_{max}$ .

The RPD and average relative percentage deviation (ARPD) of the proposed HSS method are compared with the Fattahi et al. [12]; Özgüven et al. [33]; Bagheri et al. [16] and Birgin et al. [19] from the literature. The ARPD is evaluated with Equation 4.2. The number of instances for each method is defined as I ( $L = 1, \dots, I$ ) notation at Equation 4.2.

$$ARPD = \sum_{L=1}^I \frac{RPD}{I} \quad (4.2)$$

In Table 8, the proposed HSS method found the minimum ARPD value for all twenty benchmark problems. When the obtained results are analyzed; the proposed HSS method is effective for the FJSS problems.

The proposed HSS method found the new job sequence for the MFJS9 benchmark problem The Gant schema of the MFJS9 benchmark problem is given in Fig. 10. It can be seen from Fig. 10, the best  $C_{max}$  is found 1060.

The second test instance is consisting of three different problems (K-A1, K-A2 and K-B1). The instances are developed by Kacem et al. [7,47]. These problems are also used by several studies in the literature for testing. The proposed new HSS's results are compared with the Kacem et al. [7,47], Xia and Wu [48]; Gao et al. [11] and Bagheri et al. [16] results from the literature.



The results are given in Table 9. It can be seen from Table 9 the proposed new HSS is found the best values of these three benchmark instances. The Gant schema of K-B1 in this problem group is presented in Fig. 11.

**Table 9.** The comparison of the  $C_{max}$  for the second benchmark instances.

Problem	K-A1 <sup>a</sup>	K-A2 <sup>b</sup>	K-B1 <sup>c</sup>	
$i*k$	8*8	10*10	15*10	
$j$	27	30	56	
$C_{max}$	Kacem et al. [7,47]	14	7	11
	Xia and Wu [48]	15	7	12
	Gao et al. [11]	14	7	11
	Bagheri et al. [16]	14	7	11
	Proposed HSS	14	7	11

a Benchmark Problems 8\*8 [7]

b Benchmark Problems 10\*10 [7]

c Benchmark Problems 15\*10 [47]

The proposed HSS is compared with the Kacem and SFJS-MFJS benchmark instances from the literature. The results are given in Tables 10 and 11.

**Table 10.** The performance of the proposed new HSS compared with Kacem benchmark problems.

Algorithm	Proposed new HSS ( $C_{max}$ )		
	Equal	Better	Total
Kacem et al. [7,47]	3		3
Xia and Wu [48]	1	2	3
Gao et al. [11]	3		3
Bagheri et al. [16]	3		3

In Table 10, the proposed new HSS method is given a better makespan ( $C_{max}$ ) for two problems according to the Xia and Wu [48] method. Also, the proposed new HSS method is given equal makespan ( $C_{max}$ ) for eleven problems according to Kacem et al [7,47], Xia and Wu [48], Gao et al. [11], and Bagheri et al. [16] methods from the literature.

It can be seen in Table 11, the proposed new HSS method is given the better makespan ( $C_{max}$ ) for 77 instances according to the Fattahi et al. [12]; Özgüven et al. [33]; Bagheri et al. [16], and Birgin et al. [19]'s methods. Also, the proposed new HSS method is given equal makespan ( $C_{max}$ ) for 103 instances according to the Fattahi et al. [12]; Özgüven et al. [33]; Bagheri et al. [16], and Birgin et al. [19]'s methods from the literature.

**Table 11.** The performance of the proposed new HSS compared with SFJS-MFJS benchmark problems.

Algorithm	Proposed new HSS ( $C_{max}$ )			
	Equal	Better	Total	
[12]	HSA/SA <sup>a</sup>	10	10	20
	HSA/TS <sup>b</sup>	10	10	20
	HTS/TS <sup>c</sup>	10	10	20
	HTS/SA <sup>d</sup>	9	11	20
	ISA <sup>e</sup>	9	11	20
	ITS <sup>f</sup>	9	11	20
[33]	MILP <sup>g</sup>	14	6	20
[16]	AIA <sup>h</sup>	14	6	20
[19]	AMILP <sup>i</sup>	18	2	20

a Hierarchical approach and SA heuristic for assignment problem and SA heuristic for sequencing problem.

b Hierarchical approach and SA heuristic for assignment problem and TS heuristic for sequencing problem.

c Hierarchical approach and TS heuristic for assignment problem and TS heuristic for sequencing problem.

d Hierarchical approach and TS heuristic for assignment problem and SA heuristic for sequencing problem.

e Integrated approach with simulated annealing heuristic

f Integrated approach with tabu search heuristic

g Mixed-integer linear programming

h Artificial immune algorithm

i A mixed-integer linear programming

**Table 8.** The comparison results of the first twenty benchmark instances from the literature.

Problem	i,j,k	LB	Fattahi et al. (2007)												Özgülven et al. (2010)		Bagheri et al. (2010)		Birgin et al. (2013)		Proposed HSS													
			HSA/SA <sup>a</sup>		RPD	HSA/TS <sup>b</sup>		RPD	HTS/TS <sup>c</sup>		RPD	HTS/SA <sup>d</sup>		RPD	ISA <sup>e</sup>	RPD	ITS <sup>f</sup>	RPD	MILP <sup>g</sup>	RPD	AIA <sup>h</sup>	RPD	AMILP <sup>i</sup>	RPD	HSS	RPD								
			C <sub>max</sub>	CPU		C <sub>max</sub>	CPU		C <sub>max</sub>	CPU		C <sub>max</sub>	CPU		C <sub>max</sub>	CPU		C <sub>max</sub>	CPU		C <sub>max</sub>	CPU		C <sub>max</sub>	CPU		C <sub>max</sub>	CPU		C <sub>max</sub>	CPU		C <sub>max</sub>	CPU
SEJS1	2*2*2	66	66	12	-	66	1	-	66	1	-	66	2	-	66	25	-	66	1	-	66	0.02	-	66	0.03	-	66	0	-	66	1	-		
SEJS2	2*2*2	107	107	13	-	107	1	-	107	1	-	107	3	-	107	35	-	107	1	-	107	0	-	107	0.03	-	107	0.01	-	107	1	-		
SEJS3	3*2*2	221	221	14	-	221	1	-	221	1	-	221	5	-	221	40	-	221	1	-	221	0.02	-	221	0.04	-	221	0.05	-	221	1	-		
SEJS4	3*2*2	355	355	14	-	355	1	-	355	1	-	355	7	-	355	45	-	355	1	-	355	0	-	355	0.04	-	355	0.02	-	355	1	-		
SEJS5	3*2*2	119	119	14	-	119	2	-	119	1	-	119	9	-	119	50	-	119	1	-	119	0.06	-	119	0.04	-	119	0.04	-	119	1	-		
SEJS6	3*3*2	320	320	18	-	320	3	-	320	1	-	320	7	-	320	50	-	320	2	-	320	0.03	-	320	0.04	-	320	0.01	-	320	1	-		
SEJS7	3*3*5	397	398	19	-	398	4	-	398	1	-	398	9	-	398	55	-	398	2	-	398	0.02	-	398	0.04	-	398	0	-	398	1	-		
SEJS8	3*3*4	253	253	17	-	253	5	-	253	2	-	256	10	1.2	253	35	-	253	2	-	253	0.02	-	253	0.05	-	253	0.04	-	253	1	-		
SEJS9	4*3*5	210	210	19	-	210	6	-	210	2	-	210	11	-	215	55	2.3	215	3	2.3	210	0.03	-	210	0.05	-	210	0.01	-	210	1	-		
SEJS10	5*3*5	516	516	21	-	516	7	-	516	4	-	516	10	-	516	55	-	516	3	-	516	0.02	-	516	0.05	-	516	0.02	-	516	1	-		
MEJS1	5*3*6	396	479	22	21.0	491	55	24.0	469	15	18.4	469	30	18.4	488	60	23.2	548	9	38.4	468	0.44	18.2	468	9.23	18.2	468	0.26	18.2	468	7	18.2		
MEJS2	5*3*7	396	495	62	25.0	482	55	21.7	482	12	21.7	468	30	18.2	478	60	20.7	457	8	15.4	446	6.49	12.6	448	9.35	13.1	446	0.87	12.6	446	24	12.6		
MEJS3	6*3*7	396	553	82	39.6	538	75	35.9	533	20	34.6	538	50	35.9	599	107	51.3	606	8	53.0	466	4.14	17.7	468	10.06	18.2	466	1.66	17.7	466	32	17.7		
MEJS4	7*3*7	496	656	102	32.3	650	85	31.0	634	27	27.8	618	80	24.6	703	195	41.7	870	9	75.4	564	1779.03	13.7	554	10.54	11.7	554	27.43	11.7	554	253	11.7		
MEJS5	7*3*7	414	650	105	57.0	662	110	59.9	625	40	51.0	625	64	51.0	674	240	62.8	729	10	76.1	514	50.98	24.2	527	10.61	27.3	514	4.55	24.2	514	219	24.2		
MEJS6	8*3*7	469	762	125	62.5	785	130	67.4	717	96	52.9	730	102	55.7	856	330	82.5	816	50	74.0	635	3600	35.4	635	22.18	35.4	634	52.48	35.2	634	180	35.2		
MEJS7	8*4*7	619	1020	197	64.8	1081	290	74.6	964	129	55.7	947	190	53.0	1066	480	72.2	1048	240	69.3	935	3600	51.1	879	24.82	42.0	879	1890	42.0	879	6000	42.0		
MEJS8	9*4*7	619	1030	230	66.4	1122	325	81.3	970	405	56.7	922	182	48.9	1328	610	114.5	1220	370	97.1	905	3600	46.2	884	26.94	42.8	884	3600	42.8	884	7200	42.8		
MEJS9	11*4*8	764	1180	330	54.5	1243	660	62.7	1105	660	44.6	1105	330	44.6	1148	840	50.3	1124	680	47.1	1192	3600	56.0	1088	30.76	42.4	1137	3600	48.8	1060	7200	38.7		
MEJS10	12*4*8	944	1538	425	62.9	1615	600	71.1	1404	960	48.7	1384	430	46.6	1546	850	63.8	1737	763	84.0	1276	3600	35.2	1267	30.94	34.2	1251	3600	32.5	1208	7200	28.0		
ARPD			48.59		52.96		41.22		39.69		58.30		62.98		31.02		28.53		28.57		27.10													

<sup>a</sup> Hierarchical approach and simulated annealing (SA) heuristic for assignment problem and SA heuristic for sequencing problem.

<sup>b</sup> Hierarchical approach and SA heuristic for assignment problem and tabu search (TS) heuristic for sequencing problem.

<sup>c</sup> Hierarchical approach and TS heuristic for assignment problem and TS heuristic for sequencing problem.

<sup>d</sup> Hierarchical approach and TS heuristic for assignment problem and SA heuristic for sequencing problem.

<sup>e</sup> Integrated approach with SA heuristic.

<sup>f</sup> Integrated approach with TS heuristic.

<sup>g</sup> Mixed-integer linear programming

<sup>h</sup> Artificial immune algorithm

<sup>i</sup> A mixed-integer linear programming

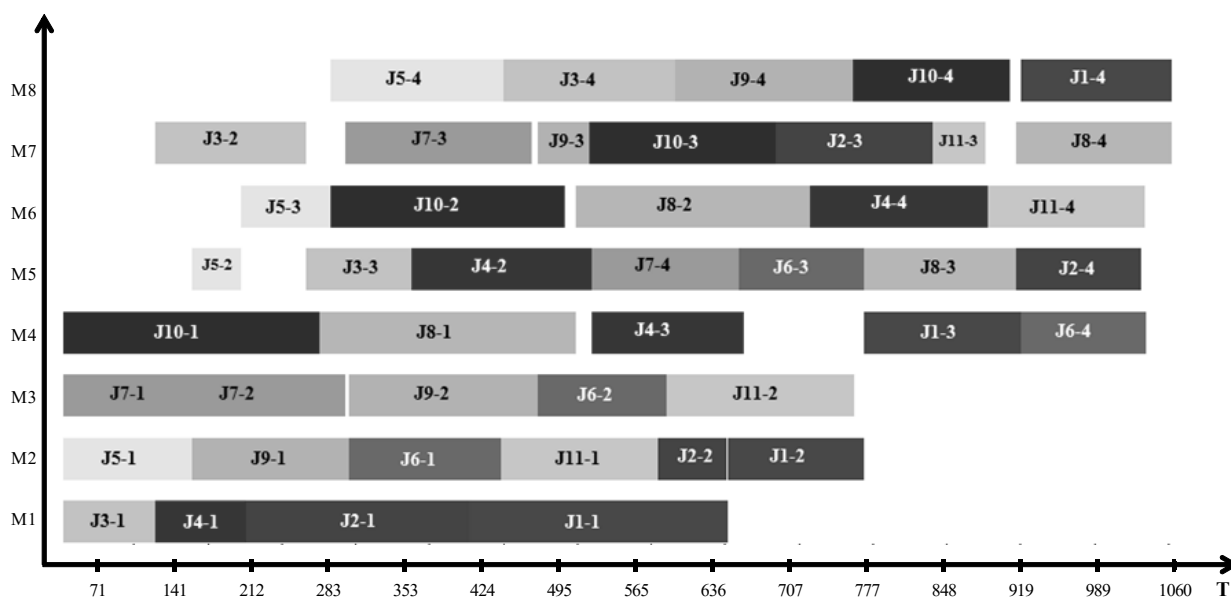


Figure 10. Gantt Schema of the MFJS9 instance.

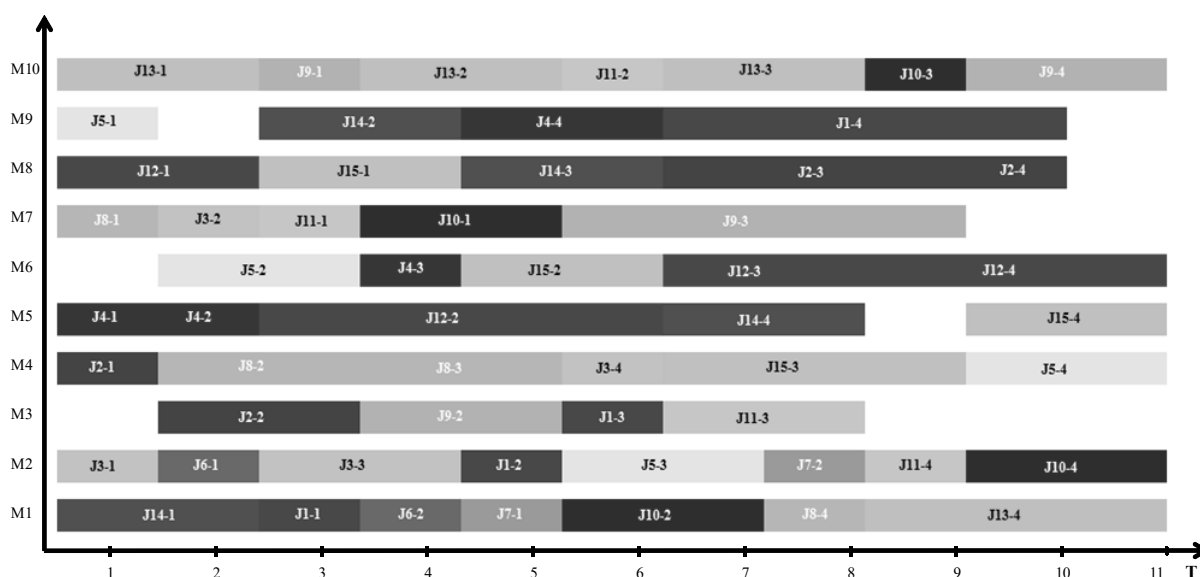


Figure 11. The Gantt schema of K-B1.

### 5. Conclusion and future research

The flexible job shop is extra routing sub-problems of the job shop scheduling problems. The FJSS is known as an NP-hard problem from the literature. In this study, a new HSS method is proposed to solve the FJSS problems. The proposed HSS method is iterated the local and global search method for the initial population. The HSS method is consisting of the initial population, reference set, subset, reference set updating, population sub updating, reproduction, crossover, mutation operators, and their ratio. To determine the best parameter set of the proposed HSS for solving the FJSS problems a full factorial experimental design is

made. The performance of the proposed HSS method is examined on the benchmark problems. There exist several problems with various sizes in the literature. First, the examinations on the problem groups consisting of 20 examples and developed by Fattahi et al. [12]. The proposed HSS method is found more efficient results for these problems. The second test problem is developed by Kacem et al. consisting of 3 instances [7,47]. When analyzed the results of the tests. The developed new HSS method is seen to produce efficient results on these benchmark instances. According to the computational results, the proposed new HSS method is influential in terms of reduced makespan for the FJSS problems. The proposed new

HSS is an efficient problem-solving technique for FJSS problems.

For future research, the proposed HSS heuristics may be used for multi-objective FJSS problems.

### Author's Contributions

Safa KÜLAHLI: Methodology, Data curation, Writing-original draft, Visualization, Investigation  
Orhan ENGİN: Supervision, Methodology, Validation, Writing-original draft, Investigation, Conceptualization,  
İsmail KOÇ: Methodology, Software, Writing-original draft, Visualization.

### Ethics

There are no ethical issues after the publication of this manuscript.

### References

1. Zhang, G, Gao, L, Shi, Y. 2011. An effective genetic algorithm for the flexible job-shop scheduling problem. *Expert System with Application*; 38: 3563-3573.
2. Yazdani, M, Amiri, M, Zandieh, M. 2010. Flexible job-shop scheduling with parallel variable neighborhood search algorithm. *Expert System with Application*; 37: 678-687.
3. Rossi, R, Tarim, SA, Hnich, B, Prestwic, S, Karacaer, S. 2010. Scheduling internal audit activities: a stochastic combinatorial optimization problem. *Journal of combinatorial optimization*; 19: 325- 346.
4. Karimi, H, Rahmati, SHA, Zandieh, M. 2012. An efficient knowledge-based algorithm for the flexible job shop scheduling problem. *Knowledge-Based System*; 36: 236-244.
5. Hwang, S, Cheng, ST. 2001. Combinatorial optimization in real-time scheduling: Theory and Algorithms. *Journal of combinatorial optimization*; 5: 345- 375.
6. Brucker, P, Schlie, R. 1990. Job-shop scheduling with multi-purpose machines. *Computing*; 45: 369-375.
7. Kacem, I, Hammadi S, Borne P. 2002. Approach by localization and multi-objective evolutionary optimization for flexible job-shop scheduling problems. *IEEE Transactions on Systems, Man, and Cybernetics*; 32: 1-13.
8. Tay, J, Wibowo, D. 2004. An Effective Chromosome Representation for Evolving Flexible Job Shop Schedules. In: Genetic and Evolutionary Computation GECCO - Eds: Deb K: Springer Berlin Heidelberg, 210-221.
9. Ong, Z, Tay, J, Kwoh, C. 2005. Applying the Clonal Selection Principle to Find Flexible Job-Shop Schedules, Artificial Immune Systems. Eds: Jacob C, Pilat M, Bentley P, Timmis J: Springer Berlin Heidelberg, 442-455.
10. Ho, N, Tay, J, Lai, E. 2007. An effective architecture for learning and evolving flexible job-shop schedules. *European Journal of Operational Research*; 179: 316-333.
11. Gao, J, Sun, L, Gen, M. 2008. A hybrid genetic and variable neighborhood descent algorithm for flexible job shop scheduling problems. *Computer Operation Research*; 35: 2892-2907.
12. Fattahi, P, Mehrabad, MS, Jolai, F. 2007. Mathematical modeling and heuristic approaches to flexible job shop scheduling problems. *Journal of Intelligent Manufacturing*; 18: 331-342.
13. Gholami, M, Zandieh, M. 2008. Integrating simulation and genetic algorithm to schedule a dynamic flexible job shop. *Journal of Intelligent Manufacturing*; 20: 481-498.
14. Xing, L, Chen, YW, Zhao, Q, Xiong, J. 2009. A knowledge-based ant colony optimization for flexible job shop scheduling problems. *Applied Soft Computing*; 10: 888-896.
15. Zhang, G, Shao, X, Li, P, Gao, L. 2009. An effective hybrid particle swarm optimization algorithm for multi-objective flexible job-shop scheduling problem. *Computers & Industrial Engineering*; 56: 1309-1318.
16. Bagheri, A, Zandieh, M, Mahdavi, I, Yazdani, M. 2010. An artificial immune algorithm for the flexible job-shop scheduling problem. *Future Generation Computer Systems*; 26: 533-541.
17. Guohui, Z, Liang, G, Yang, S. 2010. Genetic algorithm and tabu search for multi objective flexible job shop scheduling problems. *International Conference on Computing, Control, and Industrial Engineering (CCIE)*; 251-254.
18. Wang, S, Yu, J. 2010. An effective heuristic for flexible job-shop scheduling problem with maintenance activities. *Computers & Industrial Engineering*; 59: 436-447.
19. Birgin, EG, Feofiloff, P, Fernandes, CG, EL. de Melo, Oshiro MTI, Ronconi DP. 2013. A MILP model for an extended version of the Flexible Job Shop Problem. *Optimization Letters*; 8: 1417-1431.
20. Demir, Y, İşleyen, SK. 2013. Evaluation of mathematical models for flexible job-shop scheduling problems. *Applied Mathematical Modelling*; 37: 977-988.
21. Yuan, Y, Xu, H. 2013. Flexible job shop scheduling using hybrid differential evolution algorithms. *Computers & Industrial Engineering*; 65: 246-260.
22. Demir, Y, İşleyen SK. 2014. An effective genetic algorithm for flexible job-shop scheduling with overlapping in operations. *International Journal of Production Research*; 52: 3905-3921.
23. Abdelmaguid, TF. 2015. A neighborhood search function for flexible job shop scheduling with separable sequence-dependent setup times. *Applied Mathematical Computing*; 260: 188-203.
24. Gao, KZ, Suganthan, PN, Chua, TJ, Chong, CS, Cai, TX, Pan, QK. 2015. A two-stage artificial bee colony algorithm scheduling flexible job-shop scheduling problem with new job insertion. *Expert System Applied*; 42: 7652-7663.
25. González, MA, Vela, CR, Varela, R. 2015. Scatter search with path relinking for the flexible job shop scheduling problem. *European Journal Operation Research*; 245: 35-45.
26. Ishikawa, S, Kubota, R, Horio, K. 2015. Effective hierarchical optimization by a hierarchical multi-space competitive genetic algorithm for the flexible job-shop scheduling problem. *Expert System with Application*; 42: 9434-9440.
27. Singh, MR, Mahapatra, SS. 2016. A quantum behaved particle swarm optimization for flexible job shop scheduling. *Computers & Industrial Engineering*; 93: 36-44.
28. Zabihzadeh, SS, Rezaeian, J. 2016. Two meta-heuristic algorithms for flexible flow shop scheduling problem with robotic transportation and release time. *Applied Soft Computing*; 40: 319-330.
29. Li, X, Peng, Z, Du, B, Guo, J, Xu, W, Zhuang. 2017. Hybrid artificial bee colony algorithm with a rescheduling strategy for solving



- flexible job shop scheduling problems. *Computers and Industrial Engineering*; 113: 10- 26.
30. Shen, L, Dauzère-Pérès, S, Neufeld, JS. 2018. Solving the flexible job shop scheduling problem with sequence-dependent setup times. *European Journal of Operational Research*; 265: 503-516.
31. Min, D, Dunbing, T, Adriana, G, Salido, MA. 2019. Multi-objective optimization for energy-efficient flexible job shop scheduling problem with transportation constraints. *Robotics-Integrated Manufacturing*; 59: 143-157.
32. Li, JQ, Deng, JW, Li, CY, Han, YY, Tian, J, Zhang, B, Wang, CG. 2020. An improved Jaya algorithm for solving the flexible job shop scheduling problem with transportation and setup times. *Knowledge-Based Systems*; 200: 106032.
33. Özgüven, C, Özbakır, L, Yavuz, Y. 2010. Mathematical models for job-shop scheduling problems with routing and process plan flexibility. *Applied Mathematical Modelling*; 34: 1539-1548.
34. Engin, O, Yılmaz, MK, Baysal, ME, Sarucan, A, 2013. Solving fuzzy job shop scheduling problems with availability constraints using a scatter search method. *Journal of Multi-Valued Logic and Soft Computing*; 21: 317-334.
35. Engin, O, Kahraman, C, Yılmaz, MK, 2009. A Scatter Search Method for Multi Objective Fuzzy Permutation Flow Shop Scheduling Problem: A Real-World Application, 169-189, Computational Intelligence in Flow Shop and Job Shop Scheduling, Springer, Uday K. Chakraborty (Ed.), ISBN:978-3-642-02836-6.
36. Marti, R. 2003. Principles of Scatter Search, Leeds School of Business, University of Colorado, Campus Box 419, Boulder, CO.
37. Naderi, B, Ruiz, R. 2014. A scatter search algorithm for the distributed permutation flow shop scheduling problem. *European Journal Operation Research*; 239: 323-334.
38. Cano, DB, Santana, JB, Rodriguez, CC, DelAmo IJG, Torres MG, Garcia, FJM, Batista, BM, Perez, JAM, Vega, JMM, Martin, RR. 2004. Nature-inspired components of the Scatter Search, Technical Report.
39. Oktay, S, Engin, O. 2006. Scatter search method for solving industrial problems: literature survey. *Journal of Engineering and Natural Sciences*; 3: 144- 155.
40. Glover, F, 1998. A template for scatter search and path relinking. *Artificial Evolution*; 1363: 3-51.
41. Glover, F, Laguna, M, Marti, R. 2000. Fundamentals of scatter search and path relinking. *Control Cybernetics*; 29: 653-684.
42. Marti, R. 2006. Scatter search - Wellsprings and challenges. *European Journal Operation Research*; 169: 351-358.
43. Marti, R, Laguna, M, z, F. 2006. Principles of scatter search. *European Journal Operation Research*; 169: 359-372.
44. Engin, O, Ceran, G, Yılmaz, MK. 2011. An efficient genetic algorithm for hybrid flow shop scheduling with multiprocessor task problems. *Applied Soft Computing*; 11(3): 3056-3065.
45. Kahraman, C, Engin, O, Kaya, I, Yılmaz, MK. 2008. An application of effective genetic algorithms for solving hybrid flow shop scheduling problems. *International Journal of Computational Intelligence Systems*; 1(2): 134- 147.
46. Fattahi, P, Jolai, F, Arkat, J. 2009. Flexible job shop scheduling with overlapping in operations. *Applied Mathematical Modelling*; 33: 3076-3087.
47. Kacem, I., Hammadi, S., Borne, P. 2002. Pareto-optimality approach for flexible job-shop scheduling problems: hybridization of evolutionary algorithms and fuzzy logic. *Mathematics and computers in simulation*, 60(3-5): 245-276.
48. Xia, W, Wu, Z, 2005. An effective hybrid optimization approach for multi-objective flexible job-shop scheduling problems. *Computers & Industrial Engineering*; 48(2): 409-425.



# Analysis of Factors Affecting Coronaphobia by Analytical Network Process

Edanur Sonel<sup>1</sup> , Şeyda Gür<sup>2</sup> , Tamer Eren<sup>3\*</sup> 

<sup>1</sup> Kırıkkale University, Department of Industrial Engineering, Kırıkkale

<sup>2</sup> Harran University, Organized Industrial Zone Vocational School, Şanlıurfa

<sup>3</sup> Kırıkkale University, Department of Industrial Engineering, Kırıkkale

\* [tamereren@gmail.com](mailto:tamereren@gmail.com)

\*Orcid: 0000-0001-5282-3138

Received: 16 March 2021

Accepted: 6 December 2021

DOI: 10.18466/cbayarfbe.898038

## Abstract

Coronavirus, which has spread worldwide and become a pandemic, threatens human health both physically and mentally. Physical threats consist of permanent damage, which is not yet clear, and symptoms such as high fever, shortness of breath experienced by individuals infected with coronavirus. Mental threats, on the other hand, cause fear of coronavirus, that is, coronaphobia and various psychological problems. The purpose of the study is to determine the factors affecting coronaphobia and to reduce or eliminate their effect on people. For this purpose, high priority factors obtained as a result of the ANP method should be examined and studies should be carried out to reduce or eliminate the effects of these factors. In this study, the factors affecting coronaphobia were determined and analyzed in order to reduce and eliminate coronaphobia. This analysis was carried out by the analytical network process (ANP), one of the Multi-Criteria Decision Making (MCDM) methods. According to the priority values obtained as a result of comparing relationships and relationships established by the ANP method; the most important criterion affecting coronavirus fear is the criterion of psychological factors. The most important sub-criteria are weak immune system, hygiene concern and stress disorder, respectively. In this study, the factors affecting coronavirus fear were discussed in general. Among the factors discussed, weighted scores were obtained by establishing bilateral relations using the ANP method. The factors covered in the study consist of 3 main criteria and 14 main criteria covered by these criteria.

**Keywords:** Coronavirus, Fear of Coronavirus, Coronaphobia, Community Psychology

## 1. Introduction

Epidemics are phenomena whose effects and consequences are unpredictable. Epidemics, which are deadly factors for humans and animals, have deeply affected individual and social life and have caused significant changes [1]. The history of epidemics dates back to when humanity began to cultivate the land. A close relationship between man and nature has led to many diseases carried by animals also starting to appear in humans and causing deaths [2].

When the history of epidemics experienced by people is examined, it is seen that many diseases such as cholera, smallpox, tuberculosis, plague, malaria, SARS, MERS, ebola are fought. The cholera epidemic has led people to increase hygiene measures, the smallpox epidemic to find a vaccine, the tuberculosis epidemic to develop live vaccines and the plague quarantine measures [3]. A new

type of coronavirus (Covid-19) is an epidemic that creates this effect today and becomes a pandemic.

Coronavirus is a single-stranded RNA virus in the family coronaviridae [4]. Coronavirus of zoonotic origin has taken over the entire world as it begins to transmit from person to person.

With increasingly spreading coronavirus that are passed from person to person; high fever, fatigue, dry cough, muscle pain, shortness of breath, palpitations, diarrhea, headache, conjunctivitis, lost in the senses of smell and taste and is determined with symptoms such as respiratory problems [5].

In addition to symptoms and disease, it was understood that some patients who tested positive for coronavirus had open and closed disease symptoms such as burning and dry cough in their lungs even after a short time.

During the scans, light gray spots are often displayed in the lungs of patients, this scar tissue in the lung does not allow physiological breathing, such tissue changes cause permanent damage [6]. That the virus can stick to cells in almost all tissues; it is observed that it can cause permanent damage to the heart, blood vessels, kidneys and brain and with its psychological effects, this condition becomes more complicated [1].

Outbreaks are known to have traumatic effects, raising the level of anxiety and stress [7]. For this reason, it is considered natural for Epidemic conditions to affect mood [8].

Factors such as loss of function due to disease in patients, pain caused by the disease usually negatively affect psychology. In healthy individuals at risk of an epidemic, conditions such as the danger of contracting the disease, the possibility of losing their job, freedoms and some opportunities, the inability to maintain their routine life negatively affect psychology and turn into behavioral disorders [9].

Psychological problems and behavioral disorders caused by the pandemic also raise the concept of coronaphobia, which was raised after the coronavirus pandemic. Coronaphobia is the fear felt by the virus and the effects that come with the virus. In this study, the factors affecting coronaphobia were determined and analyzed in order to reduce and eliminate coronaphobia. This analysis was carried out by the Analytical Network Process (ANP), one of the Multi-Criteria Decision Making (MCDM) methods.

MCDM is the evaluation of a finite number of options using a large number of criteria, mostly weighted for the purpose of selection, ranking, classification, prioritization or elimination [10].

ANP is a method that expresses problems in the form of a network by defining relationships and aspects between criteria and also takes into account indirect interactions and feedback that may be between criteria that are not directly related [11]. The fact that the method considers the effects of the criteria on each other shows us the robustness of the solution process in the problem. Without the commitment to a single direction, each criterion can affect both the criteria in its own group and all other criteria. In other words, the ANP method was preferred because it takes into account internal and external dependencies.

The purpose of the study is to determine the factors affecting coronaphobia and to reduce or eliminate their effect on people. For this purpose, high priority factors obtained as a result of the ANP method should be examined and studies should be carried out to reduce or eliminate the effects of these factors. The criteria determined in the study were obtained by examining the studies found in the literature and investigating the effects of coronavirus fear on humans.

## 2. Materials and Methods

A decision is a general expression of a person's choices within the alternatives that he or she faces at any moment [12]. Multi-criteria decision making can be defined as the selection process that the decision maker makes using at least two criterias in a set of countable finite or uncountable numbers of options [13].

The ANP method eliminates the need to model the problem by adhering to a single direction, taking into account the relationships between factors in the decision-making process. In the ANP method developed by Thomas L. Saaty, the decision-making problem is modeled by a network structure and the dependencies between factors at the modeling stage and the internal dependencies within the factor are taken into account. The ANP method provides a more effective and realistic solution of decision-making problems with this structure [11]. Researchers have found the opportunity to apply the ANP method on different subjects in the literature. It is used in many areas, such as choosing a service provider in logistics, choosing a location, choosing a green supplier, selecting R&D projects, choosing maintenance strategies, and selecting personnel [14-19].

### 2.1. Analytical Network Process Method Steps

1. Decision-making problem, main and sub-criteria are determined.
2. The relationship of the criteria with each other is determined. Relationships are established between internal and external dependencies and feedback found between criteria, if any.
3. Binary comparisons between criteria are made. By the decision maker or decision group, values are given on a scale of 1-10 for comparisons.
4. Check whether the comparison matrices are consistent. To determine whether comparisons are consistent, the consistency ratio is calculated for each matrix after the comparison matrices are configured.
5. Super-matrices are formed sequentially. A super matrix is a segmented Matrix and each matrix division shows the relationship between two criteria contained in a system [20].
6. The best alternative is determined and the choice is made [21].

## 3. Results

This study was conducted to determine the priority values of factors and factors affecting coronaphobia. Helping studies to reduce/eliminate the effects of coronaphobia on humans is one of the goals of the study. Factors affecting coronaphobia were analyzed by ANP method from MCDM methods. The purpose of this analysis is to determine the priority values of factors affecting coronaphobia and to support studies to defeat coronaphobia.



**Table 1.** Criteria and Descriptions.

Criteria	Sub-Criteria	Descriptions
Psychological Factors	Fear of losing	People worry about losing loved ones because of the virus.
	Isolation concern	The obligation to stay in quarantine and the fear of being away from public life.
	Stress disorder	A state of inability to control your feelings that causes people to feel helpless
	Worry about getting out of comfort zone	The anxiety people feel when they have to go outside of the actions they are used to.
Outer Factors	Negative media news	Negative, unreal and exaggerated news announced by the media.
	Case numbers	Increased rate of coronavirus spread and expansion of risky areas.
	Deaths	Increased mortality and fear of death in the immediate vicinity of people.
	Ambiguity	The obscurity brought by the pandemic process.
	Distrust of the health sector	The lack of a reduction in the number of deaths and cases is a lack of confidence due to the occupancy of health institutions.
	Inadequate measures	People don't follow the rules of social distance, use the wrong mask, and can't adapt to the pandemic.
	Hygiene concern	Sensitivity to hygiene.
Personal Factors	Unconscious society	Society acting uninformed and unconscious, the desire to socialize.
	Weak immune system	Having chronic ailments and a weak immunity.
	Lack of information	Lack of knowledge about coronavirus and its propagation pathways.

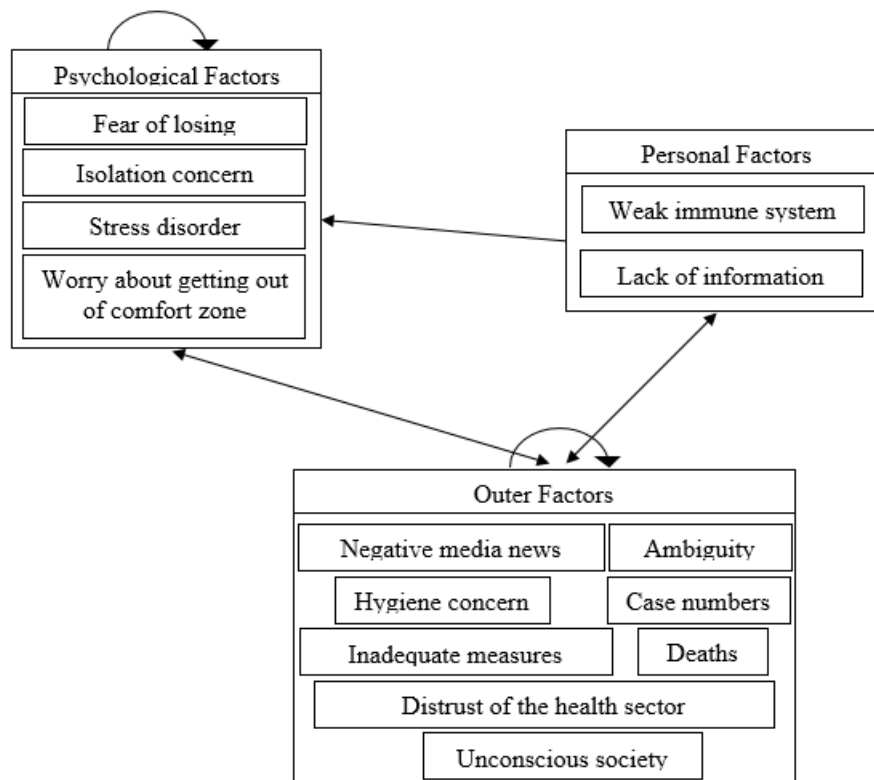


**Figure 1.** Network structure established according to ANP method.

**Table 2.** Comparisons for Main Criteria.

Outer Factors	>=9.5	9	8	7	6	5	4	3	2	1	2	3	4	5	6	7	8	9	>=9.5	Personal Factors
Outer Factors	>=9.5	9	8	7	6	5	4	3	2	1	2	3	4	5	6	7	8	9	>=9.5	Psychological Factors
Personal Factors	>=9.5	9	8	7	6	5	4	3	2	1	2	3	4	5	6	7	8	9	>=9.5	Psychological Factors

**Table 3.** Calculated Priority Values for Criteria.

Criteria	Criteria Weights	Sub-Criteria	Sub-Criteria Weights
Psychological Factors	0.79755	Fear of losing	0.01263
		Isolation concern	0.16810
		Stress disorder	0.44336
		Worry about getting out of comfort zone	0.37591
		Negative media news	0.01094
		Case numbers	0.07445
Outer Factors	0.18313	Deaths	0.08281
		Ambiguity	0.00793
		Distrust of the health sector	0.02097
		Inadequate measures	0.28432
		Hygiene concern	0.51526
Personal Factors	0.01932	Unconscious society	0.00331
		Weak immune system	0.88975
		Lack of information	0.11025

Criteria used in the study were determined by reviewing the literature and following the agenda. Criteria determined are divided into 3 groups: psychological factors, external factors and personal factors. Criteria and descriptions are shown in Table 1. While determining the criteria, the posts on the agenda and social media were examined with two experts examining human behavior, and also studies on corona in the literature were examined. As a result, criteria were determined, and evaluations were made with the same experts.

ANP expresses problems in the form of a network, defining relationships between criteria and aspects of relationships. Thanks to this network, it takes into account indirect interactions and feedback that may occur between elements that are not directly related [11]. Figure 1 shows the network structure established in the study.

An example of binary comparisons is the comparison table for the main criteria in Table 2. Bilateral comparisons and evaluations were carried out by a team of 3-4 people working in the field of Health. In Table 3, there are priority values calculated for the criteria. According to the priority values obtained as a result of comparing relationships and relationships established by the ANP method; the most important criteria affecting coronavirus fear is the criteria of psychological factors. The most important sub-criteria are; it is a weak immune system, hygiene anxiety and stress disorder.

Each of these sub-criteria are included in different main criteria. Looking at the main criteria with the highest priority, it seems that stress disorder, one of the most important sub-criteria, is also found in this title. In this context, it can be said that the sub-criteria of lack of knowledge in personal factors, which is the main criteria of lowest priority, is also one of the sub-criteria of low priority.

#### 4. Conclusion and Discussion

The coronavirus pandemic, which has become a universal problem, has made the risk factor more important for all societies. Although there were many risks in social life before the pandemic, the struggle and measures were also insufficient, as the risks concerned a certain segment of society. Along with other social problems, the epidemic experienced today has also been a tool for many social problems and psychological problems that have a return [22].

As part of the Coronavirus outbreak, differences in user's digital content consumption habits are observed along with social changes. There have been increases in digital content consumption with the need for education, health data monitoring, cultural and entertainment content. Studies aimed at evaluating the functionality of entertainment content and humor as a treatment tool against the devastating effects of social trauma on the collective, individual, consciousness and post-traumatic stress disorder have been conducted. In order to achieve

this goal, analyses were conducted in terms of confronting, accepting and strengthening individual and social resistance to the reality of trauma, fun content related to coronavirus pandemic, which can be considered individual and social trauma [23]. The change in consumption not only increased the production of content but also raised the concept of click feed and caused News and content that did not reflect the truth. This also affects people's access to accurate information and their anxiety status [18]. Changes in social life; it also affected people's use of social media and an increase in social media usage times was observed [24].

Several studies have been conducted on the effects of coronavirus on social life and the psychological problems it causes. According to research, many factors such as people's shopping cultures, traditional behaviors, working conditions and communication have changed due to the pandemic process [25]. Many studies have been conducted on people's emotional states, levels of fear and intolerance. The studies were evaluated using survey and interview methods on different samples or groups.

In a study that examined burnout, coronavirus fear, depression, occupational satisfaction levels and related factors of health workers, the results showed variability according to the demographic characteristics of the participants. It is believed that physical fatigue and stress and negative mental state experienced due to the intense pace in the pandemic process can reduce nurses job satisfaction and this can lead to burnout [26]. It is important to understand their specific sources of anxiety and fear before effective approaches are developed to support healthcare professionals. Another important point is that health professionals are assured that their concerns are being noticed and studies are being conducted to develop approaches that mitigate their concerns to the extent possible [27]. Doctors and other health workers play an important preliminary role in the management of the pandemic. Their emotional load and anxiety levels are on the rise as physicians struggle on the front lines of the coronavirus crisis. A study conducted in Israel investigated anxiety, pandemic-related stress and endurance among physicians and evaluated the potential impact of psychological endurance on anxiety among physicians [28].

The pandemic process causes changes in mood, such as anxiety, stress and fear, which negatively affect life in individuals. According to the results of a survey aimed at measuring coronavirus fear and anxiety levels applied in a sample of dental students; compared to the fear levels of men and women, it was found that women experience more fear during the pandemic process [29]. In another study conducted with a group of university students; it was concluded that students were moderately afraid of coronavirus and moderately

intolerant of uncertainty [30]. In addition to university students, studies measuring the level of fear and anxiety were also conducted with a group of Primary School students. In the study, interviews were conducted with the parents of students; it was concluded that both students and their parents felt fearful and anxious in the process [31]. A study conducted in China also examined the psychological responses of people in the first stage of the outbreak. Researchers concluded that negative emotions such as anxiety, depression and anger increased during the epidemic period, while positive emotions and life satisfaction decreased [32]. Some of the studies have also been conducted on psychological reflections of the epidemic and coping with the epidemic. Situations such as restlessness, longing, family disputes, weakening of social relationships and increasing addictions caused by routine changes are some of the effects of the epidemic on people. These effects vary depending on people and their circumstances, allowing people to resort to cognitive, relational and behavioral strategies to combat the fear of an epidemic [33].

Psychopathology research was also conducted in a study with individuals who survived coronavirus. Psychiatric consequences of infection, immune responses against both viruses as well as compulsory social isolation, and new severe psychological impact of a potentially fatal disease, is due to psychological factors such as stress, stigma concerns to infect others by others. Given the alarming effect of coronavirus infection on mental health, in order to reduce the expected burden of disease, emerging psychiatric conditions should be diagnosed and the psychopathology of coronavirus survivors should be evaluated for treatment [34-35].

In this study, factors affecting coronaphobia that change people's psychological states and behaviors during coronavirus outbreak were identified. In contrast to the studies found in the literature, the ANP method was used in this study, which allows the establishment of bidirectional relationships between factors. Analysis was carried out between factors using the ANP method. The factors covered in the study consist of 3 main criteria and 14 sub-criteria covered by these criteria. Main criteria are psychological factors, external factors and personal factors.

According to the results obtained, it is seen that the main criteria of psychological factors has the highest priority value. Therefore, the sub-criteria of the main criteria of psychological factors also take precedence. The highest priority among these sub-criteria are stress disorder, anxiety about leaving the comfort zone, anxiety about isolation and fear of losing, respectively. For other main criteria, the highest priority sub-criteria are hygiene concern for the main criteria of external factors and weak immune system for personal factors.

According to the results of the solution; individuals with coronaphobia should first treat existing psychological problems. For this purpose; stress disorders, concerns about leaving the comfort zone, isolation concerns and fears of lose should be addressed. According to the results obtained, first of all, by using the power of the media, reassuring shares that reduce this stress level can be increased. In the literature, researchers can examine whether people living with these anxiety disorders have been diagnosed with corona before and, if they have corona, how this psychology affects the course of the disease.

### Author's Contributions

Edanur SONEL: Drafted and wrote the manuscript, performed the experiment and result analysis.

Şeyda GÜR: Assisted in analytical analysis on the structure, result interpretation and helped in manuscript preparation.

Tamer EREN: Made all the checks of the work, helped in manuscript preparation.

### Ethics

There are no ethical issues after the publication of this manuscript.

### References

1. Aslan R. 2020. How does covid-19 affect physiology and psychology. *Lake District Monthly Economic and Cultural Magazine*, 8.
2. Kantürk Y.G. 2016. Health issues., Pegem Citation Index, 361-411.
3. Parıldar H. and Dikici M.F. 2020. History of pandemics. *Journal of Clinical Medicine Family Medicine*, 12.
4. Zhang, Z., Yao, W., Wang, Y., Long, C., & Fu, X. 2020. Wuhan and hubei covid-19 mortality analysis reveals the critical role of timely supply of medical resources. *Journal of Infection*, 81: 147–17. <https://doi.org/10.1016/j.jmed.2020.105980>
5. Huang, C., Wang, Y., Li, X., Ren, L., Zhao, J., Hu, Y., ... & Cao, B. 2020. Clinical features of patients infected with 2019 novel coronavirus in Wuhan. *Lancet*. 395(10223):497-506. [https://doi.org/10.1016/S0140-6736\(20\)30183-5](https://doi.org/10.1016/S0140-6736(20)30183-5)
6. T.C. Ministry of Health General Directorate of Public Health, "COVID-19 (SARS-CoV-2 Infection) References", 2020, [https://covid19bilgi.saglik.gov.tr/depo/rehberler/COVID-19\\_ehberi.pdf](https://covid19bilgi.saglik.gov.tr/depo/rehberler/COVID-19_ehberi.pdf)
7. Kwok, K. O., Li, K. K., Chan, H. H., Yi, Y. Y., Tang, A., Wei, W. I., & Wong, Y. S. 2020. Community responses during the early phase of the covid-19 epidemic in Hong Kong: risk perception. *Information Exposure and Preventive Measures*, 1-26. doi: <https://doi.org/10.1101/2020.02.26.20028217>
8. Li, J. B., Yang, A., Dou, K., Wang, L. X., Zhang, M. C., & Lin, X. Q. 2020. Chinese public's knowledge, perceived severity, and perceived controllability of the covid-19 and their associations with emotional and behavioural reactions. *Social Participation and Precautionary Behaviour: A National Survey*, 20: 1-14. <https://doi.org/10.1186/s12889-020-09695-1>
9. Bandelow B. and Michaelis S., 2015. Epidemiology of anxiety disorders in the 21st century. *Dialogues in Clinical Neuroscience*, 17: 327-335. 10.31887/DCNS.2015.17.3/bbandelow
10. Hwang C.L. and Yoon K.P. 1981. Multiple attribute decision making: methods and applications. Berlin, Springer-Verlag.
11. Saaty T.L., 1996. Dependence and feedback the analytic network process. Rws Publications, Pittsburg, ABD.
12. Baykoç Ö.F. 2001. Decision analysis lecture notes. Gazi University, Institute of Natural Sciences, Department of Industrial Engineering.
13. Ersöz F. and Kabak M. 2010. Literature research of multi-criteria decision-making methods in defense industry applications. *Journal of Defense Sciences*, 9: 97-125. doi:10.17134/sbd.85950
14. Alakaş, H. M., Gür, Ş., Özcan, E., and Eren, T. 2020. Ranking of sustainability criteria for industrial symbiosis applications based on ANP. *Journal of Environmental Engineering and Landscape Management*, 28(4): 192-201.
15. Sonel, E., Gür, Ş., and Eren, T. 2021. Analysis of factors affecting industrial symbiosis collaboration. *Environmental Science and Pollution Research*, 1-8.
16. Jharkharia, S., and Shankar, R. 2007. Selection of logistics service provider: An analytic network process (ANP) approach. *Omega*, 35(3): 274-289.
17. Cheng, E. W., Li, H., and Yu, L. 2005. The analytic network process (ANP) approach to location selection: a shopping mall illustration. *Construction Innovation*.
18. Ozkaya, G., and Erdin, C. 2020. Evaluation of smart and sustainable cities through a hybrid MCDM approach based on ANP and TOPSIS technique. *Heliyon*, 6(10): e05052.
19. Utama, D. M., Maharani, B., and Amallynda, I. 2021. Integration Dematel and ANP for The Supplier Selection in The Textile Industry: A Case Study. *Jurnal Ilmiah Teknik Industri*, 20(1): 119-130
20. Görener A. 2009. Use of analytical networking process in cutting tool supplier selection. *Journal of Aeronautics and Space Technologies*, 4: 99-110.
21. Sonel E., Gür Ş. and Eren T. 2019. City selection and analysis in health tourism with multi-criteria decision making. *International Journal of Global Tourism Research*, 3: 27-39.
22. Yıldırım S. 2020. Social-psychological view of outbreaks: case of covid-19 (coronavirus) pandemic. *Electronic Turkish Studies*, 15.
23. Budak H. 2020. Humour as a means of repair in social trauma: a breath smile in coronavirus days. *Electronic Turkish Studies*, 15.
24. Çelik R. 2020. Clickbait tactic in Click-oriented journalism: the case of coronavirus (Covid-19). *Journal of Social Sciences Research*, 9: 14-25.
25. Özdemir D. and Arpacioğlu S. 2020. The effect of social media use, health perception and health search behavior on coronavirus fear. *Current Approaches in Psychiatry*, 12: 1-1.
26. Güven F. 2020. Effects of coronavirus pandemic on culture. *Journal of Cultural Studies*, 7: 81-96. DOI: 10.46250/kulturder.783463
27. Arpacioğlu S., Baltalı Z. and Ünübol B. 2021. Burnout, Fear of covid, depression, occupational satisfaction levels and related factors in health workers in the covid-19 pandemic. *Cukurova Medical Journal*, 46: 88-100.

28. Shanafelt T., Ripp J. and Trockel M. 2020. Understanding and addressing sources of anxiety among health care professionals during the covid-19 pandemic. *Jama*, 323: 2133-2134. doi:10.1001/jama.2020.5893
29. Mosheva, M., Hertz-Palmor, N., Dorman Ilan, S., Matalon, N., Pessach, I. M., Afek, A., ... & Gothelf, D. 2020. Anxiety, pandemic-related stress and resilience among physicians during the COVID-19 pandemic. *Depression and Anxiety*, 37 (10), 965-971, <https://doi.org/10.1002/da.23085>
30. Atay, Ü.T., Dinçer, N. N., Yarkaç, F. U., & Öncü, E.2020. Covid-19 evaluation of fear and anxiety levels of dentistry specialty students in the pandemic process. *Necmettin Erbakan University Journal of Dentistry*, 2: 86-93.
31. Duman, N. 2020. Fear of covid-19 and intolerance to uncertainty in college students. *The Journal of Social Science*, 4: 426-437. <https://doi.org/10.30520/tjsosci.748404>
32. Erol M. and Erol A. 2020. Primary school students through the eyes of their parents in the process of coronavirus pandemic. *Journal of National Education*, 2020; 49: 529-551. <https://doi.org/10.37669/milliegitim.766194>
33. Sher L. 2020. COVID-19, anxiety, sleep disturbances and suicide. *Sleep Medicine*, doi: 10.1016/j.sleep.2020.04.019
34. Hatun O., Dicle A.N. and Demirci I. 2020. Psychological reflections of coronavirus outbreak and coping with epidemic. *Electronic Turkish Studies*, 15.
35. Mazza, M. G., De Lorenzo, R., Conte, C., Poletti, S., Vai, B., Bollettini, I., ... & COVID-19 BioB Outpatient Clinic Study group. 2020. Anxiety and depression in covid-19 survivors: role of inflammatory and clinical predictors. *Brain, Behavior and Immunity*, 89: 594-600. <https://doi.org/10.1016/j.bbi.2020.07.037>



## Stability Analysis of Discretized Model of Glucose–Insulin Homeostasis

İlkem Turhan Çetinkaya<sup>1\*</sup> , Mehmet Kocabıyık<sup>2</sup> , Mevlüde Yakıt Ongun<sup>3</sup> 

<sup>1</sup> Kutahya Dumlupınar University, Science and Art Faculty, Department of Mathematics, Kutahya, Turkey.

<sup>2</sup> Burdur Mehmet Akif Ersoy University, Science and Art Faculty, Department of Mathematics, Burdur, Turkey.

<sup>3</sup> Suleyman Demirel University, Science and Art Faculty, Department of Mathematics, Isparta, Turkey.

\*[ilkem.turhan@dpu.edu.tr](mailto:ilkem.turhan@dpu.edu.tr)

\*Orcid: 0000-0002-5520-310X

Received: 10 December 2020

Accepted: 23 November 2021

DOI: 10.18466/cbayarfbe.838451

### Abstract

In this paper, the mathematical model which describes the glucose-insulin homeostasis in healthy rats is considered. The model is discretized by constructing a nonstandard finite difference (NSFD) scheme to obtain the numerical solutions. The equilibrium point of the discretized model is determined and stability analysis of the discretized model is discussed. The effect of time step sizes on 4th order Runge-Kutta method and NSFD method is presented. Also, comparison of NSFD scheme solution, Runge-Kutta-Fehlberg Method (RKF45) solution and analytical solution are presented in graphical form. The effectiveness of the proposed method in the solution and interpretation of the model is observed.

**Keywords:** Glucose-Insulin homeostasis, nonstandard finite difference scheme, stability analysis.

### 1. Introduction

In mathematical biology, a lot of studies for patients with diabetes are proposed. The relationship between glucose and insulin has been mathematically modeled, improved and studied. Some of the studies can be listed as follows:

Chen et. al. developed a physiological glucose–insulin dynamic system on diabetics [1]. They aimed to examine dynamic behavior of plasma glucose and insulin on diabetic subject. They constructed a modified delay differential equation system. Dereouich and Boutayeb examined the importance of physical activity on the dynamics of glucose and insulin [2]. Neatpisarnvanit and Boston derived and evaluated two plasma insulin estimators in [3]. They used forward Euler discretization to discrete the continuous model. Finally, they compared the performances of estimator by using computer simulations and clinical data. Li and Kuang [4] generalized the dynamic model on interaction of glucose and insulin to the delay model. They proposed some lemmas, propositions and theorems about the local and global stability of the model. Also, they gave periodic solutions for the discrete delay model. Hussian and Zadeng analyzed the stability of the general glucose-insulin model [5]. They examined the importance of insulin in the disappearance of glucose by

doing numerical simulations. Wang et.al [6] proposed a delay model of the insulin therapies. They studied the dynamics of the model. They showed that the numerical results and the findings of the clinical studies agree well.

There are a lot of classical numerical methods for solving these kinds of models such as Euler Method, Runge-Kutta Method etc. But, the studies show that, it is better to prefer nonstandard discretization methods for biological models. Al-Kahby et.al. present the basic stability results of some biological models, shortcomings of some classical discretization methods and the advantage of nonstandard discretization methods [7]. In this study, because of the advantages, we prefer to use NSFD schemes developed by Mickens [8-11]. One of the advantages compared to classical discretization methods is that while classical discretization often produces difference equations which don't share their dynamics, NSFD produce difference equations that share their dynamics. In this discretization method, the critical points are same with the continuous model and the positivity solutions under positive initial conditions are preserved. Since NSFD schemes can preserve all properties of the continuous models for any discretization parameter, the method is successful on dynamical consistency. Also, while NSFD schemes give convergence results for the big step-size,

the other traditional methods don't. Since there are numerical instabilities in the classical methods, this method provide an advantage of choosing suitable denominator function. One can be referred to [12] for the detailed analysis about determining denominator function. Some studies about NSFD schemes are listed below:

Mickens studied a nonlinear reaction-advection equation which is a partial differential equation [13]. Arenas et. al. analyzed the SIRS model for modelling transmission of respiratory syncytial virus [14]. Khalsaraei and Khodadosti made some applications of NSFD to ordinary and partial differential equations [15]. Their comparisons between the standard methods and NSFD showed that nonstandard schemes perform better. Ongun and Turhan applied NSFD schemes to the HIV infection model which is a nonlinear ordinary differential equation system [16]. They examined stability analysis of the model and gave qualitative results for the fixed points which have biological meanings. Also, Ongun etc. applied NSFD schemes to a fractional-order Brusselator system [17]. They presented the dynamics of the Brusselator model and trajectories by NSFD scheme. A very detailed literature survey is presented by Patidar in [18,19]. Some of the main rules about designing NSFD schemes are summarized and some of the applications of the method in other areas are mentioned.

This study consist of six sections: in Section 2, the model is introduced and discretized through NSFD schemes. In Section 3, Jury Stability test and a theorem about the local asymptotic stability of the model are presented. Equilibrium point of the discrete system is determined, the expression of Jacobian matrix at the equilibrium point and characteristic equation are given. In Section 4, the analytical solution of the linear ordinary differential equation system is given. Section 5 presents the numerical simulations. Considering the optimized values, stability analysis of the problem is given. The effect of time step sizes on the convergence of the 4th order Runge-Kutta method and NSFD scheme is given in tabular form. The graphics for the numerical solutions of the model are presented. Finally, phase portrait of the system is given. The last section concludes the study with a summary.

## 2. Discretization of the Model

In this section, the model proposed by [20] is considered. The model describing glucose–insulin homeostasis in healthy rats is given as:

$$\begin{aligned} \frac{dI}{dt} &= -k_6 I + k_1 G \\ \frac{dG}{dt} &= -(k_2 + k_4)I + k_0 D - k_3 + k_4 I_{pi} \\ \frac{dD}{dt} &= -k_a D, \end{aligned} \quad (2.1)$$

where,  $I$ ,  $G$  and  $D$  denote to variation of blood insulin concentration, blood glucose concentration and amount of glucose in the intestine, respectively. The parameters in Eq. (2.1) are given in Table 1.

**Table 1.** The meaning of the parameters in epidemic model (2.1).

Parameters	Meanings
$k_0$	the rate constant of blood glucose incorporation from diet
$k_1$	the rate constant of insulin secretion
$k_2$	the rate constant of insulin-dependent glucose uptake by the tissues
$k_3$	the rate constant of insulin-independent glucose uptake by the tissues
$k_4$	the rate constant of liver glucose transfer
$k_6$	the rate constant of blood insulin clearance
$k_a$	the rate constant of glucose absorption
$I_{pi}$	the blood insulin concentration when the liver changes from the uptake to the production of glucose

The discretization has an important role on dynamic behavior of epidemic models; because the data's are collected in discrete-time. Since the classical discretization methods often lead to difference equations which don't share their dynamics, it is more suitable to discretize the models by nonstandard discretization methods. In the light of this information, the model given by Equations (2.1) is discretized by nonstandard finite difference method proposed by Mickens [8,11]. This discretization method is preferred because of the advantages of choosing denominator function arbitrary by local discretization. Also, NSFD method has advantage on removing numerical instabilities obtained by standard finite difference procedures.

The discretization of the model (2.1) has been done by NSFD scheme in the view of positivity conditions. To satisfy the positivity condition, the discretized procedure for the first equation of Eq. (2.1) is given as  $G(t) \rightarrow G(n)$  and  $I(t) \rightarrow I(n+1)$ . Later on, the discretized terms  $I(t) \rightarrow I(n)$  and  $D(t) \rightarrow D(n+1)$  are applied to the second equation of Eq. (2.1). Finally, by using the  $D(t) \rightarrow D(n+1)$  discretization for the last equation of Eq. (2.1), the model is rewritten as



$$\begin{aligned}
 I(n+1) &= \frac{I(n) + k_1 \phi_1 G(n)}{1 + k_6 \phi_1}, \\
 G(n+1) &= G(n) + \phi_2 \left[ -(k_4 + k_2)I(n) \right. \\
 &\quad \left. + k_0 D(n) - k_3 + k_4 I_{pi} \right], \tag{2.2}
 \end{aligned}$$

$$D(n+1) = \frac{D(n)}{1 + k_a \phi_3},$$

where  $\phi_i, i = 1, 2, 3$  are denominator functions and determined as

$$\phi_1 = \frac{e^{k_6 h} - 1}{k_6},$$

$$\phi_2 = h,$$

$$\phi_3 = \frac{e^{k_a h} - 1}{k_a}.$$

For detailed information of finding denominator functions, one can check the reference [10].

### 3. Stability Analysis of the Discretized Model

**Lemma 3.1** From the positivity of the parameters, the solution of discrete system (2.2) is positive with positive initial conditions under the assumption of

$$\frac{G(n)}{\phi_2} > (k_4 + k_2)I(n) - k_0 D(n) + k_3 - k_4 I_{pi}.$$

#### Proof

i) For  $k_6 > 0, h > 0$  and  $\phi_1, \phi_2, \phi_3 > 0$ , it is obvious that  $e^{k_6 h} > 1$ . So,  $e^{k_6 h} - 1 > 0$  is obtained. Dividing this expression into the term  $k_6$  leads to  $\frac{e^{k_6 h} - 1}{k_6} = \phi_1 > 0$ . So, the solution

$$I(n+1) = \frac{I(n) + k_1 \phi_1 G(n)}{1 + k_6 \phi_1} > 0 \text{ is positive.}$$

ii) If  $\frac{G(n)}{\phi_2} > (k_4 + k_2)I(n) - k_0 D(n) + k_3 - k_4 I_{pi}$  then,

for  $h = \phi_2 > 0$ ,

$$G(n) > \phi_2 \left[ (k_4 + k_2)I(n) - k_0 D(n) + k_3 - k_4 I_{pi} \right]$$

is obtained. So the solution

$$\begin{aligned}
 G(n+1) &= G(n) + \phi_2 \left[ -(k_4 + k_2)I(n) \right. \\
 &\quad \left. + k_0 D(n) - k_3 + k_4 I_{pi} \right] > 0
 \end{aligned}$$

is positive.

iii) For  $k_a > 0$  and  $h > 0$ , it is obvious that  $e^{k_a h} > 1$ . So,  $e^{k_a h} - 1 > 0$  is obtained. Dividing this expression

into the term  $k_a$  leads to  $\frac{e^{k_a h} - 1}{k_a} = \phi_3 > 0$ . So, the

solution  $D(n+1) = \frac{D(n)}{1 + k_a \phi_3} > 0$  is positive.

**Lemma 3.2** From the positivity of the parameters and Lemma 3.1, if  $\frac{G(n)}{I(n)} < \frac{k_6}{k_1}$ , the solution of discrete system (2.2) decreases monotonically.

**Proof** From the third equation of discrete system (2.2),

$$\frac{D(n+1)}{D(n)} = \frac{1}{1 + k_a \phi_3} = \frac{1}{e^{k_a h}} < 1 \text{ is obtained.}$$

Rewritten the second equation of system (2.2) as,  $\frac{G(n+1)}{G(n)} = 1 + \frac{\phi_2 \left[ -(k_4 + k_2)I(n) + k_0 D(n) - k_3 + k_4 I_{pi} \right]}{G(n)}$

and considering the assumption in Lemma 3.1, for

$$\frac{\phi_2}{G(n)} < \frac{1}{(k_4 + k_2)I(n) - k_0 D(n) + k_3 - k_4 I_{pi}},$$

it is obtained that

$$\begin{aligned}
 \frac{G(n+1)}{G(n)} &= 1 + \frac{\phi_2 \left[ -(k_4 + k_2)I(n) + k_0 D(n) - k_3 + k_4 I_{pi} \right]}{G(n)} \\
 &< 0 < 1.
 \end{aligned}$$

Finally, from the first equation of the system (2.2) and

the assumption  $\frac{G(n)}{I(n)} < \frac{k_6}{k_1}$ ,

$$\frac{I(n+1)}{I(n)} = \frac{I(n) + k_1 \phi_1 G(n)}{(1 + k_6 \phi_1)I(n)} < \frac{1}{1 + k_6 \phi_1} + \frac{k_1 \phi_1 k_6}{(1 + k_6 \phi_1)k_1} = 1$$

is obtained.

Locally asymptotic stability of the system depends on the eigenvalues of the Jacobian matrix at the equilibrium points. The eigenvalues are the zeros of the following characteristic polynomial

$$p(\lambda) = \lambda^n + a_1 \lambda^{n-1} + a_2 \lambda^{n-2} + \dots + a_n, \tag{3.1}$$

where  $a_1, a_2, \dots, a_n$  are constants.

**Theorem 3.1** If the solutions  $\lambda_i, i = 1, 2, \dots, n$  of Equation (3.1),  $p(\lambda) = 0$  satisfy  $|\lambda_i| < 1$ , then

i)  $p(1) = 1 + a_1 + a_2 + \dots + a_n > 0$ ,

ii)  $(-1)^n p(-1) = 1 - a_1 + a_2 - \dots + (-1)^n a_n > 0$ ,  
 (alternate in sign),

iii)  $|a_n| < 1$ . [21]

### Jury Stability Test

Let us consider the characteristic polynomial

$$p(z) = a_0 z^n + a_1 z^{n-1} + \dots + a_{n-1} z + a_n, \quad a_0 > 0.$$

The conditions of stability of the system are:

- i)  $|a_n| < a_0$ ,
- ii)  $p(1) > 0$ ,
- iii)  $\begin{cases} p(-1) > 0, & \text{for } n \text{ is even} \\ p(-1) < 0, & \text{for } n \text{ is odd} \end{cases}$ ,
- iv)  $\left. \begin{array}{l} |b_{n-1}| > |b_0| \\ |c_{n-2}| > |c_0| \\ \vdots \\ |q_2| > |q_0| \end{array} \right\} (n-2) \text{ constraints,}$

where,

$$b_k = \begin{vmatrix} a_n & a_{n-1-k} \\ a_0 & a_{k+1} \end{vmatrix}, \quad k = \overline{0, n-1},$$

$$c_k = \begin{vmatrix} b_{n-1} & b_{n-2-k} \\ b_0 & b_{k+1} \end{vmatrix}, \quad k = \overline{0, n-2},$$

$$\vdots$$

$$q_k = \begin{vmatrix} p_3 & p_{2-k} \\ p_0 & p_{k+1} \end{vmatrix}, \quad k = \overline{0, 2} \quad [21,22].$$

For the stability analysis of model, equilibrium point of Equations (2.2) are obtained as

$$E^* = (I^*, G^*, D^*) = \left( \frac{-k_3 + k_4 I_{pi}}{k_4 + k_2}, \frac{(-k_3 + k_4 I_{pi}) k_6}{(k_4 + k_2) k_1}, 0 \right).$$

Note that, the equilibrium points of continuous model (2.1) and discrete model (2.2) are same.

The Jacobian matrix is determined as

$$J(I(n), G(n), D(n)) = \begin{bmatrix} \frac{1}{1+k_6\phi_1} & \frac{k_1\phi_1}{1+k_6\phi_1} & 0 \\ \phi_2(-k_4+k_2) & 1 & \phi_2 k_0 \\ 0 & 0 & \frac{1}{1+\phi_3 k_a} \end{bmatrix}.$$

The value of Jacobian matrix at the equilibrium point and obtained characteristic polynomial are given below:

$$J(I^*, G^*, D^*) = \begin{bmatrix} \frac{1}{1+k_6\phi_1} & \frac{k_1\phi_1}{1+k_6\phi_1} & 0 \\ \phi_2(-k_4+k_2) & 1 & \phi_2 k_0 \\ 0 & 0 & \frac{1}{1+\phi_3 k_a} \end{bmatrix},$$

$$p(\lambda) = \lambda^3 - \frac{3 + 2k_6\phi_1 + 2\phi_3 k_a + k_a k_6 \phi_1 \phi_3}{(1+k_a\phi_3)(1+k_6\phi_1)} \lambda^2 - \frac{(1+k_a\phi_3)\phi_1\phi_2 k_1(k_2-k_4) - 3 - k_6\phi_1 - k_a\phi_3}{(1+k_a\phi_3)(1+k_6\phi_1)} \lambda + \frac{k_1\phi_1\phi_2(-k_4+k_2) - 1}{(1+k_a\phi_3)(1+k_6\phi_1)}, \quad (3.2)$$

where the eigenvalues are

$$\lambda_1 = \frac{1}{1+\phi_3 k_a},$$

$$\lambda_2 = \frac{2 + k_6\phi_1 + \sqrt{k_6^2\phi_1^2 - 4k_1\phi_1\phi_2(k_4-k_2)(1+k_6\phi_1)}}{2(1+k_6\phi_1)},$$

$$\lambda_3 = \frac{-2 - k_6\phi_1 + \sqrt{k_6^2\phi_1^2 - 4k_1\phi_1\phi_2(k_4-k_2)(1+k_6\phi_1)}}{2(1+k_6\phi_1)}.$$

Now, let us analyze the stability of the model at the equilibrium point.

**Theorem 3.2** The system is locally asymptotically stable at the equilibrium point  $E^*$ , if the following conditions are satisfied

- i)  $\left| \frac{-k_1 k_4 \phi_1 \phi_2 + k_1 k_2 \phi_1 \phi_2 - 1}{(1+k_a\phi_3)(1+k_6\phi_1)} \right| < 1.$
- ii)  $\frac{k_1 k_a (k_4 - k_2) \phi_1 \phi_2 \phi_3}{(1+k_a\phi_3)(1+k_6\phi_1)} > 0.$
- iii)  $\frac{k_1 k_a \phi_1 \phi_2 \phi_3 (k_2 - k_4) - 2[3 + 2(k_6\phi_1 + k_a\phi_3) + k_6 k_a \phi_1 \phi_3]}{(1+k_a\phi_3)(1+k_6\phi_1)} < 0.$   
 $\left\{ \left( k_1 \phi_1 \phi_2 (k_2 - k_4) - (1+k_6\phi_1)(1+k_a\phi_3) - 1 \right) \left( k_1 \phi_1 \phi_2 (k_2 - k_4) + k_6 \phi_1 (1+k_a\phi_3) + k_a \phi_3 \right) \right\} / \left\{ (1+k_a\phi_3)^2 (1+k_6\phi_1)^2 \right\}$
- iv)  $> \left\{ \left( (k_4 - k_2) \phi_1 \phi_2 k_1 \left( \phi_1 k_6 (1 - \phi_3 k_a) + 2 - k_a^2 \phi_3^2 \right) - k_a \phi_3 (2 + k_a \phi_3) + k_a^2 k_6 \phi_1^2 \phi_3^2 k_1 (-k_4 + k_2 \phi_2) - k_6 \phi_1 (2 + k_6 \phi_1) + \phi_1 \phi_3 k_a k_6 (-k_6 \phi_1 + k_a \phi_3 - 4) \right) / \left( (1+k_a\phi_3)^2 (1+k_6\phi_1)^2 \right) \right\}.$

**Proof** Considering Jury stability test [21,22] and the coefficients of characteristic polynomial (3.2) obtained as

$$a_1 = -\frac{3 + 2k_6\phi_1 + 2\phi_3k_a + k_a k_6\phi_1\phi_3}{(1 + k_a\phi_3)(1 + k_6\phi_1)},$$

$$a_2 = -\frac{(1 + k_a\phi_3)\phi_1\phi_2k_1(k_2 - k_4) - 3 - k_6\phi_1 - k_a\phi_3}{(1 + k_a\phi_3)(1 + k_6\phi_1)} \quad \text{and}$$

$$a_3 = \frac{k_1\phi_1\phi_2(-k_4 + k_2) - 1}{(1 + k_a\phi_3)(1 + k_6\phi_1)},$$

it is obvious that, if the conditions (i-iv) are satisfied, the equilibrium point is locally asymptotically stable.

In addition, as is known, the order of convergence in Mickens' method generally matches the order of the differential equation [23]. Also, in the view of [23,24], it can be easily seen that the order of convergence for NSFD schemes we proposed is one.

#### 4. The Analytical Solution of the System

In this section, to compare the results obtained by the NSFD schemes, the analytical solution of the system of ordinary differential equations is presented under the initial conditions  $I(0) = I_0 > 0$ ,  $G(0) = G_0 > 0$ ,

$D(0) = D_0 > 0$ . The model (2.1) is solved by elimination method. In the view of the elimination method, the system is converted to the following differential equations,

$$\left[ D^2 + k_6D + k_1(k_2 + k_4) \right] I(t) = k_0k_1c^* e^{-k_a t} + (-k_3 + k_4I_{pi})k_1,$$

$$\left[ D^2 + k_6D + k_1(k_2 + k_4) \right] G(t) = k_0c^*(k_6 - k_a)e^{-k_a t} + (-k_3 + k_4I_{pi})k_6, \quad (4.1)$$

$$(D + k_a)D(t) = 0,$$

where D is the derivation operator and  $c^*$  is the arbitrary parameter obtained from the solution of the third equation of Eq. (4.1). The characteristic equation of the first and second equations of Eq. (4.1) is obtained for the homogeneous solution as

$$m_{1,2} = \frac{-k_6 \mp \sqrt{k_6^2 - 4k_1(k_2 + k_4)}}{2}.$$

For the different cases of characteristic equation, the homogeneous solutions are obtained. Later, private solutions are obtained by using the method of undetermined coefficients. So, we can summarize the solution of system (2.1) as follows:

**i)** If  $k_6^2 - 4k_1(k_2 + k_4) > 0$ ,  $\frac{-k_6 \mp \sqrt{k_6^2 - 4k_1(k_2 + k_4)}}{2} \neq -k_a$  and  $\frac{-k_6 \mp \sqrt{k_6^2 - 4k_1(k_2 + k_4)}}{2} \neq 0$ , then

$$I(t) = c_1 e^{m_1 t} + c_2 e^{m_2 t} + \frac{k_0 k_1 c_3}{k_a^2 - k_a k_6 + k_1(k_2 + k_4)} e^{-k_a t} + \frac{-k_3 + k_4 I_{pi}}{k_2 + k_4},$$

$$G(t) = \frac{c_1(m_1 + k_6)}{k_1} e^{m_1 t} + \frac{c_2(m_2 + k_6)}{k_1} e^{m_2 t} + \frac{k_0 c_3(k_6 - k_a)}{k_a^2 - k_a k_6 + k_1(k_2 + k_4)} e^{-k_a t} + \frac{k_6(-k_3 + k_4 I_{pi})}{k_1(k_2 + k_4)},$$

$$D(t) = c_3 e^{-k_a t},$$

where, the coefficients  $c_1, c_2, c_3$  are obtained from initial conditions as,

$$c_1 = \frac{1}{m_1 - m_2} \left\{ k_1 G_0 - \frac{k_0 k_1 D_0 (k_6 - k_a)}{k_a^2 - k_a k_6 + k_1(k_2 + k_4)} - \frac{k_6(-k_3 + k_4 I_{pi})}{k_2 + k_4} - (m_2 + k_6) \left[ I_0 - \frac{k_0 k_1 D_0}{k_a^2 - k_a k_6 + k_1(k_2 + k_4)} - \frac{-k_3 + k_4 I_{pi}}{k_2 + k_4} \right] \right\},$$

$$c_2 = \frac{1}{m_2 - m_1} \left\{ -(m_1 + k_6) \left[ I_0 - \frac{k_0 k_1 D_0}{k_a^2 - k_a k_6 + k_1(k_2 + k_4)} - \frac{-k_3 + k_4 I_{pi}}{k_2 + k_4} \right] + k_1 G_0 - \frac{k_0 k_1 D_0 (k_6 - k_a)}{k_a^2 - k_a k_6 + k_1(k_2 + k_4)} - \frac{k_6(-k_3 + k_4 I_{pi})}{k_2 + k_4} \right\},$$

$$c_3 = D_0.$$

**ii)** If  $k_6^2 - 4k_1(k_2 + k_4) = 0$ ,  $\frac{k_6}{2} \neq k_a$  and  $k_6 = 0$ , then

$$I(t) = (c_1 + c_2 t) e^{-\frac{k_6}{2}t} + \frac{k_0 k_1 c_3}{k_a^2 - k_a k_6 + k_1(k_2 + k_4)} e^{-k_a t} + \frac{-k_3 + k_4 I_{pi}}{k_2 + k_4},$$

$$G(t) = \left( \frac{k_6 c_1 + c_2}{k_1} + \frac{k_6 c_2}{2k_1} t \right) e^{-k_6 t} + \frac{k_0 c_3 (k_6 - k_a)}{k_a^2 - k_a k_6 + k_1(k_2 + k_4)} e^{-k_a t} + \frac{k_6(-k_3 + k_4 I_{pi})}{k_1(k_2 + k_4)},$$

$$D(t) = c_3 e^{-k_a t},$$

where, the coefficients  $c_1, c_2, c_3$  are obtained from initial conditions as,

$$c_1 = -\frac{k_0 k_1 D_0}{k_a^2 - k_a k_6 + k_1(k_2 + k_4)} - \frac{-k_3 + k_4 I_{pi}}{k_2 + k_4} + I_0,$$

$$c_2 = k_1 \left\{ G_0 - \frac{k_6(-k_3 + k_4 I_{pi})}{k_1(k_2 + k_4)} - \frac{k_0 D_0 (k_6 - k_a)}{k_a^2 - k_a k_6 + k_1(k_2 + k_4)} + \frac{k_0 k_6 D_0 k_1}{k_a^2 - k_a k_6 + k_1(k_2 + k_4)} + \frac{k_6(-k_3 + k_4 I_{pi})}{k_2 + k_4} \right\},$$

$$c_3 = D_0.$$

iii) If  $k_6^2 - 4k_1(k_2 + k_4) < 0$ ,

$$I(t) = (c_1 \cos(bt) + c_2 \sin(bt)) e^{-\frac{k_6}{2}t} + \frac{k_0 k_1 c_3}{k_a^2 - k_a k_6 + k_1(k_2 + k_4)} e^{-k_a t} + \frac{-k_3 + k_4 I_{pi}}{k_2 + k_4},$$

$$G(t) = \left( \left( c_2 b + \frac{k_6 c_1}{2} \right) \frac{1}{k_1} \cos(bt) + \frac{1}{k_1} \left( -c_1 b + \frac{k_6 c_2}{2} \right) \sin(bt) \right) e^{-k_6 t} + \frac{k_0 c_3 (k_6 - k_a)}{k_a^2 - k_a k_6 + k_1(k_2 + k_4)} e^{-k_a t} + \frac{k_6(-k_3 + k_4 I_{pi})}{k_1(k_2 + k_4)},$$

$$D(t) = c_3 e^{-k_a t},$$

where, the coefficients  $c_1, c_2, c_3$  are obtained from initial conditions as,

$$c_1 = -\frac{k_0 k_1 D_0}{k_a^2 - k_a k_6 + k_1(k_2 + k_4)} - \frac{-k_3 + k_4 I_{pi}}{k_2 + k_4} + I_0,$$

$$c_2 = \frac{1}{b} \left\{ k_1 \left[ G_0 - \frac{k_6(-k_3 + k_4 I_{pi})}{k_1(k_2 + k_4)} - \frac{k_0 D_0 (k_6 - k_a)}{k_a^2 - k_a k_6 + k_1(k_2 + k_4)} - \frac{k_6}{2} \left[ -\frac{k_0 D_0 k_1}{k_a^2 - k_a k_6 + k_1(k_2 + k_4)} - \frac{-k_3 + k_4 I_{pi}}{k_2 + k_4} + I_0 \right] \right] \right\},$$

$$c_3 = D_0.$$

## 5. Results and Discussion

In this study, since discrete-time dynamic systems have advantages over continuous-time dynamic systems, we convert a continuous time dynamic system to a discrete-time dynamic system. One of them is that the data in real life are collected in discrete time. Also discrete-time dynamic systems present more complicated dynamical behaviors.

In this section, first, we analyze the stability of the discretized model. Then, we approached the problem by 4-th order Runge-Kutta method and NSFD scheme to observe the convergence of the methods. The numerical solution of the epidemic model is also obtained by RKF45 method. The effectiveness of the numerical methods is compared in Fig. 1-3 with obtained analytical solutions. Finally, the graphics for different glucose intake are presented. Maple package programme is used in all calculations.

The numerical calculations are carried out for the parameters:

$$k_0 = 0.01, k_1 = 0.7, k_2 = 0.0005, k_3 = 1, k_4 = 0.05, k_6 = 0.5, k_a = 0.15, I_{pi} = 800, h = 0.01.$$

These parameters are chosen approximately from the optimized parameters in [20].

Now, let us analyze the stability of the problem. By considering Jury stability test,

- i) Since  $|a_0| = 1$  and  $|a_3| = 0.99352, |a_3| < a_0$ .
- ii)  $p(1) = a_0 + a_1 + a_2 + a_3 = 0.5 \times 10^{-8} > 0$ .
- iii)  $p(-1) = -a_0 + a_1 - a_2 + a_3 = -5.98702 < 0$ .
- iv) Since  $|b_0| = 0.01290894300$  and  $|b_2| = 0.01290900830, |b_2| > |b_0|$ .

So from the conditions (i- iv), the equilibrium point is locally asymptotically stable.

**Table 2.** Effect of time step sizes on the numerical methods

$h$	4-th order Runge-Kutta method	NSFD scheme
0.001	Convergence	Convergence
0.01	Convergence	Convergence
0.1	Convergence	Convergence
0.5	Convergence	Convergence
1	Convergence	Convergence
5	Convergence	Convergence
10	Divergence	Convergence
100	Divergence	Divergence

Table 2 present the effect of time step size on 4-th order Runge-Kutta method and NSFD scheme. As is seen from Table 2, the nonstandard discretization is more effective than the classical method for bigger step-size.

Also, since the model is a system of linear ordinary differential equation, the comparisons of analytical and numerical solutions are done. The results obtained by NSFD scheme, RKF45 method and analytical solution are presented in Figures 1-3.

Clearly, these figures show us the stability of the model and effectiveness of the NSFD scheme. Figures 4-6 present the variation of blood insulin concentration, blood glucose concentration and amount of glucose in the intestine on time for different amount of glucose intake ( $D_0$ ). So, when the glucose intake increases, levels of blood insulin and blood glucose increase too.

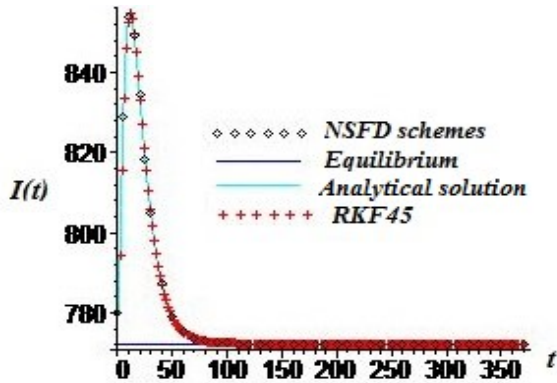


Figure 1. Numerical comparison for  $I(t)$ .

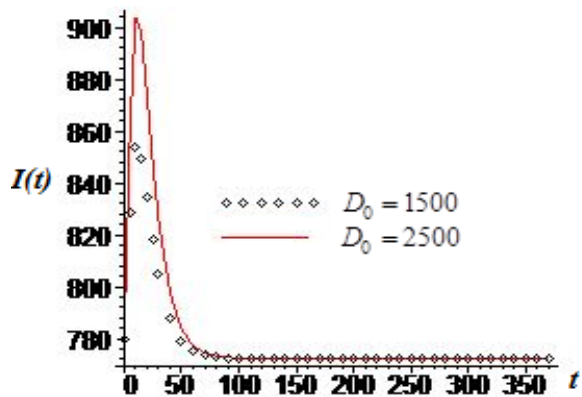


Figure 4.  $I(t)$  for different glucose intake (mg).

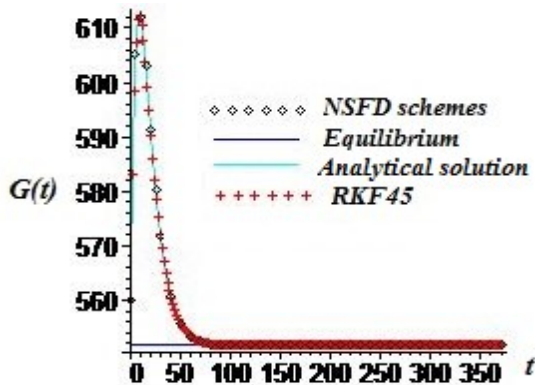


Figure 2. Numerical comparison for  $G(t)$ .

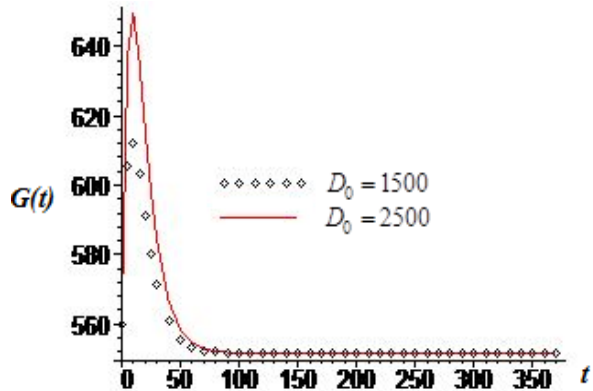


Figure 5.  $G(t)$  for different glucose intake (mg).

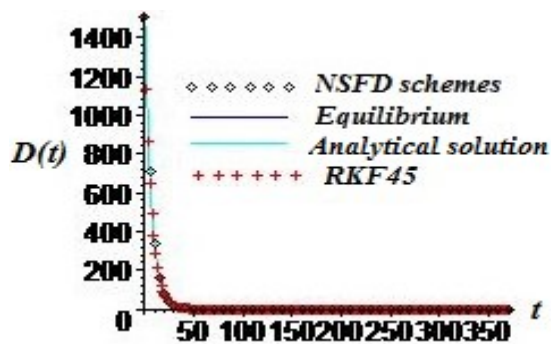


Figure 3. Numerical comparison for  $D(t)$ .

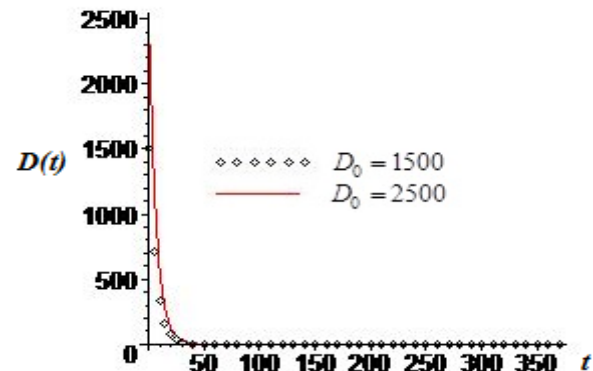


Figure 6.  $D(t)$  for different glucose intake (mg).

Finally, the phase portrait of the system is generated by Figure 7.

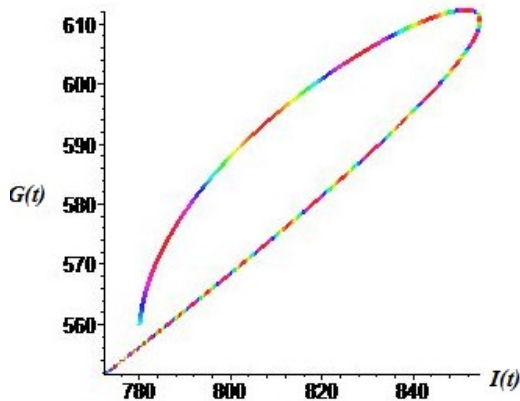


Figure 7. Phase portrait of the system.

## 6. Conclusion

In this study, a model of glucose–insulin homeostasis in healthy rats is handled. The system is discretized by NSFD schemes. It is seen that the solutions are positive for all positive initial values. The stability analysis of the model is done and it is concluded that equilibrium point is locally asymptotically stable. Convergence is achieved for larger step-size than fourth-order Runge-Kutta method. Since the considered biological model is a system of linear ordinary differential equation, it gives a chance to compare the approximate values with analytical values. So, the effectiveness of the results obtained by NSFD schemes can be seen from figures. Also, biologically, the effect of the glucose intake on blood insulin concentration, blood glucose concentration and glucose in the intestine can be seen from figures. This study shows the effectiveness of the NSFD scheme in many aspects like stability, positivity, preservation of critical points and convenience.

## Author's Contributions

İlkem Turhan ÇETİNKAYA: Drafted and wrote the manuscript, performed numerical calculations.  
Mehmet KOCABIYIK: Assisted in numerical calculations and helped in manuscript preparation.  
Mevlûde YAKIT ONGUN: Supervised the manuscript and performed the result interpretation.

## Ethics

There are no ethical issues after the publication of this manuscript.

## References

1. Chen, CL, Tsai, HW, Wong, SS. 2010. Modeling the physiological glucose–insulin dynamic system on diabetics. *Journal of Theoretical Biology*; 265: 314–322.
2. Dereouich, M, Boutayeb, A. 2002. The effect of physical exercise on the dynamics of glucose and insulin. *Journal of Biomechanics*; 35: 911–917.
3. Neatpisarnvanit, C, Boston, JR. 2002. Estimation of Plasma Insulin From Plasma Glucose. *IEEE Transactions on biomedical engineering*, 49(11): 1253-1259.
4. Li, J, Kuang, Y. Analysis of IVGTT glucose-insulin interaction models with time delay. 2001. *Discrete and Continuous Dynamical Systems- Series B*; 1(1): 103–124.
5. Hussain, J, Zadeng, D. 2014. A mathematical model of glucose-insulin interaction. *Science Vision*; 14(2): 84-88.
6. Wang, H, Li, J, Kuang, Y. 2007. Mathematical modeling and qualitative analysis of insulin therapies. *Mathematical Biosciences*; 210: 17–33.
- 7]. Al-Kahby, H, Dannan, F, Elaydi, S. Non-standard Discretization Methods for Some Biological Models. 2000. *Applications of Nonstandard Finite Difference Schemes*; 155-180.
- 8]. Mickens, RE. *Difference Equations Theory and Applications*, Atlanta, Ga, USA: Chapman & Hall, 1990.
9. Mickens, RE. *Advances in the applications of Nonstandard Finite Difference Schemes*, Singapore: Wiley-Interscience, 2005.
10. Mickens, RE. *Nonstandard finite difference models of differential equations*, World Scientific Publishing Co., Inc., River Edge, NJ, 1994.
11. Mickens, RE. 2002. Nonstandard Finite Difference Schemes for Differential Equations. *Journal of Difference Equations and Applications*; 8(9): 823-847, DOI:10.1080/1023619021000000807.
12. Mickens, RE. Calculation of denominator functions for nonstandard finite difference schemes for differential equations satisfying a positivity condition. 2006. *Numerical Methods for Partial Differential Equations*; 23(3): 672-691.
13. Mickens, RE. Exact solutions to a finite-difference model of a nonlinear reaction-advection equation: implications for numerical analysis. 1989. *Numerical Methods for Partial Differential Equations*; 5(4): 313-325.
14. Arenas, AJ, Morano, JA, Cortes, JC. Non-standard numerical method for a mathematical model of RSV epidemiological transmission. 2008. *Computers and Mathematics with Applications*; 56: 670-678.
15. Khalsaraei MM, Khodadosti, F. 2014. Nonstandard Finite Difference Schemes for Differential Equations, *Sahand Communications in Mathematical Analysis*; 1(2): 47-54.
16. Yakıt Ongun, M, Turhan, İ. 2013. A Numerical Comparison for a Discrete HIV Infection of CD4+T-Cell Model Derived from Nontandard Numerical Scheme. *Journal of Applied Mathematics*; 2013.
17. Yakıt Ongun, M, Arslan, D, Garrappa, R. 2013. Nonstandard finite difference schemes for a fractional-order Brusselator system. 2013. *Advances in Difference Equations*; 2013(102).
18. Patidar, K. C. Nonstandard finite difference methods: recent trends and further developments. 2016. *Journal of Difference Equations and Applications*; 22(6): 817-849.




19. Patidar, K.C. On the use of non-standard finite difference methods. 2005. *Journal of Difference Equations and Applications*; 11(8): 735–758.
20. Lombarte, M, Lupo, M, Campetelli, G, Basualdo, M, Rigalli, A. Mathematical model of glucose–insulin homeostasis in healthy rats. 2013. *Mathematical Biosciences*; 245: 269–277.
21. Gopal, M. Digital Control Engineering, New Delhi: New Age International (P) Limited, Publishers, 2003.
22. Gopal, M. Digital Control and State Variable Methods, Conventional and Intelligent Control Systems, New Delhi: Tata McGraw-Hill Publishing Company Limited, 2009.
23. Gurski, K.F. A simple construction of nonstandard finite-difference schemes for small nonlinear systems applied to SIR models. 2013. *Computers and Mathematics with Applications*; 66: 2165–2177.
24. Cresson, J, Pierret, F. Non standard finite difference scheme preserving dynamical properties. 2016. *Journal of Computational and Applied Mathematics*; 303: 15-30.





# Response Surface Methodology for Radioactive Strontium Adsorption on Molecular Sieves

Ekrem Çiçek<sup>1\*</sup> 

<sup>1</sup>Mehmet Akif Ersoy University, Faculty of Arts and Sciences, Department of Physics, Burdur, Turkey

\*[ecicek@mehmetakif.edu.tr](mailto:ecicek@mehmetakif.edu.tr)

\*Orcid: 0000-0001-6724-9423

Received: 8 October 2020

Accepted: 23 November 2021

DOI: 10.18466/cbayarfbe.807377

## Abstract

In the nuclear industry, the disposal of radioactive waste is a crucial issue. Strontium is one of the most dangerous radionuclides to human health. In this study, strontium 85 adsorption on molecular sieves was investigated. The factors affecting the adsorption on molecular sieves were examined. In order to increase adsorption, the sorbent (molecular sieves) was activated before contact with radioactive strontium. The response surface methodology was used to evolve the predictive regression model for adsorption of radioactive strontium on molecular sieves. The experimental and predicted maximum decontamination factor 14.23 and 12.93 was obtained, respectively. Molecular sieves were found to be useful for the removal of radioactive strontium from water solution.

**Keywords:** Response surface methodology, adsorption, radioactive strontium, molecular sieves

## 1. Introduction

Radioisotopes are delivered into the environment from nuclear facilities. During the normal functioning of nuclear power plants, radioactive liquid waste is produced besides nuclear accidents [1-3]. Due to its toxicological effect on the human health radioactive wastewater is a serious environmental concern. The sample of these health problems are cancer and carcinogenic diseases. Radioactive strontium is a main contaminant in low-level radioactive wastewaters from nuclear power plants. There are different types of cations including nonradioactive strontium in the environment [2-4].

The atomic number of elemental strontium is 38. Stable strontium is a soft, silver-gray metal. Strontium occurs naturally in the earth as a mixture of four stable isotopes. <sup>85</sup>Sr (half-life = 64.84 d) is radioactive strontium isotope which occur in the environment from routine discharges from nuclear installations and from nuclear accidents [5].

Because of its relatively long half-life and high toxicity the removal of strontium from wastewaters is of great interest. Strontium is one of the most harmful radionuclides in radioactive liquid waste. A half-life of strontium-90 28.8 years and it is a pure beta emitter of

0.546 MeV. It is generally found in many groundwater systems coming from historic nuclear waste storage sites [3, 4, 6, 7]. The contamination by the radioactive strontium increases environmental interest on the healthy water [2, 8].

In order to decrease the volume of radioactive waste, many techniques including adsorption, ion-exchange processes, evaporation have been reported. Among the methods, adsorption method is examined to be economic and effective, due to its radiation stability [2, 3, 4, 9]. Although a number of investigations have focused on the application of sorbents for the removal of radionuclide from waste solutions, however few have reviewed adsorption modelling with response surface methodology (RSM) [3, 10-12]. This study aimed to investigate molecular sieves application for the removal of strontium from waste solutions.

## 2. Materials and Methods

Molecular sieve (Merck, 105705) is used in this study. <sup>85</sup>Sr was obtained from Institute of Nuclear Chemistry and Technology, Warsaw, Poland. The radionuclidic purity of <sup>85</sup>Sr was determined by gamma spectrometry. Molecular sieve was activated for two hours at 873 K

before contact with strontium ions. Subsequently molecular sieve was added to the strontium 85. We shook the mixtures for 4 h. Thereafter the mixtures were filtered with a syringe filter. The activities of strontium 85 were measured with Polon Warszawa Analyzer (A-22p HT Power supply ZW N-21M HT Control 0/2000V). For all liquid radioactivity measurements, a volume of 10 mL solution was used. Each measurement was repeated for 10 times. The experimental decontamination factor was described as below:

$$DF = A_0 / A_f \quad (1)$$

where  $A_0$  was the initial activity of Strontium 85 feed solution (Bq/L) and  $A_f$  was the final activity (Bq/L). More details regarding experiment can be found in previous studies [12, 13].

We regulated the experimental analysis and modeling using RSM as a useful mathematical and statistical technique as described previously in details [12-16]. The response decontamination factor can be determined which is influenced by various input variables in RSM model.

The general form of RSM can be present as below:

$$DF = \beta_0 + \beta_1 X_1 + \beta_2 X_2 + \beta_{11} X_1^2 + \beta_{22} X_2^2 + \beta_{12} X_1 X_2 \quad (2)$$

$$\beta = [\beta_0 \beta_1 \beta_2 \beta_{11} \beta_{22} \beta_{12}]^T \quad (3)$$

$$\beta = (X^T \cdot X)^{-1} \cdot X^T \cdot DF \quad (4)$$

where:  $\beta$  – shows regression coefficients;

$X$  – input values;

$DF$  – decontamination factor (response).

Adsorption of strontium ions solutions onto molecular sieves;

- regression model with actual variables:

$$\widehat{DF} = 7.66 - 123.1SD - 0.00042A_0 + 1257SD^2 - 0.00711SDA_0 \quad (5)$$

valid for the range:

$$0.05 \leq SD \leq 0.15 \text{ (%w/v)}; 4037 \leq A_0 \leq 8992 \text{ (Bq/L)}$$

The calculation details can be found in previous studies [12- 19]. All calculations were done by means of Minitab 19 software.

### 3. Results and Discussion

The ANOVA was employed to test the accuracy of the calculated model. According to the results the model was compatible where the probability value was 0.016. F value was 11.96 it was indicating that the experimental decontamination factor obtained by changing the factor levels were statistically meaningful at the 94% confidence limit.  $R^2$  value should be close to 1 for a better statistical model. The mathematical model is adequate for the prediction radioactive strontium 85 removal by molecular sieves sorption since  $R^2 = 0.94 > (0.75)$ . Lack of fit F and p values are 32.17 and 0.129 ( $P > 0.05$ ), respectively. Lack of fit was not significant and this means that the model is adequate [19, 20].

**Table 1.** Strontium 85 experimental design for molecular sieves.

Run number (N)	Factors (input values)				Response		
	Amount of sorbent (g/100ml)	level <sup>a</sup> $x_1$	Initial activity of Strontium 85 Bq/L $C_0$ (Bq/L)	level <sup>a</sup> $x_2$	Final activity Bq/L	Decontamination Factor (DF)	
						Experimental $DF$	Predicted $DF$
1	0.15	1	8992	1	762.13	11.80	11.35
2	0.05	-1	8992	1	2141.12	4.20	4.91
3	0.15	1	4037	-1	283.68	14.23	12.93
4	0.05	-1	4037	-1	1298.78	3.11	2.96
5	0.15	1	6514.5	0	661.71	9.84	11.59
6	0.05	-1	6514.5	0	1651.13	3.95	3.38
7	0.1	0	8992	1	1714.54	5.24	4.99
8	0.1	0	4037	-1	1200.13	3.36	4.81
9	0.1	0	6514.5	0	1379.29	4.72	4.34
10	0.1	0	6514.5	0	1266.07	5.15	4.34

a -1 = low value. 0 = center value. +1 = high value.

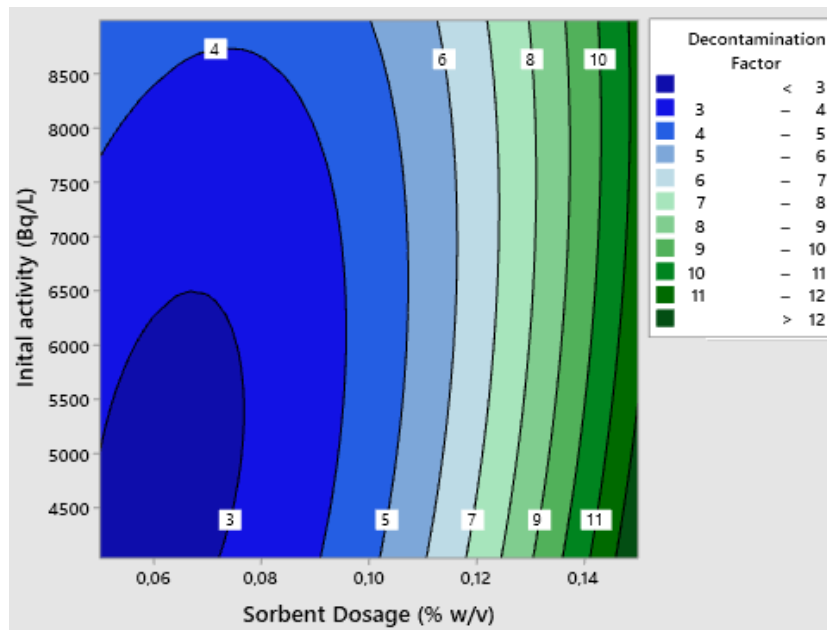


**Figure 1.** Response surface plot of decontamination factor response depending on for molecular sieves- Radioactive strontium.

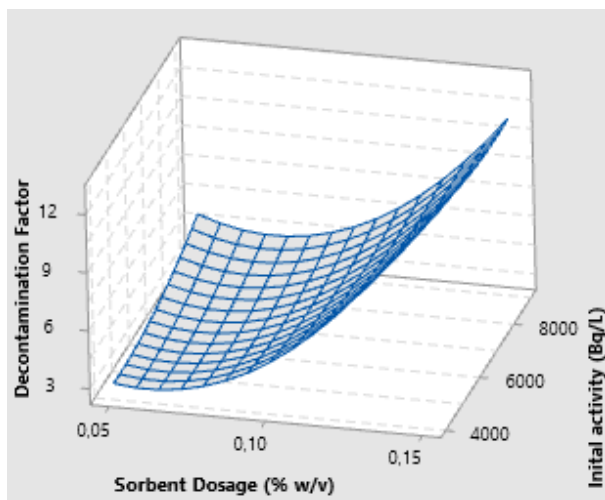


**Figure 2.** 3D-Response surface plot of decontamination factor for molecular sieves- Radioactive strontium.

The experimental and predicted minimum decontamination factor 3.11 and 2.96 was obtained, respectively. The experimental and predicted maximum decontamination factor is 14.23 and 12.93 respectively.

In a previous study, the optimal conditions for zeolite 3A were found to be of initial activity of <sup>85</sup>Sr feed solution =8992 Bq/L and sorbent dosage 0.1 %w/v. A maximal decontamination factor (experimentally) was 41.67 [12]. In this study, decontamination factor of 5.24 was found experimentally for molecular sieves in same conditions.

Strontium is one of the prominent radionuclides in radioactive wastewater. There are many techniques for the removal of radionuclides from wastewater.

Among these removal techniques, adsorption is simple and has tremendous efficiency. The adsorption capacities rise as the sorbent dosage augmentation. The diverse cations interfere with the strontium adsorption on molecular sieves through the purification. Radioactive wastewater such as strontium generated from the nuclear fuel cycle. Radioactive elements have huge potential of collection in plants causes important environmental and health problems [2- 4].

#### 4. Conclusions

In this study, initial activity and the influence of sorbent amount on decontamination factor were investigated by means of RSM. It was found that experimental design and RSM are the efficient approaches for modeling of the removal efficiency of strontium ions.

#### Acknowledgements

This study has been supported by the Marie Curie Transfer of Knowledge scheme 6th EU Technological research and Development Framework Program, AMERAC project (No: MTKD-CT-2004-509226).

#### Author's Contributions

Ekrem ÇİÇEK: Drafted and wrote the manuscript, performed the experiment and result analysis.

#### Ethics

There are no ethical issues after the publication of this manuscript.

## References

1. Honda, MC, Aono, T, Aoyama, M, Hamajima, Y, Kawakami, H, Kitamura, M, Masumoto, Y, Miyazawa, Y, Takigawa, M, Saino, T. 2012. Dispersion of artificial caesium-134 and -137 in the western North Pacific one month after the Fukushima accident. *Geochemical Journal*; 46: 1-9.
2. Munthali, MW, Johan, E, Aono, H, Matsue, N. 2015. Cs<sup>+</sup> and Sr<sup>2+</sup> adsorption selectivity of zeolites in relation to radioactive decontamination. *Journal of Asian Ceramic Societies*; 3: 245-250.
3. Zhang, L, Wei, J, Zhao, X, Li, F, Jiang, F, Zhang, M, Cheng, X. 2016. Competitive adsorption of strontium and cobalt onto tin antimonite. *Chemical Engineering Journal*; 285: 679-689.
4. Hasan, S, Iasir, ARM, Ghosh, TK, Gupta, BS, Prelas, MA. 2019. Characterization and adsorption behavior of strontium from aqueous solutions onto chitosan-fuller's earth beads. *Healthcare*; 7: 52-70.
5. Burger A, Lichtscheidl I. 2019. Strontium in the environment: Review about reactions of plants towards stable and radioactive strontium isotopes. *Science of The Total Environment*; 653: 1458-1512.
6. Pathak, P. 2017. An assessment of strontium sorption onto bentonite buffer material in waste repository. *Environmental Science and Pollution Research*; 24: 8825-8836.
7. Sureda, R, Martinez-Llado, X, Rovira, M, Pablo, JD, Casas, I, Gimenez, J. 2010. Sorption of strontium on uranyl peroxide: Implications for a high-level nuclear waste repository. *Journal of Hazardous Materials*; 181: 881-885.
8. Lee, HS, Lee, J, Yoon, B, Yim, Y, Choi, I, Cho, H, Lee, S, Baik, K, Park, JH, Huh, YJ. 2013. Removal characterization of <sup>133</sup>Cs and <sup>127</sup>I in a water treatment process using a laboratory scale experiment. *Water Supply*; 13(5): 1289-1294.
9. Rahman, ROA, Ibrahim, HA, Hung, YT. 2011. Liquid radioactive wastes treatment: A review. *Water*; 3: 551-565.
10. Tayyebi, A, Outokesh, M, Moradi, S, Doram, A. 2015. Synthesis and characterization of ultrasound assisted "graphene oxide-magnetite" hybrid. and investigation of its adsorption properties for Sr(II) and Co(II) ions. *Applied Surface Science*; 353: 350-362.
11. Chen, C, Hu, J, Shao, D, Li, J, Wang, X. 2009. Adsorption behavior of multiwall carbon nanotube/iron oxide magnetic composites for Ni(II) and Sr(II). *Journal of Hazardous Materials*; 164: 923-928.
12. Cicek, E, Cojocaru, C, Zakrzewska-Trznadel, G, Harasimowicz, M, Miskiewicz, A. 2012. Response surface methodology for the modeling of <sup>85</sup>Sr adsorption on zeolite 3A and pumice. *Environmental Technology*; 33(1): 51-59.
13. Cicek, E, Cojocaru, C, Zakrzewska-Trznadel, G, Jaworska, A, Harasimowicz, M. 2008. Response surface methodology for cobalt removal from aqua solutions using Isparta pumice and zeolite 4A adsorbents. *Nukleonika*; 53(S2): 121-128.
14. Cicek, E. 2009. Response surface methodology for cobalt removal from aqua solutions using nevshehir and Kayseri pumice adsorbents. *Asian Journal of Chemistry*; 21(7): 5727-5736.
15. Myers, RH, Montgomery, DC. Response Surface Methodology: Process and Product Optimization Using Designed Experiments; John Wiley & Sons: New York. 2 ed. 2002.
16. Akhnazarova, S, Kafarov, V. Experiment Optimization in Chemistry and Chemical Engineering; Mir Publishers: Moscow. 1982.
17. Khayet, M, Cojocaru, V, Zakrzewska-Trznadel, G. 2008. Response surface modelling and optimization in pervaporation. *Journal of Membrane Science*; 321: 272-283.
18. Cojocaru, C, Macoveanu, M. 2003. Modeling and Optimization of Diesel Oil Spill Removal from Water Surface Using Shredded Strips of Polypropylene as the Sorbent. *Environmental Engineering and Management Journal*; 2(2): 145-154.
19. Le, MH, Behera, SK, Park, HS. 2010. Optimization of operational parameters for ethanol production from Korean food waste leachate. *International Journal of Environmental Science & Technology*; 7: 157-164.
20. Chauhan, B, Gupta, R. 2004. Application of statistical experimental design for optimization of alkaline protease production from *Bacillus* sp. RGR-14. *Process Biochemistry*; 39(12): 2115-2122.

## Decolorization Potential of *Pleurotus ostreatus*, *Lentinula edodes* and *Ganoderma lucidum* against Solvaderm Brown MF-GO Textile Dye

Fatih Kalyoncu<sup>1\*</sup> , Yurdanur Akyol<sup>2</sup> 

<sup>1</sup> Manisa Celal Bayar University, Faculty of Science, Biology Department, Manisa, Turkey

<sup>2</sup> Manisa Science High School, Manisa, Turkey

\*[fatih.kalyoncu@cbu.edu.tr](mailto:fatih.kalyoncu@cbu.edu.tr)

\*Orcid: 0000-0003-3912-9373

Received: 27 February 2021

Accepted: 7 October 2021

DOI: 10.18466/cbayarfbe.887824

### Abstract

Biological decolorization of Solvaderm Brown MF-GO was comparatively studied using three different macrofungi strains (*Pleurotus ostreatus* (Jacq.) P. Kumm., *Lentinula edodes* (Berk.) Pegler and *Ganoderma lucidum* (Curtis) P. Karst.). In the medium, the inceptive concentrations of dye were 250, 500 and 1000 mg/L, respectively. Whole fungi studied decolorized Solvaderm Brown to varying degrees. Fungi strains resulted in the good decolorization at low dye concentration, but mycelia negatively affected from increasing dye concentrations.

**Keywords:** Decolorization, Macrofungi, Solvaderm Brown, Textile dye

### 1. Introduction

Synthetic dyes are used in paper and textile industries. Remediation of effluents from these industries is quite difficult. Today, strict regulations about wastewater evacuation have been compulsory in some countries. This strict inspection, in connective with transnational repression has been besetting the very survival of the textile production for instance “eco labels” on products for the US and European [1].

Many applied treatment methods for dyed wastewaters occurring combined processes entailing varied combinations of chemical, physical and biological processes [2-4]. These processes have restricted performance and endured from some disability for example that usage of chemicals and sludge formation, expensive substructure requirements and high operating exes. Conventionally effluent remedy plants reliant prompted sludge systems are not sufficient for the wastewater, since the using bacterial methods for dye wastewaters may result generation of colorless compounds that more toxic than the parents such as aromatic amines [5]. However, the need for an economically and technically convincing remediation method, a bustle of developing technologies are being suggested and tried at several phases of commercialization [6].

By far, white rot fungi is most powerful in overthrow synthetic dyes [7, 8]. Exclusively *Pleurotus* species, are

usually more permissive to high levels of dyes than bacteria [9, 10]. White rot fungi are capable of aerobic mineralization and lignin de-polymerization in nature. These fungi to produce extracellular lignin modifying enzymes [8]. Also, *Pleurotus* species are good ligninolytic enzyme producers against some pollutants and textile dye effluents [11, 12]. Nevertheless, no information is existing respecting the use of *Pleurotus ostreatus*, *Lentinula edodes* and *Ganoderma lucidum* for the decolorization of Solvaderm Brown. The main goal of this research was to in comparison with evaluate the potential of *Pleurotus ostreatus*, *Lentinula edodes* and *Ganoderma lucidum* to degrade Solvaderm Brown textile dye.

### 2. Materials and Methods

This research was performed with three strains of white-rot fungi (*Ganoderma lucidum* MCC52, *Lentinula edodes* MCC29, *Pleurotus ostreatus* MCC07). These fungi were stored in the Mushroom Culture Collection (MCC) of the Biology Department, Manisa Celal Bayar University, Turkey and protected on PDA slants at 4°C until use.

All fungus were transferred on Petri dishes having Kirk's basal media. This medium were supplemented with Solvaderm Brown dye concentrations of 250, 500 and 1000 mg/L. Agar discs (6 mm) of 7 days old cultures on Kirk's medium at 27°C used as inoculum. All plugs cut under aseptic conditions from the agar

plates and were transferred onto the center of the dye added plates for each replicate. Also, non-inoculated dishes deposited as controls for abiotic decolorization [6]. All fungus were tested in three parallel tests. Petri dishes were stored at 27°C for 30 days. Mycelial expansion was viewed by gauging radial appendage of the mycelium as explained by literature [13] with a digital caliper on each plate. The average mycelial development was calculated according to three replicates. A colorless zone seen when the fungus degraded the dye.

Also, mycelial discs (6 mm) were used as inoculum for spectrophotometric analyses of decolorization period. 50 ml liquid medium that having Solvaderm Brown (250, 500 and 1000 mg/L) and Kirk's basal media was prepared in Erlenmeyer flasks. Liquid media were autoclaved at 121°C for 15 min. Each one was inoculated with five agar disc and incubated in shaker incubator at 27°C, 120 rpm/min [14]. Decolorization of dyes in the liquid medium were monitored at regular intervals during the research.

0.5 ml samples were afflicted from each Erlenmeyer at orderly time spaces, and residuary dye was measured directly by a UV-visible spectrophotometer at the 610 nm maximal wavelength of absorbance. Absorbance rates were used for the computations of decolorization performance. Kirk's medium in distilled water was used as control [6]. The data offered are the means of the results of 3 repeats with a standard error of less than 5%.

### 3. Results and Discussion

Synthetic dyes are the generally used dyestuffs in the paper and textile industry. Solvaderm Brown is widely preferred synthetic dye was used for the definition of decolorization capacity of three white-rot fungi strains, in this study.

The efficacy of dyestuff levels on the development of fungi studied is indicated in Figure 1. All organisms were unfavorably affected from a spawning level of dye in medium, resulting in remarkably lower mycelial development. Rising levels of Solvaderm Brown in the medium caused up to 2 and 4 times lower mycelial development for all organisms used, respectively (Figure 1). Parallel outcomes have been declared in literature that amaranth dye was used. It has been declared that 100 mg of this dye shows a more toxic effect on the development of *Trametes versicolor* than a lower dye level (33 mg) in the similar medium [15].

As showed in Figure 1; the mycelial development was delayed when the fungi were revealed to rising dye levels, the decolorization performances of the fungi were not retrograded that much for Solvaderm Brown (Figure 2). Figure 2, depict the dye removal performance of each fungus used at 250, 500 and 1000

mg/L levels, respectively. In Figure 2; rising concentration of Solvaderm Brown unfavorably affected the decolorization performance of the fungi to changing degrees. Fungi may be arranged as to their decolorization performances when they were revealed to 250 mg/L dye level in the medium for Solvaderm Brown as follows: *L. edodes* (19%) > *P. ostreatus* (8%) > *G. lucidum* (5%), respectively.

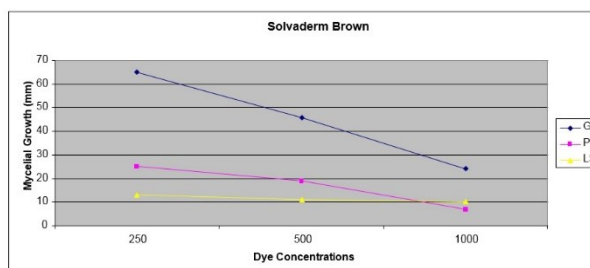


**Figure 1.** Effect of various Solvaderm Brown concentrations on mycelial growth at 23<sup>rd</sup> day; GL: *Ganoderma lucidum*; PO: *Pleurotus ostreatus*; LS: *Lentinula edodes*.

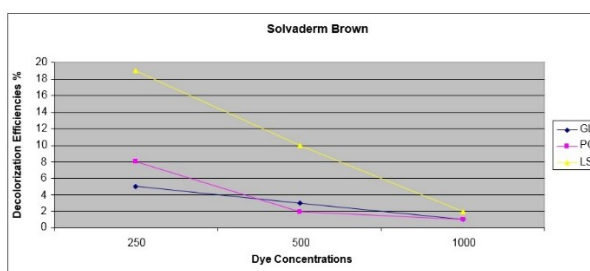


**Figure 2.** Decolorization efficiencies for each fungus species for Solvaderm Brown at 23<sup>rd</sup> day; GL: *Ganoderma lucidum*; PO: *Pleurotus ostreatus*; LS: *Lentinula edodes*.

It has been declared in the references that the some white-rot fungi are aerobically biotransformed or mineralized some textile dyes [5, 7, 9, 16]. As crosschecked with some references, we were able to decolorize meaningfully higher levels of dye (250, 500 and 1000 mg/L) in our research. Reife and Freeman [17] remarked that azo dyes, according to their chemical form, are more robust to decolorization than are anthraquinones. Such that wild-type strains of *Pleurotus ostreatus* are the resistant, since the drop in decolorization performance due to the rising dye level was around 4-14%, while the other fungi were meaningfully affected drop in decolorization performance: *P. ostreatus* ≥ 60%, *P. djamor* ≥ 34%, and *P. citrinopileatus* ≥ 19%. These results are in relevance to the other studies related to *Pleurotus sp.* [4, 5, 10, 11]. Yeşilada et al. [18] declared that *Pleurotus ostreatus* showed 97%, 89%, and 84% decolorization efficiency for 264 mg/L azo dyes, called Astrazone Red, Blue and Black, respectively. *Phanerochaete chrysosporium* is also can decolorize textile wastewaters. Different decolorization stages (40%-

73%) are reached in Kirk's medium for eight dyes by this fungus [6].

#### 4. Conclusions

In this research, three white-rot fungi strains were used to show the decolorization capacity of Solvaderm Brown dye. A fungus talented of decolorizing one dye has different abilities for others. There is a need to identify fungi that are capable of decolorizing dye effluent and the inhibitory effects of dyes on fungal development. Results of this research could conduce to a better knowledge of the decolourization capacities of three fungus strains (*Pleurotus ostreatus*, *Lentinula edodes* and *Ganoderma lucidum*) for Solvaderm Brown that has not been researched in detail up to the present. Results appearing from this study supply a background useful to propose new eco-friendly alternatives for the effluent remediation of textile industries. This research shows the decolorization capacity of wild fungi isolated from nature.

#### Author's Contributions

Fatih KALYONCU: Drafted and wrote the manuscript, performed the experiment and result analysis.

Yurdanur AKYOL: Assisted in analytical analysis on the structure, supervised the experiment's progress, result interpretation and helped in manuscript preparation.

#### Ethics

There are no ethical issues after the publication of this manuscript.

#### References

1. Bıyık, H, Kalyoncu, F, Oryasin, E, Azbar, N, Kalmış, E, Basbülbul, G. 2009. Evaluation of wild and commercial types of *Pleurotus* strains for their ability to decolorize cibacron black W-NN textile dye. *African Journal of Microbiology Research*; 3: 325-329.
2. Azbar, N, Yonar, T, Kestioglu, K. 2004. Comparison of various advanced oxidation processes and chemical treatment methods for COD and color removal from a polyester and acetate fiber dyeing effluent. *Chemosphere*; 55: 35-43.
3. Galindo, C, Kalt, T. 1999. UV/H<sub>2</sub>O oxidation of azo dyes in aqueous media: evidence of a structure – degradability relationship. *Dyes and Pigments*; 42: 199-207.
4. Robinson, T, McMullan, G, Marchant, R, Nigam, P. 2001. Remediation of dyes in textile effluent: a critical review on current treatment technologies with a proposed alternative. *Bioresource Technology*; 77: 247-255.
5. Banat, I.M, Nigam, P, Singh, D, Marchant, R. 1996. Microbial decolorization of textile dye containing effluents: a review. *Bioresource Technology*; 58: 217-227.
6. Kalmış, E, Azbar, N, Kalyoncu, F. 2008. Evaluation of two wild types of *Pleurotus ostreatus* (MCC07 and MCC20) isolated from nature for their ability to decolorize Benazol Black ZN textile dye in comparison to some commercial types of white rot fungi: *Pleurotus ostreatus*, *Pleurotus djamor* and *Pleurotus citrinopileatus*. *Canadian Journal of Microbiology*; 54: 366-370.
7. Balan, D.S.L, Monteiro, R.T.R. 2001. Decolorization of textile indigo dye by ligninolytic fungi. *Journal of Biotechnology*; 89: 141-145.
8. Wesenberg, D, Kyriakides, I, Agathos, S.P., 2003. White-rot fungi and their enzymes for the treatment of industrial dye effluents. *Biotechnology Advances*; 22: 161-187.
9. Hou, H, Zhou, J, Wang, J, Du, C, Yan, B. 2004. Enhancement of laccase production by *Pleurotus ostreatus* and its use for the decolorization of anthraquinone dye, *Process Biochemistry*; 39: 1415-1419.
10. Levin, L, Papinutti, L, Forchiassin, F. 2004. Evaluation of Argentinean white rot fungi for their ability to produce lignin-modifying enzymes and decolorize industrial dyes. *Bioresource Technology*; 94: 169-176.
11. Nilsson, I, Möller, A, Mattiasson, B, Rubindamayugi, M.S.T, Welander, U. 2006. Decolorization of synthetic and real textile wastewater by the use of white-rot fungi. *Enzyme and Microbial Technology*; 38: 94-102.
12. Zhao, X, Hardin, I.R. 2007. HPLC and spectrophotometric analysis of biodegradation of azo dyes by *Pleurotus ostreatus*. *Dyes and Pigments*; 73: 322-325.
13. Weitz, J.H, Ballard, A.L, Campbell, C.D, Killham, K. 2001. The effect of culture conditions on the mycelial growth and luminescence of naturally bioluminescent fungi. *FEMS Microbiology Letters*; 202: 165-170.
14. Tien, M, Kirk, T.K. 1988. Lignin peroxidase of *Phanerochaete chrysosporium*. *Methods of Enzymology*; 161: 238-249.
15. Ramsay, J.A, Nguyen, T. 2002. Decoloration of textile dyes by *Trametes versicolor* and its effect on dye toxicity. *Biotechnology Letters*; 24: 1757-1761.
16. Eichlerova, I, Homolka, L, Nerud, F. 2006. Ability of industrial dyes decolorization and ligninolytic enzymes production by different *Pleurotus* species with special attention on *Pleurotus calypttratus* strain CCBAS 461. *Process Biochemistry*; 41: 941-946.
17. Reife, A, Freeman, S. 1996. Environmental chemistry of dyes and pigments. *John Wiley & Sons, New York*, 75-90.
18. Yesilada, O, Asma, D, Cing, S. 2003. Decolorization of textile dyes by fungal pellets. *Process Biochemistry*; 38: 933-938.





## Spectroscopic analyses on the binding interaction of thiosemicarbazone-derived Cu(II) complex with DNA/BSA

Mükerrem Fındık<sup>1\*</sup> , Asuman Uçar<sup>2</sup> , Emine Güler Akgemci<sup>3</sup> 

<sup>1</sup> Necmettin Erbakan University, A.K. Education Faculty, Department of Chemistry Education, Research Laboratory, Konya, Turkey

<sup>2</sup> Agri Ibrahim Cecen University, Education Faculty, Department of Science Education, Ağrı, Turkey

<sup>3</sup> Necmettin Erbakan University, A.K. Education Faculty, Department of Chemistry Education, Konya, Turkey

\* [mmukerrem@gmail.com](mailto:mmukerrem@gmail.com)

\*Orcid: 0000-0002-9441-0814

Received: 30 March 2021

Accepted: 1 June 2021

DOI: 10.18466/cbayarfbe.902377

### Abstract

Cu(II) complex of 2-hydroxy-5-methoxyacetophenone-N(4)-ethyl thiosemicarbazone (Cu(HMAET)Cl) was synthesized and characterized by spectroscopic methods such as FT-IR, <sup>1</sup>H-NMR and UV-Vis. The Cu(II) complex's DNA-binding capacity was studied with the UV-Vis absorption titration and ethidium bromide (EB) displacement experiment using *E. coli* DNA. The results demonstrated that the Cu(II) complex could intercalate in the DNA's base pairs. The binding constant was found as  $2.8 \times 10^7 \text{ M}^{-1}$ . Also, the interaction study of the Cu(II) complex with bovine serum albumin (BSA) was investigated using the UV-Vis absorption and fluorescence spectroscopy techniques. It was concluded that the Cu(II) complex interacts strongly with BSA.

**Keywords:** Thiosemicarbazone, copper(II) complex, DNA/BSA binding, fluorescence quenching, absorption

### 1. Introduction

Studies on the interaction of DNA and small molecules, which are of great importance in human life, are important for developing new pharmaceutical molecules [1-3]. DNA is an important intracellular target for anticancer drugs as it regulates most biochemical processes occurring in cellular systems [4-6]. Therefore, a drug should be designed to bind specifically to DNA. Generally, complexes interact with DNA by intercalating between base pairs or binding to the grooves of the DNA. These non-covalent binding modes' weak interactions are reversible and less toxic to healthy cells [7]. Therefore, it is very important to prepare such metal complexes.

Researchers know that Cu(II) complexes, which have a wide range of biological activity, show anti-inflammatory, antiviral, and antitumor properties [3,8,9]. It has been observed that the presence of copper ions in the complexes increases the effectiveness of the drug and organic therapeutic agents [10]. Besides, Cu(II) complexes can lead to oxidative cleavage of DNA by means of chemical oxidants [11]. In the last ten years, many Cu(II) complexes with strong DNA binding

and cutting ability have been synthesized. Most of them show excellent anticancer and apoptosis regulating effects [12,13]. Cu(II) complexes are also promising in preparing less toxic anticancer drugs [14-16]. Recently, many researchers have been working on the interaction between Cu(II) complexes and serum albumin, such as Human serum albumin (HSA)/bovine serum albumin (BSA), because proteins, like DNA, are also targets of anticancer drugs [7,17]. HSA and BSA are the most abundant carrier proteins in animal plasma [18]. BSA is often chosen as a model protein because of its structural similarity with HSA, has the advantages of low cost, high stability, good water solubility, wide availability, and easy binding with different compounds [17,19].

Therefore, in this study, the thiosemicarbazone-derived Cu(II) complex was synthesized and investigated the binding interaction with DNA and BSA using UV-Vis absorption and fluorescence spectroscopy techniques.

### 2. Materials and Methods

#### 2.1. Chemicals and Apparatus

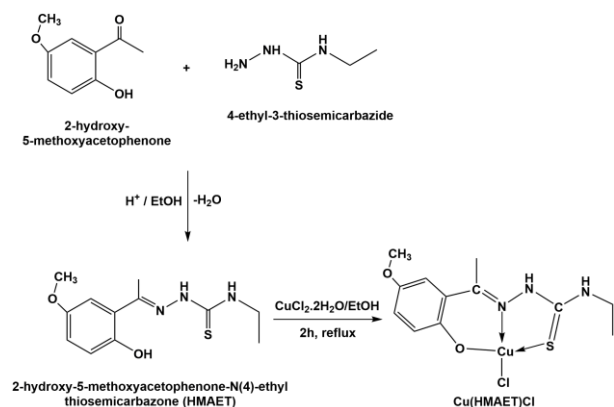
4-Ethyl-3-thiosemicarbazide, 2-hydroxy-5-methoxyacetophenone, bovine serum albumin (BSA),

ethidium bromide (EB), copper(II) chloride dihydrate ( $\text{CuCl}_2 \cdot 2\text{H}_2\text{O}$ ) and sodium chloride ( $\text{NaCl}$ ) were purchased from Sigma Aldrich. Ethyl alcohol (EtOH) and *N,N*-dimethylformamide (DMF) were obtained from Merck.

Perkin-Elmer 2400 CHN elemental analyzer was used for elemental analysis (C, H, and N) of the sample. A Bruker AC 400 (400 MHz) NMR spectrometer was used to record the  $^1\text{H}$ -NMR spectrum. Perkin-Elmer Spectrum 100 with Universal ATR Polarization Accessory (Shelton, USA) was used for the FT-IR spectrum. Absorbance spectra were monitored by Shimadzu UV-1800 double beam spectrophotometer. Fluorescence spectra were obtained using a PTI Quantmaster 400 Fluorometer spectrophotometer.

## 2.2. Synthesis of HMAET and $\text{Cu}(\text{HMAET})\text{Cl}$

HMAET and  $\text{Cu}(\text{HMAET})\text{Cl}$  was synthesized from the previous study by following the related procedure: HMAET; equimolar solutions of 2-hydroxy-5-methoxyacetophenone and 4-ethyl-3-thiosemicarbazide were dissolved in 30 mL of absolute EtOH and 2-3 drops of conc.  $\text{H}_2\text{SO}_4$  was added. The mixture was stirred for 2 h at room temperature. The resulting solid was filtered and recrystallized twice with an EtOH/water mixture.  $\text{Cu}(\text{HMAET})\text{Cl}$ ; 1.5 mmol of the HMAET was dissolved in EtOH (30 mL) with gentle heating. An equimolar amount of  $\text{CuCl}_2 \cdot 2\text{H}_2\text{O}$  was dissolved in the minimum quantity of the same solvent and added dropwise to the HMAET solution. The mixture was refluxed for approximately 2 h, and then slowly evaporated at  $35^\circ\text{C}$  until sufficient solid formed. The resulting solid was filtered and washed with anhydrous ether [20,21].



**Scheme 1.** Synthesis of  $\text{Cu}(\text{HMAET})\text{Cl}$ .

The synthesis procedure of the ligand and complex is given in the Scheme 1. Dark green crystals, yield 67.5 %; mp:  $153\text{--}154^\circ\text{C}$ . Anal. calc. ( $\text{C}_{12}\text{H}_{15}\text{ClCuN}_3\text{O}_2\text{S}$ ); C, 39.56; H, 4.15; N, 11.53; S, 8.80 %. Found: C, 39.59; H, 4.17; N, 11.56; S, 8.91 %.  $^1\text{H}$ -NMR (400 MHz,  $\text{DMSO-d}_6$ ):  $\delta$  (ppm): 8.74 (s, 1H,  $-\text{NH}$ ), 6.82 (s, 1H,  $\text{H}_{\text{Ar}}$ ), 6.98

(d, 2H,  $\text{H}_{\text{Ar}}$ ), 3.81 (s, 3H,  $-\text{OCH}_3$ ), 3.78 (m, 2H,  $-\text{CH}_2$ ), 2.38 (s, 3H,  $-\text{CH}_3$ ), 1.31 (t, 3H,  $-\text{CH}_3$ ). FT-IR ( $\text{cm}^{-1}$ ): 3442, 3261, 1626, 1568, 1523, 1260, 1217, 1036, 823, 778, 526, 443, 315, 284, 179.

## 2.3. DNA binding study

The *E. coli* DNA binding experiments of  $\text{Cu}(\text{HMAET})\text{Cl}$  were investigated using a UV-Vis spectrometer. Absorbance measurements were obtained with different concentrations of *E. coli* DNA (0.1–1.4  $\mu\text{M}$ ) in distilled water with Tris-HCl buffer (5 mM Tris/50 mM NaCl, pH 7.2) by adding to the  $\text{Cu}(\text{HMAET})\text{Cl}$  (50  $\mu\text{M}$  in DMF).

## 2.4. Displacement experiment with EB

Displacement experiments of EB were studied by fluorescence spectroscopy. Interaction has been recorded by the gradual addition of different concentrations of  $\text{Cu}(\text{HMAET})\text{Cl}$  to Tris-HCl buffer (5 mM Tris/50 mM NaCl, pH 7.2) solution of EB-DNA (10  $\mu\text{M}$ ). The measurements were recorded after waiting half an hour.

## 2.5. Interaction with BSA

Fluorescence spectra measurements were recorded in phosphate-buffered saline (PBS) at pH 7.5 to study the interaction of  $\text{Cu}(\text{HMAET})\text{Cl}$  with BSA. The emission spectra were initially monitored using 2 mL of BSA solution (1  $\mu\text{M}$ ), following the incremental additions (0–2.5  $\mu\text{M}$ ) of  $\text{Cu}(\text{HMAET})\text{Cl}$ . In addition, the absorbance measurement of BSA solution (10  $\mu\text{M}$  in PBS) was investigated in the presence and the absence of  $\text{Cu}(\text{HMAET})\text{Cl}$  (4  $\mu\text{M}$  in DMF).

## 2.6. Statistical analysis

For statistical analysis, experiments were run in triplicate. Plots were prepared according to the average.

## 3. Results and Discussion

### 3.1. Characterizations of $\text{Cu}(\text{HMAET})\text{Cl}$

The FT-IR spectrum of  $\text{Cu}(\text{HMAET})\text{Cl}$  (Figure 1) showed a band at  $3261\text{ cm}^{-1}$ , which is attributed to the  $\nu(\text{N-H})$  band [22]. It was seen that  $\nu(\text{C=N})$  and  $\nu(\text{N-N})$  bands peaked at  $1523\text{ cm}^{-1}$  and  $1036\text{ cm}^{-1}$ , respectively [23,24]. Vibrations of  $\nu(\text{C-S})$  which became from  $\nu(\text{C=S})$  bond after coordination occurred at  $823\text{ cm}^{-1}$  [25]. The bands observed at 179, 315, 443 and  $526\text{ cm}^{-1}$  are  $\nu(\text{Cu-Cl})$ ,  $\nu(\text{Cu-S})$ ,  $\nu(\text{Cu-N})$  and  $\nu(\text{Cu-O})$  bonds, respectively, indicating the formation of the  $\text{Cu}(\text{II})$  complex.

The  $^1\text{H}$ -NMR spectrum of  $\text{Cu}(\text{HMAET})\text{Cl}$  was monitored in  $\text{DMSO-d}_6$  solvent (Figure 2). The signals at 1.31 ppm correspond to the methylene protons of the ethyl group, whilst the  $-\text{CH}_2$  protons of the ethyl group appeared as a multiplet at 3.78 ppm [26,27]. The singlet assigned to  $-\text{CH}_3$  of the azomethine group occurred at

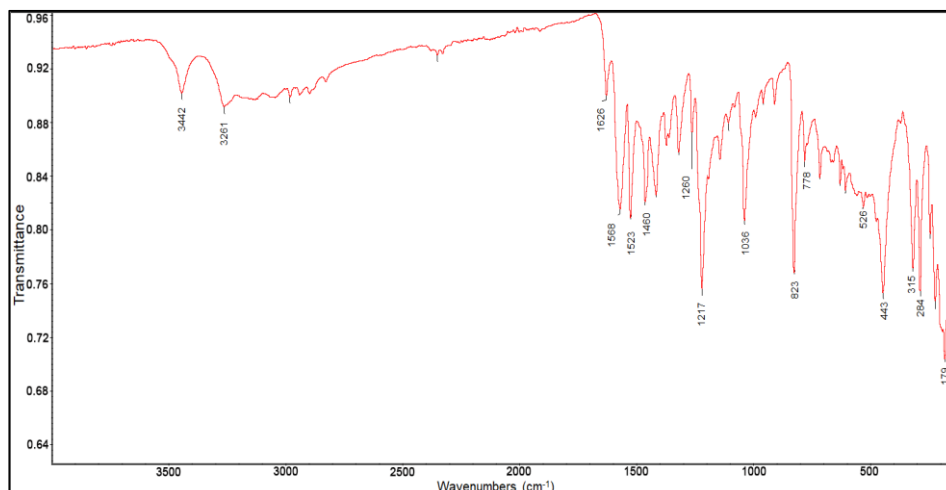


Figure 1. FT-IR spectrum of Cu(HMAET)Cl.

2.38 ppm [28]. A singlet corresponding to the  $-OCH_3$  group was observed at 3.81 ppm [29]. The aromatic protons showed signals at 6.82 and 6.98 ppm. The thiocarbonyl attached  $-NH$  proton was observed at 8.74 ppm.

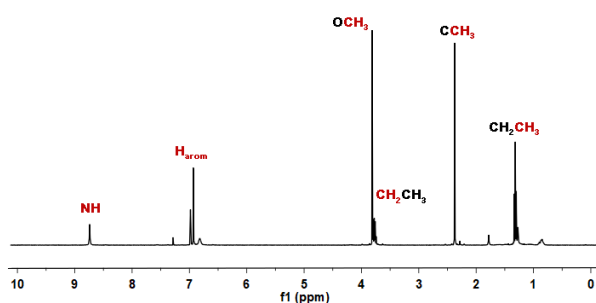


Figure 2.  $^1H$ -NMR spectrum of Cu(HMAET)Cl.

The electronic spectrum was monitored in DMF in the 235–465 nm region at room temperature (Figure 3). Cu(HMAET)Cl showed intraligand transitions at 310 and 265 nm attributed to  $n/\pi^*$  and  $\pi/\pi^*$  transitions, respectively [39]. The band at 370 nm corresponding to the ligand to metal charge transfer transitions [31] can be the evidence of the combination of  $S \rightarrow Cu$ ,  $N \rightarrow Cu$ ,  $O \rightarrow Cu$ , and the ligand to metal charge transfer transition (LMCT) [32].

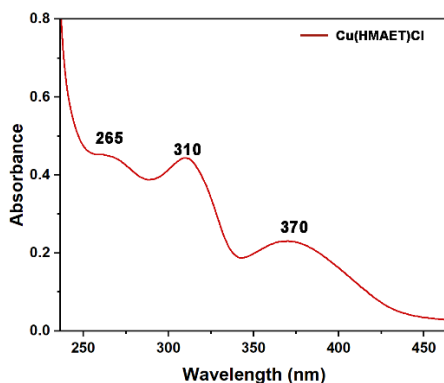


Figure 3. UV-Vis spectrum of Cu(HMAET)Cl.

## 3.2. DNA binding experiments

### 3.2.1. UV absorption spectra of DNA

Interaction studies of DNA and metal complexes are important for understanding the mechanism of interaction and designing effective chemotherapeutic agents and new anticancer drugs [33–35]. UV-Visible absorption titration experiment was performed to examine the Cu(II) complex and *E. coli* DNA binding interaction. Figure 4A shows the absorption spectra of the Cu(II) complex in the presence and absence of *E. coli* DNA. Absorption titration was carried out by adding different concentrations of *E. coli* DNA (0.1–1.4  $\mu M$ ; 5 mM Tris-HCl/50 mM NaCl, pH:7.2) to the Cu(II) complex (50  $\mu M$ ). After increasing the amount of *E. coli* DNA to the Cu(II) complex, the spectrum showed a hypochromism of about 5 %, 15 %, and 9 % with a blue shift of 6, 3, and 22 nm at 282, 324, and 408 nm. According to the results obtained, the binding to *E. coli* DNA was confirmed from the Cu(II) complex's absorption changes. The amount of binding interaction between *E. coli* DNA and the Cu(II) complex was described using the binding constant  $K_b$ , which is calculated from Eq. (1) [36,37].

$$\frac{[DNA]}{(\varepsilon_a - \varepsilon_f)} = \frac{[DNA]}{(\varepsilon_b - \varepsilon_f)} + \frac{1}{K_b(\varepsilon_b - \varepsilon_f)} \quad (1)$$

Where [DNA] is the concentration of *E. coli* DNA,  $\varepsilon_f$ ,  $\varepsilon_a$ , and  $\varepsilon_b$  correspond to the extinction coefficient for the free complex,  $A_{obsd}/[complex]$ , and the extinction coefficient for the complex in the fully bound form, respectively.  $K_b$  was found by calculating the ratio of slope/intercept in the linear plot of  $[DNA]/(\varepsilon_a - \varepsilon_f)$  vs. [DNA] (Figure 4B). The binding constant ( $K_b$ ) value for the interaction of the Cu(II) complex with *E. coli* DNA was found as  $2.8 \times 10^7 M^{-1}$ . The  $K_b$  value of the Cu(II) complex confirms that it binds to the DNA helix via the intercalative mode [11,34,36].

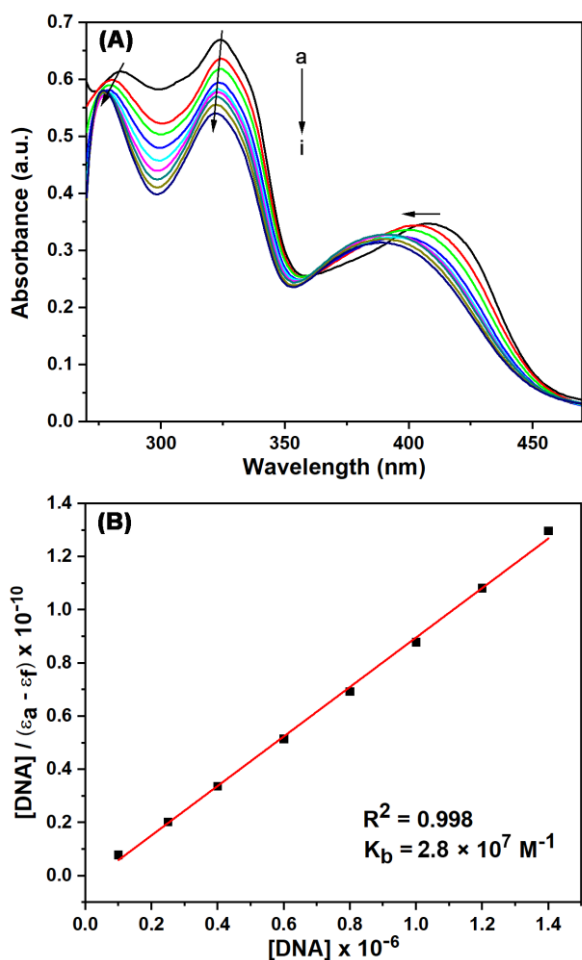


**Figure 4.** (A) Absorption spectrum of Cu(HMAET)Cl (50  $\mu\text{M}$ ) at various concentrations of *E. coli* DNA: a) 0.0  $\mu\text{M}$ ; b) 0.1  $\mu\text{M}$ ; c) 0.25  $\mu\text{M}$ ; d) 0.4  $\mu\text{M}$ ; e) 0.6  $\mu\text{M}$ ; f) 0.8  $\mu\text{M}$ ; g) 1.2  $\mu\text{M}$ ; h) 1.4  $\mu\text{M}$ . (B) The plot of  $[\text{DNA}]/(\epsilon_a - \epsilon_f)$  vs.  $[\text{DNA}]$  for the titration of Cu(HMAET)Cl with *E. coli* DNA.

### 3.2.2. Ethidium Bromide (EB) Displacement

Known as an intercalator, EB can intercalate into double-stranded DNA. Free EB and DNA have very weak fluorescence. When EB intercalates the double-stranded DNA, the fluorescence intensity of the compound becomes extremely strong. However, by intercalating some compounds to DNA, the DNA binding sites of EB are decreased, causing the fluorescence of the EB-DNA system to be quenched [10,11,38]. EB displacement assay for the Cu(II) complex was performed by fluorescence method. The study was carried out by titration of the Cu(II) complex varying between 2.5 and 11.5  $\mu\text{M}$  into 10  $\mu\text{M}$  DNA and 10  $\mu\text{M}$  EB solution. After adding each aliquot, the emission spectra of the DNA-EB complex, which was applied as an excitation wavelength of 540 nm, were recorded between 550 nm and 760 nm. The fluorescence spectra of the DNA-EB in the presence and absence of the Cu(II) complex (Figure 5A) show that

the fluorescence intensity of DNA-EB is quenched significantly in each addition with increasing amounts of the Cu(II) complex. This result indicated that the Cu(II) complex was able to replace EB in the DNA helix. Thus the Cu(II) complex can bind to DNA via intercalative binding mode. The Stern–Volmer (S-V) constant was used for the quenching efficiency of the Cu(II) complex [39],

$$F^0/F = 1 + K_{SV} [Q] \quad (2)$$

where  $F/F^0$ ,  $K_{SV}$ ,  $[Q]$  are the fluorescence intensities in the presence/absence of the Cu(II) complex, the linear S-V quenching constant, and concentration of the Cu(II) complex, respectively. The  $K_{SV}$  value is calculated from the ratio of slope/intercept in the linear plot of  $[Q]$  vs.  $F^0/F$  and is found to be  $2.8 \times 10^6 \text{ M}^{-1}$  (Figure 5B).

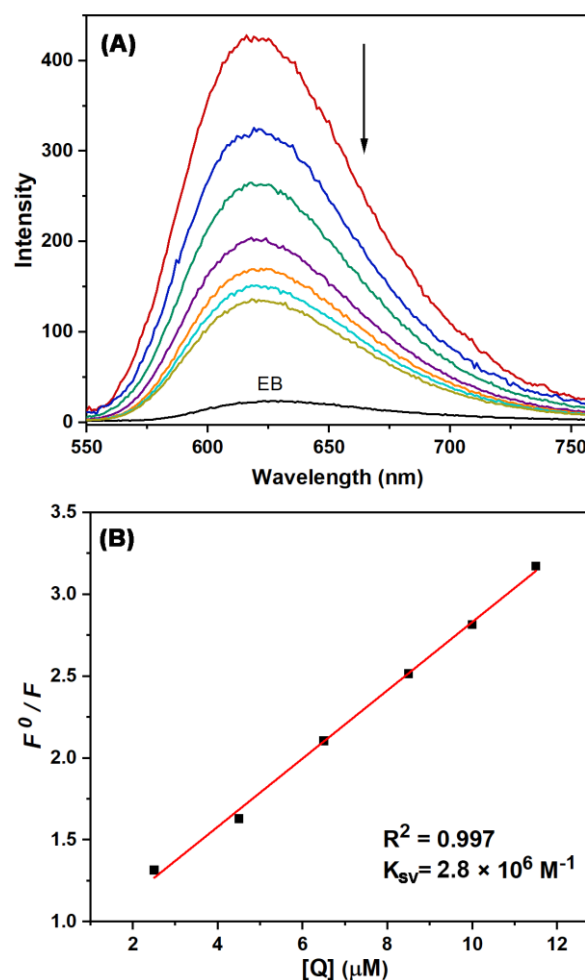


**Figure 5.** (A) Fluorescent quenching with increasing Cu(HMAET)Cl to DNA/EB Conditions:  $[\text{EB}] = 10 \mu\text{M}$ ,  $[\text{DNA}] = 10 \mu\text{M}$ ,  $[\text{Cu(II) complex}] = 2.5\text{--}11.5 \mu\text{M}$ . (B) S-V plot of fluorescence titrations of Cu(HMAET)Cl with *E. coli* DNA.

### 3.3. BSA binding experiments

#### 3.3.1. Fluorescence Quenching of BSA

One of the most effective techniques used to study interactions between compounds and BSA is fluorescence spectroscopy.

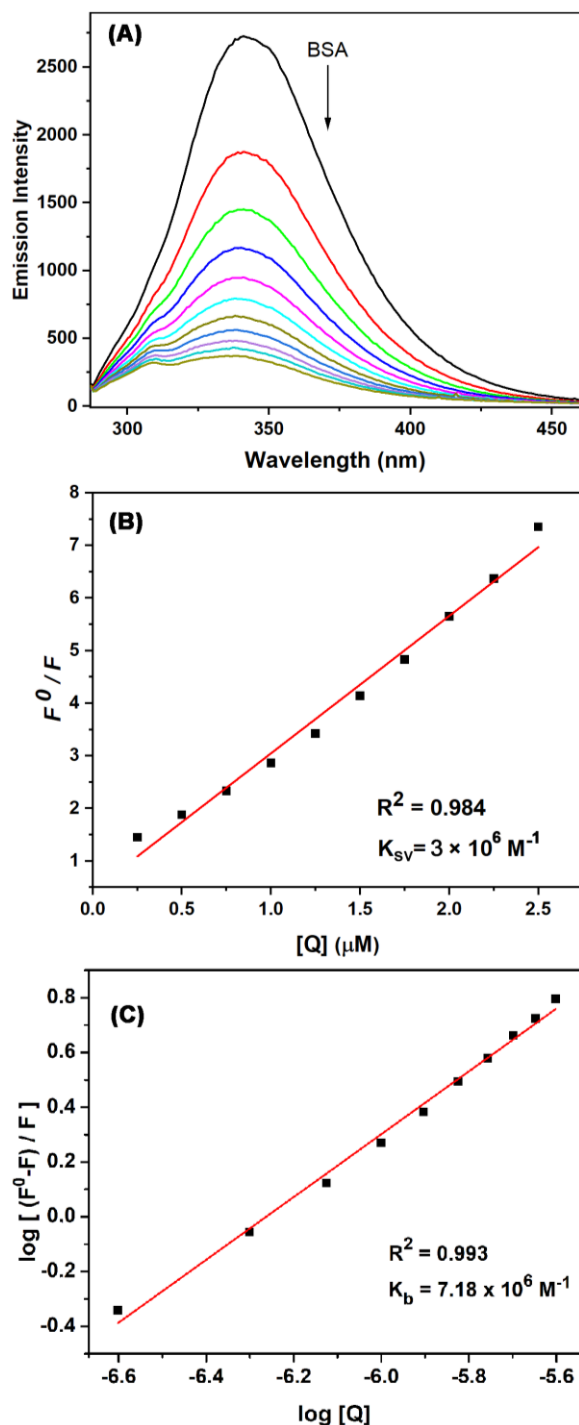


**Figure 6.** (A) Fluorescence quenching of BSA (1  $\mu\text{M}$ ;  $\lambda_{\text{ex}}=280$ ;  $\lambda_{\text{em}}=341$  nm) in presence/absence of various concentrations of Cu(HMAET)Cl (0–2.5  $\mu\text{M}$ ); (B) S-V plot of Cu(HMAET)Cl with BSA; (C) Scatchard plot of Cu(HMAET)Cl with BSA.

Fluorescence of the BSA is due to the fluorophore groups in its structure, such as tryptophan, tyrosine, and phenylalanine. When any compound interacts with BSA, fluorescence intensity quenches [18,36].

The variations in the BSA fluorescence intensity were noted over the range of 285–460 nm ( $\lambda_{\text{ex}} = 280$  nm) with the incremental addition of the Cu(II) complex (0–2.5  $\mu\text{M}$ ) to a fixed concentration of BSA (1  $\mu\text{M}$ ) prepared in PBS buffer solution (pH = 7.5). The quenching of the BSA fluorescence (Figure 6A) with the addition of the Cu(II) complex was observed at  $\lambda = 341$  nm with a percentage of 86.39 %, along with a hypsochromic shift of 6 nm. The main reason for this was that the protein's active sites are embedded in a hydrophobic environment [40,41].

These results showed that the Cu(II) complex had a definite interaction with the BSA protein. The S-V equation has been used to interpret the possible quenching mechanism.

$$\frac{F^0}{F} = 1 + K_q \tau_0 [Q] = 1 + K_{SV} [Q] \quad (3)$$

Where  $F/F^0$ ,  $K_q$ ,  $[Q]$  and  $\tau_0$  the fluorescence intensities in the presence/absence of the complex, the bimolecular quenching rate constant, the concentration of the complex, and the average lifetime ( $10^{-8}$  s) of protein without complex, respectively.  $K_{SV}$  is the S-V quenching constant and is equal to  $K_q \tau_0$ . The value of  $K_{SV}$  was obtained as slope of the linear plot of  $F^0/F$  vs.  $[Q]$  and was found to be  $3 \times 10^6 \text{ M}^{-1}$ . The  $K_q$  was found to be  $3 \times 10^{14} \text{ M}^{-1} \text{ s}^{-1}$  (Figure 6B).

If any molecule binds to BSA's active site, the Scatchard equation is used to calculate the equilibrium binding constant and the number of binding sites [42].

$$\log[(F^0 - F)/F] = \log K_b + n \log [Q] \quad (4)$$

Where  $F/F^0$ ,  $K_b$ , and  $n$  are the fluorescence intensity in the presence/absence of the complex, the binding constant of the complex with BSA, and the number of binding sites. The  $K_b$  and  $n$  were calculated from the intercept and slope in the linear plot of  $\log[(F^0-F)/F]$  vs.  $\log [Q]$ , respectively and was found to be  $7.18 \times 10^6 \text{ M}^{-1}$  and  $n = 1.14$  (Figure 6C). A binding site value close to 1 indicates that there is only one binding site between the Cu(II) complex and BSA. The obtained  $K_q$  and  $K_b$  values prove that there is a strong interaction between the Cu(II) complex and BSA.

#### 3.3.2. UV absorption spectra of BSA

Comparing the characteristic absorption spectra of pure BSA and BSA-complex solutions determines whether the complexes bind to BSA statically or dynamically. Static quenching causes a change in the absorption

**Table 1.** Binding constants for DNA/protein with compounds.

Complex	DNA		BSA/HSA		Ref.
	$K_b (M^{-1})$	$K_{sv} (M^{-1})$	$K_b (M^{-1})$	$K_{sv} (M^{-1})$	
Cu(phen)(H <sub>2</sub> O)L <sub>2</sub> Cu(dmphen)L <sub>2</sub>	1.4 x 10 <sup>4</sup> 6.4 x 10 <sup>4</sup>	-	-	-	1
[Cu(L <sub>1</sub> )(phen)][Cu(L <sub>1</sub> (phen)]·5H <sub>2</sub> O [Cu(L <sub>2</sub> )(1,10-phen)](ClO <sub>4</sub> )	-	2.20 x 10 <sup>4</sup> 2.27 x 10 <sup>4</sup>	-	-	8
[Cu(phen)(gln)(H <sub>2</sub> O)]NO <sub>3</sub> ·H <sub>2</sub> O [Cu(dmphen)(gln)(H <sub>2</sub> O)]ClO <sub>4</sub>	3.62 x 10 <sup>3</sup> 7.33 x 10 <sup>3</sup>	4.40 x 10 <sup>3</sup> 4.26 x 10 <sup>4</sup>	-	1.17 x 10 <sup>4</sup>	9
qCuBBPc	2.97 x 10 <sup>5</sup>	1.003 x 10 <sup>5</sup>	-	-	11
H <sub>3</sub> L-Cu	-	-	4.42 x 10 <sup>4</sup>	1.19 x 10 <sup>4</sup>	18
CuL	2.15 x 10 <sup>6</sup>	-	-	-	43
[Cu(H <sub>2</sub> L <sup>1</sup> )(imH)(H <sub>2</sub> O)].3H <sub>2</sub> O [Cu(H <sub>2</sub> L <sup>3</sup> )(imH) <sub>2</sub> ].H <sub>2</sub> O	1.76 x 10 <sup>3</sup> 0.85 x 10 <sup>3</sup>	11.73 x 10 <sup>3</sup> 5.42 x 10 <sup>3</sup>	-	10.48 x 10 <sup>3</sup> 29.64 x 10 <sup>3</sup>	44
C <sub>51</sub> H <sub>42</sub> Cu <sub>2</sub> N <sub>4</sub> O <sub>6</sub>	4 x 10 <sup>5</sup>	-	-	-	45
Cu <sub>2</sub> (μ <sub>2</sub> -Br) <sub>2</sub> (η <sup>1</sup> -S-9-Hanttc) <sub>2</sub> (Ph <sub>3</sub> P) <sub>2</sub>	10.36 x 10 <sup>4</sup>	1.02 x 10 <sup>4</sup>	14.09 x 10 <sup>6</sup>	15.6 x 10 <sup>5</sup>	46
Cu(HMAET)Cl	2.8 x 10 <sup>7</sup>	2.8 x 10 <sup>6</sup>	7.18 x 10 <sup>6</sup>	3 x 10 <sup>6</sup>	<b>This work</b>

spectrum of the fluorophore group with the formation of a new complex-BSA, while no change in the dynamic quenching absorption spectrum is observed. The absorption spectrum of the BSA solution and the Cu(II) complex-BSA was given in Figure 7. The increase in the absorption intensity without any shifting with the addition of the Cu(II) complex (4 μM) on BSA (10 μM) indicates static quenching [34,41,42].

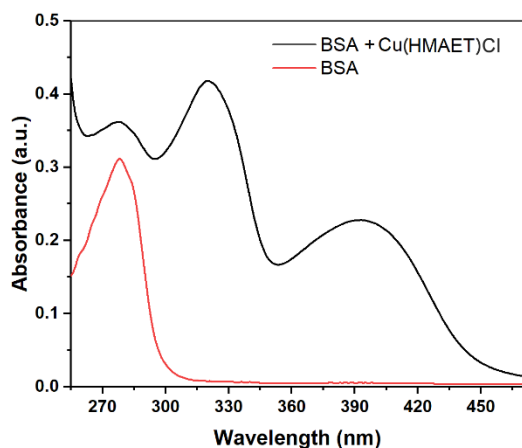


**Figure 7.** Absorption spectrum of BSA (10 μM) and BSA with Cu(HMAET)Cl (4 μM).

#### 4. Conclusion

This paper is containing the synthesis of the the Cu(II) complex of thiosemicarbazone prepared by the combination of 2-hydroxy-5-methoxyacetophenone and

4-ethyl-3-thiosemicarbazide. The Cu(II) complex was characterized by elemental analysis, UV-Vis, FT-IR, and <sup>1</sup>H-NMR spectroscopies. When the spectral changes in the absorption spectra of the Cu(II) complex with increasing *E. coli* DNA addition were examined, hypochromism and small shifts to blue were observed in the Cu(II) complex. The binding constant of the Cu(II) complex with *E. coli* DNA was calculated as 2.8×10<sup>7</sup> M<sup>-1</sup>. The Cu(II) complex exhibits hypochromism and small shifts in blue

wavelength and has a binding constant less than 10<sup>6</sup>, the  $K_b$  value, proving that the Cu(II) complex interacts by intercalating binding to DNA. In the study of displacement with EB performed using fluorescence spectroscopy, which is another important spectroscopic technique that examines the interaction of the Cu(II) complex with DNA, significant reductions in EB-DNA emission intensity were observed with increasing the Cu(II) complex concentration. This result confirms that the Cu(II) complex binds to DNA via the intercalation mechanism. In BSA binding studies, the  $K_b$  value of emission spectroscopy shows considerable interaction between BSA and the Cu(II) complex, while the absorption study has shown that this interaction is by a static quenching mechanism. When the binding interactions of the previously studied copper complexes with both DNA and BSA were evaluated, it was found that the Cu(HMAET)Cl complex had a good binding effect with DNA/BSA (Table 1). It is thought that these results obtained with the Cu(II) complex will be useful in understanding the mechanism of biomolecules and



complexes and in the development of new potential anticancer agents.

### Acknowledgement

The author is grateful to Dr. Suray Pehlivanoglu, Department of Molecular Biology and Genetics, Faculty of Science, Necmettin Erbakan University, Konya, for providing *E. coli* DNA.

### Author's Contributions

Mükerrem FINDIK: Drafted and wrote the manuscript, performed the experiment and result analysis.

Asuman UÇAR: Performed the experiment and result analysis and helped in manuscript preparation.

Emine Güler AKGEMCİ: Assisted in analytical analysis on the structure, supervised the experiment's progress, result interpretation and helped in manuscript preparation.

### Ethics

There are no ethical issues after the publication of this manuscript.

### References

1. Eremina, JA, Lider, EV, Sukhikh, TS, Klyushova, LS, Perepechaeva, ML, Sheven, DG, Berezin, AS, Grishanova, AY, Potkin VI. 2020. Water-soluble copper(II) complexes with 4,5-dichloro-isothiazole-3-carboxylic acid and heterocyclic N-donor ligands: Synthesis, crystal structures, cytotoxicity, and DNA binding study. *Inorganica Chimica Acta*; 510: 119778.
2. Kaya, B, Yılmaz ZK, Şahin, O, Aslim, B, Ülküseven, B. 2020. Structural characterization of new zinc(II) complexes with N<sub>2</sub>O<sub>2</sub> chelating thiosemicarbazidato ligand; Investigation of the relationship between their DNA interaction and in vitro antiproliferative activity on human cancer cells. *New Journal of Chemistry*; 44: 9313-9320.
3. Karami, K, Rahimi, M, Zakariazadeh, M, Buyukgungor, O, Amirghofran, Z. 2018. New phosphorus ylide palladacyclic: Synthesis, characterization, X-Ray crystal structure, biomolecular interaction studies, molecular docking and in vitro cytotoxicity evaluations. *Journal of Organometallic Chemistry*; 878: 60-76.
4. Beebe, SJ, Celestine, MJ, Bullock, JL, Sandhaus, S, Arca, JF, Crokek, DM, Ludvig, TA, Foster, SR, Clark, JS, Beckford, FA, Tano, CM, Tonsel-White, EA, Gurung, RK, Stankavich, CE, Tse-Dinh, YC, Jarrett, WL, Holder, AA. 2020. Synthesis, characterization, DNA binding, topoisomerase inhibition, and apoptosis induction studies of a novel cobalt(III) complex with a thiosemicarbazone ligand. *Journal of Inorganic Biochemistry*; 203: 110907.
5. Milani, NC, Maghsoud, Y, Hosseini, M, Babaei, A, Rahmani, H, Roe, SM, Gholivand, K. 2020. A new class of copper(I) complexes with imine-containing chelators which show potent anticancer activity. *Applied Organometallic Chemistry*; 34(8): 5526.
6. Gupta, RK, Sharma, G, Pandey, R, Kumar, A, Koch, B, Li, PZ, Xu, Q, Pandey, DS. 2013. DNA/Protein Binding, Molecular Docking, and in Vitro Anticancer Activity of Some Thioether-Dipyrrinato Complexes. *Inorganic Chemistry*; 52(24): 13984-13996.
7. Asadi, Z, Zarei, L, Golchin, M, Skorepova, E, Eigner, V, Amirghofran, Z. 2020. A novel Cu(II) distorted cubane complex containing Cu<sub>4</sub>O<sub>4</sub> core as the first tetranuclear catalyst for temperature dependent oxidation of 3,5-di-tert-butyl catechol and in interaction with DNA&protein (BSA). *Spectrochimica Acta Part A: Molecular and Biomolecular Spectroscopy*; 227: 117593.
8. Bhunia, A, Vojtisek, P, Bertolasi, V, Manna, SC. 2019. Tridentate Schiff base coordinated trigonal bipyramidal/square pyramidal copper(II) complexes: Synthesis, crystal structure, DFT/TD-DFT calculation, catecholase activity and DNA binding. *Journal of Molecular Structure*; 1189: 94-101.
9. Kiraz, S, İnci, D, Aydın, R, Vatan, Ö, Zorlu, Y, Cavaş, T. 2019. Antiproliferative activity of copper(II) glutamine complexes with N,N donor ligands: Synthesis, characterization, potentiometric studies and DNA/BSA interactions. *Journal of Molecular Structure*; 1194: 245-255.
10. Balakrishnan, N, Haribabu, J, Dhanabalan, AK, Swaminathan, S, Sun, S, Dibwe, DF, Bhuvanesh, N, Awale, S, Karvemu, R. 2020. Thiosemicarbazone(s)-anchored water soluble mono- and bimetallic Cu(II) complexes: Enzymes-like activities, biomolecular interactions, anticancer property and real-time live cytotoxicity. *Dalton Transactions*; 49(22): 9411-9424.
11. Amitha, GS, Vasudevan, S. 2020. DNA binding and cleavage studies of novel Betti base substituted quaternary Cu(II) and Zn(II) phthalocyanines. *Polyhedron*; 190: 114773.
12. Liu, MC, Lin, TC, Sartorelli, AC. 1992. Synthesis and antitumor activity of amino derivatives of pyridine-2-carboxaldehyde thiosemicarbazone. *Journal of Medicinal Chemistry*; 35(20): 3672-3677.
13. Zarei, L, Asadi, Z, Samolova, E, Dusek, M, Amirghofran, Z. 2020. Pyrazolate as bridging ligand in stabilization of self-assembled Cu(II) Schiff base complexes: Synthesis, structural investigations, DNA/protein (BSA) binding and growth inhibitory effects on the MCF7, CT-26, MDA-MB-231 cell lines. *Inorganica Chimica Acta*; 509: 119674.
14. Bhunia, A, Mistri, S, Manne, RK, Santra, MK, Manna, SC. 2019. Synthesis, crystal structure, cytotoxicity study, DNA/protein binding and molecular docking of dinuclear copper(II) complexes. *Inorganica Chimica Acta*; 491: 25-33.
15. Kumar, P, Gorai, S, Santra, MK, Mondal, B, Manna, D. 2012. DNA binding, nuclease activity and cytotoxicity studies of Cu(II) complexes of tridentate ligands. *Dalton Transactions*; 41(25): 7573-7581.
16. Lu, JJ, Bao, JL, Wu, GS, Xu, WS, Huang, MQ, Chen, XP, Wang, YT. 2013. Quinones Derived from Plant Secondary Metabolites as Anti-cancer Agents. *Anti-Cancer Agents in Medicinal Chemistry*; 13(3): 456-463.
17. Rahman, AJ, Sharma, D, Kumar, D, Pathak, M, Singh, A, Kumar, V, Chawla, R, Ojha, H. 2021. Spectroscopic and molecular modelling study of binding mechanism of bovine serum albumin with phosmet. *Spectrochimica Acta Part A: Molecular and Biomolecular Spectroscopy*; 244: 118803.
18. Mo, D, Shi, J, Zhao, D, Zhang, Y, Guan, Y, Shen, Y, Bian, H, Huang, F, Wu, S. 2021. Synthesis and characterization of Fe<sup>III</sup>/Co<sup>III</sup>/Cu<sup>I</sup> complexes with Schiff base ligand and their hybrid proteins, SOD activity and asymmetric catalytic oxidation of sulfides. *Journal of Molecular Structure*; 1223: 129229.
19. Rani, JJ, Jayaseeli, AMI, Rajagopal, S, Seenithurai, S, Chai, JD, Raja, JD, Rajasekaran, R. 2021. Synthesis, characterization, antimicrobial, BSA binding, DFT calculation, molecular docking and cytotoxicity of Ni(II) complexes with Schiff base ligands. *Journal of Molecular Liquids*; 328: 115457.

20. Akgemci, EG, Saf, AO, Tasdemir, HU, Türkkkan, E, Bingol, H, Turan, SO, Akkiprik, M. 2015. Spectrophotometric, voltammetric and cytotoxicity studies of 2-hydroxy-5-methoxyacetophenone thiosemicarbazone and its N(4)-substituted derivatives: A combined experimental-computational study. *Spectrochimica Acta Part A: Molecular and Biomolecular Spectroscopy*; 136: 719-725
21. Türkkkan, E, Sayin, U, Erbilin, N, Pehlivanoglu, S, Erdogan, G, Tasdemir, HU, Saf, AO, Guler, L, Akgemci, EG. 2017. Anticancer, antimicrobial, spectral, voltammetric and DFT studies with Cu(II) complexes of 2-hydroxy-5-methoxyacetophenone thiosemicarbazone and its N(4)- substituted derivatives. *Journal of Organometallic Chemistry*; 831: 23-35.
22. Beckford, FA, Thessing, J, Shalowski, Jr M, Mbarushimana, PC, Brock, A, Didion, J, Woods, J, Gonzalez-Sarrias, A, Seeram, NP. 2011. Synthesis and characterization of mixed-ligand diimine-piperonal thiosemicarbazone complexes of ruthenium(II): Biophysical investigations and biological evaluation as anticancer and antibacterial agents. *Journal of Molecular Structure*; 992: 39-47.
23. Ishaq, M, Taslimi, P, Shafiq, Z, Khan, S, Salmas, RE, Zangeneh, MM, Saeed, A, Zangeneh, A, Sadeghian, N, Asari, A, Mohamad, H. 2020. Synthesis, bioactivity and binding energy calculations of novel 3-ethoxysalicylaldehyde based thiosemicarbazone derivatives. *Bioorganic Chemistry*; 100: 103924.
24. Zhang, X, Li, S, Yang, L, Fan, C. 2007. Synthesis, characterization of Ag(I), Pd(II) and Pt(II) complexes of a triazine-3-thione and their interactions with bovine serum albumin. *Spectrochimica Acta Part A: Molecular and Biomolecular Spectroscopy*; 68(3): 763-770.
25. Huseynovaa, M, Farzaliyev, V, Medjidov, A, Aliyeva, M, Taslimi, P, Sahin, O, Yalçın, B. 2020. Novel zinc compound with thiosemicarbazone of glyoxylic acid: Synthesis, crystal structure, and bioactivity properties. *Journal of Molecular Structure*; 1200: 127082.
26. Balakrishnan, N, Haribabu, J, Krishnan, DA, Swaminathan, S, Mahendiran, D, Bhuvanesh, NSP, Karvembu, R. 2019. Zinc(II) complexes of indole thiosemicarbazones: DNA/protein binding, molecular docking and in vitro cytotoxicity studies. *Polyhedron*; 170: 188-201.
27. Kalaierasi, G, Umadevi, C, Shanmugapriya, A, Kalaivani, P, Dallemer, F, Prabhakaran, R. 2016. DNA(CT), protein(BSA) binding studies, anti-oxidant and cytotoxicity studies of new binuclear Ni(II) complexes containing 4(N)-substituted thiosemicarbazones. *Inorganica Chimica Acta*; 453: 547-558.
28. Kılıç-Cıkla, I, Güveli, S, Yavuz, M, Bal-Demirci, T, Ülküseven, B. 2016. 5-Methyl-2-hydroxy-acetophenone-thiosemicarbazone and its nickel(II) complex: Crystallographic, spectroscopic (IR, NMR and UV) and DFT studies. *Polyhedron*; 105: 104-114.
29. Arafath, MA, Adam, F, Razali, MR, Ahmed Hassan, LE, Ahamed, MBK, Majid, AMSA. 2017. Synthesis, characterization and anticancer studies of Ni(II), Pd(II) and Pt(II) complexes with Schiff base derived from N-methylhydrazinecarbothioamide and 2-hydroxy-5-methoxy-3-nitrobenzaldehyde. *Journal of Molecular Structure*; 1130: 791-798.
30. Mathews, NA, Jacob, JM, Begum, PMS, Kurup, MRP. 2020. Cu(II) and Zn(II) complexes from a thiosemicarbazone derivative: Investigating the intermolecular interactions, crystal structures and cytotoxicity. *Journal of Molecular Structure*; 1202: 127319.
31. Nyawade, EA, Sibuyi, NRS, Meyer, M, Lalancette, R, Onani, MO. 2021. Synthesis, characterization and anticancer activity of new 2-acetyl-5-methyl thiophene and cinnamaldehyde thiosemicarbazones and their palladium(II) complexes. *Inorganica Chimica Acta*; 515: 120036.
32. Jacob, JM, Kurup, MRP, Nisha, K, Serdaroglu, G, Kaya, S. 2020. Mixed ligand copper(II) chelates derived from an O, N, S- donor tridentate thiosemicarbazone: Synthesis, spectral aspects, FMO, and NBO analysis. *Polyhedron*; 189: 114736.
33. Omondi, RO, Ojwach, SO, Jagany, D. 2020. Review of comparative studies of cytotoxic activities of Pt(II), Pd(II), Ru(II)/(III) and Au(III) complexes, their kinetics of ligand substitution reactions and DNA/BSA interactions. *Inorganica Chimica Acta*; 512: 119883.
34. Ayyannan, G, Mohanraj, M, Gopiraman, M, Uthayamalar, R, Raja, G, Bhuvanesh, N, Nandhakumar, R, Jayabalakrishnan, C. 2020. New Palladium(II) complexes with ONO chelated hydrazone ligand: Synthesis, characterization, DNA/BSA interaction, antioxidant and cytotoxicity. *Inorganica Chimica Acta*; 512: 119868.
35. Bağda, E, Yabas, E, Bağda, E. 2017. Analytical approaches for clarification of DNA double decker phthalocyanine binding mechanism: as an alternative anticancer chemotherapeutic. *Spectrochimica Acta Part A: Molecular and Biomolecular Spectroscopy*; 172: 199-204.
36. Bashiri, M, Jarrahpour, A, Nabavizadeh, SM, Karimian, S, Rastegari, B, Haddadi, E, Turos, E. 2021. Potent antiproliferative active agents: novel bis Schiff bases and bis spiroβ-lactams bearing isatin tethered with butylene and phenylene as spacer and DNA/BSA binding behavior as well as studying molecular docking. *Medicinal Chemistry Research*; 30: 258-284.
37. Kalantari, R, Asadi, Z. 2020. DNA/BSA binding of a new oxovanadium (IV) complex of glycyglycine derivative Schiff base ligand. *Journal of Molecular Structure*; 1219: 128664.
38. Tyagi, N, Singh, O, Mishra, RK, Ghosh, K. 2020. Bio-macromolecular interaction studies: Synthesis, crystal structure of water-soluble manganese(II) complexes. *Inorganica Chimica Acta*; 512: 119882.
39. Lakowicz, JR. Principles of fluorescence spectroscopy. New York: Springer Science & Business Media, 2013.
40. Shanmugapriya, A, Dallemer, F, Prabhakaran, R. 2018. Synthesis, characterisation, crystal structures and biological studies of palladium(II) complexes containing 5-(2-hydroxy-3-methoxyphenyl)-2,4-dihydro[1,2,4]triazole-3-thione derivatives. *New Journal of Chemistry*; 42(23): 18850-18864.
41. Haribabu, J, Sabapathi, G, Tamizh, MM, Balachandran, C, Bhuvanesh, NSP, Venuvanalingam, P, Karvembu, R. 2018. Water-Soluble Mono- and Binuclear Ru(η<sup>6</sup>-p-cymene) Complexes Containing Indole Thiosemicarbazones: Synthesis, DFT Modeling, Biomolecular Interactions, and In Vitro Anticancer Activity through Apoptosis. *Organometallics*; 37(8): 1242-1257.
42. Feng, XZ, Lin, Z, Yang, LJ, Wang, C, Bai, CL. 1998. Investigation of the interaction between acridine orange and bovine serum albumin. *Talanta*; 47(5): 1223-1229.
43. Abdel-Rahman, LH, Abu-Dief, AM, Moustafa, H, Hamdan, SK. 2017. Ni(II) and Cu(II) complexes with ONNO asymmetric tetradentate Schiff base ligand: synthesis, spectroscopic characterization, theoretical calculations, DNA interaction and antimicrobial studies. *Applied Organometallic Chemistry*; 31(2): e3555.
44. Palmucci, J, Mahmudov, KT, Guedes da Silva, MFC, Marchetti, F, Pettinari, C, Petrelli, D, Vitali, LA, Quassinti,





- L, Bramucci, M, Lupidi, G, Pombeiro, AJL. 2016. DNA and BSA binding, anticancer and antimicrobial properties of Co(ii), Co(ii/iii), Cu(ii) and Ag(i) complexes of arylhydrazones of barbituric acid. *RSC Advances*; 6: 4237-4249.
45. Sedighipoor, M, Kianfar, AH, Mahmood, WAK, Azarian, MH. 2017. Synthesis and electronic structure of novel Schiff bases Ni/Cu (II) complexes: Evaluation of DNA/serum protein binding by spectroscopic studies. *Polyhedron*; 129: 1-8.
46. Khan, A, Paul, K, Singh, I, Jasinski, JP, Smolenski, VA, Hotchkiss, EP, Kelley, PT, Shalit, ZA, Kaur, M, Banerjee, S, Royd, P, Sharma, R. 2020. Copper(I) and silver(I) complexes of anthraldehyde thiosemicarbazone: synthesis, structure elucidation, in vitro anti-tuberculosis/cytotoxic activity and interactions with DNA/HSA. *Dalton Transaction*; 49: 17350-17367.



# Adsorptive Removal of Tartrazine Dye by Poly(N-vinylimidazole-ethylene glycol dimethacrylate) And Poly(2-hydroxyethyl methacrylate-ethylene glycol dimethacrylate) Polymers

Ayşe Dinçer<sup>1\*</sup> , Tülin Aydemir<sup>1</sup> 

<sup>1</sup> 1Manisa Celal Bayar University, Faculty of Science and Arts, Chemistry Department, 45140, Manisa, Turkey<sup>2</sup>

\*[ayse.dincer@cbu.edu.tr](mailto:ayse.dincer@cbu.edu.tr)

\*Orcid: 0000-0001-6158-1775

Received: 28 January 2021

Accepted: 29 November 2021

DOI: 10.18466/cbayarfbe. 869963

## Abstract

Poly(N-vinylimidazole-ethylene glycol dimethacrylate (P(VI-EGDMA) ) and poly(2-hydroxyethyl methacrylate-ethylene glycol dimethacrylate (P(HEMA-EGDMA) ) were synthesized as adsorbents for adsorptive removal of tartrazine dye from aqueous solutions. To achieve maximum tartrazine adsorption, some parameters were examined, and pH was found to be an important factor for the adsorption on P(VI-EGDMA). As the temperature increased, removal amount of tartrazine was increased. The experimental capacities were found as 265.5 mg/g and 45.15 mg/g for P(VI-EGDMA) and P(HEMA-EGDMA), respectively. The experimental data well correlated with Freundlich isotherm. The estimated  $\Delta H^\circ$  values were found as 12.76 kJ/mol and 10.40 kJ/mol for P(VI-EGDMA) and P(HEMA-EGDMA), respectively. Adsorption was demonstrated to be endothermic in nature. The characterization of these polymers was done by using FTIR, TGA and SEM analysis.

**Keywords:** Adsorption isotherms, dye removal, poly(N-vinylimidazole-ethylene glycol dimethacrylate), poly(2-hydroxyethyl methacrylate-ethylene glycol dimethacrylate), tartrazine.

## 1. Introduction

The industry, which develops to encounter the needs of the contemporary world, unfortunately causes environmental pollution. Pollution adversely affects the health of all living organisms and this has many sources. Dyes in industrial wastewaters are one of the pollution sources and they are utilized in many industries such as textile, food, leather, plastics, cosmetics, and paper [1–3]. Some dyes can have toxic effects, they can be mutagenic or cancerogenic. Researchers apply different techniques such as electrochemical methods, precipitation, filtration, photocatalytic degradation and adsorption to remove pollutants from wastewaters [4–8]. Among the various techniques, adsorption is measured as most efficient and adaptable in practice. Different researchers have investigated the adsorption of dyes on natural or synthetic materials [9,10].

Tartrazine (E102 or FD&C Yellow 5) is an azobenzene synthetic azo dye and its structure traits a trisodium salt of 3-carboxy-5-hydroxy-1 (p-sulfophenyl)-4-(sulfophenyl azo) pirazolone. This dye is used in many commercial food goods like drinks, soups, puddings, cakes, soups and candies or in medicinal capsules,

syrops [11]. It is an alternative colorant to beta carotene to achieve similar color because of its lower price. Excessive consumption of tartrazine can cause allergic reactions, migraines, lupus, hyperactivity and behavioral problems [12,13].

In the present work, adsorption of tartrazine on P(VI-EGDMA), and P(HEMA-EGDMA) polymers using various variables are reported. Adsorption isotherms are applied to understand the mechanisms of dye adsorption onto polymers. The thermodynamic parameters also were evaluated. The characterizations of the adsorbents were done by FTIR, TGA and SEM analysis.

## 2. Materials and Methods

### 2.1. Materials

Tartrazine (FD & C Yellow No. 5, C.I. 19140) was provided by KRK Gıda, Istanbul, Turkey. Ethanol, methanol, acetone, 1,1'-azobis(cyclohexane-carbonitrile) (ABCN), acetone, 2-hydroxyethyl methacrylate (HEMA), N-vinylimidazole (VI), acetonitrile (ACN), ethylene glycol dimethacrylate (EGDMA), NaOH and HCl were supplied from Sigma Aldrich (USA).

## 2.2. Preparation of P(VI-EGDMA), and P(HEMA-EGDMA)

Two types of polymers, based on VI and HEMA as monomers, were prepared. 1 mmol monomer was firstly dissolved in 2 mL ACN (as a solvent) and then 5 mmol EGDMA (as a crosslinker) and 10 mg ABCN (as an initiator) were added to the solution. Then nitrogen gas purged for 5 min to remove the dissolved oxygen. Polymerization was completed after the tubes were incubated at 60°C for 24 h. The consisting polymers were crushed and powdered. Then the polymers were washed by ethanol and acetone to remove the excess of unreacted monomers and dried in vacuo for 24 h.

## 2.3. Spectrophotometric analysis

The standard tartrazine solutions prepared in distilled water and spectrophotometric measurements were taken at 426 nm where the maximum absorption is observed.

## 2.4. Characterization

P(VI-EGDMA) and P(HEMA-EGDMA) polymers were characterized by Fourier Transform Infrared (FTIR) Spectroscopy (Spectrum BX, Perkin Elmer), scanning electron microscope (SEM) (Quanta 250 FEG/FEI) and by TGA/DSC (TGA analyzer, Perkin Elmer SII Exstar 7300).

## 2.5. Adsorption Studies

Batch adsorption experiments were set and the effect of contact time (15-90 min), amount of adsorbent (5-25 mg), pH (pH 2.0-10.0), temperature (20-60°C) and dye concentration (16-1870 mg/L) on tartrazine adsorption was examined. The polymers were removed by centrifugation at the end of the pre-determined times and the unadsorbed tartrazine in the supernatant were analyzed spectrophotometrically.

The following equation (2.1) is used for the calculation of the amount of dye adsorbed on the polymers:

$$q_e = \frac{(C_0 - C_e) \times V}{m} \quad (2.1)$$

$q_e$ : the amount of dye adsorbed (mg/g),  
 $C_0$ : the initial dye concentration (mg/L),  
 $C_e$ : the equilibrium dye concentration (mg/L),  
 $V$ : the volume of solutions (L)  
 $m$ : amount of the adsorbent (g).

## 2.6. Desorption and Reusability studies

The regeneration of the dye adsorbed P(HEMA-EGDMA) was done using 0.01 M NaOH, methanol and acetone, respectively. For the regeneration of the dye adsorbed P(VI-EGDMA), 1 M NaOH, methanol and acetone is used, respectively. Then the polymers were dried and used for the adsorption of the dye again. The equation 2.2 is used to calculate the percentage of tartrazine dye desorbed:

$$D = \frac{\text{Amount of dye desorbed}}{\text{Amount of dye absorbed}} \times 100 \quad (2.2)$$

where D, is the percentage of desorption.

## 3. Results and Discussion

### 3.1. Characterization

#### 3.1.1. FTIR Analysis

FTIR spectra of P(VI-EGDMA), and P(HEMA-EGDMA) are given in Fig. 1. The polymers were formerly dried at 60 °C for 24 h to prevent water-related interferences. For P(VI-EGDMA), the sharp peak at 1732  $\text{cm}^{-1}$  is attributed to the stretching of the carbonyl groups of EGDMA. The peaks around 1456  $\text{cm}^{-1}$  and 1267  $\text{cm}^{-1}$  could be assayed as imidazole group and the peak at 1156  $\text{cm}^{-1}$  is stretching vibrations of CH. The peak at 2987  $\text{cm}^{-1}$  could be due to CH stretching vibration and the stretching band of OH peak is seen at 3656  $\text{cm}^{-1}$ . For P(HEMA-EGDMA), OH stretching vibration spectrum is seen around at 3617  $\text{cm}^{-1}$ , CH stretching vibration is seen at 2957  $\text{cm}^{-1}$ , carbonyl stretching vibration is at 1731  $\text{cm}^{-1}$ , C=C stretching vibrations are at 1455 and 1265  $\text{cm}^{-1}$ , and CH stretching vibrations are seen at 1164 and 960  $\text{cm}^{-1}$ .

#### 3.1.2. SEM Analysis

SEM analysis gives information about the morphology of the synthesized polymers [14]. As seen from figure 1(b), P(VI-EGDMA) has a porous surface and there are holes and cavities. It should be also noticed that the adsorption capacity was highly depended on the polymer's surface structure. The porous surface structure should be considered as the factor enhancing the surface area. The surface of poly(HEMA-EGDMA) had no surface cavities and this situation negatively affected its dye adsorption capacity.

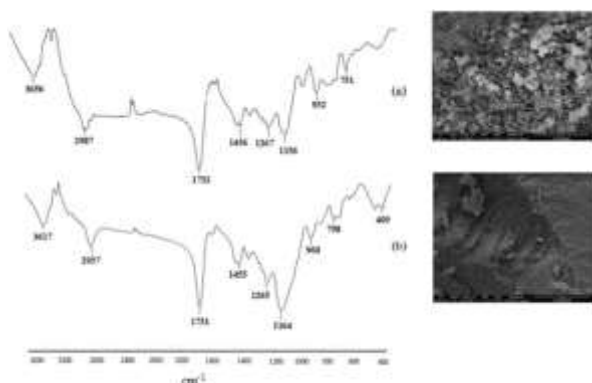


**Figure 1.** FTIR spectrum and SEM micrographs of (a) P(VI-EGDMA), (b) P(HEMA-EGDMA) (Magnifications: 25.000 ×).

### 3.1.3. Thermogravimetric Analysis

TGA was implemented to determine the chemical composition of the adsorbents. First order derivative of TGA curves reveals the temperature at which the maximum decrease of mass occur [15]. Fig. 2 displays the TGA results of P(VI-EGDMA) and P(HEMA-EGDMA). From the thermal analysis, it was observed that in case of all polymers, the loss of water was observed at the first decomposition stage (30 °C-100 °C). Main mass loss was occurred about 300–500 °C for all polymers. In the first stage of degradation of P(VI-EGDMA) at 310 °C, a mass loss of 21.6 wt.% was observed. On the other hand, degradation of P(VI-EGDMA) took place primarily in the second step of degradation at 425 °C with a very high persistent mass loss of 77.85 wt.%. In the differential thermal gravimetry (DTG) curve of P(HEMA-EGDMA), two peaks were seen at temperatures of 335 °C and 440 °C which show that the weight loss by thermal decomposition occurred in two steps. The weight losses corresponding to these temperature steps were calculated as 45.8 wt % and 82.16 wt %, respectively.

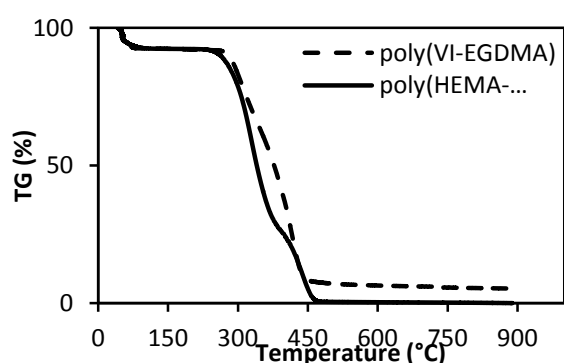


**Figure 2.** TGA curves of P(VI-EGDMA) and P(HEMA-EGDMA).

### 3.2. Batch adsorption studies

The contact time is the one of the significant parameters that examined at adsorption studies. Ten milligrams of polymers were added to 16 mg/L tartrazine solution. The contact time was changed from 15 to 90 min then the suspension was centrifuged, and the absorbance of the supernatant was measured. The adsorption efficiency of tartrazine increased in 1 h and the time needed to reach the equilibrium was found as 45 min for these polymers (Figure 3A).

The adsorption studies were performed at 20-60°C to examine the effect of temperature. The adsorption increased with the increasing of the temperature and the maximum adsorption was occurred at 40°C for both polymers (Fig. 3B). The adsorption capacity of the polymers increased with the temperature increase so the solubility of the dye molecules might increase and this may cause the increase in diffusion rate with the expansion of the polymer pores [16].

pH of the dye solution was adjusted to pH 2.0-10.0 by using 0.1 M NaOH or 0.1 M HCl in order to examine the pH effect. Then each polymer was treated with pH adjusted 16 mg/L dye solution. The contact time and the temperature were kept at the optimum values. In this study, dye adsorption was highly dependent to pH of the solution for P(VI-EGDMA). The dye adsorption capacity of P(VI-EGDMA) decreased sharply as the pH levels increased from 2.0 to 8.0. For this polymer calculated adsorption capacity in acidic region was higher than those in other pH values. So, the further assays were done at pH 2.0. At pH 2.0, since the imidazole groups in P(VI-EGDMA) are positively charged and the sulfonic acid groups in the dye are negatively charged, the dye adsorption is at maximum level due to the electrostatic attraction between them. As the pH value increases, especially the charge state of the imidazole groups changes, this time there is a decrease in adsorption because of the repulsion between the polymer and dye molecules. Additionally, at high pH values, there is a competition between OH<sup>-</sup> ions and the dye ions causing a decrease in sorption of the dye [17]. P(HEMA-EGDMA) polymer does not contain ionizable groups. However, the OH groups in both HEMA and tartrazine have the capacity to make hydrogen bonds. An interaction occurs between the dye and the polymer through the formation of hydrogen bonds.

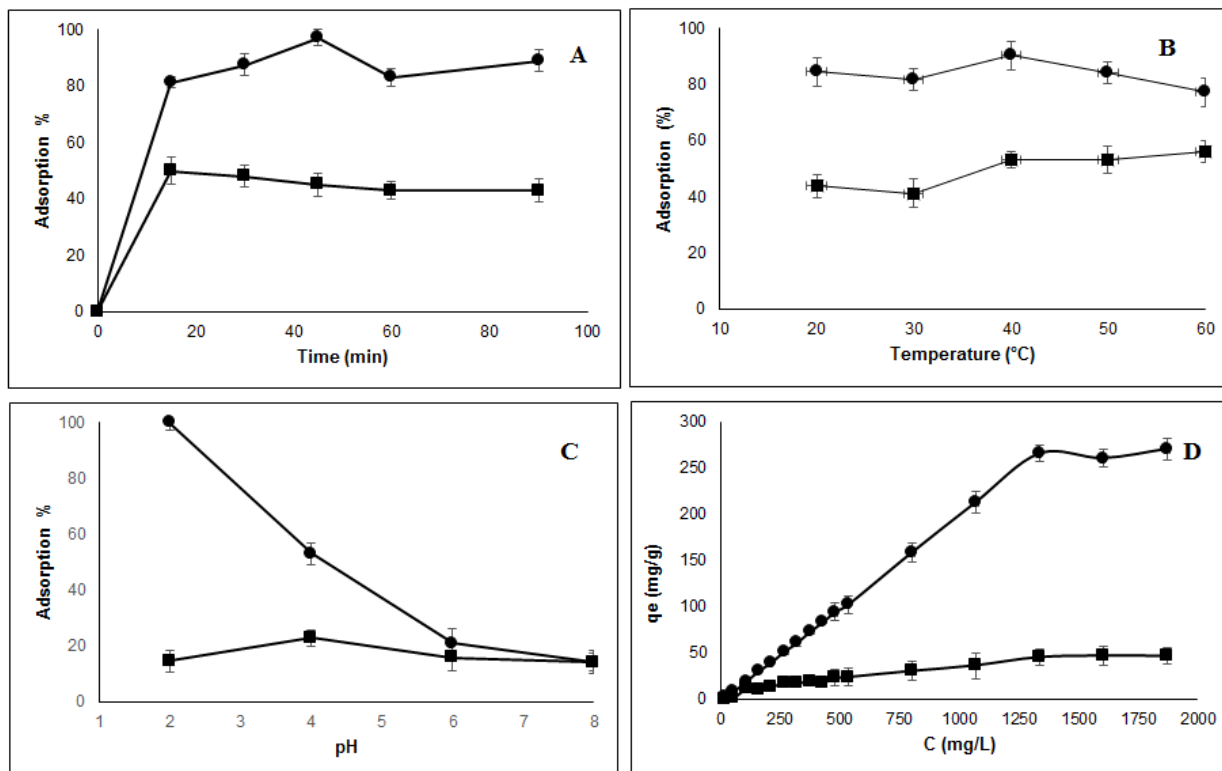


**Figure 3.** A. Effect of contact time (Tartrazine solution: 16 mg/L, polymer dose 10 mg for P(VI-EGDMA) and 15 mg for P(HEMA-EGDMA). B. Effect of temperature (Tartrazine solution: 16 mg/L, incubation time 45 min; polymer dose 10 mg for P(VI-EGDMA) and 15 mg for P(HEMA-EGDMA). C. Effect of pH (Tartrazine solution: 16 mg/L, incubation time 45 min, polymer dose 10 mg for P(VI-EGDMA) and 15 mg for P(HEMA-EGDMA), temperature 40 °C.); D. Effect of tartrazine concentration (incubation time 45 min; polymer dose 10 mg for P(VI-EGDMA) (-●-) and and 15 mg for P(HEMA-EGDMA) (-■-), temperature 40 °C.).

P(HEMA-EGDMA) is a non-ionic polymer and the sorption of tartrazine on P(HEMA-EGDMA) was found to be pH independent. Also, adsorption of the dye on P(HEMA-EGDMA) were seemed to be negatively affected due to presence of other ions when the pH of the medium was set to a known value by HCl, or NaOH. So, further studies were carried out in aqueous medium for P(HEMA-EGDMA) (Fig 3C).

Effect of dye concentration was studied between 16 mg/L-1870 mg/L tartrazine solution and other parameters were kept at optimum values. As the initial tartrazine concentration increased, the amount of dye adsorbed on P(VI-EGDMA) increased. Dye adsorption on P(HEMA-EGDMA) was not so high as P(VI-EGDMA) and this is due to non-ionic character of the polymer. As shown in Fig. 3D, the amount of dye adsorbed became constant at high dye concentrations. This could be because of saturation of the limited active sites of the adsorbents above a certain dye concentration [18]. Maximum tartrazine adsorption capacities were found as 265.5 mg/g and 45.15 mg/g for P(VI-EGDMA) and P(HEMA-EGDMA) , respectively.

### 3.3. Thermodynamic parameters

The thermodynamic parameters ( $\Delta G^\circ$ ,  $\Delta H^\circ$ ,  $\Delta S^\circ$ ) are calculated. The following equations (3.1) and (3.2) were used to calculate these parameters, respectively.

$$Kc = X_e / (C_i - X_e) \quad (3.1)$$

$Kc$ : Equilibrium constant of the adsorption process  
 $X_e$ : The equilibrium concentration of dye adsorbed, mmol/L,  
 $C_i$ : The initial dye concentration, mmol/L.

$Kc$  was evaluated at 293, 313, 323 K, and calculated according to Eq. (3) (Table 1). The following equation was used to calculate the free energy ( $\Delta G^\circ$ ):

$$\Delta G^\circ = -RT \ln Kc \quad (3.2)$$

The standard enthalpy ( $\Delta H^\circ$ ) and entropy ( $\Delta S^\circ$ ) of the adsorption were determined from the graphic drawn between  $\ln Kc$  vs.  $1/T$  (Fig 4) (Eq 3.3) [19].

$$\ln Kc = (\Delta S^\circ/R) - (\Delta H^\circ/RT) \quad (3.3)$$

R: The gas constant, 8.314 J/mol K

T: The absolute temperature,

$\Delta H^\circ$  and  $\Delta S^\circ$  values were found from the slope,  $\Delta H^\circ/R$  and the intercept  $\Delta S^\circ/R$  respectively. The calculated values of the thermodynamic parameters ( $\Delta G^\circ$ ,  $\Delta H^\circ$ ,  $\Delta S^\circ$ ) are shown in Table 2. These results displayed that the adsorption of tartrazine on P(VI-EGDMA) and P(HEMA-EGDMA) is endothermic.

It is obvious that the entropy increases follows: P(VI-EGDMA) > P(HEMA-EGDMA). It means that the adsorbent of P(VI-EGDMA) gave a less order system than P(HEMA-EGDMA). The negative  $\Delta S^\circ$  value reflected that no noteworthy changes occurred in the internal structure of P(HEMA-EGDMA) during adsorption of tartrazine. Gibbs free energy change ( $\Delta G^\circ$ ) values were positive and this indicated that adsorption process was unspontaneous.

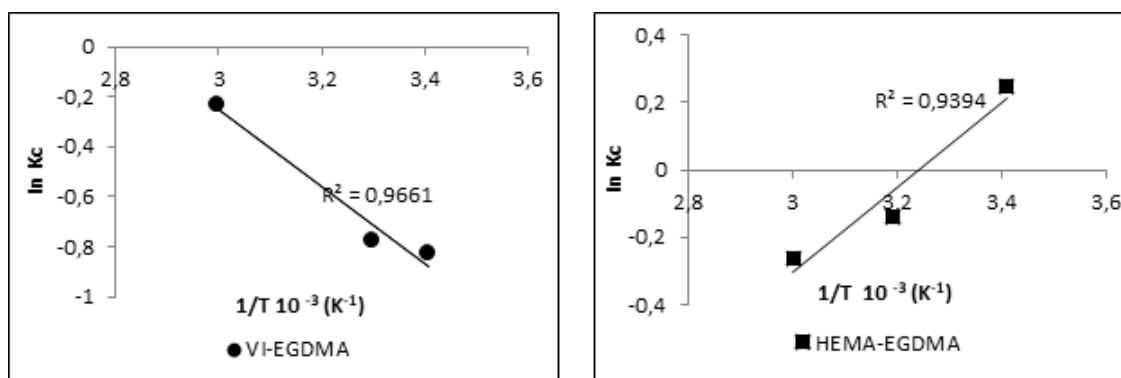


Fig.4.  $\ln Kc$  versus  $1/T \cdot 10^{-3}$  for dye adsorption on polymers.

Table 1. Thermodynamic parameters.

Polymer	$Kc$			$\Delta G^\circ$ (kJ/mol)			$\Delta H^\circ$ (kJ/mol)	$\Delta S^\circ$ (J/molK)
	293 K	313 K	323 K	293 K	313 K	323 K		
P(VI-EGDMA)	0.44	0.32	0.43	2.0	2.96	2.22	12.76	36.20
P(HEMA-EGDMA)	1.28	0.87	0.59	-0.60	0.36	1.42	10.40	-33.68

### 3.4. Adsorption isotherms

The adsorption data was evaluated by linear forms of Freundlich (Eq 3.4) and Langmuir (Eq 3.5) isotherms [20,21].

$$\log qe = \log k_F + 1/n \log C_e \quad (3.4)$$

$qe$ : amount of dye adsorbed at equilibrium

$K_F$ : adsorption capacity

$n$ : adsorption intensity

When  $\log qe$  was plotted against  $\log C_e$ ,  $1/n$  value is calculated from the slope. (Fig. 5, Table 3).

$$\frac{C_e}{q_e} = \frac{1}{Q_{max} \cdot b} + \frac{C_e}{Q_{max}} \quad (3.5)$$

$Q_{max}$ : Maximum adsorption capacity (mg/g),

$b$ : (L/mg) Langmuir isotherm constant, relates to

adsorption energy (Figure 5). Calculated Langmuir constants  $Q_{max}$  and  $b$  are displayed in Table 3.  $Q_{max}$  values were found as 102.04 (mg/g) and 76.92 (mg/g) for P(VI-EGDMA) and for P(HEMA-EGDMA), respectively.

The essential characteristic of the Langmuir isotherm can be defined in terms of a dimensionless equilibrium parameter,  $R_L$ , which is usually expressed as (Eq 3.6):

$$R_L = 1 / (1 + bC_0) \quad (3.6)$$

Where  $b$  is the Langmuir constant and  $C_0$  is the initial dye concentration ( $\text{mg L}^{-1}$ ). The  $R_L$  is a measure of whether the adsorption process is favorable or unfavorable.

The isotherms shapes are:

$0 < R_L < 1$	Favorable
$R_L = 1$	Linear
$R_L > 1$	Unfavorable
$R_L = 0$	Irreversible

$R_L$  values were between 0–1, showing that the adsorption process were favorable for P(VI-EGDMA) and P(HEMA-EGDMA) (Table 2).  $R^2$  values of Freundlich isotherms were higher than Langmuir isotherms and displayed the suitability of Freundlich isotherm than Langmuir isotherm. Tartrazine adsorption studies also performed with some adsorbents and adsorption capacities are listed in Table 3.

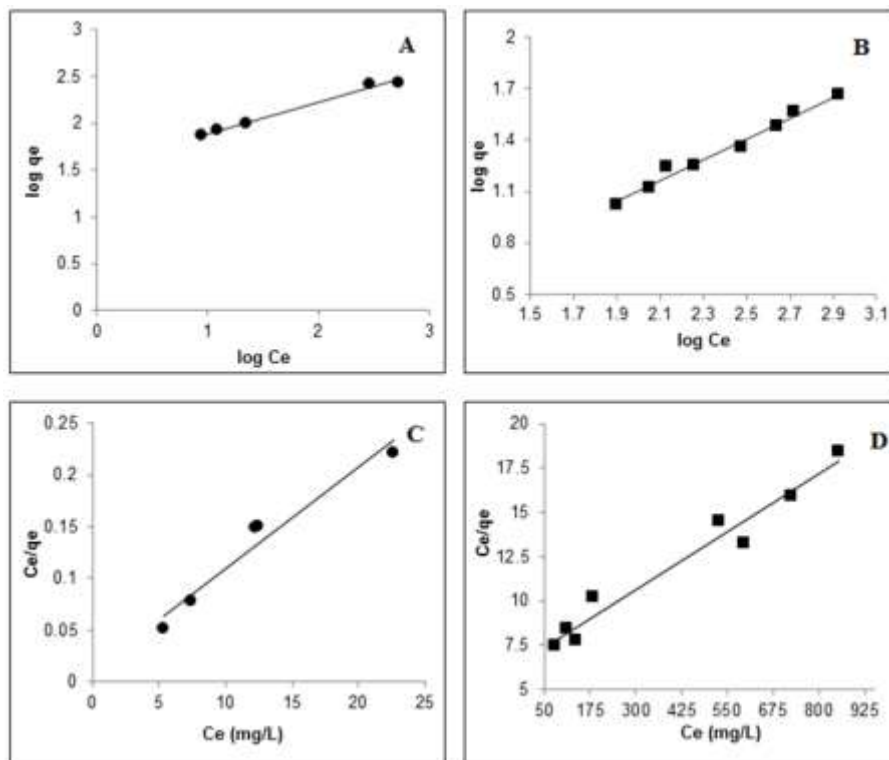


**Figure 5:** Freundlich (A-B) and Langmuir (C-D) isotherms for tartrazine adsorption on P(VI-EGDMA) (●-) and P(HEMA-EGDMA) (■-).

**Table 2.** Freundlich and Langmuir isotherm parameters

	Freundlich Isotherm			Langmuir Isotherm			
	1/n	$K_F$	$R^2$	$Q_{max}$ (mg/g)	b (L/mg)	$R_L$	$R^2$
P(VI-EGDMA)	0.34	35.42	0.991	102.04	0.8379	0.001	0.948
P(HEMA-EGDMA)	0.61	1.28	0.982	76.92	0.0019	0.3567	0.961

### 3.5. Desorption studies and reusability of the adsorbent

The regeneration and reuse of an adsorbent are important from an economic point of view. This study performed at room temperature for all polymers. Adsorption of tartrazine was performed at pH 2.0 on P(VI-EGDMA). Desorption studies were carried out using 1 M NaOH and more than 70% tartrazine could be recovered from the polymer. For the reusability of P(VI-EGDMA), adsorption/desorption cycle was repeated seventeen times. After seventeen usages of the same polymer, the dye binding capacity of P(VI-EGDMA) decreased about 34%. Regeneration of P(HEMA-EGDMA) was done by using 0.01 M NaOH solution. For P(HEMA-EGDMA) recovery of the dye was achieved as about 85%. The reusability of P(HEMA-EGDMA) was successfully performed for five times without significant reduction in adsorption of tartrazine.

**Table 3.** Comparison of tartrazine adsorption capacities of various adsorbents

Adsorbent type	Adsorption capacity (mg/g)	References
Activated Red Mud	136.98	[22]
Alkali Activated Fly Ash	174.40	[23]
Lantana carbon	90.9	[24]
Sawdust	4.71	[25]
Silver nanoparticle decorated multiwalled carbon nanotubes	84.04	[26]
In this study		
P(VI-EGDMA)	102.04	
P(HEMA-EGDMA)	76.92	





#### 4. Conclusion

In this study, P(VI-EGDMA), and P(HEMA-EGDMA) were synthesized as adsorbents for removal of tartrazine dye. Optimization of the contact time is necessary to determine the time to reach the equilibrium and for this study it calculated as 45 min for all polymers. The adsorption was highly depended on pH for P(VI-EGDMA) and at pH 2.0 maximum adsorption was obtained. Adsorption on P(HEMA-EGDMA) were not affected by pH and the experiments were performed in aqueous media. The thermodynamic parameters of the adsorption help in prediction of how the adsorption of dye molecules might change with temperature.  $\Delta H^{\circ} > 0$  showed that tartrazine dye adsorption on P(VI-EGDMA) and P(HEMA-EGDMA) was endothermic. The adsorption isotherms of P(VI-EGDMA), P(HEMA-EGDMA) were correlated with Freundlich isotherm model.

#### Author's Contributions

Ayşe DİNÇER, Tülin AYDEMİR: Drafted and wrote the manuscript, performed the experiment and result analysis.

Ayşe DİNÇER, Tülin AYDEMİR: Assisted in analytical analysis on the structure, supervised the experiment's progress, result interpretation and helped in manuscript preparation.

#### Ethics


There are no ethical issues after the publication of this manuscript.

#### References

1. El-Sayed, BA, Mohamed, WAA, Galal, HR, Abd El-Bary, HM, Ahmed, MAM. 2019. Photocatalytic study of some synthesized MWCNTs/TiO<sub>2</sub> nanocomposites used in the treatment of industrial hazard materials. *Egypt Journal of Petroleum*; 28:247–52.
2. Singh, PK, Singh, RL. 2017. Bio-removal of Azo Dyes: A Review. *International Journal of Applied Sciences and Biotechnology*; 5:108–26.
3. Saxena, M, Sharma, N, Saxena, R. 2020. Highly efficient and rapid removal of a toxic dye: Adsorption kinetics, isotherm, and mechanism studies on functionalized multiwalled carbon nanotubes. *Surfaces and Interfaces*; 21:100639.
4. Fatima, B, Siddiqui, SI, Ahmed, R, Chaudhry, SA. 2019. Green synthesis of f-CdWO<sub>4</sub> for photocatalytic degradation and adsorptive removal of Bismarck Brown R dye from water. *Water Resources and Industry*; 22:100119.
5. Liu, H, Zhang, J, Lu, M, Liang, L, Zhang, H, Wei J. 2020. Biosynthesis based membrane filtration coupled with iron nanoparticles reduction process in removal of dyes. *Chemical Engineering Journal*; 387:124202.
6. Hisada, M, Tomizawa, Y, Kawase, Y. 2019. Removal kinetics of cationic azo-dye from aqueous solution by poly- $\gamma$ -glutamic acid biosorbent: Contributions of adsorption and complexation/precipitation to Basic Orange 2 removal. *Journal of Environmental Chemical Engineering*; 7:103157.
7. Hussain, S, Kamran, M, Khan, SA, Shaheen, K, Shah, Z, Suo, H, Khan, Q, Shah BA, Rehman WU, Al-Ghamdi, YO, Ghadi, U. 2021. Adsorption, kinetics and thermodynamics studies of methyl orange dye sequestration through chitosan composites films. *International Journal of Biological Macromolecules*; 168:383–94.
8. Kong, Q, Wang, X, Lou, T. 2020. Preparation of millimeter-sized chitosan/carboxymethyl cellulose hollow capsule and its dye adsorption properties. *Carbohydrate Polymers*; 244:116481.
9. Morais da Silva, PM, Camparotto, NG, Figueiredo, Neves, T de, Grego, Lira, KT, Mastelaro, VR, Siqueira, Franco, Picone, C, Prediger, P. 2020. Effective removal of basic dye onto sustainable chitosan beads: Batch and fixed-bed column adsorption, beads stability and mechanism. *Sustainable Chemistry and Pharmacy*; 18:100348.
10. Xu, MY, Jiang, HL, Xie, ZW, Li, ZT, Xu, D, He, FA. 2020. Highly efficient selective adsorption of anionic dyes by modified  $\beta$ -cyclodextrin polymers. *Journal of the Taiwan Institute Chemical Engineers*; 108:114–28.
11. Basu, A, Suresh, Kumar G. 2015. Thermodynamics of the interaction of the food additive tartrazine with serum albumins: A microcalorimetric investigation. *Food Chemistry*; 175:137–42.
12. Vidal, M, Garcia-Arrona, R, Bordagaray, A, Ostra, M, Albizu, G. 2018. Simultaneous determination of color additives tartrazine and allura red in food products by digital image analysis. *Talanta*; 184:58–64.
13. Amsaraj, R, Mutturi, S. 2020. Real-coded GA coupled to PLS for rapid detection and quantification of tartrazine in tea using FT-IR spectroscopy. *Lwt Food Science and Technology*; 2020:110583.
14. Drzeżdżon, J, Jacewicz, D, Sielick, a A, Chmurzyński, L. 2019. A review of new approaches to analytical methods to determine the structure and morphology of polymers. *TrAC - Trends in Analytical Chemistry*; 118:470–6.
15. Ng, HM, Saidi, NM, Omar, FS, Ramesh, K, Ramesh, S, Bashir, S. 2018. Thermogravimetric Analysis of Polymers. *Encyclopedia of Polymer Science and Technology*, 2018:1–29.
16. Ahmad, MA, Ahmad, Puad, NA, Bello, OS. 2014. Kinetic, equilibrium and thermodynamic studies of synthetic dye removal using pomegranate peel activated carbon prepared by microwave-induced KOH activation. *Water Resources and Industry*; 6:18–35.
17. Yan, YZ, Nagappan, S, Yoo, JM, Nechikkattu, R, Park, SS, Ha, CS. 2020. Polyethyleneimine-grafted polysilsesquioxane hollow spheres for the highly efficient removal of anionic dyes and selective adsorption of Cr(VI). *Journal of Environmental Chemical Engineering* 2020:104814.
18. Alrobei, H, Prashanth, MK, Manjunatha, CR, Kumar, CBP, Chitrabanu, CP, Shivaramu, PD, Kumar, KY, Raghu, MS. 2021. Adsorption of anionic dye on eco-friendly synthesised reduced graphene oxide anchored with lanthanum aluminate: Isotherms, kinetics and statistical error analysis. *Ceramic International*; 47(7): 10322–10331.
19. Bensalah, H, Younsi, SA, Ouammou, M, Gurlo, A, Bekheet, MF. 2020. Azo dye adsorption on an industrial waste-transformed hydroxyapatite adsorbent: Kinetics, isotherms, mechanism and regeneration studies. *Journal of Environmental Chemical Engineering*; 8:103807.
20. Chen, H, Deng, X, Ding, G, Qiao, Y. 2019. The synthesis, adsorption mechanism and application of polyethyleneimine functionalized magnetic nanoparticles for the analysis of synthetic colorants in candies and beverages. *Food Chemistry*; 293:340–7.
21. Ghaedi, M, Sadeghian, B, Pebdani, AA, Sahraei, R,

- Daneshfar, A, Duran, C. 2012. Kinetics, thermodynamics and equilibrium evaluation of direct yellow 12 removal by adsorption onto silver nanoparticles loaded activated carbon. *Chemical Engineering Journal*; 187:133–41.
22. Bacioiu, IG, Stoica L, Constantin, C, Stanescu, AM. 2017. Removal of Tartrazine from Aqueous Solution by Adsorption on Activated Red Mud. *Water, Air & Soil Pollution*; 228.
23. Dakshene, M, Jain, R. 2010. Adsorptive removal of tartrazine (E 102) over alkali activated fly ash. *Asian Journal of Chemistry*; 22:7733–7738.
24. Gautam, RK, Gautam, PK, Banerjee, S, Rawat, V, Soni, S, Sharma, SK, Chattopadhyaya, MC. 2015. Removal of tartrazine by activated carbon biosorbents of *Lantana camara*: Kinetics, equilibrium modeling and spectroscopic analysis. *Journal of Environmental and Chemical Engineering*; 3:79–88.
25. Banerjee, S., Chattopadhyaya, M. C. 2017. Adsorption characteristics for the removal of a toxic dye, tartrazine from aqueous solutions by a low cost agricultural by-product. *Arabian Journal of Chemistry*; 10: S1629–S1638.
- 26 Goscianska, J, Pietrzak, R. 2015. Removal of tartrazine from aqueous solution by carbon nanotubes decorated with silver nanoparticles. *Catalysis Today*; 249:259–264

## A Mixed N-Heterocyclic Carbene/Triphenylphosphine Palladium(II) Complex for Suzuki-Miyaura Cross-Coupling Reactions

Deniz Demir Atlı<sup>1\*</sup> 

<sup>1</sup>Manisa Celal Bayar University, Faculty of Science and Letters, 45140, Manisa, Turkey

\*[deniz.demir@cbu.edu.tr](mailto:deniz.demir@cbu.edu.tr)

\*Orcid: 0000-0001-8442-4916

Received: 24 May 2021

Accepted: 23 November 2021

DOI: 10.18466/cbayarfbe.941916

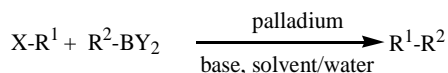
### Abstract

In this work, a novel compound, 1-(2,5-dimethylbenzyl)benzimidazole (**1**) was prepared by N-alkylation of benzimidazole with 2,5-dimethylbenzyl chloride in the presence of KOH base. Quaternization of **1** with 2,5-dimethylbenzyl chloride gave 1,3-bis(2,5-dimethylbenzyl)benzimidazolium chloride (**2**) salt. The reaction of **2** with palladium(II) acetate, PPh<sub>3</sub>, LiCl and Et<sub>3</sub>N gave [PdCl<sub>2</sub>{1,3-bis(2,5-dimethylbenzyl)benzimidazolium-2-ylidene}(PPh<sub>3</sub>)] (**3**) complex. The prepared compounds were characterized by spectroscopic methods and elemental analysis. The palladium complex **3** was used as catalyst in Suzuki–Miyaura cross-coupling reactions of some aryl bromides and chlorides with phenylboronic acid. In the reactions of the all aryl bromides, the catalyst displayed excellent activity and biphenyl compounds were achieved in >99% yields. High activity was observed with some aryl chlorides.

**Keywords:** Benzimidazolium, N-heterocyclic carbene, palladium, Suzuki-Miyaura cross-coupling

### 1. Introduction

Cross-coupling reaction is one of the most important reactions in organic chemistry. A carbon-carbon bond is formed in this reaction that takes place between an organo(pseudo)halide electrophile and an organometallic nucleophile. It is differently called depending on the nucleophile used. The reaction of a halide with a stable organoboron compound in the presence of a base and a palladium catalyst, known Suzuki-Miyaura cross-coupling reaction, was firstly performed in 1979 (Scheme 1) [1-3]. Since then, numerous studies on these type reactions using palladium, nickel, cobalt, iron, ruthenium and rhodium catalysts have been reported [4-9].



R<sup>1</sup> = aryl, alkenyl, alkynyl; X = halide;

R<sup>2</sup> = aryl, alkyl; Y = organic group

**Scheme 1.** Palladium catalyzed Suzuki-Miyaura cross-coupling reaction.

N-heterocyclic carbenes (NHCs) are among the most interesting ligands in organometallic chemistry.

Due to strong  $\sigma$ -donor and weak  $\pi$ -acceptor features, they compose stable transition metal complexes. Palladium NHC complexes have been intensely studied as efficient cross-coupling catalysts [10-13]. PPh<sub>3</sub> is inexpensive and air-stable chemical. Besides the NHC, a labile phosphine ligand contributes to the stability of a mixed NHC/phosphine palladium(II) complex. Such compounds can be prepared by different methods. The most commonly used one is the reaction of dimeric halide bridged [(NHC)PdX<sub>2</sub>]<sub>2</sub> complex with a phosphine ligand [14]. Another method is the reaction of [(NHC)PdX<sub>2</sub>(py)] with phosphine and an alkali halide [15]. Also, the reaction of a NHC precursor with a palladium(II) compound, phosphine, a base and an alkali halide can be used to prepare NHC/phosphine Pd(II) complexes [16]. They have been employed as efficient catalysts in many reactions such as Suzuki coupling, telomerization of butadiene, C-S bond formation and Mizoroki-Heck reaction [17-20].

In this study, a 1-alkylbenzimidazole, a benzimidazolium salt and a palladium(II) complex containing NHC and PPh<sub>3</sub> ligands were synthesized for the first time. The prepared compounds were characterized. Also, the catalytic activity of NHC-

Pd(II) complex in Suzuki coupling reactions of some aryl bromides and chlorides with phenylboronic acid was tested.

## 2. Experimental

### 2.1. General Remarks

All experimental studies were performed in air. The chemical agents were employed as purchased. Elemental analysis, NMR, FT-IR and LC-MSMS measurements were carried through CHNS-932 (LECO) elemental analyzer, Varian 400 MHz NMR spectrophotometer, Perkin Elmer spectrophotometer and SHIMADZU LC-MSMS-8040 mass spectrometer, respectively.

### 2.2. Synthesis of the compounds

#### 2.2.1. 1-(2,5-dimethylbenzyl)benzimidazole (1)

KOH (1.91 g, 34.03 mmol) was added to an ethanolic solution of benzimidazole (4.02 g, 34.03 mmol) and the mixture was stirred at room temperature for 2h. Then, 2,5-dimethylbenzyl chloride (5.1 mL, 34.03 mmol) was added. It was refluxed for 24h. After filtration, EtOH was removed. Water (100 mL) was added. The product was extracted with CH<sub>2</sub>Cl<sub>2</sub> (3x30 mL). Organic part was dried by adding Na<sub>2</sub>SO<sub>4</sub>. After filtration, the filtrate was concentrated. The product was crystallized by adding n-hexane. Yield: 6.60 g, 82%.  $\nu_{\text{CN}}$ : 1495 cm<sup>-1</sup>. <sup>1</sup>H NMR (400 MHz, CDCl<sub>3</sub>):  $\delta$  = 7.84 (dd, J = 6.5, 2.5 Hz, 1H, Ar-H), 7.79 (s, 1H, NCHN), 7.35 – 7.24 (m, 3H, Ar-H), 7.11 (d, J = 7.6 Hz, 1H, Ar-H), 7.06 (d, J = 7.5 Hz, 1H, Ar-H), 6.76 (s, 1H, Ar-H), 5.26 (s, 2H, NCH<sub>2</sub>), 2.25 (s, 3H, Me), 2.23 (s, 3H, Me) ppm. <sup>13</sup>C NMR (100 MHz, CDCl<sub>3</sub>):  $\delta$  = 144.01, 143.25, 136.34, 134.23, 133.00, 132.94, 130.88, 129.29, 128.81, 123.12, 122.35, 120.53, 110.00, 47.09, 21.07, 18.76 ppm. Anal. Calcd. for C<sub>16</sub>H<sub>16</sub>N<sub>2</sub>(%): C, 81.31; H, 6.84; N, 11.86. Found: C, 81.29; H, 6.83; N, 11.99.

#### 2.2.2. 1,3-bis(2,5-dimethylbenzyl)benzimidazolium chloride (2)

The mixture of 2,5-dimethylbenzyl chloride (0.51 mL, 3.36 mmol) and **1** (0.72 g, 3.05 mmol) in DMF (2 mL) was stirred at 80 °C for 5h. White solids were precipitated by adding excess Et<sub>2</sub>O. The product was recrystallized from EtOH/Et<sub>2</sub>O (1/3). Yield: 1.08 g, 91%.  $\nu_{\text{CN}}$ : 1563 cm<sup>-1</sup>. <sup>1</sup>H NMR (400 MHz, CDCl<sub>3</sub>):  $\delta$  = 11.98 (s, 1H, NCHN), 7.43 (dt, J = 7.0, 3.5 Hz, 2H, Ar-H), 7.41 – 7.34 (m, 2H, Ar-H), 7.06 (q, J = 7.7 Hz, 4H, Ar-H), 6.88 (s, 2H, Ar-H), 5.86 (s, 4H, NCH<sub>2</sub>), 2.34 (s, 6H, Me), 2.22 (s, 6H, Me) ppm. <sup>13</sup>C NMR (100 MHz, CDCl<sub>3</sub>):  $\delta$  = 144.88, 136.56, 133.32, 131.66, 131.36, 130.42, 130.12, 128.82, 127.20, 113.96, 51.54, 22.00, 19.19 ppm. Anal. Calcd. for C<sub>25</sub>H<sub>27</sub>N<sub>2</sub>Cl(%): C, 76.79; H, 6.98; N, 7.17. Found: C, 75.78; H, 6.91; N, 7.42.

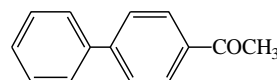
#### 2.2.3. [PdCl<sub>2</sub>{1,3-bis(2,5 dimethylbenzyl) benzimidazolin -2-ylidene}(PPh<sub>3</sub>)] (3)

The mixture of **2** (0.22 g, 0.58 mmol), PPh<sub>3</sub> (0.15 g, 0.58 mmol), LiCl (0.74 g, 17.4 mmol), Pd(OAc)<sub>2</sub> (0.13 g, 0.58 mmol) and Et<sub>3</sub>N (0.4 mL, 2.9 mmol) in MeCN (10 mL) was stirred at 70 °C overnight. The precipitated solid was isolated with filtration and washing excess water. It was recrystallized from CH<sub>2</sub>Cl<sub>2</sub>/n-pentane (1/3). Yield: 0.33 g, 72%.  $\nu_{\text{CN}}$ : 1436 cm<sup>-1</sup>. <sup>1</sup>H NMR (400 MHz, CDCl<sub>3</sub>):  $\delta$  = 7.47 (dd, J = 12.0, 7.7 Hz, 6H, Ar-H), 7.39 – 7.33 (m, 3H, Ar-H), 7.19 (td, J = 7.6, 2.5 Hz, 6H, Ar-H), 7.04 (dd, J = 6.1, 3.1 Hz, 2H, Ar-H), 6.97 (d, J = 7.6 Hz, 4H, Ar-H), 6.87 (d, J = 8.0 Hz, 2H, Ar-H), 6.75 (dd, J = 6.1, 3.1 Hz, 2H, Ar-H), 5.88 (d, J = 15.8 Hz, 2H, NCH<sub>2</sub>), 5.02 (d, J = 15.5 Hz, 2H, NCH<sub>2</sub>), 2.33 (s, 6H, Me), 2.08 (s, 6H, Me) ppm. <sup>13</sup>C NMR (100 MHz, CDCl<sub>3</sub>):  $\delta$  = 176.55 (C<sub>carbene</sub>), 136.17, 134.64, 134.35, 134.24, 131.88, 131.24, 130.38, 130.01, 129.48, 128.91, 128.67, 128.47, 128.35, 123.48, 112.43, 50.99, 21.06, 19.39 ppm. Anal. Calcd. for C<sub>43</sub>H<sub>41</sub>N<sub>2</sub>PPdCl<sub>2</sub>(%): C, 65.03; H, 5.21; N, 3.53. Found: C, 64.30; H, 5.72; N, 3.68.

### 2.3. General catalytic procedure

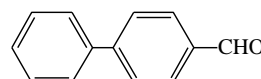
Catalyst (7.9 mg, 0.01 mmol), aryl halide (1 mmol), K<sub>2</sub>CO<sub>3</sub> (0.21 g, 1.5 mmol), phenylboronic acid (0.18 g, 1.5 mmol) were introduced in a flask. DMF (2mL) and water (2 mL) were added. The mixture was stirred at 80 °C for 2h. It was diluted with water (20 mL). After extraction with CH<sub>2</sub>Cl<sub>2</sub> (3x10 mL), drying with Na<sub>2</sub>SO<sub>4</sub>, and filtration procedures, the solvent was removed under reduced pressure. The known cross-coupling products were purely obtained by column chromatography and defined by <sup>1</sup>H NMR.

#### 4-acetylbiphenyl (4a)



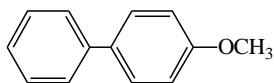
<sup>1</sup>H NMR (400 MHz, CDCl<sub>3</sub>):  $\delta$  = 8.07-8.00 (m, 2H, Ar-H), 7.72-7.66 (m, 2H, Ar-H), 7.67-7.60 (m, 2H, Ar-H), 7.52-7.37 (m, 3H, Ar-H), 2.64 (s, 3H, Me) ppm [21].

#### Biphenyl-4-carbaldehyde (4b)



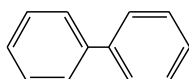
<sup>1</sup>H NMR (400 MHz, CDCl<sub>3</sub>):  $\delta$  = 10.05 (s, 1H, COH), 7.96-7.93 (m, 2H, Ar-H), 7.76-7.73 (m, 2H, Ar-H), 7.64-7.61 (m, 2H, Ar-H), 7.50-7.45 (m, 2H, Ar-H), 7.43-7.40 (m, 1H, Ar-H) ppm [22].

#### 4-Methoxybiphenyl (4c)

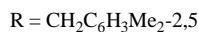
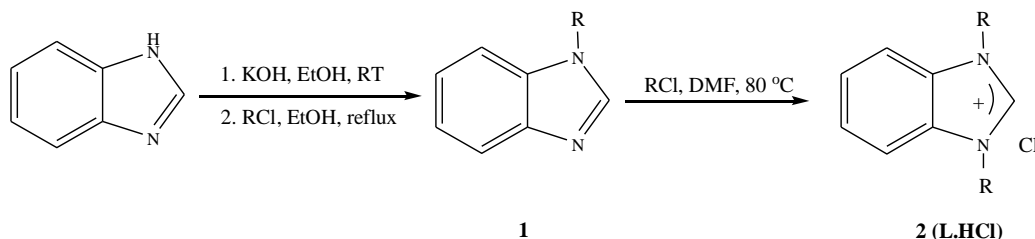


$^1\text{H}$  NMR (400 MHz,  $\text{CDCl}_3$ ):  $\delta = 7.58\text{-}7.53$  (m, 4H, Ar-H), 7.45-7.41 (m, 2H, Ar-H), 7.34-7.29 (m, 1H, Ar-H), 7.01-6.98 (m, 2H, Ar-H), 3.87 (s, 3H, Me) ppm [22].

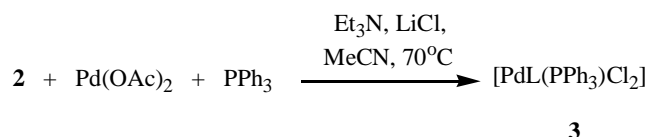
#### Biphenyl (4d)



$^1\text{H}$  NMR (400 MHz,  $\text{CDCl}_3$ ):  $\delta = 7.64\text{-}7.61$  (m, 4H, Ar-H), 7.49-7.44 (m, 4H, Ar-H), 7.39-7.35 (m, 2H, Ar-H) ppm [22].



**Scheme 2.** Synthesis of **1** and **2**.



**Scheme 3.** Synthesis of **3**.

The all prepared compounds were characterized by elemental analysis, NMR and FT-IR. According to the elemental analysis data, **1-3** have the anticipated formulations. NMR spectra validate the expected structures (Figures 1-3). In  $^1\text{H}$  NMR spectra of the **1-3**, aromatic proton and methyl signals appear at 6.75-7.84 ppm and 2.08-2.34 ppm, respectively. NCHN signal was observed at 7.79 ppm for **1**. The same signal for **2**, a salt compound, appeared at 11.98 ppm. It is characteristic that a singlet signal is present in the low field in  $^1\text{H}$  NMR spectrum for the acidic proton of the benzimidazolium salt. This low field signal disappears for **3**. This signifies that deprotonation takes place [25]. The number of phenyl proton peaks in the range of 7.0-8.0 ppm increases due to the presence of  $\text{PPh}_3$  ligands in **3** [15]. The singlet signals of the methylene protons at 5.86 ppm in the  $^1\text{H}$  NMR

### 3. Results and Discussion

Synthetic procedures for **1** and **2** are included in scheme 2. The benzimidazolium salt **2** was prepared in two steps using existing methods in the literature [23, 24]. Firstly, the compound **1** was obtained by N-alkylation of benzimidazole with 2,5-dimethylbenzyl chloride using KOH base in ethanolic medium. The reaction of **1** with 2,5-dimethylbenzyl chloride in DMF gave **2** in high yield.

The mixed  $\text{PPh}_3/\text{NHC}$  palladium(II) complex (**3**) was prepared by modifying the method used by Chan et al. [16]. The reaction of palladium(II) acetate with **2**,  $\text{PPh}_3$  and  $\text{LiCl}$  in the presence of  $\text{Et}_3\text{N}$  in MeCN gave the expected product in 72% yield (Scheme 3). As far as is known, palladium(II) acetate has not been previously used for this method. This route has the advantage that the desired phosphine complexes can be obtained from NHC precursors without isolating any intermediates. **3** is soluble in  $\text{CH}_2\text{Cl}_2$ ,  $\text{CHCl}_3$ , dmsO, dmf and insoluble in MeCN, pentane, water and  $\text{Et}_2\text{O}$ . The all compounds are stable in air.

spectrum of **2** become dublet signals at 5.02 and 5.88 ppm in that of **3**. So, the methylene protons are diastereotopic as mentioned previously [22, 26]. In  $^{13}\text{C}$  NMR spectrum of **3**, carbene carbon signal was observed at 176.55 ppm [15, 27]. The peaks observed in LC-MSMS at 723.30 and 355.25 show  $[\text{M}-2\text{Cl}]^+$  and  $[\text{M}-2\text{Cl}-\text{PPh}_3-\text{Pd}]^+$  fragments, respectively (Figure 4).  $\nu_{\text{CN}}$  peaks were monitored at 1495, 1563 and 1436  $\text{cm}^{-1}$  in FT-IR spectra of **1-3**.

The preliminary catalytic tests of NHC palladium(II) complex **3** were done for Suzuki-Miyaura coupling reactions of some aryl bromides and chlorides with phenylboronic acid. The experiments were performed by using 1% mol catalyst in DMF/water (1/1) at 80 °C for 2h.  $\text{K}_2\text{CO}_3$  was employed as base. No optimization study was done. The cross-coupling products were

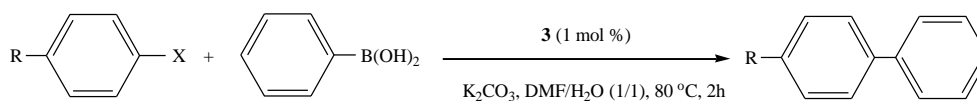
isolated by purifying with column chromatography and percentage yields were calculated. <sup>1</sup>H NMR spectra of them are given in figures 5-8. When aryl bromides were used, each biphenyl compound was obtained in >99% yield. Complex **3** exhibited excellent activity for aryl bromides under the studied conditions (Table 1, entries 1,3,5,7). Catalytic activity was also studied with aryl chlorides. The studied all aryl chlorides led to lower yields than the aryl bromides. It has been previously reported that this is due to the slow oxidative addition of aryl chlorides to palladium [28]. 4'-chloroacetophenone and 4-chlorobenzaldehyde bearing electron withdrawing groups led to the biaryls in good yields (Table 1, entries 2 and 4). While chlorobenzene formed biphenyl in 30% yield, the yield was only 5% with 4-

chloroanisole bearing donating methoxy group (Table 1, entries 6 and 8). It is understood from these results that decrease in electron density on aryl chlorides causes increase in activity. These results are consistent with the literature [29,30].

#### 4. Conclusion

In this study, 1-(2,5-dimethylbenzyl)benzimidazole, 1,3-bis(2,5-dimethylbenzyl)benzimidazolium chloride and [PdCl<sub>2</sub>{1,3-bis(2,5-dimethylbenzyl)benzimidazol-2-ylidene}(PPh<sub>3</sub>)] compounds were successfully prepared and characterized. Palladium(II) complex was tested as catalyst in the Suzuki-Miyaura cross-coupling reactions of some aryl bromides and chlorides with phenylboronic acid in aqueous media.

**Table 1.** Suzuki-Miyaura cross-coupling reactions catalyzed by **3**.



Entry	R	X	Product	Yield(%)
1	-COCH <sub>3</sub>	Br	<b>4a</b>	>99
2	-COCH <sub>3</sub>	Cl	<b>4a</b>	76
3	-CHO	Br	<b>4b</b>	>99
4	-CHO	Cl	<b>4b</b>	77
5	-OCH <sub>3</sub>	Br	<b>4c</b>	>99
6	-OCH <sub>3</sub>	Cl	<b>4c</b>	5
7	-H	Br	<b>4d</b>	>99
8	-H	Cl	<b>4d</b>	29

#### Author's Contributions

Deniz DEMİR ATLI: Performed the experiments and wrote the manuscript.

#### Ethics

There are no ethical issues after the publication of this manuscript.

#### References

- Miyaura, N, Yamada, K, Suzuki, A. 1979. A new stereospecific cross-coupling by the palladium-catalyzed reaction of 1-alkenylboranes with 1-alkenyl or 1-alkynyl halides. *Tetrahedron Letters*; 20(36): 3437-3440.
- Miyaura, N, Suzuki, A. 1979. Stereoselective synthesis of arylated (E)-alkenes by the reaction of alk-1-enylboranes with aryl halides in the presence of palladium catalyst. *Journal of the Chemical Society, Chemical Communications*; 19: 866-867.
- Pagett, AB, Lloyd-Jones, GC. Suzuki-Miyaura cross-coupling. In: Denmark SE et al. (ed.) *Organic Reactions*, Wiley, UK, 2019, pp 547-620.
- Talukder, MM, Cue, JMO, Miller, JT, Gamage, PL, Aslam, A, McCandless, GT, Biewer, MC, Stefan, MC. 2020. Ligand steric effects of  $\alpha$ -diimine nickel(II) and palladium(II) complexes in the Suzuki-Miyaura cross-coupling reaction. *ACS Omega*; 5(37): 24018-24032.
- D'Accriscio, F, Ohleier, A, Nicolas, E, Demange, M, Boullay, OTD, Saffon-Merceron, N, Fustier-Boutignon, M, Rezabal, E, Frison, G, Nebra, N, Mezaillies, N. 2020. [(dcp)Ni( $\eta$ 2-



- Arene)] precursors: Synthesis, reactivity, and catalytic application to the Suzuki–Miyaura reaction. *Organometallics*; 39(10): 1688-1699.
6. Ansari, RM, Kumar, LM, Bhat, BR. 2018. Air-stable cobalt(II) and nickel(II) Complexes with schiff base Ligand for catalyzing Suzuki–Miyaura cross-coupling reaction. *Russian Journal of Coordination Chemistry*; 44: 1-8.
  7. Key, RJ, Tengco, JMM, Smith, MD, Vannucci, AK. 2019. A molecular/heterogeneous nickel catalyst for Suzuki–Miyaura coupling. *Organometallics*; 38(9): 2007-2014.
  8. Ansari, RM, Bhat, BR. 2017. Schiff base transition metal complexes for Suzuki–Miyaura cross-coupling reaction. *Journal of Chemical Sciences*; 129: 1483-1490.
  9. Kadu, BS. 2021. Suzuki–Miyaura cross coupling reaction: recent advancements in catalysis and organic synthesis. *Catalysis Science&Technology*; 11(4): 1186-1221.
  10. Pirkel, N, Grosso, AD, Mallick, B, Doppiu, A, Gooben LJ. 2019. Dihalogen-bridged NHC–palladium(I) dimers: synthesis, characterisation and applications in cross-coupling reactions. *Chemical Communications*; 55(36): 5275-5278.
  11. Kaloğlu, N, Özdemir, İ. 2019. PEPPSI-Pd-NHC catalyzed Suzuki–Miyaura cross-coupling reactions in aqueous media. *Tetrahedron*; 75(15): 2306-2313.
  12. Sharma, KN, Satrawala, N, Srivastava, AK, Ali, M, Joshi, RK. 2019. Palladium(II) ligated with selenated NHC based (Se, CNHC, N<sup>-</sup>) type pincer: An efficient catalyst for Mizoroki–Heck and Suzuki Miyaura coupling in water. *Organic&Biomolecular Chemistry*; 17(40): 8969-8976.
  13. Vaishya, V, Patider, S, Plania, M. 2021. Imidazolium/triazolium based NHC–Palladium complexes and their application in catalysis. *Materials Today: Proceedings*; 43: 3181-3187.
  14. Schmid, TE, Jones, DC, Songis, O, Furst, MRL, Slawin, AMZ, Cazin, CSJ. 2013. Mixed phosphine/N-heterocyclic carbene palladium complexes: synthesis, characterization and catalytic use in aqueous Suzuki–Miyaura reactions. *Dalton Transactions*; 42(20): 7345-7353.
  15. Aktaş, A, Erdemir, F, Celepci, DB, Gök, Y, Aygün, M. 2019. Mixed phosphine/N- heterocyclic carbene–palladium complexes: synthesis, characterization, crystal structure and application in the Sonogashira reaction in aqueous media. *Transition Metal Chemistry*; 44: 229-236.
  16. Chan, KT, Tsai, YH, Lin, WS, Wu, JR, Chen, SJ, Liao, FX, Hu, CH, Lee, HM. 2009. Palladium complexes with carbene and phosphine ligands: Synthesis, structural characterization, and direct arylation reactions between aryl halides and alkynes. *Organometallics*; 29(2): 463-472.
  17. Liao, CY, Chan, KT, Tu, CY, Chang, YW, Hu, CH, Lee, HM. 2009. Robust and electron-rich cis-palladium(II) complexes with phosphine and carbene ligands as catalytic precursors in Suzuki coupling reactions. *Chemistry-A European Journal*; 2009(15): 405-417.
  18. Mesnager, J, Lammel, P, Jeanneau, E, Pinel, C. 2009. Mixed N-heterocyclic carbene and phosphine palladium complexes for telomerization of butadiene with methanol. *Applied Catalysis A- General*; 368(1-2): 22-28.
  19. Fu, CF, Liu, YH, Peng, SM, Liu, ST. 2010. C–S bond formation catalyzed by N-heterocyclic carbene palladium phosphine complexes. *Tetrahedron*; 66(12): 2119-2122.
  20. Pytkowicz, J, Roland, S, Mangeney, P, Meyer, G, Jutand, A. 2003. Chiral diaminocarbene palladium(II) complexes: synthesis, reduction to Pd(0) and activity in the Mizoroki–Heck reaction as recyclable catalysts. *Journal of Organometallic Chemistry*; 678(1-2): 166-179.
  21. Zhang, J, Zhang, W, wang, Y, Zhang, M. 2008. Palladium-iminodiacetic acid immobilized on pH-responsive polymeric microspheres: Efficient quasi-homogeneous catalyst for Suzuki and Heck reactions in aqueous solution. *Advanced Synthesis & Catalysis*; 350(13): 2065-2076.
  22. Demir Atlı, D. 2020. Synthesis and catalytic application of cyclopentadienyl nickel(II) N-heterocyclic carbene complexes. *Journal of Coordination Chemistry*; 73(10): 1530-1537.
  23. Özdemir, İ, Şahin, N, Gök, Y, Demir, S, Çetinkaya, B. 2005. In situ generated 1-alkylbenzimidazole–palladium catalyst for the Suzuki coupling of aryl chlorides. *Journal of Molecular Catalysis A: Chemical*; 234(1-2): 181-185.
  24. Yıldırım, İ, Aktaş, A, Celepci, DB, Kırbağ, S, Kutlu, T, Gök, Y, Aygün, M. 2017. Synthesis, characterization, crystal structure, and antimicrobial studies of 2-morpholinoethylsubstituted benzimidazolium salts and their silver(I)-N-heterocyclic carbene complexes. *Research on Chemical Intermediates*; 43: 6379-6393.
  25. Achar, G, Agarwal, P, Brinda, KN, Malecki, JG, Keri, RS, Budagumpi, S. 2018. Ether and coumarin-functionalized (benz)imidazolium salts and their silver(I)-N-heterocyclic carbene complexes: Synthesis, characterization, crystal structures and antimicrobial studies. *Journal of Organometallic Chemistry*; 854: 64-75.
  26. Kandil, S, Kariuki, BM, McGuian, C, Westwell, AD. 2021. Synthesis, biological evaluation and X-ray analysis of bicalutamide sulfoxide analogues for the potential treatment of prostate cancer. *Bioorganic & Medicinal Chemistry Letters*; 36: 127817.
  27. Mansour, W, Suleiman, R, Fettouhi, M, Ali, BE. 2020. Soft heteroleptic N-heterocyclic carbene palladium(II) species for efficient catalytic routes to alkyneones via carbonylative Sonogashira coupling. *ACS Omega*; 5(37): 23687-23702.
  28. Doucet, H. 2008. Suzuki–Miyaura cross-coupling reactions of alkylboronic acid derivatives or alkyltrifluoroborates with aryl, alkenyl or alkyl halides and triflates. *European Journal of Organic Chemistry*; 2008(12): 2013-2030.
  29. Zhou, YB, Li, CY, Lin, M, Ding, YJ, Zhan, ZP. 2015. A polymer-bound monodentate-P-ligated palladium complex as a recyclable catalyst for the Suzuki–Miyaura coupling reaction of aryl chlorides. *Advanced Synthesis & Catalysis*; 357(11): 2503-2508.
  30. Shahnaz, N, Banik, B, Das, P. 2013. A highly efficient schiff-base derived palladium catalyst for the Suzuki–Miyaura reactions of aryl chlorides. *Tetrahedron Letters*; 54: 2886-2889.

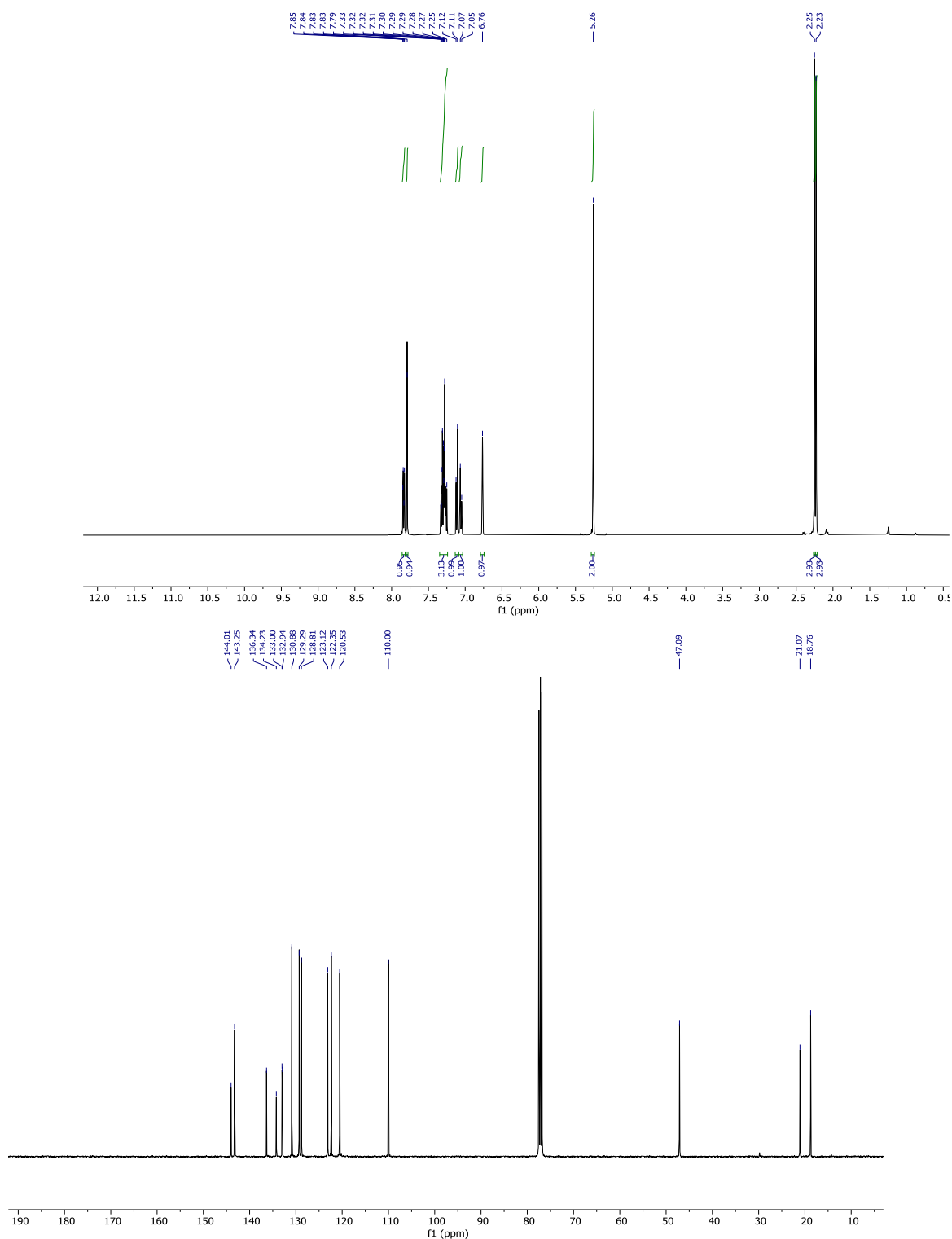


Figure 1.  $^1\text{H}$  and  $^{13}\text{C}$  NMR spectra of 1.



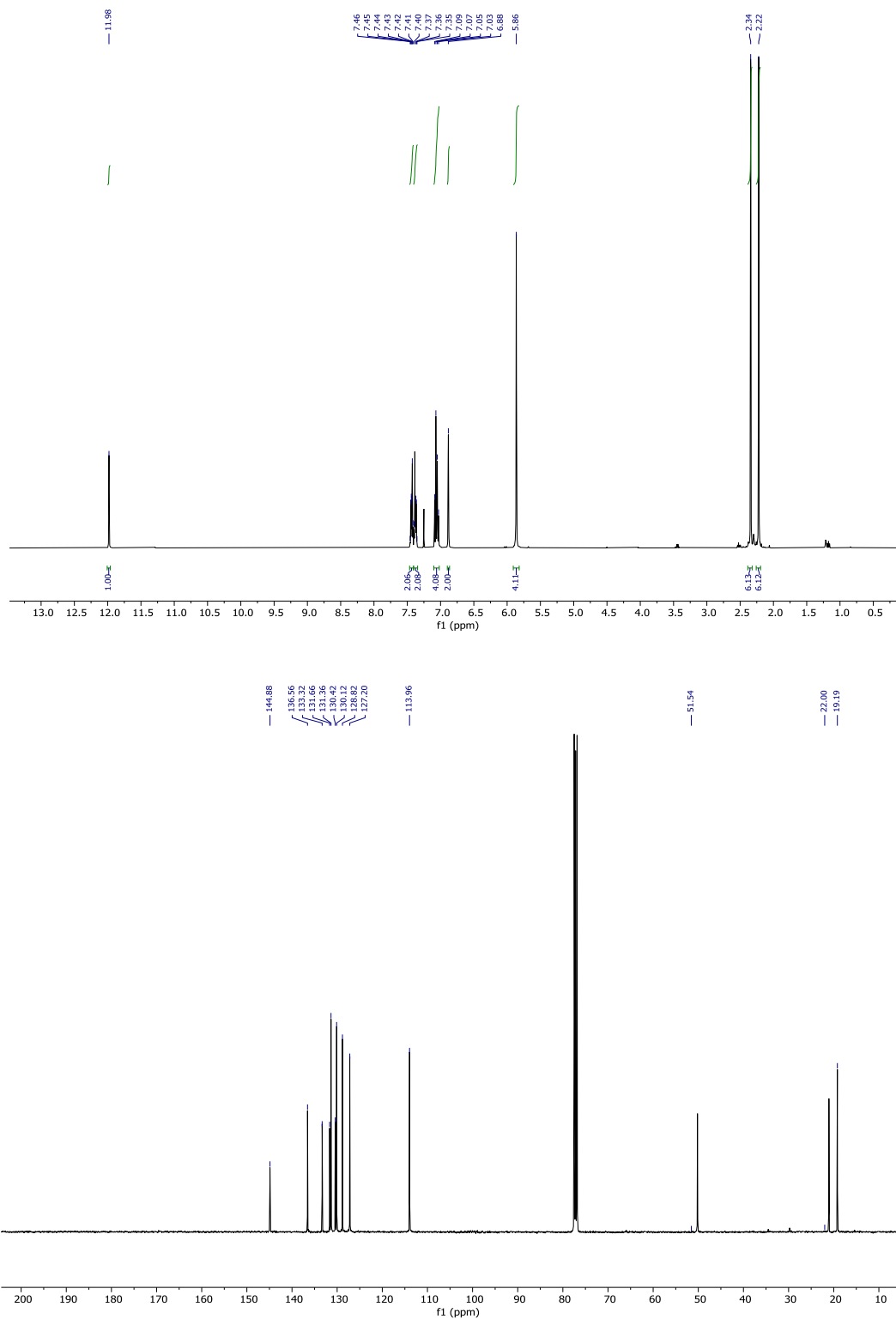


Figure 2.  $^1\text{H}$  and  $^{13}\text{C}$  NMR spectra of 2.

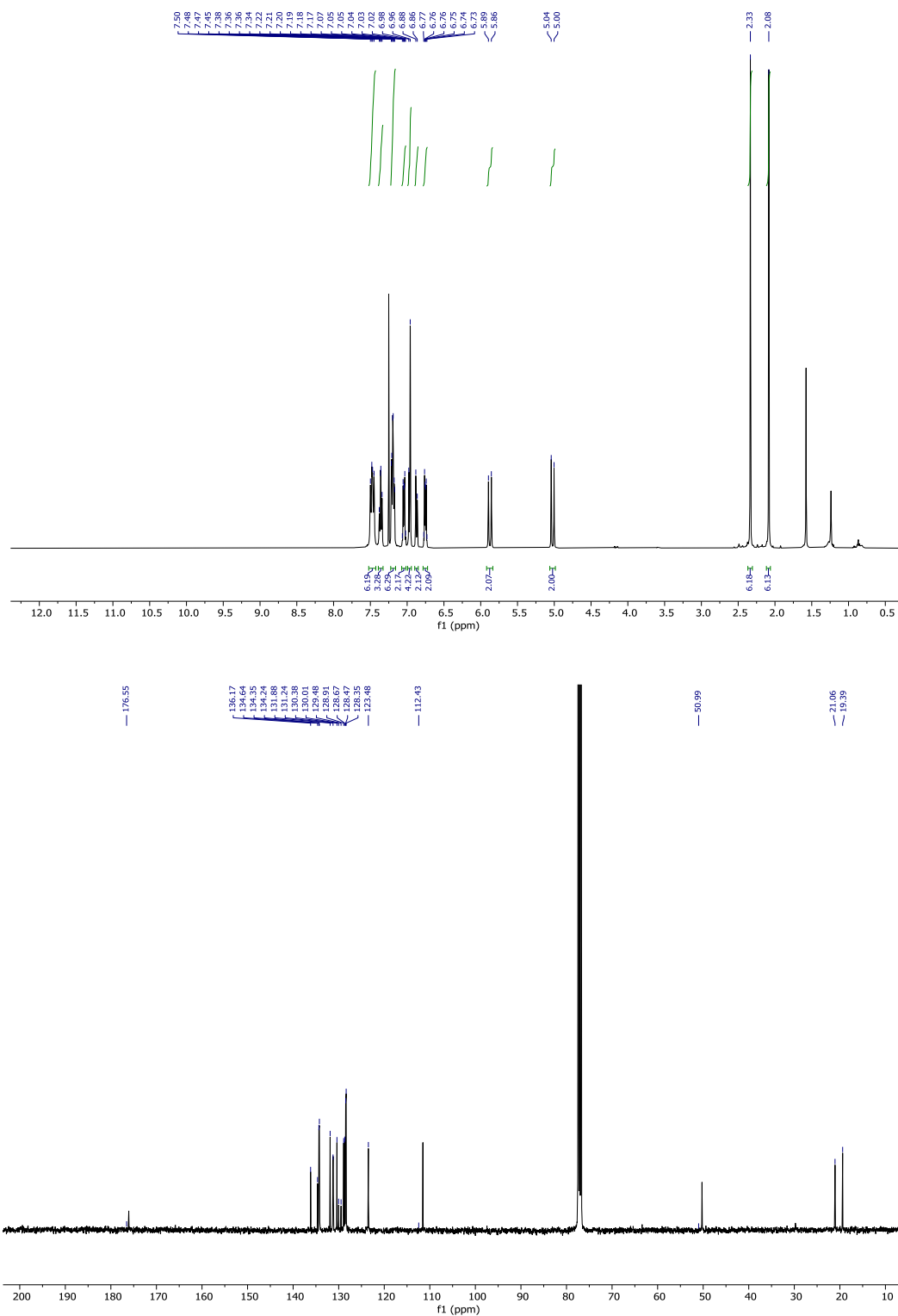


Figure 3.  $^1\text{H}$  and  $^{13}\text{C}$  NMR spectra of 3.

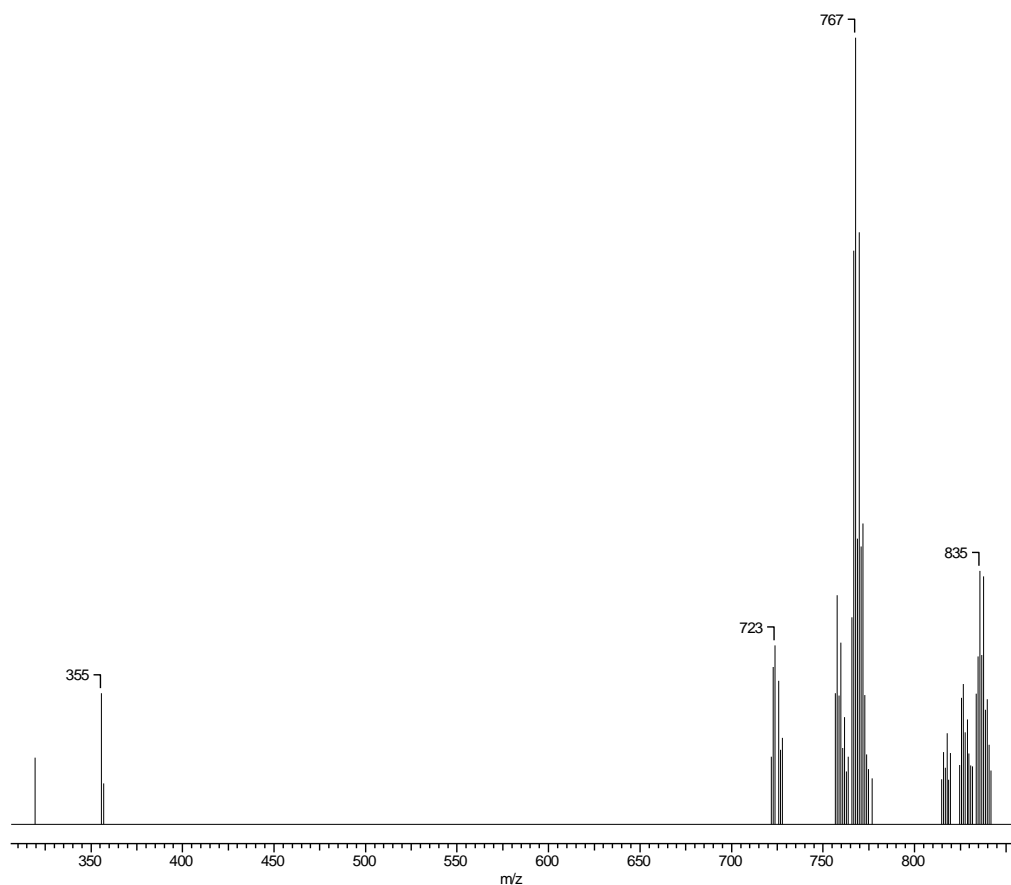


Figure 4. LC-MSMS spectrum of **3**.

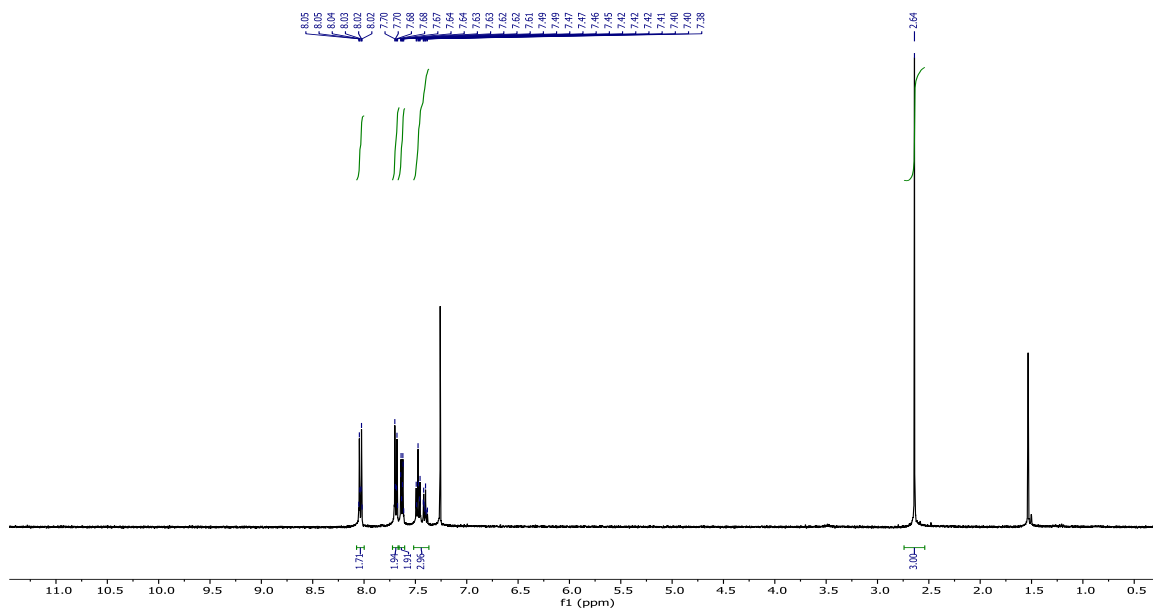


Figure 5. <sup>1</sup>H NMR spectrum of 4-acetylbiphenyl.

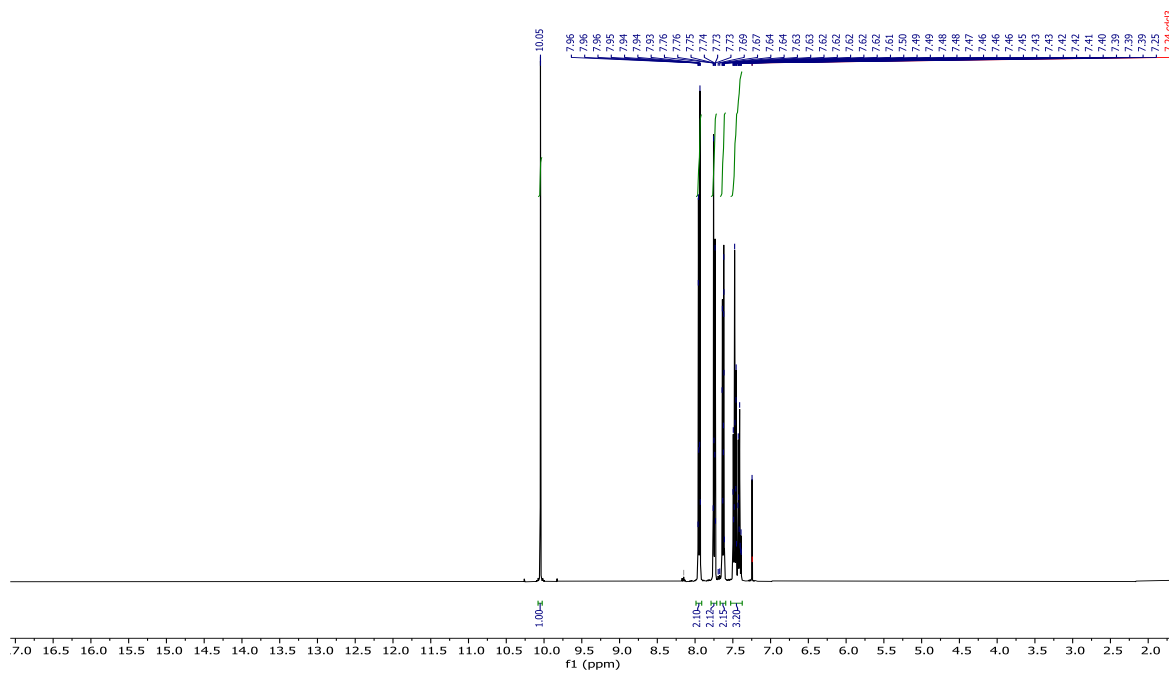


Figure 6.  $^1\text{H}$  NMR spectrum of biphenyl-4-carbaldehyde.

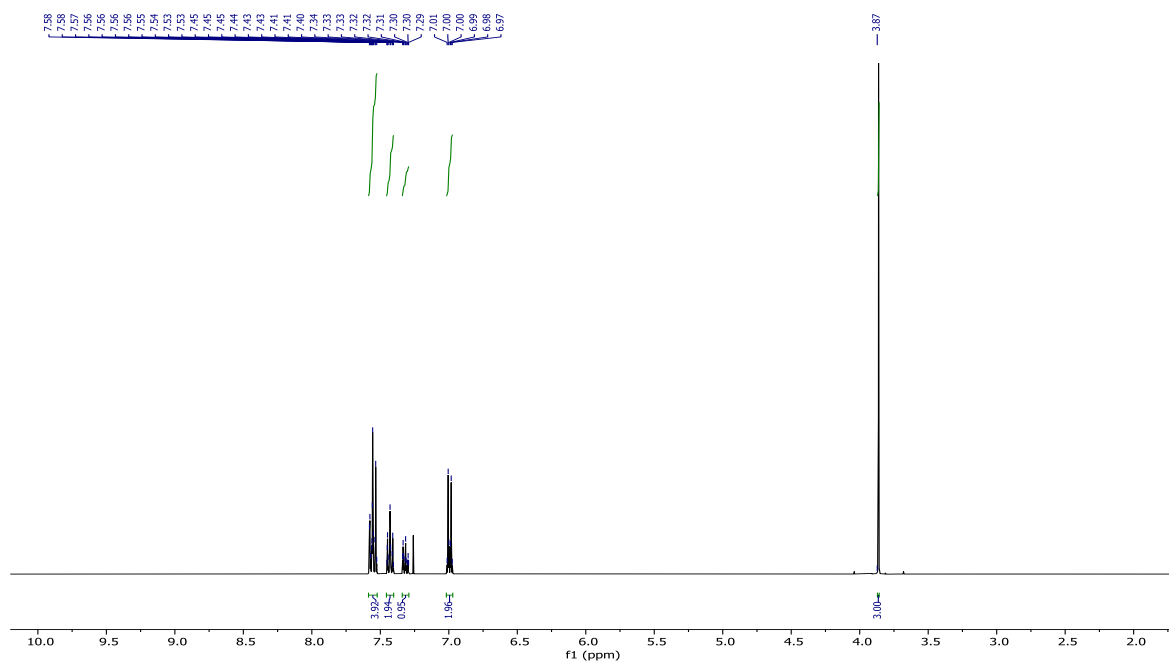


Figure 7.  $^1\text{H}$  NMR spectrum of 4-methoxybiphenyl.

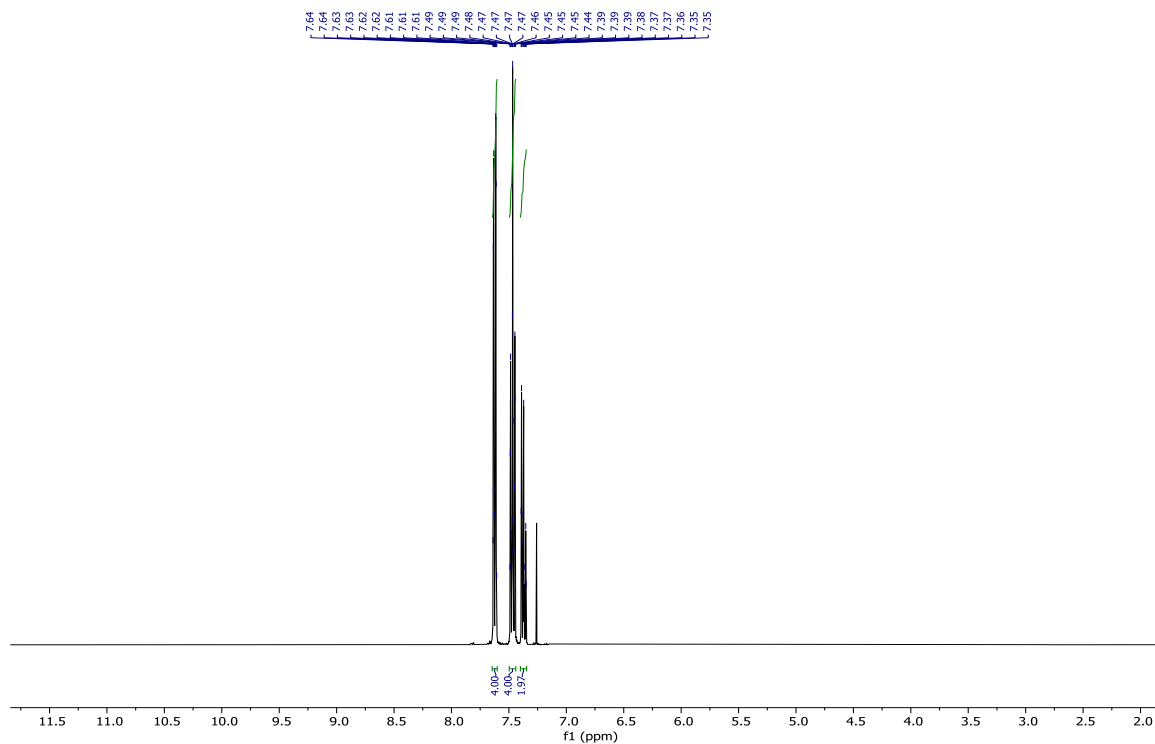


Figure 8. <sup>1</sup>H NMR spectrum of biphenyl.



# The Study on The Cooling of The Hot Side of The Thermoelectric Modules Utilized For High Cooling Requirements\*

Anıl Başaran<sup>1\*</sup> , Uğur Pehlivanoglu<sup>2</sup> 

<sup>1</sup> Manisa Celal Bayar Üniversitesi, Makine Mühendisliği Bölümü Manisa, Türkiye

<sup>2</sup> ISM Makine Elektrik Sanayi ve Ticaret A.Ş. Tasarım Merkezi

\* [anil.basaran@cbu.edu.tr](mailto:anil.basaran@cbu.edu.tr)

\*Orcid: 0000-0003-0651-1453

Received: 19 March 2021

Accepted: 24 June 2021

DOI: 10.18466/cbayarfb.899975

## Abstract

Thermoelectric modules (TEM) without moving parts are systems that can create a cooling effect in a short time, operate quietly and most importantly do not require working fluids for cooling. In the current study, TEM selection and design were made for 300 W cooling requirement. It is known that the cooling effects of the thermoelectric modules are directly proportional to the effective cooling of the hot side of the thermoelectric module. In this respect, air and water cooler for the hot side were investigated to provide maximum COP values via effective cooling of the hot side of the TEMs. The heat sinks and fan combinations were analyzed and optimized to cool the hot side of the TEM. Different fan speeds, heat sink geometries, and heat sink locations were discussed to cool the hot side. Heat sink dimensions were optimized for specific air velocity and the thermal resistance of the thermal paste was also considered. In addition to the heat sinks and fan combinations, the water-cooling systems were investigated for the cooling of the hot side of the TEMs. Considering the thermal paste effects and leakage risk in the designs, direct-contact and non-contact water-cooled designs have been realized. In the non-contact design, the effects of aluminum and copper materials on heat transfer were discussed in addition to the impact of geometry. It was found that air-cooled systems give rise to higher temperatures at the hot side of the TEM than water cooling system. Therefore, it is concluded that water cooling systems are more effective solutions for high-capacity TEMs cooling applications.

**Keywords:** Thermoelectric module, Numerical simulation, Peltier module, TEM air cooling, TEM water cooling.

## 1. Introduction

Thermoelectric modules (TEMs) are systems that can create refrigeration by taking advantage of the Peltier effect. For this reason, TEMs are commonly defined as "Peltier modules" in the industry. TEMs are formed by the serial connection of P type semiconductors with low energy level and N type semiconductors with high energy level. Thanks to these semiconductors, TEMs can transfer heat by using the energy levels of electrons. The current passing through the P and N type semiconductors carries the energy from the cold surface to the hot surface. In other words, when current is passed through the thermoelectric element, the Peltier effect occurs and while one side of the module is cooling, the other side heats up [1].

Studies on the cooling effect of TEMs are available in the literature. Riffat et al. [2] investigated the

performance of thermoelectric cooling systems with two different configurations. In the first configuration, the authors placed the finned surface on the cold side of the thermoelectric element, while in the second configuration, they placed phase change material. A finned heat pipe was used to cool the hot side of TEM in both configurations. With their study, the author concluded that the use of phase-change materials increases the cooling performance of the thermoelectric element.

Venkatesan and Venkataramanan [3] conducted experimental and simulation studies focus on developing performance specifications on a typical thermoelectric cooler. Their study involves voltage, current and cooling capacity for various hot side temperature ranges of the TEM. The authors simulated the TEM performance via CFD techniques for the TEM hot side temperature ranges of 303.15-333.15 K.

Ahiska and Ahiska [4] conducted a study on the capabilities of the thermoelectric module for cooling the computer processor. In their work, they discussed two- and single-phase fluid flow as well as fan-air combination as cooling options for the hot side of TEM. They found that the two-phase system had about five times more cooling effect than the air-cooling system.

Deniz et al. [5] performed an experimental study on the performance of TEMs connected in series. They discussed air and water-cooling systems for voltage values of TEMs in the range of 5 to 15 V. In their study, it is observed that the coefficient of performance (COP) obtained in the air-cooled system was higher than the water-cooled system. Besides, as a result of their experiments, it is found that high COP values obtained at low voltage values in both systems.

Jeong [6] carried out a theoretical investigation to optimize TEMs. The author proposed a novel one-dimensional analytic model. The model is used to determine optimum current, which maximizes the COP, by using the cooling capacity, the hot and cold side temperatures, the thermal and electrical contact resistances and the properties of thermoelectric material, but not by the length of a thermoelement.

Jeong [7] also conducted a theoretical investigation to optimize thermoelectric modules for maximization of cooling capacity. The author proposed a novel one-dimensional analytic model, in which the thermal resistances of heat exchangers as well as the thermal and electrical contact resistances inherent in the modules are taken into account. In the study, it was showed the effects of thermal resistances and the contact resistances on maximum cooling capacity, COP, the optimum electric current and thermoelement length.

Peter et al. [8] proposed a calculation procedure to define the optimum thermoelement length with the aim of maximizing cooling capacity and efficiency. Their model included the effect of the heat source temperature, heat sink temperature and the thermal resistance of the heat sink.

Another study on cooling capacity of the thermoelectric modules conducted by Yamanashi [9]. Yamanashi [9] investigated the optimum operation condition for a thermoelectric module to maximize COP. The author used a TEM with heat exchanger in the study.

Wang et al. [10] performed a study on COP of the TEMs. They concluded that the maximum COP values can be obtained by dividing the finite total thermal conductance into the hot side heat exchanger and the cold side heat exchanger.

Kishore et al. [11] investigated cooling performance of wearable thermoelectric coolers. The author stated that

external thermal resistance at hot side have great impacts on the TEM material behavior, design and performance of the TEM, and that these impacts are a fundamental challenge in achieving high efficiency for on-body applications. In their study, Kishore et al. [11] analyzed combined effect of heat source/sink thermal resistances and thermoelectric material properties on thermoelectric cooler performance.

TEMs have main advantages such as lightness, small size, silent and non-vibration working, easy to temperature control, no need working fluid like refrigerant, no requirement of maintenance [12]. On the other hand, TEMs are not widespread in cooling applications with high capacity due to their low cooling performance. Keeping the hot sides at a low temperature improves the cooling performance of TEMs. In this study, novel water and air coolers for the hot side of TEMs to be used in high-capacity cooling applications have been investigated. It is thus aimed to provide a contribution for the adaption of TEMs to applications with high cooling needs with high efficiency. For this purpose, different from the other studies in literature, TEM selections have been carried out for 300 W high cooling capacities. A cooling system with TEM designed for this cooling capacity has not been encountered in the literature. The selected TEMs have given rise to a high heat transfer dissipation rate at the hot side of the TEMs. The new heat sink-fan combinations, as well as novel water coolers, have been investigated for dissipation of the heat from the hot side of the TEMs. In the new heat sink-fan combinations, different air velocities, heat sink geometries and locations on TEMs have been discussed and heat sink dimension have been optimized. Direct contact and non-contact cooling water channels are designed for novel water cooler design. Vortex generators to increase heat transfer in direct contact designs have been examined. In non-contact designs, multi small diameter channels have been considered. The effect of material properties on TEM hot side temperature have also been discussed in non-contact designs.

## 2. Materials and Methods

### 2.1. Selection of TEMs

The TEMs, also called peltier modules, are semiconductor devices and they can generate a temperature difference between both sides because of the current supplied to them. As with all cooling devices, the Coefficient of Performance (COP) is the most important criteria when selecting a TEM. The COP can be written as Eqn. (2.1) for a TEM:

$$COP = \frac{\dot{Q}_c}{\dot{W}_e} \quad (2.1)$$

where  $\dot{Q}_c$  is the cooling capacity desired from TEM and  $\dot{W}_e$  is the required electrical work supplied to TEM in order to provide  $\dot{Q}_c$ .



The required electrical power is supplied to TEM via current in a certain voltage [17]. The input power is as follow

$$\dot{W}_e = V \times I \quad (2.2)$$

where  $V$  and  $I$  are voltage and current, respectively. According to Eqn. (2.2), it is obvious that the current and voltage of the TEM are important to maximize the COP of the TEM. On the other hand, they affect to cooling capacity of the TEM due to changing temperature differences between hot and cold sides of the TEM. Therefore, the definition of optimal current and voltage values that minimize input power plays a key role when choosing TEM for a cooling application. Other important parameters should be considered as the determination of hot side temperature and of the temperature difference between both side of the TEM.

In the current study, the selection of the TEM is carried out for  $\dot{Q}_c = 300$  W cooling capacity. The hot-side temperature of the TEM is defined as  $50^\circ\text{C}$  to dissipate heat to ambient at  $30^\circ\text{C}$ . The temperature difference between the cold and hot side of the TEM is  $50^\circ\text{C}$  to create a cooling effect via low temperature. Two type TEM which are FPH1-19922S1 [14] and FPH1-12712AC [15] is selected for 300 W cooling capacity. It is considered to obtain 300 W cooling capacity by using FPH1-19922S1 and FPH1-12712AC modules together. The geometrical details of the selected modules are presented in Figure 1.

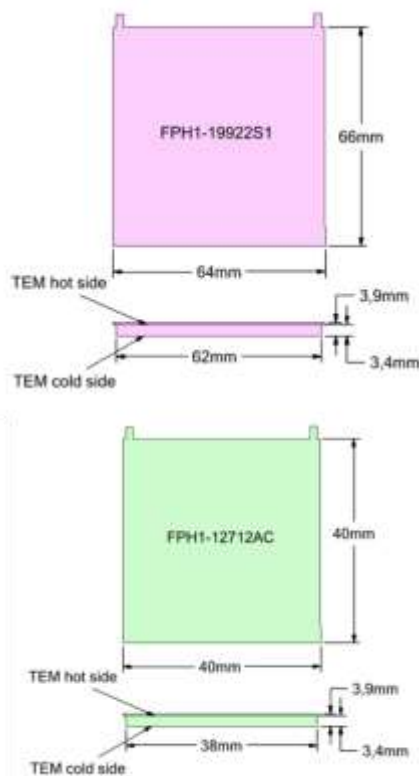


**Figure 1.** Geometrical details of (a) FPH1-19922S1 and, (b) FPH1-12712AC [14,15].

The performance curves of the selected FPH1-19922S1 and FPH1-12712AC modules are given in Figure 2. For the  $50^\circ\text{C}$  hot-side temperature, 22 A current is selected for operation of FPH1-19922S1 while 12.5 A is chosen for FPH1-12712AC. In this operation condition, the performance values of the selected TEMs are presented in Table 1. According to Table 1, two FPH1-19922S1 and one FPH1-12712AC are employed for  $\dot{Q}_c = 300$  W cooling capacity.

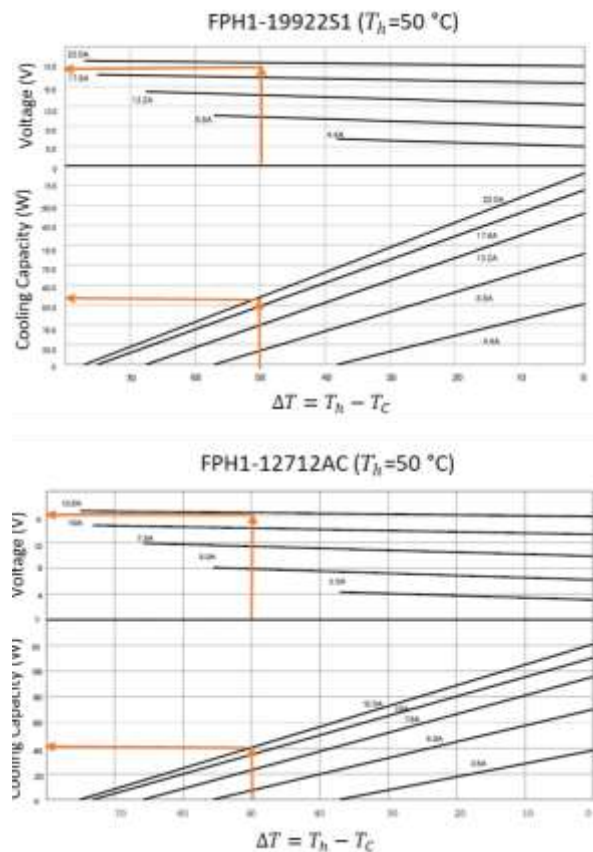


**Figure 2.** Performance curves of FPH1-19922S1 and FPH1-12712AC [14,15].

**Table 1.** The performance values of the selected TEMs.

	FPH1-19922S1	FPH1-12712AC
Voltage, $V$ (volt)	25	16
Current, $I$ (A)	22	12.5
Power, $\dot{W}_e$ (W)	550	200
Cooling capacity, $\dot{Q}_c$ (W)	130	40
COP (-)	0.236	0.2

TEM is a cooling device, and its energy interactions are given in Figure 3. in terms of the first law of thermodynamics. It can easily be observed in Figure 3 that heat dissipation from the hot side ( $\dot{Q}_h$ ) of TEM is the sum of the cooling capacity and input power according to the first law of thermodynamics.

Thus, the heat dissipation rate from the hot side of TEM can be written as follow

$$\dot{Q}_h = \dot{Q}_c + \dot{W}_e \quad (2.3)$$

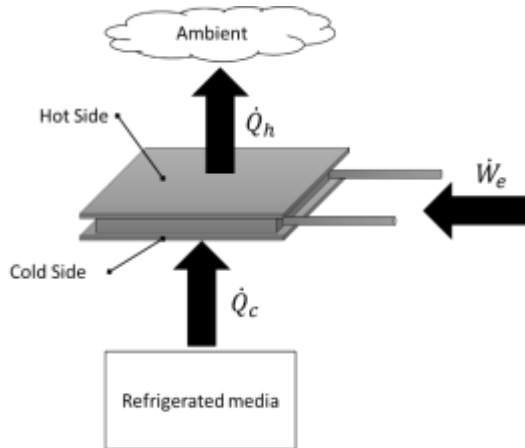


**Figure 3.** Energy interactions of a TEM.

The minimal total heat dissipation from the hot side decreases the input power of TEM for the constant cooling capacity. It is obvious that this situation improves the COP of the TEM. Hence, effective cooling of the hot side of TEM gains great importance for the applications. In the selected TEMs, FPH1-19922S1 has 680 W heat dissipation rates whereas FPH1-12712AC has 240 W.

## 2.2. Design of air-cooled for hot side of TEM

The removal of heat from the hot side of TEM at a high rate facilitates to reach the desired cooling capacity with low power. In other words, it increases COP. One of the ways of removing heat from the hot side is using a heat sink-fan combination. While the heat sink increases the heat transfer area, the fan creates forced convection between the fins of the heat sink.

In this study, 680 and 240 W heat should be dissipated from the hot sides of the selected TEMs to provide the desired cooling capacity. Designs of heat sink have been performed as an air-cooler for hot side of TEMs. The designs have been simulated, analyzed, and optimized by the HeatSinkCalculator [16] tool. For driving air between the designed heat sink fins, a high-capacity fan with a blade diameter of 120 mm and an airflow rates up to 271 CFM has been employed. The fan curve given in the Table 2 has been implemented in the

HeatSinkCalculator [16] tool. The placement of the heat sink-fan combination is given in Figure 4.

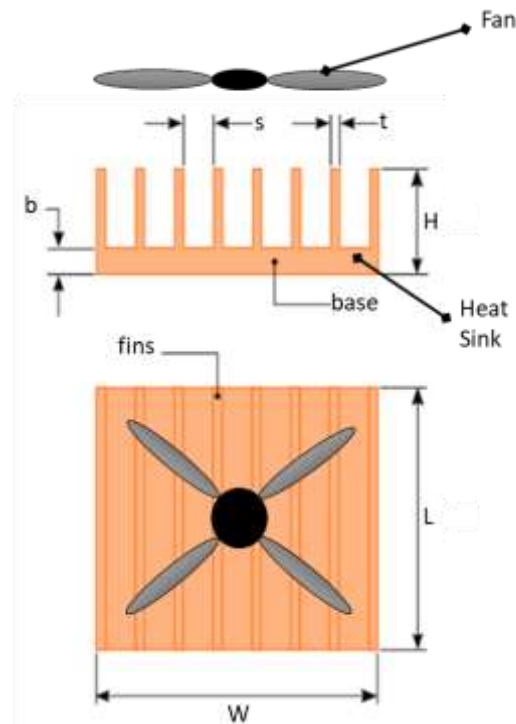


**Figure 4.** Front and top view of the heat sink-fan combination and dimensions of the heat sink.

Three heat sinks have been designed considering the dimensions of the fan and TEM. The designs are given in Figure 5. and they have been simulated and optimized using the HeatSinkCalculator [16]. The designs have been simulated for L values range between 63 and 120 mm, H values ranged from 20 to 70 mm and W values varied from 63 to 120 mm for FPH1-19922S1 TEM. Similarly, for FPH1-12712AC, L, H and W values have been changed in the designs at the ranges 63-100 mm, 20-60 mm and 63-120 mm, respectively. For these designs, the b, t, and s dimensions shown in Figure 4. have been optimized to minimize the source temperature (in other words, hot side temperature). It is worth to note here that the thermal resistance of the thermal paste has been considered in the simulations in the HeatSinkCalculator [16]. The thermal conductivity of the thermal paste has been assumed as 1.5 W/mK. Another assumption is that radiation in the heat sink is ignored.

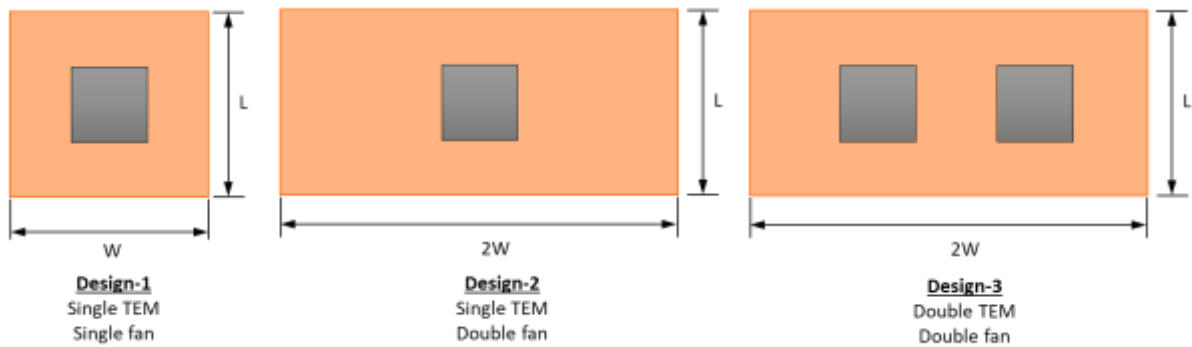


**Figure 5.** Simulated heat sink-fan system design for the investigated TEMs.

**Table 2.** Fan curve.

Air Volume (CFM)	Static Pressure (in-H <sub>2</sub> O)
0	1.2
25	1.15
50	1.1
75	1
100	0.7
125	0.5
150	0.42
175	0.45
200	0.4
225	0.3
250	0.2

### 2.3. Design of water-cooled for hot-side of TEM

Considering its thermophysical properties, water is a better heat carrier than air. Water is a good cooler alternative for the high heat disposal that occurs on the hot side of TEMs depended upon the high cooling capacity. For this reason, two different water-cooling units, direct contact, and non-contact, are designed to cool the hot side of TEM. In direct contact design, the water at 35 °C used as the coolant is in direct contact with the hot side of the TEM. Direct contact design is presented in Figure 6. There is no solid wall between the water and the hot surface of the TEM. With this approach, the thermal resistance of the solid wall and thermal paste between the water and the hot surface is eliminated. Thus, it is aimed to increase the efficiency of heat transfer. In addition, by placing vortex generators in the channel, turbulent flow is created in the channel at low water inlet velocities. Thus, it is aimed to increase the heat transfer coefficient in regions close to the hot surface of TEM. Another advantage of direct contact design is that it can be manufactured from a polymer material. This situation provides both time and costs savings in terms of manufacturing. The width and length of the design has been determined based on the dimension of the TEM (Figure 1).

On the other hand, it is very difficult to seal in direct contact design. Therefore, the non-contact design has been realized to cool TEM hot side with water at 35 °C. The non-contact design and its dimensions are given in the Figure 7. In the non-contact design, channels with a small hydraulic diameter (6.667 mm) are used to regulate the flow and increase the heat transfer coefficient. The walls between the channels act as a fin and contribute to heat transfer. Although sealing is provided with this design, the solid wall and thermal paste between the hot surface and the water cause thermal resistance. This situation causes a slight decrease in the heat transfer rate. In order to reduce the thermal resistance, a design made of copper material with a higher thermal conductivity than aluminum is included in this study. However, it is worth to emphasize here that although the copper material decreases the thermal resistance, it increases the cost. The dimension of the design has been determined based on the TEM dimension (Figure 1). In this respect, the non-direct contact surface dimension has been applied as 63 mm × 63mm. According to total width and length, 5 × 10 mm channels have been designed (Figure 7). The one channel cross-sectional area is 50 mm<sup>2</sup>.

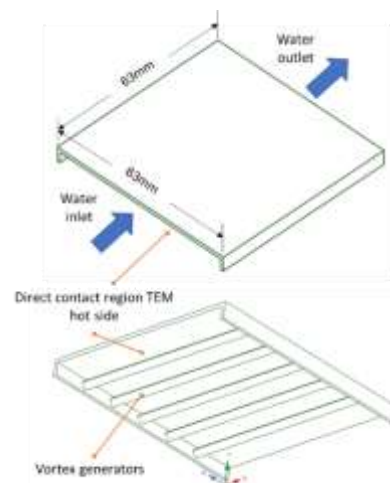


**Figure 6.** Direct contact design as a water-cooled unit.

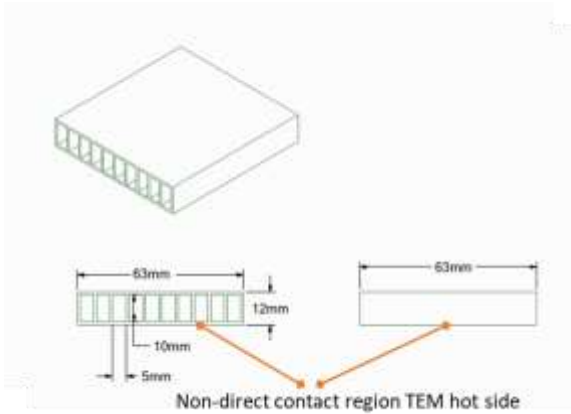


**Figure 7.** Non-direct contact design as a water-cooled unit.

### 2.3.1. Numerical Simulation of water-cooled designs

In this study, the direct contact and non-contact designs have been investigated numerically. A finite volume method has been used to solve the governing equations given in Eqns. (2.4) -(2.8) [13]. The governing equations (the mass, momentum, and energy conservation equations) for the steady incompressible flow, neglecting the viscous dissipation, are given as follows

$$\frac{\partial u}{\partial x} + \frac{\partial v}{\partial y} + \frac{\partial w}{\partial z} = 0 \quad (2.4)$$

$$\begin{aligned} \rho \left( u \frac{\partial u}{\partial x} + v \frac{\partial u}{\partial y} + w \frac{\partial u}{\partial z} \right) \\ = - \frac{\partial p}{\partial x} \\ + \mu \left( \frac{\partial^2 u}{\partial x^2} + \frac{\partial^2 v}{\partial y^2} + \frac{\partial^2 w}{\partial z^2} \right) \end{aligned} \quad (2.5)$$

$$\begin{aligned} \rho \left( u \frac{\partial v}{\partial x} + v \frac{\partial v}{\partial y} + w \frac{\partial v}{\partial z} \right) \\ = - \frac{\partial p}{\partial y} \\ + \mu \left( \frac{\partial^2 u}{\partial x^2} + \frac{\partial^2 v}{\partial y^2} + \frac{\partial^2 w}{\partial z^2} \right) \end{aligned} \quad (2.6)$$

$$\begin{aligned} \rho \left( u \frac{\partial w}{\partial x} + v \frac{\partial w}{\partial y} + w \frac{\partial w}{\partial z} \right) \\ = - \frac{\partial p}{\partial z} \\ + \mu \left( \frac{\partial^2 u}{\partial x^2} + \frac{\partial^2 v}{\partial y^2} + \frac{\partial^2 w}{\partial z^2} \right) \end{aligned} \quad (2.7)$$

$$\begin{aligned} \rho C_p \left( u \frac{\partial T}{\partial x} + v \frac{\partial T}{\partial y} + w \frac{\partial T}{\partial z} \right) \\ = k \left( \frac{\partial^2 T}{\partial x^2} + \frac{\partial^2 T}{\partial y^2} + \frac{\partial^2 T}{\partial z^2} \right) \end{aligned} \quad (2.8)$$

The numerical simulations have been performed with Ansys FLUENT R19.2 Academic Version [18]. Due to the geometrical difference of the designs, different computational domains have been considered for the direct contact and non-contact designs. The small-scale channels in the non-contact design are parametric. Therefore, one channel has been evaluated as a computational domain in the simulations to save computation time and effort. The direct contact design includes a channel with vortex generators, as seen in Figure 6. Thus, this channel has been used as the computational domain in the numerical simulation of the non-contact design. The small-scale channels in the non-contact design are parametric. Therefore, one channel has been considered as a computational domain in the simulations of non-contact designs to save computation time and effort. The computational domains of the designs are presented in Figure 8.

According to the Figure 6 and Figure 8, the hydraulic diameter of the water channel is 5.723 mm in direct contact design. Due to the vortex generator, there are very small cross-sections between walls and corners of vortex generators through the channel. These cross-sections have a 0.872 mm characteristic length. Considering this characteristic length, for  $\dot{m}=200$  kg/h, Reynolds number is computed as 2729. The flow regime inside the channel is turbulent because of higher values of Reynolds number than 2300. In the non-contact design, the water flows in the channels with a 50 mm<sup>2</sup> cross-section. In addition, the channels have a 6.667mm hydraulic diameter. In this condition, Reynolds number is 1135 in a channel for  $\dot{m}=200$  kg/h. Hence, the flow in the non-contact design is laminar.

As stated earlier, the heat dissipation rate from the hot site of TEM is 680 W for FPH1-19922S1 module. This heat rate should be removed from the 62 x 62 mm surface of the TEM. Therefore, heat flux at TEM hot surface has been calculated as 171.327 kW/m<sup>2</sup>. In the numerical simulation, this heat flux has been applied as a boundary condition at direct contact and non-contact regions in the water-cooled designs.

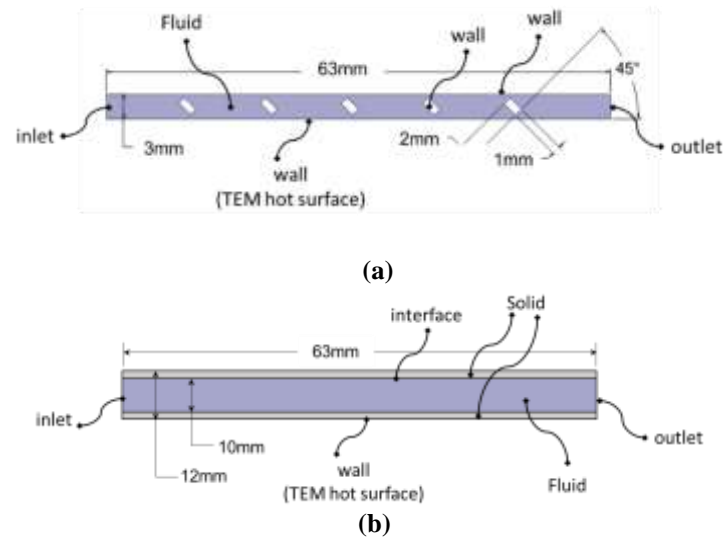


**Figure 8.** Computational domains (a) direct contact, (b) non-direct contact designs.

In the simulations, the flow has been numerically computed as 3D, turbulent, incompressible for direct contact design. The turbulent flow in direct contact design has been computed with standard k-epsilon. Similarly, 3D, laminar and incompressible flow has been simulated for non-contact design. In the numerical model, the convection terms have been discretized using the second-order upwind scheme while the diffusion terms are discretized using the central difference scheme. The SIMPLE algorithm has been used to couple the pressure and velocity. Convergence of the iterative solution has been insured when the residual of all the variables is less than the specified values. The specified convergence criteria are  $10^{-3}$  for continuity,  $10^{-5}$  for momentum, and  $10^{-6}$  for energy. The computational domain of direct contact design consists of 312356 elements while there are 76882 rectangular elements in the computational domain of non-direct design. The mesh independence of the solution has been assured for both designs.

### 3. Results and Discussion

Table 3 shows heat sink optimized dimensions for both FPH1-19922S1 and FPH1-12712AC TEMs. Dimensions have been optimized to minimize the hot-side temperature of the TEMs. The dimensions H, L, and W have been optimized at the upper value of the optimization range in all considered designs of both TEMs. The basic dimensions H, L, and W have been as high as possible due to the high heat flux arising on the hot side of the TEMs. A similar situation is valid for the optimized dimensions b, t, and s. In all designs simulated for FPH1-19922S1 and FPH1-12712AC TEMs, the base thicknesses have been determined as the upper value of the optimization range (1-15 mm). Heat conduction resistance of metal materials is generally higher than heat convection resistance. With the maximum thickness of the base, the heat is transferred

over the heat sink by conduction in the longest possible way instead of convection. This allows heat to be expelled at a high rate from the hot side of the TEM thanks to lower thermal resistance in the heat sink. As one can observe from the Table 3, as a result of the optimization, the t and s values have been minimized; the number of fins has been increased. In this way, the heat transfer surface area has been increased. The heat transfer coefficient can be improved by increasing the heat transfer surface area. But it should not be forgotten that increasing the number of fins and decreasing the distance between them may cause a decrease in the air velocity between the fins of the heat sink. This situation can give rise to a decrease in the heat transfer coefficient at the airside. In the current study, this problem has been avoided by using a high-capacity fan, and a basis has been created for using as many fins as possible.

Fin efficiency, flow rate, and pressure drop of the air flowing over the fins of the heat sink are given in the Table 4. According to Table 4, Design-2 and Design-3 have the same fin efficiency in both TEMs due to their similar geometric features. The fin efficiencies of Design-2 and Design-3 are 0.74 in FPH1-19922S1 and are 0.78 in FPH1-12712AC. It is worth to mention here that the same fan is used in all simulations. The Design-1 simulated for TEMs has lower fin efficiency than Designs-2 and Designs-3. The main reason is that Design-1 causes lower air velocity and high-pressure drop between the fins. This situation decreases the heat transfer coefficient between the fins and, hence, decreases the fin efficiency.

**Table 3.** The optimized heat sink dimensions for both FPH1-19922S1 and FPH1-12712AC TEMs.

	FPH1-19922S1			FPH1-12712AC		
	Design-1	Design-2	Design-3	Design-1	Design-2	Design-3
H (mm)	70	70	70	60	60	60
L (mm)	120	120	120	100	100	100
W (mm)	120	240	240	120	240	240
b (mm)	14.5	15	15	15	15	15
t (mm)	1	1	1	1	1	1
s (mm)	1.25	1.3	1.32	1.2	1.13	1.13
$N_f$	54	105	104	55	113	113

**Table 4.** Fin efficiency, flow rate, and pressure drop of the air flowing over the fins of the heat sink designs.

	FPH1-19922S1			FPH1-12712AC		
	Design-1	Design-2	Design-3	Design-1	Design-2	Design-3
$\eta_f$	0.701	0.742	0.743	0.748	0.783	0.784
$\nu$ (m <sup>3</sup> /s)	0.0354	0.0531	0.0535	0.0307	0.0449	0.0448
$\Delta p$ (Pa)	250	153	151	259	189	190

As mentioned earlier, FPH1-19922S1 and FPH1-12712AC as two different TEMs cause different hot side heat removal rates and COP values (Table 1). The heat to be removed from the hot-side of the FPH1-19922S1 TEM is 680 W at  $\Delta T=50$  °C ( $\Delta T=T_h - T_c$ ) while it is 240 W for FPH1-12712AC TEM. At these conditions, FPH1-19922S1 and FPH1-12712AC TEMs can provide 130 and 40 W cooling capacity, respectively. The thermal performances of the designs have been analyzed for these heat transfer rates. A comparison of the designs in terms of the highest temperature on the hot side of the modules and the lowest temperature on the cold side of the modules is presented in Table 5. According to Table 5, the maximum temperatures in the simulated designs for FPH1-19922S1 are 92.3 °C in Design-1, 89.4 °C in Design-2 and 98.9 °C in Design-3. Design-2 has been exhibited the lowest maximum temperature at the hot-side of the TEM. Unlike Design-2, Design-3 has been caused the highest hot side temperature with 98.9 °C for FPH1-19922S1. In Design-1, the maximum temperature has been determined as 92.3 °C. The

simulated temperature distributions for FPH1-19922S1 and FPH1-12712AC TEMs are given in Figure 9 and Figure 10, respectively. It can be seen from Figure 9 and Figure 10 that the highest temperature occurs at the midpoint of the modules. Accordingly Figure 9, doubling the width of the heat sink (Design-2) for the FPH1-19922S1 has been resulted in only a 3.142% reduction in maximum temperature. When Design-1 and Design-3 are examined, it is seen that using two TEMs separately with two narrow heat sinks instead of placing two TEMs in a single large heat sink results in lower maximum temperatures. Similar results can be observed in the FPH1-12712AC TEM with a lower heat rejection. According to Figure 10, the lowest maximum temperature for the hot side of the TEM has been exhibited by Design-2 with 64.3 °C. It is followed by Design-1 with 65.7 °C and Design-3 with 67.6 °C, respectively. For the FPH1-12712AC module, doubling the width of the heat sink (Design-2) instead of the single narrow heat sink (Design-1) has caused the maximum temperature on the hot side of the module to drop by only 2.13%.

**Table 5.** Maximum temperature at hot side of TEMs ( $T_h$ ) and minimum temperature at cold side of the TEMs ( $T_c$ ) for investigated heat sink-fan combinations.

	FPH1-19922S1 ( $\dot{Q}_h=680$ W/ $COP=0.236$ )			FPH1-12712AC ( $\dot{Q}_h=240$ W/ $COP=0.2$ )		
	Design-1	Design-2	Design-3	Design-1	Design-2	Design-3
$T_h$ (°C)	92.3	89.4	98.9	65.7	64.3	67.6
$T_c$ (°C)	42.3	39.4	48.9	15.7	14.3	17.6

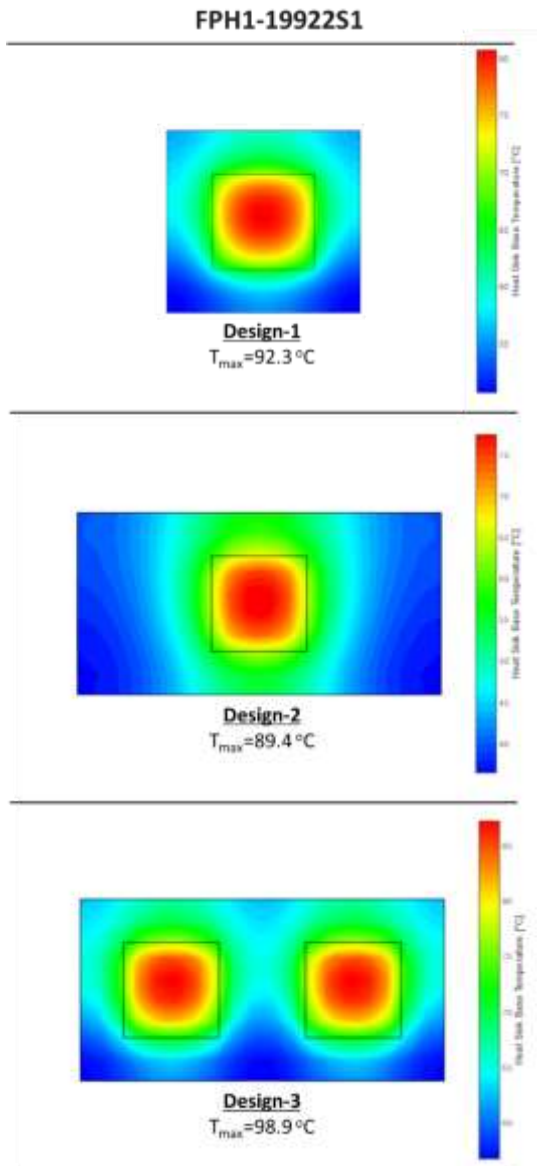


**Figure 9.** The simulated temperature distributions for FPH1-19922S1 TEM.

As explained before, the temperature difference between the cold and hot sides of the TEMs has been determined as 50 °C. The simulated lowest maximum temperature for the hot side of FPH1-19922S1TEM is 89.4 °C (Figure 9). In this case, the temperature of the cold side of the TEM is 39.4 °C. With its air-cooled heat sink designs, the FPH1-19922S1 module cannot create a cooling effect at 30 °C ambient temperature. In the FPH1-12712AC module, the simulated lowest maximum temperature for the hot side is 64.3 °C (Figure 10) and the lowest temperature for the cold side is 14.3 °C. This temperature value on the cold side of FPH1-12712AC has been reached with Design-2, and a close temperature can be obtained with Design-1. Accordingly, it is possible to provide a cooling effect in an environment at 30 °C with the FPH1-12712AC module.

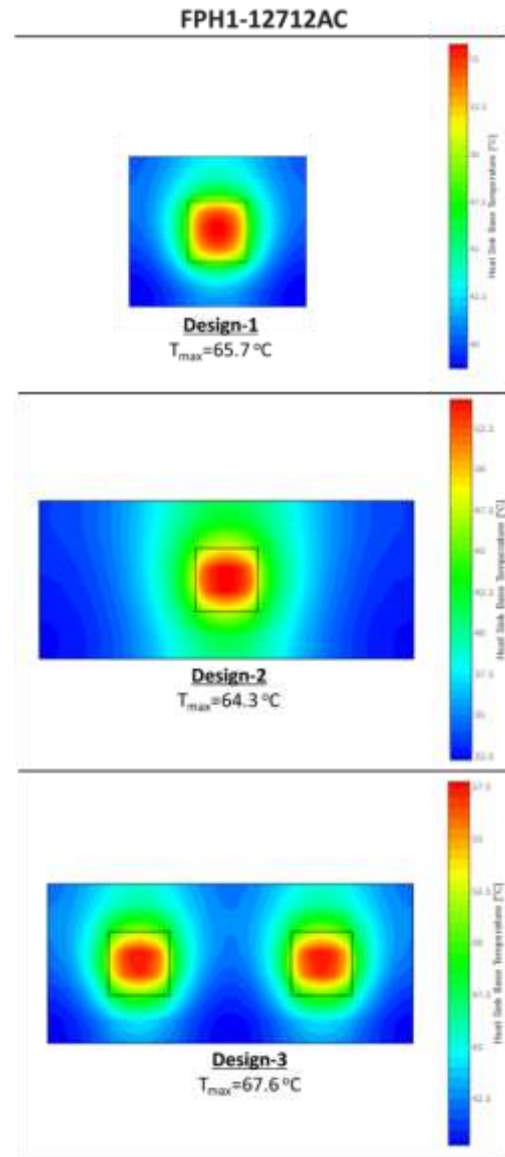


**Figure 10.** The simulated temperature distributions for FPH1-12712AC TEM.

For better performance, water-cooled designs have been considered as well as air-cooled designs. The temperature contour of the direct contact design is given in the Figure 11. According to the Figure 11, the highest temperature is 52.9 °C while the lowest temperature is 42.1 °C on the TEM hot surface. On the surfaces that coincide with the back of the vortex generator, it is seen that the temperature decreases 42 °C. The main reason of this decrease is that the vortex generators disrupt the flow pattern and create mixed flow (in other words flow with vortex). The mixed flow regions can be seen in Figure 12. In these mixed-flow regions, the heat transfer coefficient increases significantly and cools the surface. For this design, the simulated average temperature on the hot surface of TEM is 43.31 °C.

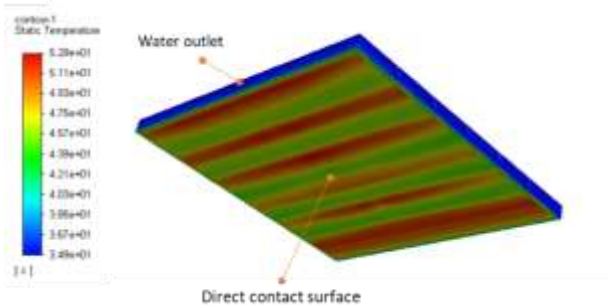


**Figure 11.** The temperature contour of the direct contact design.

In another water-cooled design, the effect of the material is also taken into account besides the channel geometry. The temperature distribution occurring in the non-direct design made of copper material is given in the Figure 13. The highest temperature occurring on the TEM hot surface is 75.9 °C. When the temperature is in the range of 50-55 °C in the regions corresponding to the entrance of the channel, the temperature increases towards the channel outlet. According to the temperature map given in the figure, water enters at 35 °C and leaves the channel at 41.4 °C. With the heat flux provided by TEM, there is an increase of 6.4 °C in the temperature of the cooling water. The heat transfer rate of the water, heated by heat flux provided by the TEM, has decreased along the channel due to the decrease of the finite temperature difference between the hot surface of TEM and water. This situation caused the TEM hot surface temperature to increase towards the channel outlet. The average temperature of the TEM hot surface has been simulated as 68.96 °C.

Similarly, the simulated temperature distribution of the non-contact design made of aluminum material is given in the Figure 14. A similar situation has been encountered with the copper material non-direct design. TEM hot surface temperature has increased towards the outlet due to the heating of the cooling water. According to the simulation results, the temperature average of the TEM hot surface is 75.22 °C in the aluminum non-direct design.

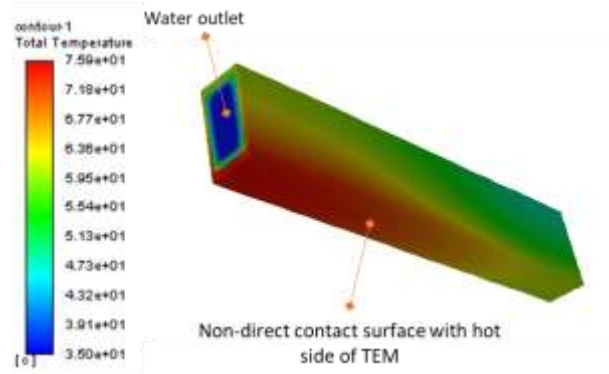


**Figure 13.** The temperature contour of the non-direct contact design made of copper.

By using aluminum instead of copper, the heat transfer coefficient of the solid wall is reduced by approximately 50%. This situation causes the average temperature of the TEM hot surface to increase by 6.26 °C (8.62%).

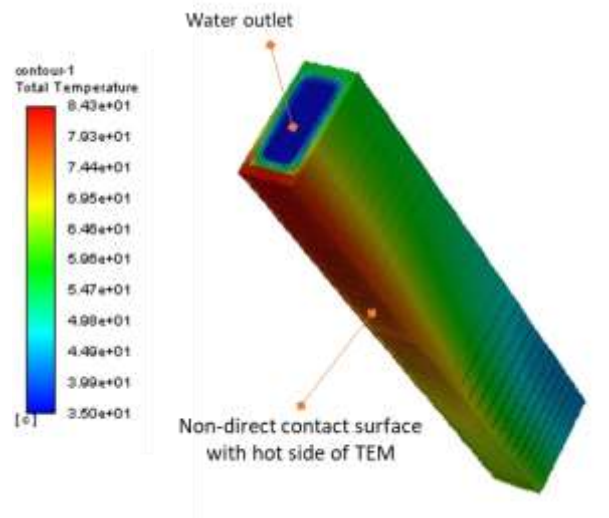


**Figure 14.** The temperature contour of the non-direct contact design made of copper.

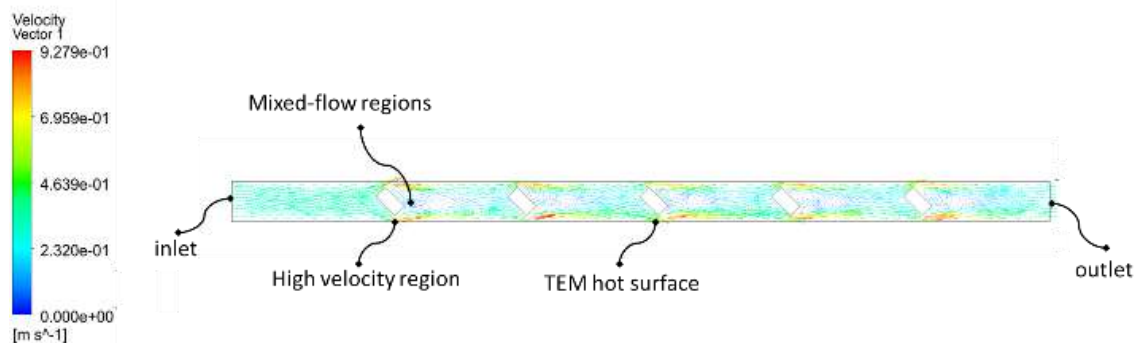


**Figure 12.** Representation of velocity vectors and mixed flow regions.



#### 4. Conclusion

For cooling applications having TEM, the energy that must be dissipated from the hot side is always much higher than absorbed energy from the cold side of the TEM according to first law of thermodynamics (Eqn. (2.3)). Temperature difference between hot and cold side of the TEM is also a matter which must be considered because as the temperature difference increases, cooling capacity of the TEM decreases. Therefore, cooling of the hot side of the TEMs is crucial for the cooling applications. For cooling of hot side of the TEMS, a proper way can be found by using the heat sinks and fan combinations and water-cooling systems as shown in this study.

Accordingly air-cooled designs to cool the hot side of the TEM for 300 W refrigeration capacity, doubling the width of the heat sink (for one TEM) instead of the single narrow heat sink caused reductions in the maximum temperature at the hot side of the TEMs. But these reductions in the maximum temperature at the hot side of the TEMs were between 2-4%.

In this study, it is also observed that using two TEMs separately with two narrow heat sinks instead of placing two TEMs in a single large heat sink results in lower maximum temperatures at the hot side of TEMs.

It concluded that air-cooled system give rise to higher temperatures at the hot side of the TEM than water cooling system. In the water-cooling designs, elimination of thermal resistance of the solids between water and the hot side of the TEMs and creating turbulent flow via vortex generation improved cooling performance of the designs.

#### Acknowledgement

This research was supported by ISM Makine Elektrik Sanayi ve Ticaret A.Ş. We would like to thank our colleagues in the Ismart Department of ISM Makine Elektrik Sanayi ve Ticaret A.Ş., who helped the research with great expertise and enthusiasm.

#### Author's Contributions

Anil BAŞARAN: Drafted and wrote the manuscript, performed the energy analysis, numerical simulations and result analysis.

Uğur PEHLİVANOĞLU: Performed selection of TEMs and fan, assisted in analytical analysis on the structure, supervised the energy analysis, result interpretation and helped in manuscript preparation.

#### Ethics

There are no ethical issues after the publication of this manuscript.

\*This study was presented at The III. National University-Industry Cooperation R&D and Innovation Congress.

#### References

1. Rowe, D.M. Application of thermoelectric cooling. In. CRC Handbook of Thermoelectrics, CRC Press Inc., Boca Raton, 1995, pp 617- 683.
2. Riffat, S.B., Omer, S.A. and Ma, X. 2001. A novel thermoelectric refrigeration system employing heat pipes and a phase change material: an experimental investigation. *Renewable Energy* 23, 313–323.
3. Venkatesan, K., Venkataramanan, M. 2020. Experimental and smulation studies on thermoelectric cooler: a performance study approach. *International Journal of Thermophysics* 41 (4), 1-23.
4. Ahıska, R. and Ahıska, K. 2007. Esnek iki fazlı termoelektrik CPU soğutucusu. *Gazi Üniv. Müh. Mim. Fak. Dergisi* 22 (2), 347-351.
5. Deniz, E.B., Kavak, B., Arslan, K. 2015. Seri Bağlı Ardışık Termoelektrik Soğutucuların Soğutma Performanslarının Deneysel İncelenmesi. *NWSA-Engineering Sciences*, 10.03.1A0357.
6. Jeong, E.S. 2014. A new approach to optimize thermoelectric cooling modules. *Cryogenic*, 59, 38-43.
7. Jeong, E.S. 2021. Optimization of thermoelectric modules for maximum cooling capacity. *Cryogenics* 114, 103241.
8. Pettes, A.M., Hodes, M.S., Goodson, K.E. 2009. Optimized thermoelectric refrigeration in the presence of thermal boundary resistance. *IEEE Trans Adv Pack* 32, 423-430.
9. Yamanashi, M. 1996. A new approach to optimum design in thermoelectric cooling systems. *Journal of Applied Physics* 80, 5494-5502.
10. Wang, X., Yu, J., Ma, M. 2013. Optimization of heat sink configuration for thermoelectric cooling system based on entropy generation analysis. *International Journal of Heat and Mass Transfer* 63, 361-365.
11. Kishore, R.A., Nozariasbmarz, A., Poudel, B., Sanghadasa, M. and Priya, S. 2019. Ultra-high performance wearable thermoelectric coolers with less materials. *Nature communications* 10 (1), 1-13.
12. Meng, J.H., Wu, H.C., Gao, D.Y., Kai, Z., Lu, G., Yan, W.M. 2021. A novel super-cooling enhancement method for a two-stage thermoelectric cooler using integrated triangular-square current pulses. *Energy* 217, 119360.
13. Çengel, Y.A., Boles, M.A., Kanoğlu, M. Thermodynamics: An Engineering Approach (9<sup>th</sup> Ed.), McGraw-Hill Education: NY, USA, 2018, pp:684.
14. Specification of FPH1-19922S1 TEM produced by Zmax Thermoelectric cooler and device manufacturer
15. Specification of FPH1-12712AC TEM produced by Zmax Thermoelectric cooler and device manufacturer.
16. Heat Sink Calculator Online Heat Sink Analysis and Design Tool. <https://www.heatsinkcalculator.com/> (accessed at 06.03.2021).
17. Versteeg, H.K. and Malalasekera, W. An introduction to computational fluid dynamics: the finite volume method. Pearson education: London, UK , 2007.
18. ANSYS® FLUENT, Release 19.2 Student Version



# Comparative Performance Analysis of Surface Mounted Permanent Magnet Synchronous Generators

Tuğberk Özmen<sup>1\*</sup>, Nevzat Onat<sup>2</sup>

<sup>1</sup> Vocational School of Manisa Technical Sciences, 45140, Manisa-Turkey

<sup>2</sup> Department of Electrical and Electronics Engineering, Manisa Celal Bayar University, 45140, Manisa-Turkey

\* [tugberk.ozmen@cbu.edu.tr](mailto:tugberk.ozmen@cbu.edu.tr)

\*Orcid: 0000-0002-8636-6091

Received: 29 June 2021

Accepted: 23 November 2021

DOI: 10.18466/cbayarfbe.959474

## Abstract

One of the generator types used in generation electrical energy is permanent magnet synchronous generator (PMSG). In this study, a surface mounted permanent magnet synchronous machine with a 1.5 kW inner rotor was used as a reference generator. The finite element analysis of this generator was conducted via commercial finite element analysis (FEA) software. As a result, phase current and voltages waveforms were measured at a rated load. The characteristics of the PMSG under loaded and unloaded working conditions were examined through the measurements on the experimental setup designed in Electrical Machines Laboratory at the Faculty of Engineering of Manisa Celal Bayar University. The values obtained from the open-circuit tests were compared with the simulation and manufacturer's catalog data. This paper also contrasted line voltages measured and simulated at 450 rpm as rated speed.

**Keywords:** Finite elements method, PMSG, surface mounted PMSG.

## 1. Introduction

Permanent magnet synchronous machines (PMSM) that contain magnets in the rotor are smaller in volume, lighter in weight and have less copper losses, higher power density, and higher efficiency compared to conventional electrical machines [1,2]. Permanent magnet synchronous machines are used as both a motor and a generator in areas such as automotive, space technologies, computer hardware, medical electronics, military applications, robotics, and wind energy systems. Permanent magnet synchronous generators are one of the generator types utilized in converting mechanical energy into electrical energy in wind energy systems.

Electromagnetic analysis of direct-drive permanent magnet synchronous generators can be conducted via finite element method (FEM) and their design can be improved [1, 3, 4]. The auxiliary tooth structure indicated for the stator structure of PMSGs can reduce short circuit current, cogging torque, and torque ripple [5]. Additionally, the computational and experimental performance findings of PMSG can be compared [6]. Design improvements were made to increase the torque capacity of PMSG and close values were obtained as a result of comparison between FEM and analytical

results [7-10]. The effects of magnet type on PMSG performance were examined in [11-13]. Measurements were made on the experimental setup and the design parameters were compared for the cases in which different magnets were used [11]. Since the amount of magnet to be used in PMSG is an important factor on the cost of the machine, design studies were carried out to reduce the amount of magnet used in the rotor and improve the output power [14-17]. PMSGs are classified as radial or axial depending on the path followed by the magnetic flux. In the hybrid design where radial and axial parts are used together, the power density value is increased 9.4 times [18]. The performance of PMSGs can also be examined over the number of phases. The output parameters of the PMSG designed as five phases were compared by using analytical calculation, FEM, and experimental measurement results. In addition, the study indicated that torque ripples decreases if a PMSG is designed as a five-phase process [19, 20]. And experimental setups and performance tests required for real-time measurements of PMSGs were provided in the study [21- 23]. A short-circuit fault is a serious safety threat to generators. In terms of reliability, the short-circuit current should be limited to a certain range [24-26]. In order for the generators to be more resistant to failure, studies have been carried out on the winding structure

[27-29]. Cooling methods are also important in terms of design for the effective and safe operation of magnets [30].

In this study, magnetic and electrical analyzes of the PMSG used as a reference were conducted through commercial FEA software. The real-time performance of the generator driven by an induction motor was measured designing an experimental setup. No-load and loaded measurements were made for the reference generator and the induction motor which is rotated by AC motor driver at variable speed. For transient measurements of the generator, National Instrument (NI) data collecting modules and LabVIEW™ software were employed.

The following is a summary of how this paper is organized. Nameplate of the reference generator, values of the design parameters, magnetic and electrical results of the finite element analysis are presented in Section 2 and 3. Section 4 describes the experimental set-up along with the results. Section 5 reviews the comparisons between the nameplate values and the results obtained by the finite element approach and experiments. Discussion and the concluding points are summarized in Section 6 and Section 7.

## 2. Reference Permanent Magnet Synchronous Generator

A radial flux surface mounted PMSG with an inner rotor is utilized in this study. Table 1 lists the reference generator's catalog information while Table 2 provides the values related to the design parameters. The model of the reference generator is shown in Figure 1.

**Table 1.** Nameplate values of the reference generator.

Parameters	Values
Rated output power	1500 W
Rated rotational speed	450 rpm
Required torque at rated power	35 Nm
Magnet material	NdFeB
Starting torque	< 0.7 Nm
Weight	16.9 kg
Rotor inertia	0.011 kgm
Insulation	H class

**Table 2.** Design specification of reference generator.

Parameters	Values
Number of slot	72
Number of poles	16
Stator outer diameter	221.5 mm
Rotor outer diameter	157.5 mm
Air gap distance	1 mm
Pole arc ratio	% 84.774
Magnet thickness	5.32 mm
Offset distance	0 mm

## 3. Finite Element Analysis of the Reference Generator

The finite element method is a useful, low-cost and numerical method that can be used in the analysis of electrical machines based on the solution of differential equations [31]. In order for the method to give more accurate results, it is important that the machine parts are meshed in an appropriate number and the time step is selected with the appropriate value [32]. PMSG was analyzed with FEA software based on finite element method which were created approximately 250000 finite elements mesh and the time step is chosen 0.5 ms. The graph of the phase currents and voltages of PMSG obtained from the two-dimensional analysis of FEA software are respectively presented in Figures 2 and 3. As a result of the analysis, the phase current and voltage of PMSG were obtained as 14.5 A and 37.7 V at a rated load. These values correspond to an active power value of approximately 500 W per phase at a power factor of 0.9.



(a)



(b)

**Figure 1.** (a) Stator and (b) rotor of the reference generator.

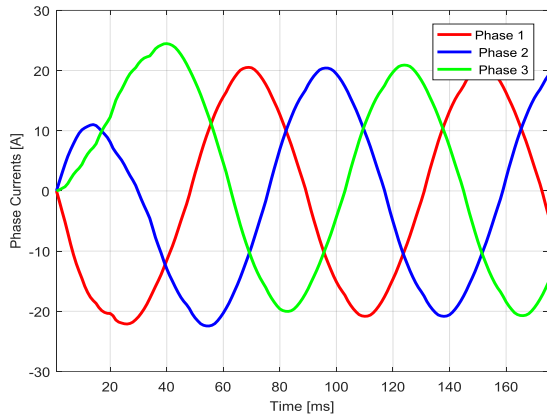


**Figure 2.** Phase current waveform at rated load

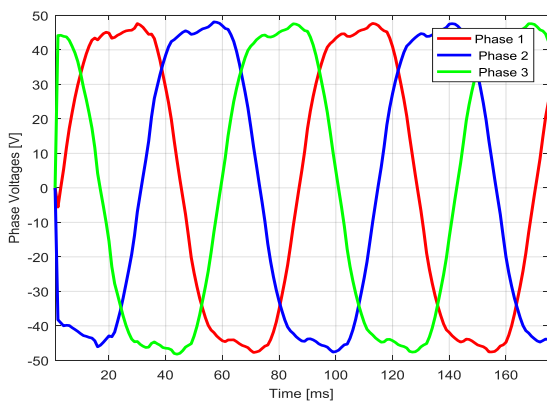


**Figure 3.** Phase voltages waveform at rated load

The magnetic flux density distributions of PMSG operating at no-load and rated load are provided respectively in Figures 4 and 5. According to the results of the no-load operating condition, the magnetic flux density in the stator yoke is about 1.2 T, 1.4 T in the stator teeth and 0.7 T in the rotor yoke. According to the results of full-load operating condition, the magnetic flux density in the stator yoke is approximately 1.25 T, 1.5 T in the stator teeth, and around 1 T in the rotor yoke.

#### 4. Experimental Results

An experimental set-up was developed in the Electrical Machines Laboratory at the Faculty of Engineering of Manisa Celal Bayar University to measure the PMSG, which was utilized as a reference. The paper focuses on the characteristics of the PMSG under loaded and unloaded working conditions by examining the measurements. Figure-6 shows the experimental set-up of the reference PMSG consisting of an AC motor driver, an induction motor with 4 poles and 1.1 kW power, a load, energy analyzers, and an oscilloscope.

Cogging torque, induced voltage, THD and core losses can be examined with the no-load operation tests. The measurements made under the no-load operating conditions of the PMSG revealed that there are different

induced voltages at variable speed in the stator windings. Since there is no current in the stator windings in this experiment, the open circuit voltage depends only on the rotation speed. Open circuit voltage values of the PMSG were obtained between 45V and 75V at speed which are between 300 rpm and 750 rpm. Figure 7 displays the result graphic of the no-load test and this graph shows the operational mode of the generator in case of a possible failure.

Due to the reverse magnetic field occurring in the short circuit fault in the PMSG stator windings, demagnetization may occur on the magnets and this can be damage to the machine. In the short circuit experiment, the current values depending on the speed were measured as shown in Figure-8. In the experiment, the highest short circuit current was approximately 5.5 A at 31 rpm. The saturation level of the machine can be determined with the graph obtained from the short circuit test.

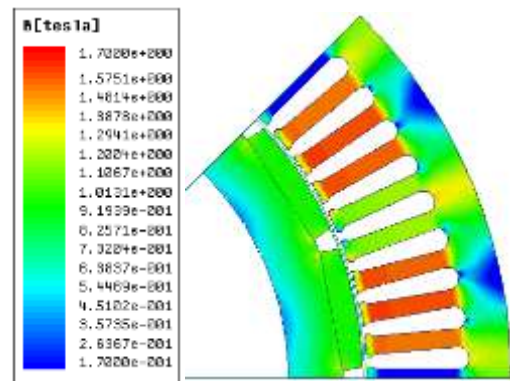


**Figure 4.** Magnetic flux density distribution at no load condition

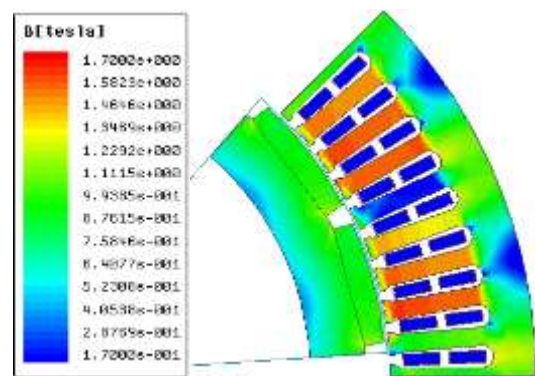


**Figure 5.** Magnetic flux density distribution at rated load condition

During the load operation tests, current, voltage and speed parameters were analyzed while the load values were taken into account. Figure 9 provides the voltage graph indicating the currents at different speeds. Due to the experimental setup, it is seen that the V-I characteristic behaves as a constant voltage-current

since the generator cannot be loaded sufficiently. The data obtained from this test are used for system design with voltage control in small power wind turbine systems with direct battery connection.

The line voltage graph depending on the speed at different ohmic loads can be seen in Figure 10. This graph indicates that for the same loading condition, the value of the line voltage increases as the speed increases.

The change in generator output current and speed under constant load was also investigated in the experiment. As seen in Figure 11, the change is linear. The slope of the line, on the other hand, increases as the amount of steady load increases. In small power wind turbine applications connected to the battery system through the rectifier, the input current must be within a certain range in order to extend the life of the battery which charged with a constant voltage. By using the data of the speed-current test, this current value can be commented on.

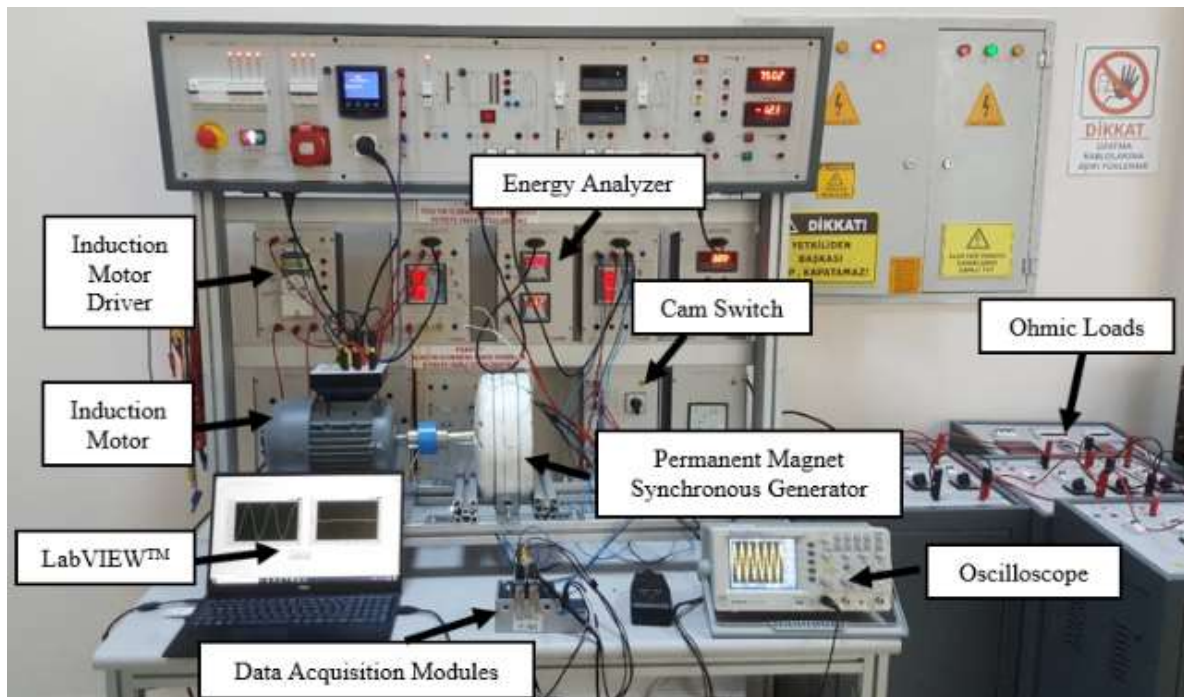


**Figure 6.** Experimental set-up

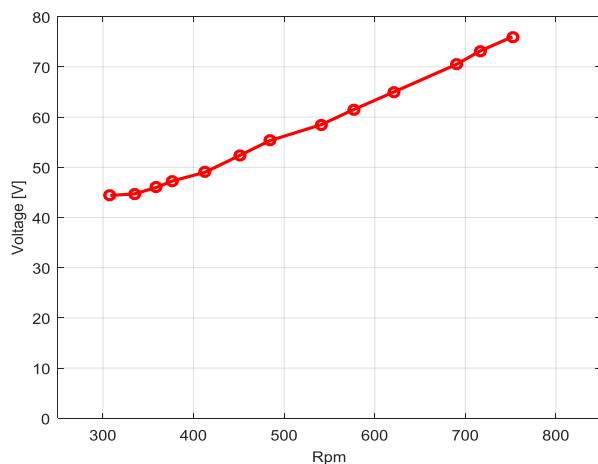


**Figure 7.** Experimental results of the induced voltage at no load condition.

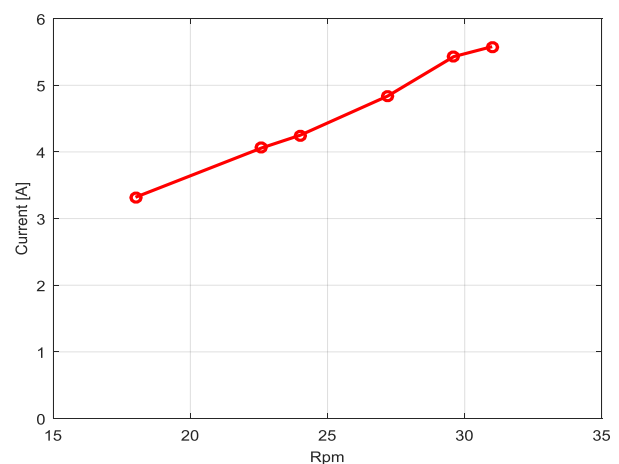


**Figure 8.** Short circuit experimental results.

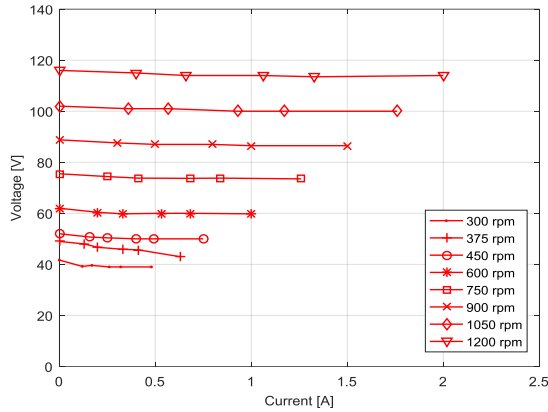


**Figure 9.** Voltage graph depending on the load current at different speed.

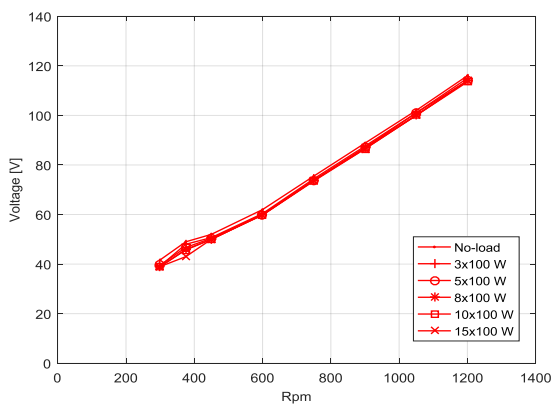


**Figure 10.** Voltage graph depending on the speed at different loads.

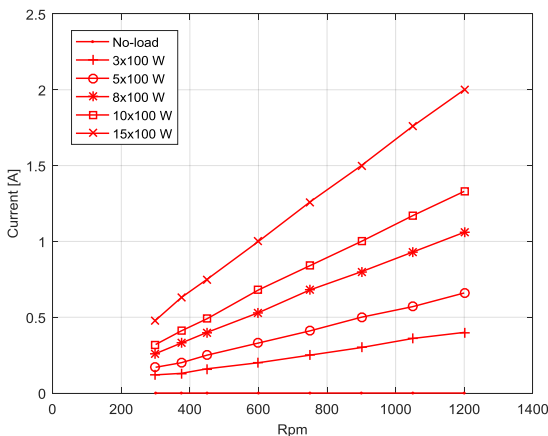


**Figure 11.** Load current graph depending on the speed at different loads.

In this study, a conductor and a coil are placed to the winding structure of the reference generator for measurement purposes. The graph of the induced voltage in a conductor and a coil in the no-load operation test is given in Figure 12. These data can be used to test the reliability of the results obtained from software using the finite element method. The value obtained in the experiments was measured about 10 percent lower than the value obtained in the software.

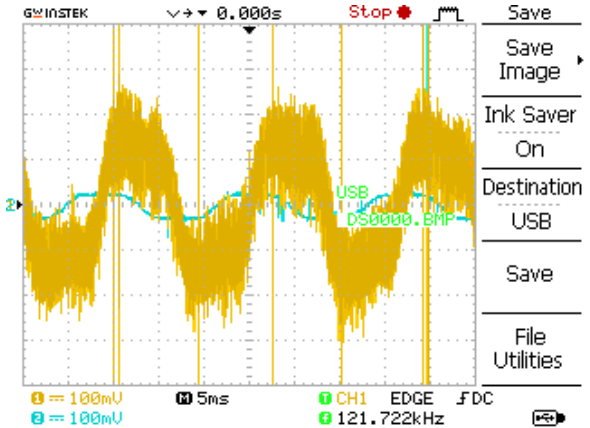


**Figure 12.** The induced voltage in a conductor and coil.

The experiment setup in Figure 6 was also used for the sudden load operation. Data acquisition modules of National Instruments (NI) company were utilized for measurements, as previously reported. Voltage and current signals were measured with NI 9242 and NI 9246 modules, respectively. These signals were transferred to the computer through LabVIEW™ software.

Figure 13 lists the curves of the current signals related to the sudden load operation performed with the reference PMSG rotating at 450 rpm while the curves related to the voltage signals is provided in Figure 14. When all load groups were turned on at the 77th millisecond of the experiment, the current values rapidly increased, while the voltage value decreased. As can be observed, the voltage dropped by roughly 4.11 percent when the load was activated. According to this result, it is seen that the reliability coefficient of the generator is high in sudden load changes.

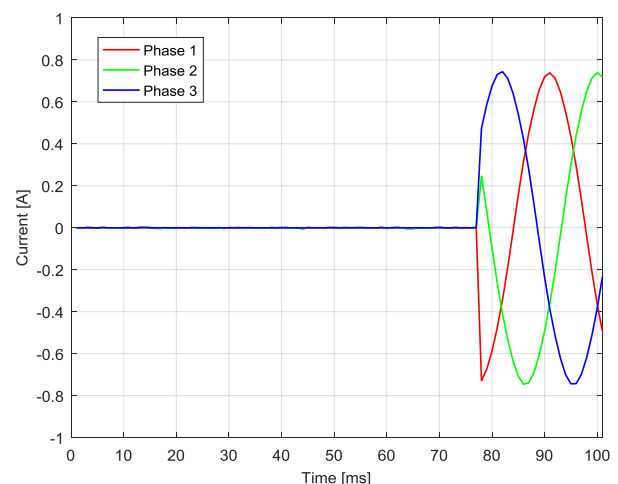


**Figure 13.** The sudden load operation current waveform

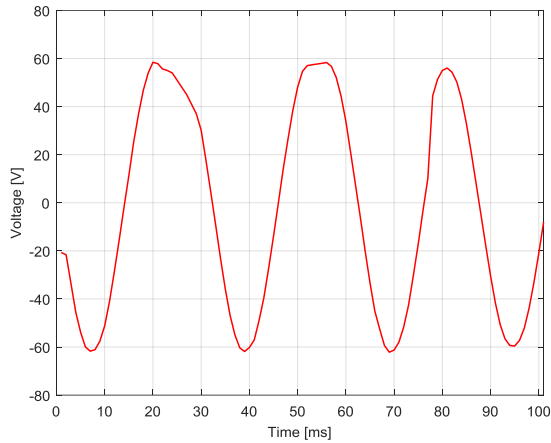


**Figure 14.** The sudden load operation voltage waveform

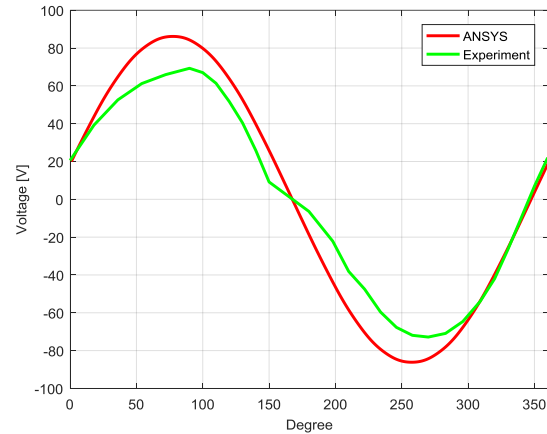


**Figure 16.** Simulated and experimental waveform of no-load phase voltages

### 5. Comparison Between FEA, Nameplate and Experiments

The comparison of open circuit values which were obtained from the manufacturer's catalog of the reference generator, from experiments and simulations is shown in Figure 15. The difference between curves is most likely due to the difference in magnet strength of the real and simulated generators.

In Figure 16, the line voltage curve acquired from the measurements conducted in the PMSG rotated at 450 rpm in no-load operating conditions was compared to the curve obtained from simulation results. As can be seen in Figure 16, there is a difference of approximately 17.7% in the maximum values of the voltage between the simulation and test results. It is seen that the experimentally obtained values are lower than the data provided by the FEA software under ideal conditions.

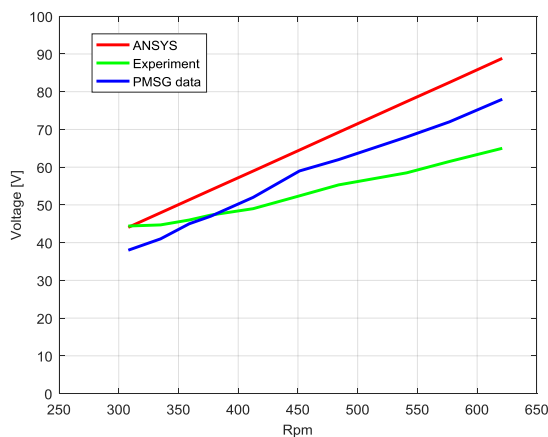


**Figure 15.** Simulated, experimental and catalog waveform of no-load phase voltage.

### 6. Discussion

As a result of the finite element analysis of the reference generator conducted via the Maxwell 2D software, phase current at rated load was found as 14.5 A and phase voltage was 37.7 V. In the magnetic analysis carried out through FEA software, it is seen that the magnetic flux density values in different parts of the machine remained within acceptable limits for both no-load and loaded operating conditions. In the no-load experiment which was done for certain speeds between 300 rpm and 750 rpm, the induced voltage in the phase windings was measured between 45 V and 75 V. Current value was measured as 5.5 A at 30 rpm in the short circuit test. The behavior of the reference generator under different load and speed conditions was investigated in the load experiments. The software values achieved under no-load operating conditions are higher than the experiment results and catalog data. The test results were found to be generally lower than the catalog data. The voltage value specified in the catalog for the no-load operation at nominal speed is 9.38% lower than the value obtained in the simulation and 11.19% higher than the value obtained in the experiment.

### 7. Conclusion

Surface mounted PMSGs provide significant advantages, especially in direct-drive variable-speed turbines (such as wind turbines, mini hydroelectric power plant turbines). With the elimination of the multilayer gearbox, crucial technical benefits such as higher reliability, longer life, lower weight are achieved. They do, however, they also contain important limitations which are electromagnetic, thermal and cooling that limit their development at high power. In this study, the performance of a small powerful generator manufactured for vertical axis wind turbines was analyzed and compared in terms of simulation, experiment, and catalog information. In general, it was



confirmed that actual operating conditions provide lower performance outputs compared to simulation values. The thermal effects generated by the heating of the winding and surface magnets under real operating conditions, as well as extra losses in the mechanical connection, were determined to be the reason of this disparity. According to the results, it can be said that PMSGs produce very stable outputs against sudden load changes and voltage ripples remain at an acceptable level. The specific contribution of this study is to measure the induced voltages in a conductor and coil which placed in the winding structure of an existing PMSG and compare these values with the results obtained in the FEM software. The fact that the values obtained from the software and the values obtained in the experiments were similar, proved the reliability of the analyzes to be made with the software before the PMSGs were produced. The benefits of various control strategies for increasing the output power of the reference generator will be examined in a subsequent study.

#### Authors' Contributions

Tuğberk ÖZMEN: Drafted and wrote the manuscript, conducted the experiment, and analyzed the results.

Nevzat ONAT: Supervised the experiment's progress, interpretation process of the results and helped preparing the manuscript.

#### Ethics

There are no ethical issued after the publication of this manuscript.

#### References

1. Duan, G, Wang, H, Guo, H, Gu, G. 2010. Direct drive permanent magnet wind generator design and electromagnetic field finite element analysis. *IEEE Transactions on Applied Superconductivity*; 20(3): 1883-1887.
2. Zhou, J, Li, S, Li J, Zhang, J. A Combined Control Strategy of Wind Energy Conversion System with Direct-Driven PMSG, 31st Youth Academic Annual Conference of Chinese Association of Automation, Wuhan, China, 2016, pp 369-374.
3. Deng, QL, Huang, SD, Peng, L. 2009. FEM analysis design on low speed direct-driven permanent magnet generator for wind turbine. *Micromotors Servo Technique*; 42: 9-12.
4. Chen, J, Nayar, CV, Xu, L. 2000. Design and finite-element analysis of an outer-rotor permanent-magnet generator for directly coupled wind turbines. *IEEE Transactions on Magnetics*; 36: 3802-3809.
5. He, Y, Zhao, W, Tang, H, Ji, J. 2020. Auxiliary teeth design to reduce short-circuit current in permanent magnet generators. *CES Transactions on Electrical Machines and Systems*; 4(3): 198-205.
6. Chan, TF, Wang, W, Lai, LL. 2010. Permanent-magnet synchronous generator supplying an isolated load. *IEEE Transactions on Magnetics*; 46(8): 3353-3356.
7. Tapia, JA, Pyrhonen, J, Puranen, J, Lindh, P, Nyman, S. 2012. Optimal design of large permanent magnet synchronous generators. *IEEE Transactions on Magnetics*; 49(1): 642-650.
8. Liuzzi, G, Ludici, S, Parasiliti, F, Villani, M. 2003. Multiobjective optimization techniques for the design of induction motors. *IEEE Transactions on Magnetics*; 39(3): 1261-1264.
9. Sudhoff, SD, Cale, J, Cassimere, B, Swinney, M. Genetic Algorithm Based Design of a Permanent Magnet Synchronous Machine, IEEE International Conference on Electric Machines and Drives (IEMDC), San Antonio, TX, 2005, pp 1011-1019.
10. Sadeghi, S, Parsa, L. 2011. Multiobjective design optimization of five-phase halfbach array permanent-magnet machine. *IEEE Transactions on Magnetics*; 47(6): pp. 1658-1666.
11. Jang, SM, Seo, HJ, Park, YS, Park, HI, Choi, JY. 2012. Design and electromagnetic field characteristic analysis of 1.5 kW small scale wind power generator for substitution of Nd-Fe-B to ferrite permanent magnet. *IEEE Transactions on Magnetics*; 48(11): 2933-2936.
12. Sun, T, Kwon, SO, Lee, JJ, Hong, JP. Investigation and Comparison of System Efficiency on the PMSM Considering Nd-Fe-B Magnet and Ferrite Magnet, INTELEC 2009-31st International Telecommunications Energy Conference, Incheon, Korea (South), 2009, pp 1-6.
13. Dorrell, DG, Hsieh, MF, Knight, AM. 2012. Alternative rotor designs for high performance brushless permanent magnet machines for hybrid electric vehicles. *IEEE Transactions on Magnetics*; 48(2): 835-838.
14. Fang, H, Wang, D. 2016. A novel design method of permanent magnet synchronous generator from perspective of permanent magnet material saving. *IEEE Transactions on Energy Conversion*; 32(1): 48-54.
15. Kowal, D, Sergeant, P, Dupre, L, Karmaker, H. 2015. Comparison of frequency and time-domain iron and magnet loss modeling including PWM harmonics in a PMSG for a wind energy application. *IEEE Transactions on Energy Conversion*; 30(2): 476-486.
16. Yamazaki, K, Fukushima, N. 2010. Iron loss model for rotating machines using direct eddy current analysis in electrical steel sheets. *IEEE Transactions Energy Conversion*; 25(3): 633-641.
17. Huang, WY, Bettayeb, A, Kaczmarek, R, Vannier, JC. 2010. Optimization of magnet segmentation for reduction of eddy-current losses in permanent magnet synchronous machine. *IEEE Transactions Energy Conversion*; 25(2): 381-387.
18. Ishikawa, T, Amada, S, Segawa, K, Kurita, N. 2017. Proposal of a radial-and axial-flux permanent-magnet synchronous generator. *IEEE Transactions on Magnetics*; 53(6): 1-4.
19. Kumar, RR, Singh, SK, Srivastava, RK, Saket, RK. 2020. Dynamic reluctance air gap modeling and experimental evaluation of electromagnetic characteristics of five-phase permanent magnet synchronous generator for wind power application. *Ain Shams Engineering Journal*; 11(2): 377-387.
20. Kumar, RR, Singh, SK, Srivastava RK. Thermal Modelling of Dual Stator Five-Phase Permanent Magnet Synchronous Generator, IEEE Transportation Electrification Conference (ITEC-India), Pune, India, 2017, pp 1-6.
21. Cano, L, Arribas, L, Cruz, I. 2004. 1.5 kW permanent magnets synchronous generator experimental bench test. *Department of Renewable Energie, CIEMAT*.



22. Advanced Energy, Permanent magnet generator performance testing, Report, January 23, 2014.
23. Standard IEC 60034-4. Rotating Electrical Machines. Part 4: Methods for Determining Synchronous Machine Quantities from Tests. Jun 1997
24. Zhao, W, Xu, L, Liu, G. 2018. Overview of permanent-magnet fault-tolerant machines: Topology and design. *CES Transactions on Electrical Machines and Systems*; 2(1): 51-64.
25. Wang, S, Sun, Y, Huang, Z, Mu, S. 2018. Analysis of stator internal phase-to-phase short circuit in the 12-phase synchronous generator with rectifier-load system. *IEEE Transactions on Energy Conversion*; 33(1): 299-311.
26. Song, X, Wang, Y, Liu, D, Wang, S, Liang, D. 2019. Short-circuit characteristics of a high temperature superconducting wind turbine generator employing a segmented armature winding. *IEEE Transactions on Applied Superconductivity*; 29(5): 1-5.
27. Afinowi, IAA, Zhu, ZQ, Guan, Y, Mipo, JC, Farah, P. 2016. Electromagnetic performance of stator slot permanent magnet machines with/without stator tooth-tips and having single/double layer windings. *IEEE Transactions on Magnetics*; 52(6): 1-10.
28. Choi, G, Jahns, TM. 2016. Reduction of eddy current losses in fractional-slot concentrated-winding synchronous PM machines. *IEEE Transactions on Magnetics*; 52(7): 1-4.
29. Li, D, Zou, T, Qu, R, Jiang, D. 2018. Analysis of fractional-slot concentrated winding PM vernier machines with regular open-slot stators. *IEEE Transactions on Industry Applications*; 54(2): 1320-1330.
30. Tong, W, Wu, S, An, Z, Zhang, H, Tang, R. Cooling System Design and Thermal Analysis of Multibrid Permanent Magnet Wind Generator, 2010 International Conference on Electrical and Control Engineering, Wuhan, China, 2010, pp 3499–3502.
31. Gulbahce, MO, Kocabas, DA, Nayman, F. Investigation of The Effect of Pole Shape on Braking Torque for a Low Power Eddy Current Brake by Finite Elements Method, 2013 8th International Conference on Electrical and Electronics Engineering (ELECO), Bursa, Turkey, 2013, pp 263-267.
32. Gulbahce, MO, Kocabas, DA, Habir, I. Finite Elements Analysis of a Small Power Eddy Current Brake, proceedings of 15th International Conference MECHATRONIKA, Prague, Czech Republic, 2012.

# Regenerative Braking of Hub Type Brushless Direct Current Machine Used on Electric Bicycle

Alper Kağan Candan<sup>1\*</sup> , Hayati Mamur<sup>1</sup> 

<sup>1</sup>Manisa Celal Bayar University, Faculty of Engineering, Department of Electrical and Electronics Engineering, 45140, Manisa, Turkey

\*[kagan.candan@cbu.edu.tr](mailto:kagan.candan@cbu.edu.tr)

\*Orcid: 0000-0003-0320-7317

Received: 18 February 2021

Accepted: 6 December 2021

DOI: 10.18466/cbayarfbe.866972

---

## Abstract

Electric motors are more efficient than internal combustion engines. This puts forward electric vehicles more popular than fossil fuel vehicles. However, electric vehicles have limited range because of insufficient batteries. For this reason, studies focus on increasing the range of electric vehicles. Regenerative braking is a solution that helps this problem. In this study, a new regenerative braking modeling was recommended and applied on a brushless direct current machine (BLDC) of electric bicycle. Energy recovery is attained at the different speeds by means of the recommended model. The modeling results were compared with the application results and they verified each other. The analyses have showed that gain and efficiency which attain from the regenerative braking increased at higher speeds of hub type BLDC. Ultimately, the energy recovery of 6.37% was saved by means of the regenerative braking of the hub type BLDC used on electric bicycle at 320 RPM.

**Keywords:** Electric bicycle, electric vehicle, energy saving, hub BLDC, regenerative braking

---

## 1. Introduction

Today, the main energy sources are fossil fuels for vehicles [1]. Due to oil crisis, their environmental pollutions and exhaustible characteristics, fossil fuels are desired to replace with alternative energy sources [2]. In this way, countries will also be able to reduce their dependence on oil [3]. These developments will make electric vehicles a popular subject with the addition of new studies in this field.

Electric vehicles have several advantages such as low emission, high efficiency and silent operation [4]. However, their limited range of battery systems prevents to become more common [5]. Internal combustion engines (ICEs) are used to move in traditional fossil fuel vehicles, but electric vehicles utilize electric motor for moving [6]. This makes possible regenerative braking which is impossible in ICE's [7].

Regenerative braking is a system that helps increasing the range of electric vehicles [8]. Braking is made with friction by the mechanical way in traditional vehicles. Brake pads rub on rotating disc when the speed

deceleration is wanted. Meanwhile, the kinetic energy of rotating wheels converts into heat energy and dissipate environment [3, 9]. The regenerative braking system (RBS) allows the energy save while stopping the electric vehicle. Electric machine in the electric vehicle starts working as a generator when the braking command is taken. Energy flow occurs into battery and this energy is stored [10]. Thus, system efficiency is increased besides the range of electric vehicle. Amplitude of back electromotive force (EMF) generated during regenerative braking changes with motor rotation speed. Therefore, the generated voltage should be boosted at low speeds for storing energy to the battery [11, 12]. This situation can be solved with a boost converter.

Regenerative braking is an effective method in deceleration and generation of energy, but it is not proper to use alone as brake. Therefore, it should be used with mechanical braking. Because RBS is not effective at low speeds and it may not stop the vehicle during an electric fault [13].

When the literature is examined, some studies related to regenerative braking are seen. These studies generally

mention about the energy attain from regenerative braking. There was a study about the braking torque which aim and succeed increasing efficiency [1]. But there was an additional braking system in this study. In another study, several switching methods were applied to a brushless direct current machine (BLDC) and stopping time and gained energy were researched. However, that was only done for two speed values [6]. A study investigated the current that flows into battery during regenerative braking. The current flowing into battery was measured for nine different speeds and an inference was made about the regeneration current and speed [2]. However, the obtained voltage during regenerative braking was increased with different method instead of an external boost converter. There was also a research that increased the regenerative braking voltage with an external boost converter. Consumed and recycled energy were measured for five different speeds. But that research was not done with a hub BLDC machine [9].

In this study consist of RBS modeling and application for a hub type BLDC machine which using on electric bicycle. A new model realized in MATLAB/Simulink has been verified with a real implementation setup. The obtained voltage during regenerative braking increased with an external boost converter. By means of this study, how much energy save was realized was determined as percentage for certain speed and certain motor working period when regenerative braking is executed on the hub type BLDC machine. The energy recovery that obtained from the regenerative braking was clearly observed at different speeds. A considerable amount of energy recovery was achieved.

In the first part of this study, a general subject introduction is indicated. After mentioning the used materials in the second part, how simulation and experiment studies were done are explained in the third part in detail. In forth part, the findings and interpretation are presented about the experiment and application results. Inferences from the study are specified in the fifth part.

## 2. Materials

### 2.1. Brushless Direct Current (BLDC) Machine

One of the most important parts of electric bicycle and other electric vehicles is the electric machine that provides movement. BLDC machines are the most used machines in electrical vehicles [14]. Especially, the hub type BLDC machine is the most preferred one [3]. The hub type BLDC machines consists many poles in the stator [15]. Therefore, they can generate higher torque values. This machine has some advantages such as high efficiency, noiseless operation, low maintenance and long operation life [11]. In BLDCs, electronic commutation is applied via driver [16, 17]. The location of rotor can be obtained by means of hall effect sensors.

Three hall effect sensors are enough in three phase BLDC machines. Switching equipment is triggered after sensors signal is processed according to the angle value [18].

### 2.2. BLDC Driver

Switching is done with the help of driver. There are totally six semiconductor switching equipment's in three phase BLDC machine and each phase take two of them [10]. The basic equivalent circuit of BLDC driver is presented in Figure 1.

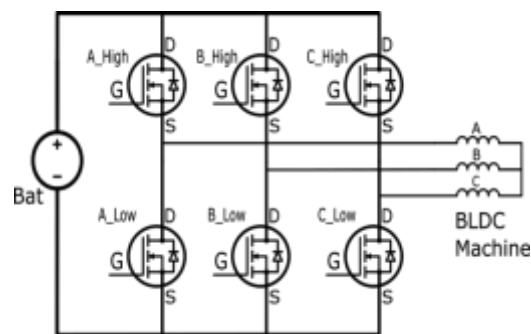


Figure 1. BLDC driver basic equivalent circuit.

There are six switching conditions according to signals that obtained from hall sensors in BLDCs. Triggered switching equipment's according to the hall sensors are given in Table 1.

Table 1. Triggered switching equipment according to the hall sensors.

	Hall Sensor Signals			Switching Equipment		
	A	B	C	A	B	C
1	1	0	1	High	Low	
2	1	0	0		Low	High
3	1	1	0	Low		High
4	0	1	0	Low	High	
5	0	1	1		High	Low
6	0	0	1	High	Low	

### 2.3. Boost Converter

The generated voltage which attained from the hub type BLDC machine during regenerative braking is not higher than the battery voltage for charging. A boost converter is required to do that illustrated in Figure 2.

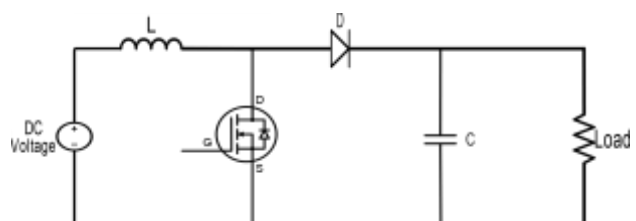
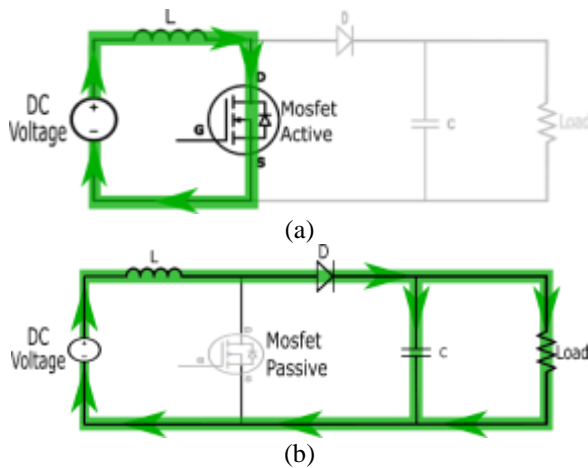


Figure 2. Boost converter basic equivalent circuit.

### 3. Method

In this section, a simulation and application of RBS applied to a hub type BLDC machine used on electric bicycles is presented. The hub type BLDC machine was worked as a motor for 12 seconds. At the end of this period, it was stopped with RBS. Gained energy from RBS and consumed energy of system were measured and how much recycling were been achieved was calculated as percentage.



**Figure 3.** switching Equipment (a) turned on (b) turned off situation.

#### 3.1. Simulation

The simulation studies were carried out in MATLAB/Simulink. A system overview is illustrated in Figure 4.

In simulation modeling, a “Permanent Magnet Synchronous Machine” block was chosen as a component that provide movement. Phase number was adjusted three. Back EMF shape was selected trapezoidal. Torque was chosen as the mechanical input. Stator phase resistance was chosen  $0.01 \Omega$ , stator phase inductance was chosen  $250 \mu\text{H}$ , inertia was  $0.1344 \text{ kg}\times\text{m}^2$ , viscous damping was  $0.084 \text{ N} \times \text{m} \times \text{s}$ , pole pairs was 23, static friction and initial condition was zero.  $120^\circ$  was entered for Back EMF flat area. Flux leakage generated by magnets was selected as machine constant and  $0.023354$  was entered.

The hub type BLDC machine works as a generator for 12 seconds in simulation. Energy was provided by battery. Battery type was selected lead-acid and adjusted 36 V. Energy which provided to the hub type BLDC

machine is cut out at the end of period via switches that located output of driver. Simultaneously, the switches which located input of the boost converter are closed. Meanwhile, the hub type BLDC machine which continues rotate work as a generator and induce voltage in the coil terminals. Induced voltage is increased to higher level than battery via boost converter. Thus, current is occurred from the hub type BLDC machine into the battery and energy is stored in battery. Battery acts like a load during regenerative braking. Therefore, rotation ends quickly.

#### 3.2. Application

Test bench was set up around of the hub type BLDC machine that is used in electric vehicles. The hub type BLDC machine starts operating as a motor for 12 seconds with start command. Energy flows to the hub type BLDC machine from battery via driver circuit during this period. Relays in relay board replace the contacts to another position after 12 seconds is expired. Thus, connection between driver and the hub type BLDC machine is cut out. The hub type BLDC machine is connected to three phase rectifier. Voltage is induced on the coils of the hub type BLDC which continues rotation and energy is generated at the same time. Generated energy is stored after it is directed into three phase rectifier and boost converter. The open circuit scheme of system designed for application is presented in Figure 5.

Three phases hub type BLDC machine was used during application. The system setup is shown in Figure 6. Eight cables were used of the hub type BLDC machine. Three of them were thicker than other five and those were phases cables. Three of five were reserved for sensors that determine rotor position. The remaining two cables were used to energies sensors and they were supplied with 5 V. The signals which were come from sensors were processed with STM32F07VG electronic board. The STM32F407VG electronic board gives outputs according to the written code. Those outputs provided movement of the hub type BLDC machine.

Energy was supplied to system by batteries. Batteries were selected lead-acid type. System control was realized with the STM32F407VG control board. That electronic card was coded with own library in MATLAB/Simulink. Real time data can be sent from board to computer by means of UART module.

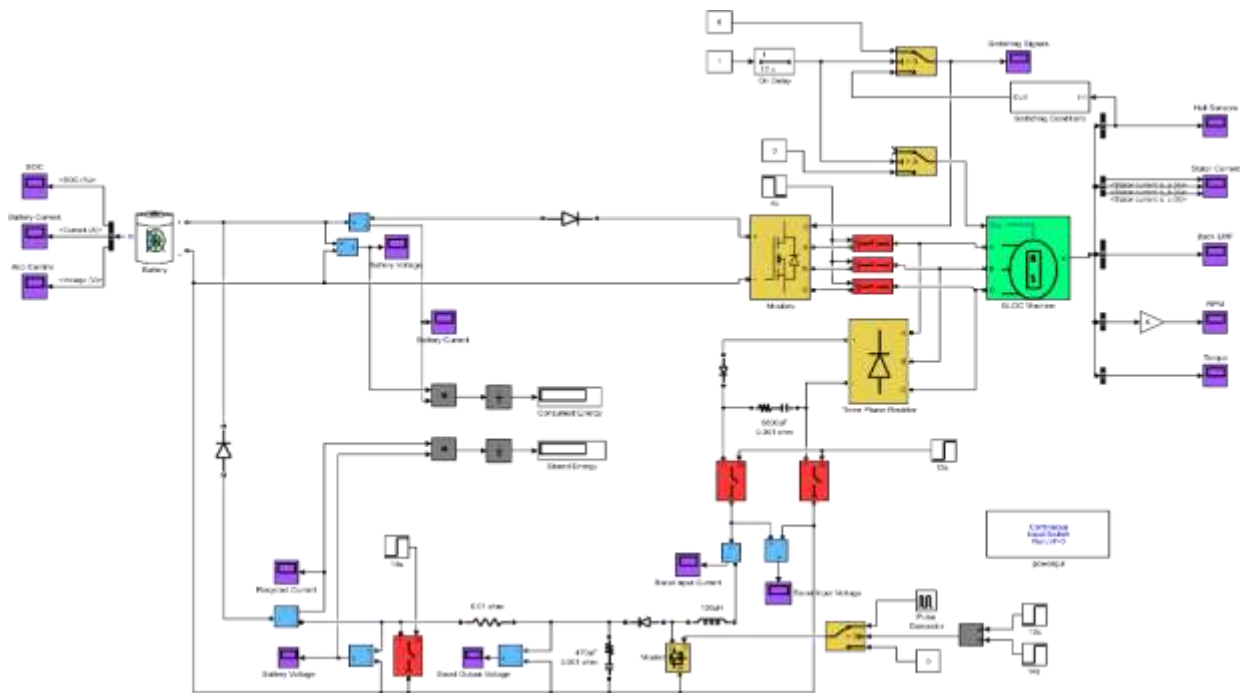


**Figure 4.** System overview.

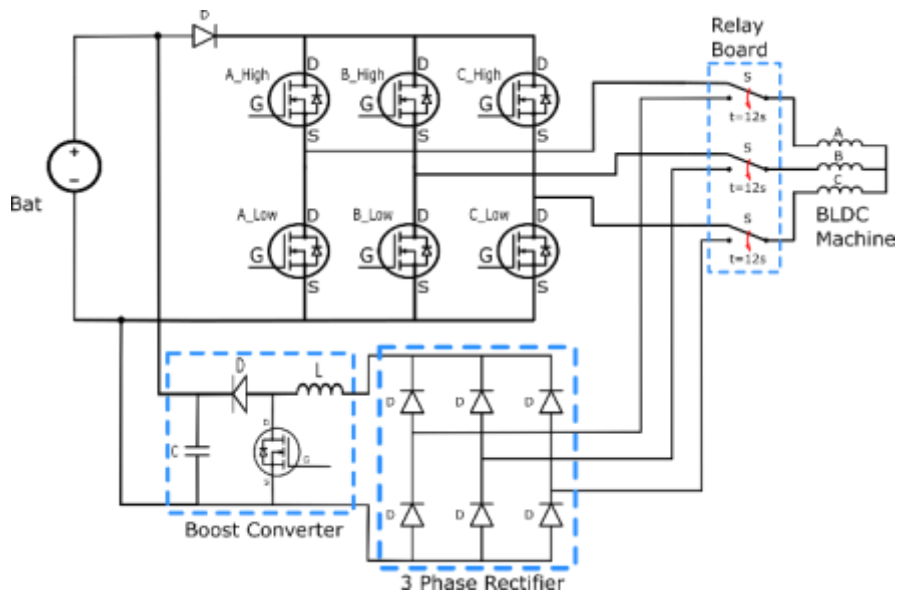


**Figure 5.** Designed system scheme.

The STM32F407VG control board sent required data's to driver circuit for movement of the hub type BLDC machine. Semiconductor switching equipment's were turned on in accordance with signals which transmitted driver circuit. The hub type BLDC machine coils was energized via semiconductor switching equipment with the signals that implemented to driver circuit and then movement was begun.

The V connector in the driver circuit shown in Figure 6 is input of energy that to be transferred from battery to

motor. A, B and C terminals were connected to the hub type BLDC machine phases. IR2104 D1-D3 elements were half bridge motor drivers. OC1-OC6 symbolized opto-couplers and 6N137 was selected as opto-coupler. The control board sent data's to IR2104s via opto-couplers to rotate motor. Terminal 1 was used to supply energy for IR2104s. They were supplied with 12V. Terminal 2 was used to energies for opto-couplers. 5V was given to the terminal.

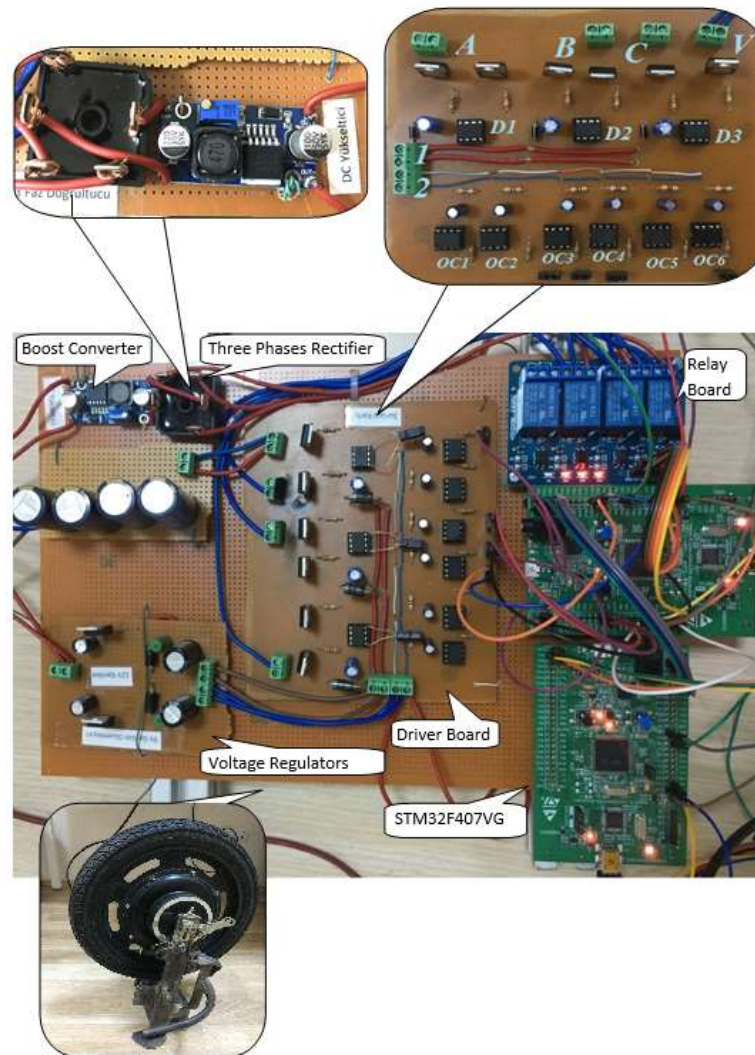


**Figure 6.** The system setup.

75NF75 mosfets were used as a semiconductor switching equipment in driver. IR2104 half bridge motor drivers were preferred to turn on mosfets. VCC pin in IR2104 was supplied by terminal 1. The capacitor that was connected between VB and VS was necessary for turning on high side mosfet. Their values were  $47 \mu\text{F}$  50 V. The diode that was connected between VCC and VB prevented the reverse current which could be occurred from the capacitor. The diode code was SB560. VS connector of IR2104 was connected one of the motor phases in other words one of A, B or C terminals. HO and LO connectors of IR2104 were used to turn on the high and low side mosfets. Both IN and SD inputs needed to be logic 1 to activate HO. IN logic 0 and SD logic 1 needed to be implemented to activate LO.

Driver board and control board were connected via 6N137 opto-couplers to protect driver for the reason of any short circuit or fault situations. Therefore, totally six

opto-couplers were used for each one of inputs (IN and SD) of the driver. Dual opto-couplers were available in the markets but they had higher propagation delay time. There were also opto-couplers which have slower propagation delay time but they were more expensive than two 6N137. Due to their advantages, 6N137 was selected for using on driver. 6N137 opto-couplers propagation delay time were at the level of nanoseconds. They turned off when their input logic 1 otherwise they turned on.

Pin 8's and pin 5's of opto-couplers were supplied by terminal 2 of driver circuit.  $R_L = 300 \Omega$  and  $R_M = 75 \Omega$  were selected for opto-couplers. Bypass capacitors values were selected  $0.1 \mu\text{F}$  50 V. Pin 2's and pin 3's connected to control board. Pin 6's were connected IN or SD input of IR2104's. Pin 7 signal was conveyed to pin 6 according to the input signal of 6N137. Due to supplied voltage levels of pin 8's of 6N137's and inputs

(IN and SD) of IR2104's were same, pin 8's and pin 7's of 6N137's were short circuit.

All the system was energized with batteries, but all equipment's could not be supplied with the same voltage level. There should be different voltage levels in system for the hub type BLDC machine, opto-couplers, half bridge drivers and sensors. Therefore, some equipment's should be supplied via voltage regulators. There were two voltage regulators, 5V and 12V, in the system. LM2576HVT-5.0 P+ and LM2576HVT-12 P+ components were used to obtain 5V and 12V.

#### 4. Results & Discussion

##### 4.1. Simulation Results

The simulation study of RBS for the hub type BLDC used on electric bicycle was carried out for 16 seconds in MATLAB/Simulink. The hub type BLDC machine was worked as a motor during 12 seconds. Regenerative braking was executed after 12 seconds. Simulation system did not contain any other braking mechanism except RBS. Thanks to this simulation study, it was possible to monitor certain parameters such as battery and BLDC parameters.

First, the stopping effect of RBS was desired to observe. The hub type BLDC machine back EMF's are illustrated in Figure 7. Figure 7a shows the back EMF's when the RBS is passive and Figure 7b shows the back EMF's when the RBS is active.

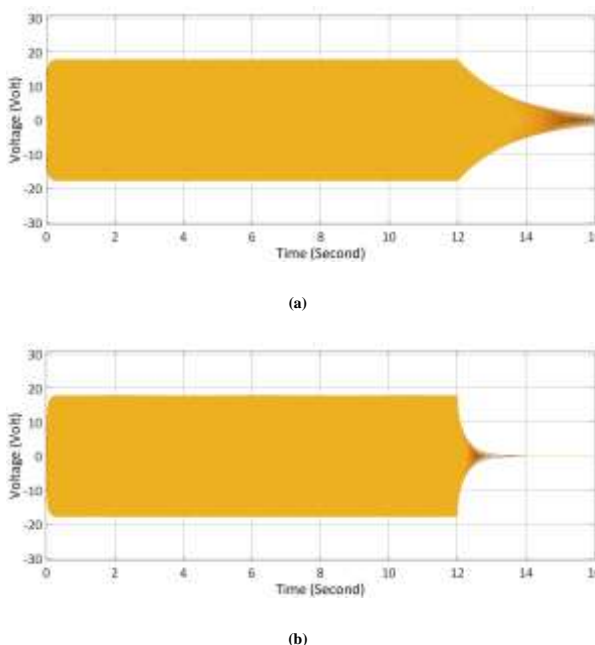


**Figure 7.** Back EMF's for RBS is a) passive b) active.

Back EMF occurred as long as the hub type BLDC machine rotates. So, it means that BLDC was stopped when the back EMF was damped. Figure 7a shows that BLDC stops after a slowdown that takes a few seconds.

If the Figure 7b is analyzed, the graphic drops sharply at 12th second and BLDC stops before one second is up.

The second observed situation was the energy recycling. When the charge status of the battery used in the system was examined, it was seen clearly whether there was energy recycling or not. The state of charge (SOC) of the battery is presented in Figure 8.

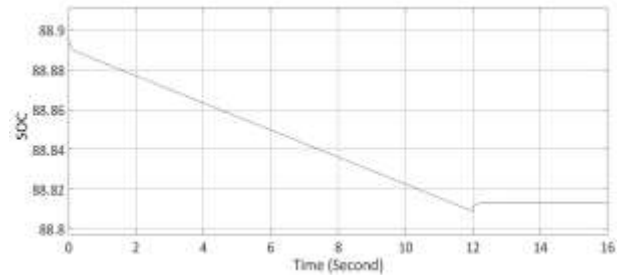


**Figure 8.** The state of charge of the battery.

At the beginning of system working lots of energy was taken from battery. Due to starting current of electric motors was high that was not an abnormal situation. After the starting, the SOC of battery decreased linearly until 12th second. That means the hub type BLDC machine rotated at a constant speed. The battery was stored energy for a short period after 12 seconds. That short period shows that the occurred regenerative braking. If the graphic is examined carefully, most of the energy stored during regenerative braking is made in the first moments of regenerative braking. After a short time, the increase ended and the SOC remained constant level. This means that regenerative braking was over. After this moment, there was no change in the SOC. This indicated that the hub type BLDC machine was stopped.

##### 4.2. Application Results

The hub type BLDC machine used in electric vehicle was run as a motor for 12 seconds in this application. End of this period, the signal was sent to relays and them was changed contact position and regenerative braking was applied. BLDC machine was idle while it was working as a motor. Battery current and voltage values were measured to calculate consumed and stored energy. The experiments were repeated at different speeds.

Current-time graph of battery is given according to BLDC speeds in Figure 9(a)-(h). Figure 9a-d is obtained under conditions where three identical batteries were used in system. Figure 9e-h presented graphs of the situations which the system was supplied by two identical batteries. In Figure 9a, starting current of motor was nearly 7 A. BLDC need 600 mA in idle working situation. Regenerative braking was implemented after 12 seconds from motor starting. The



current which was transferred to battery was measured approximately 1 A during regenerative braking. When Figure 9b was analyzed, the starting current of motor was seen higher than 1 A and regenerative braking current was 900 mA. Figure 9c showed that idle current supplied from batteries was upper than 300 mA. The current obtained by means of regenerative braking was 100 mA at the end of 12th seconds. Figure 9d which motor speed was 109 RPM indicate that BLDC extracted 250 mA from battery. The saved current was about 50 mA during regenerative braking. In Figure 9e, starting value of current was roughly 12 A, idle current was 500 mA and regenerative braking current was 800 mA. When Figure 9f was examined, the hub type BLDC saved 1.8 A at the start. Batteries provided 400 mA in the idle working. Current was measured 200 mA after 12 seconds. There was no current at the negative side in Figure 9g and Figure 9h. This means that the system could not save energy to the batteries at the speeds of 84 and 45 RPM.

This study included the simulation and application of regenerative braking in the hub type BLDC machine used on electric vehicle. The hub type BLDC machine was operated as a motor for 12 seconds. It rotated at 317 RPM. The system was supplied by 36V lead-acid battery. At the end of 12 seconds, the energy flowed to the motor was cut off with the help of switches and regenerative braking was applied. The energy obtained from the regenerative braking was stored in the battery via increasing the voltage level with the help of a boost converter.

The hub type BLDC used on electric bicycle was operated as an idle motor for 12 seconds in application. The values of 320, 237, 160, 109 RPM were achieved by means of changing PWM signals which trigger driver. Meantime, the system was supplied by the three identical 12 V lead-acid battery connected in series. The system also was supplied by two identical 12 V lead-acid battery connected in series. Meantime, the tests were done with the values of 212, 142, 84 and 45 RPM. At the end of 12 seconds, regenerative braking was applied to the hub type BLDC with the help of the relay contacts changing position. The obtained energy was

stored in the battery group by means of a rectifier and boost converter.

In the simulation study, the regenerative braking was applied to the hub type BLDC machine that rotated for 12 seconds at 317 RPM and 6.21% energy recovery was achieved. In the application, the regenerative braking was applied to the hub type BLDC machine rotating for 12 seconds at 320 RPM speed and 6.37% energy recovery was achieved. MATLAB/Simulink simulation has been verified to compatible with real system setup.

## 5. Conclusion

In this study, a simulation study was performed in MATLAB/Simulink for regenerative braking of a hub type BLDC used on electric bicycle. Its results were confirmed by an application setup. The consumed and saved energy were calculated by means of measuring current and voltage of battery in this simulation. The hub type BLDC has been rotated at 317 RPM for 12 seconds and energy recovery of 6.21% was achieved when applying the regenerative braking on the hub type BLDC. A stopping effect occurred by regenerative braking was seen clearly at BLDC machine. During the application studies, the battery current and voltage values were measured to calculate the recycled energy values. The application was carried out for different speed values. It was observed that the current drawn from the battery increased as the speed of the BLDC increased. It was also determined that the current generated by the regenerative braking decreased as the speed value decreased. The recycling rates were calculated with the measured currents and voltages. These were 6.37% at 320 RPM, 5.15% at 237 RPM, 0.57% at 160 RPM, 0.19% at 109 RPM, 3.3 % at 212 RPM and 1.34% at 142 RPM. It was noted that the recycling rates were 0% at 84 and 45 RPM since no current flowed to the battery. According to these data, the rate of recycling decreased when the BLDC speed decreased. Finally, the study showed that the regenerative braking of the hub type BLDC used on electric bicycle was a system that could be used more effectively at high-speed applications.

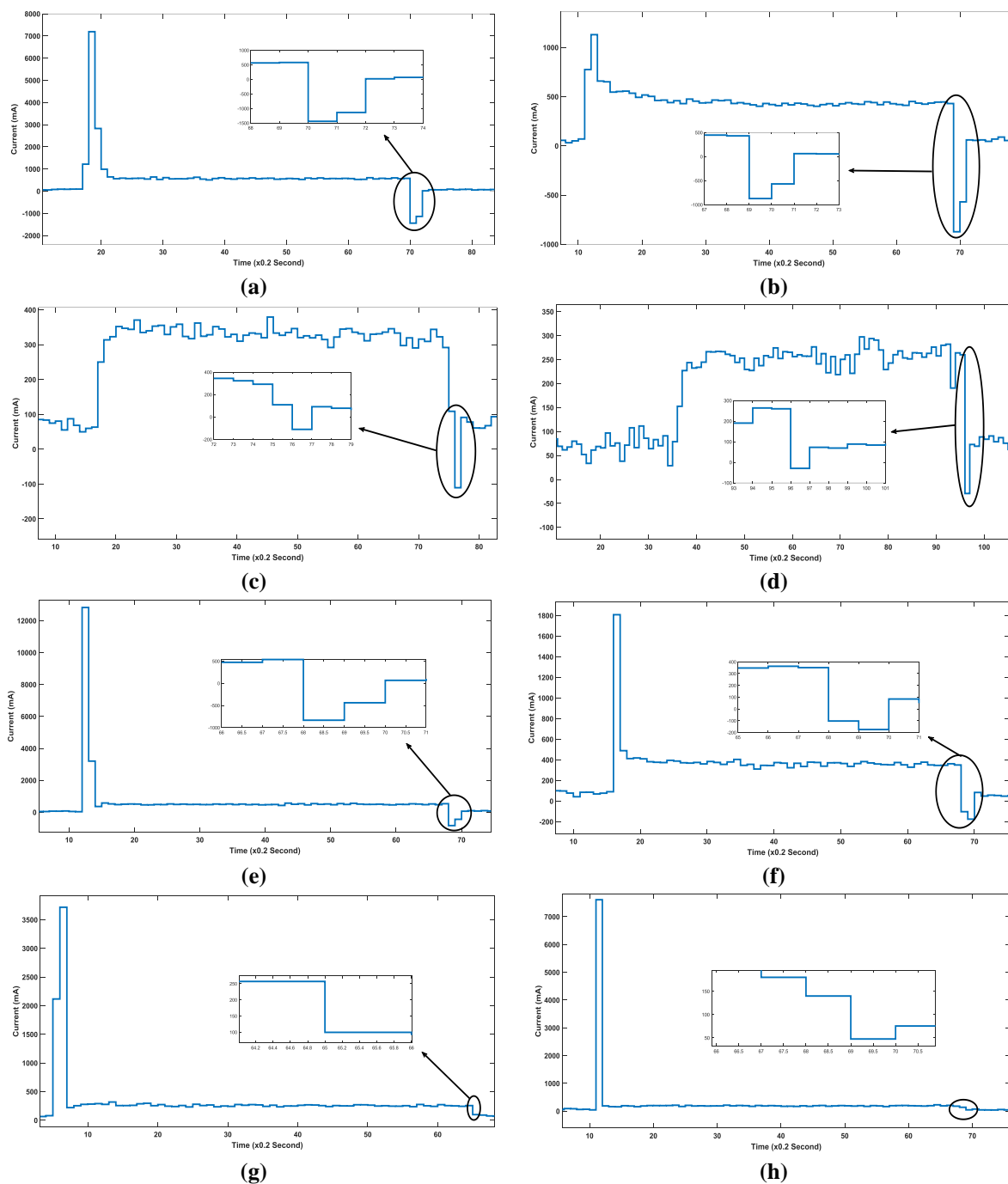


**Figure 9.** Current-time graphs at the value of (a) 320, (b) 237, (c) 160, (d) 109, (e) 212, (f) 142, (g) 84 and (h) 45 RPM.

### Acknowledgement

This work was supported by Research Project Coordination Unit of The Manisa Celal Bayar University (Project Number: 2019-003).

### Author Contributions

Alper Kağan CANDAN: Drafted and wrote the manuscript, performed the experiment and result analysis.

Hayati MAMUR: Assisted in analytical analysis on the structure, supervised the experiment's progress, result interpretation and helped in manuscript preparation.

### Ethics

There are no ethical issues after the publication of this manuscript.

## References

1. Long, B., Lim, S. T., Ryu, J. H., Chong, K. T. (2014). Energy-regenerative braking control of electric vehicles using three-phase brushless direct-current motors. *Energies*, 7(1), 99-114.
2. Hua, C. C., Kao, S. J., Fang, Y. H. (2013, November). Design and implementation of a regenerative braking system for electric bicycles with a DSP controller. In 2013 1st International Future Energy Electronics Conference (IFEEEC) (pp. 641-645). IEEE.
3. Yang, M. J., Zhou, H. L., Ma, B. Y., Shyu, K. K. (2009). A cost-effective method of electric brake with energy regeneration for electric vehicles. *IEEE Transactions on Industrial Electronics*, 56(6), 2203-2212.
4. Naseri, F., Farjah, E., Ghanbari, T. (2016). An efficient regenerative braking system based on battery/supercapacitor for electric, hybrid, and plug-in hybrid electric vehicles with BLDC motor. *IEEE Transactions on Vehicular Technology*, 66(5), 3724-3738.
5. Pan, C., Chen, L., Chen, L., Jiang, H., Li, Z., Wang, S. (2016). Research on motor rotational speed measurement in regenerative braking system of electric vehicle. *Mechanical Systems and Signal Processing*, 66, 829-839.
6. Godfrey, A. J., Sankaranarayanan, V. (2018). A new electric braking system with energy regeneration for a BLDC motor driven electric vehicle. *Engineering Science and Technology, an International Journal*, 21(4), 704-713.
7. Nian, X., Peng, F., Zhang, H. (2014). Regenerative braking system of electric vehicle driven by brushless DC motor. *IEEE Transactions on Industrial Electronics*, 61(10), 5798-5808.
8. Guo, J., Wang, J., Cao, B. (2009, June). Regenerative braking strategy for electric vehicles. In 2009 IEEE Intelligent Vehicles Symposium (pp. 864-868). IEEE.
9. Nashit, S., Adhikari, S., Farhan, S., Avinash, S., Gambhire, A. (2016). Design, fabrication and testing of regenerative braking test rig for BLDC motor. *International Research Journal of Engineering and Technology*, 3(05), 1881-1884.
10. Sindhuja, V., Ranjitham, G. (2014). Regenerative Braking System of Electric Vehicle Driven By BLDC Motor Using Neuro Fuzzy and PID. *International Journal of Innovative Research in Science, Engineering and Technology*, 3(12), 17847-17854.
11. Kivanc, O. C., Ustun, O., Tosun, G., Tuncay, R. N. (2016, October). On regenerative braking capability of BLDC motor. In IECON 2016-42nd Annual Conference of the IEEE Industrial Electronics Society (pp. 1710-1715). IEEE.
12. Bobba, P. B., Rajagopal, K. R. (2010, December). Compact regenerative braking scheme for a PM BLDC motor driven electric two-wheeler. In 2010 Joint International Conference on Power Electronics, Drives and Energy Systems & 2010 Power India (pp. 1-5). IEEE.
13. Cody, J., Göl, Ö., Nedic, Z., Nafalski, A., Mohtar, A. (2009). Regenerative braking in an electric vehicle (Doctoral dissertation, Branzowy Ośrodek Badawczo-Rozwojowy Maszyn Elektrycznych "Komet").
14. Geraee, S., Mohammadbagherpoor, H., Shafiei, M., Valizadeh, M., Montazeri, F., Feyzi, M. R. (2018). Regenerative braking of electric vehicle using a modified direct torque control and adaptive control theory. *Computers & Electrical Engineering*, 69, 85-97.
15. Elavarasi, R., SenthilKumar, P. K. (2014). An FPGA based regenerative braking system of electric vehicle driven by BLDC motor. *Indian Journal of Science and Technology*, 7(S7), 1-5.
16. Wu, H. X., Cheng, S. K., Cui, S. M. (2005). A controller of brushless DC motor for electric vehicle. *IEEE Transactions on Magnetics*, 41(1), 509-513.
17. Rakesh, M., Narasimham, P. V. R. L. (2012). Different braking techniques employed to a brushless DC motor drive used in locomotives. *International Electrical Engineering Journal*, 3(2), 784-790.
18. Karabacak, Y., Uysal, A. (2017, September). Fuzzy logic controlled brushless direct current motor drive design and application for regenerative braking. In 2017 International Artificial Intelligence and Data Processing Symposium (IDAP) (pp. 1-7). IEEE.
19. Mamur, H., Çoban, Y. (2020). Detailed modeling of a thermoelectric generator for maximum power point tracking. *Turkish Journal of Electrical Engineering & Computer Sciences*, 28, 124-139.





# AES Encrypted Real-Time Video Stream and Image Transmission from ESP32-CAM

Pınar Savaştürk<sup>1</sup> , Ömer Aydın<sup>2\*</sup> , Gökhan Dalkılıç<sup>3</sup> 

<sup>1</sup>Gebze Technical University, Faculty of Engineering, Computer Engineering, Kocaeli, Turkey

<sup>2</sup>Manisa Celal Bayar University, Faculty of Engineering, Electrical and Electronics Engineering, Manisa, Turkey

<sup>3</sup>Dokuz Eylul University, Faculty of Engineering, Computer Engineering, İzmir Turkey

\*[omer.aydin@deu.edu.tr](mailto:omer.aydin@deu.edu.tr)

\*Orcid: 0000-0002-7137-4881

Received: 04.12.2020

Accepted: 7 November 2021

DOI: 10.18466/cbayarfbe.835945

## Abstract

With the development of the technology, the demand for security has increased. Security comes to the forefront due to the increase in data produced and transmitted in real time. In this study, improvements in the security of video data transmitted in real time are proposed. Data encrypted with advanced encryption standard (AES) was transferred to the local server from the ESP32-Cam module. The encrypted data transferred was decrypted on the local server, so the user was able to access the video. In this way, the security level of the data transmitted live between the parties has been increased. Our motivation in this study is that the number of applications proposed on real-time systems is not too much.

**Keywords:** Arduino, AES, ESP32-CAM, encrypted image transmission, Nodejs, secure video transmission, security

## 1. Introduction

Along with the new technologies developed, the security of the systems installed with these technologies has also gained great importance. Security is critical, especially in systems with the live and continuous data flow. For example, systems with real-time data flow, such as images and videos, have gained importance. Therefore, a security layer has been added to increase security in the transfer of video and image data in this study. The security layer was realized on the ESP32-CAM module and the Web Server.

The main purpose of this study is to ensure that the video and image data transmitted between the parties over the wireless network are confidential. Two basic approaches were emphasized to create confidentiality.

The first approach is to send the image and video data from the ESP32-CAM module by shifting. In this way, attackers who want to receive data flowing on the Wi-Fi network can only access modified, pointless and unformed data. In this method, the transmitted data can be made to an extent incomprehensible. The Web Server, which receives shifted data, on the contrary, accesses the original data received by the camera when

it performs the inverse shift operation. This way, the Web Server can process incoming data on localhost.

In the second approach, data sent from the camera module are encrypted with an encryption algorithm such as advanced encryption standard (AES). Then, encrypted data is sent to the other party. Received data is decrypted on the Web Server and processed on localhost. In this way, the data flowing through the ESP32-CAM become more incomprehensible than shifting. In this process, it is necessary to make sure that the webserver decrypts the encrypted data in accordance with the encryption method on the camera module.

In both of these approaches, the security of the data has been increased by the possibility to re-create the original image or video, because the algorithms used are lossless.

## 2. Related Works

Secure elements were used to secure four-quarter IoT device architecture, in a study presented by Urien [1]. This architecture includes a radio system on chip (SoC), a secure element that processes transport layer security (TLS) packets and acts as an identity module, a

sensor/actuator and a general-purpose unit (GPU). The system they recommend is a low cost, low energy and safe. This system can be developed in the future using the block chain structure. This is a structure that is not in the current architecture. It will offer the possibility to be used in a public blockchain structure.

One of the structures that offers high security [2] uses a separate architecture. According to this structure, TLS server running in a secure element is used to make the established communication channels safer on a wireless network. Matters such as mutual communication security and correctness are examined more carefully with this structure. Besides, since transmission control protocol (TCP), which is one of the layered structure protocols, is used, the whole system is gathered under a standard. In this way, the common channels of the system are fully communicated. One point that can be added to this structure is that it can be included in this structure is the live video stream. In this way, an important chain link may have been added to the system.

With the platform of developing IoT devices, the security part has become more and more important. Communication protocols, which are part of this whole [3], are of great importance. A structure, which contains the message queuing telemetry transport (MQTT) protocol, has been modelled and implemented to provide security with special encryption structures. A situation similar to the sender-receiver structure has been revealed. With this structure, which is defined as secure MQTT (SMQTT), the approach that security can be increased to higher levels has been revealed. Also, if this structure can be applied to live stream data, performance analysis can be made, and the architecture can be tested on different scenarios.

Yerlikaya and Dalkılıç [4] proposed the authentication and authorization mechanism in their study. Their scheme uses HMAC-based one-time password (HOTP) for device authentication addition to the open authorization (OAuth 2.0) protocol [5, 6].

Aydın and Erhan proposed a study of secure communication for ESP-Eye. This study presented a method of security for the camera, wireless communication module and face recognition. A comprehensive solution was not presented in this study [7].

A model containing protocol bases has been introduced in the structure [8] established to ensure secure video transmission. This mechanism provided remarkably useful results. In addition, the performance results obtained for the transmission of video packages reveal the efficiency of the study. If this mechanism can be provided with less costly modules, it will find more usage and application areas in practice. Video transfer on the DJI Tello drone and analysis of the images obtained

with structures such as optical character recognition (OCR), single shot multibox detector (SSD) have revealed remarkable results [9]. According to these results, the images obtained are analyzed and meaningful structures are revealed. In addition, presenting and expressing the obtained structures in a meaningful way increase the importance of the study. It is very critical to receive, process and present the following image for the drones, which are remote control devices. These goals were successfully implemented in the study. In addition, if the security mechanism were added to the parts of the entire model, the transmitted images was secured.

In the literature, there are many studies on the encoding and transmission of pictures and moving picture experts' group (MPEG) videos [10-12, 14-16, 18]. It is also presented in various security and privacy related applications that are used and will work in such applications [13, 17, 19, 20].

### 3. Video or Image Transmission

Video transmission and display process on most systems are very important. In this study, it is aimed to make a secure video or image transfer system. To achieve this goal, the image must first be taken by ESP32-CAM module. This module acts as a data provider. The feature has been installed when customizing the module for this usage. To display the image taken from the module, it joined to a common network.

When the ESP32-CAM module is connected to a common network, it provides an Internet protocol (IP) address to broadcast. This network is a common network, including the Web Server. Within the scope of this study, the ESP32-CAM module and the desktop computer where the Web Server is installed are connected to the same access point. The user that we assume as an observer, connects to an access point via his/her computer. This access point is the same device that the ESP32-CAM and Web Server Provider Device connects to. In this way, both the observer and the camera module are connected to the same network. Once this partnership is achieved, the logs are observed in the web browser with the IP address provided by the ESP32-CAM. During this development, the necessary implementations for the ESP32-CAM module were made by Arduino IDE 1.8.12 version and Web Server was made by NodeJS with 10.16.3 version. A special-purpose library was used to show live streaming data while making the necessary improvements.

### 4. Shifted Data Transfer and Render

A model for sending the data by shifting is detailed as the first approach in the subsections. This model is vulnerable. The shifted data is sent, and the original data is obtained by a reverse process on the receiver side.

#### 4.1 ESP32-CAM Module Side

The libraries used when developing the ESP32-CAM module are as follows: "esp\_camera.h", "WiFi.h", "ArduinoWebSockets.h" and "camera\_pins.h". The camera model of the module has been chosen as CAMERA\_MODEL\_AI\_THINKER. The service set identifier (SSID) and the password of the modem to which the camera module is connected are set by default in the Arduino code development. To send data from the module to the Web Server, the host and port number of the Websocket have been determined. The IP address to host the Websocket has been provided. While determining this IP address, "ipconfig" command was run on the device that is running a Web Server (this device is a Windows 10 desktop). The "IPv4 address" obtained as a result of executing "ipconfig" command is the address that hosts the Websocket. The specified Websocket server port number in the Arduino code is 8888. Subsequently, the client object for the Websocket is created in "WebSocket Client" type.

After necessary configuration settings and parameters are set for the camera module, a successful connection of the module to the web server is ensured. Subsequently, the websocket server host address (IPv4 address) and the specified websocket server port provide a connection to the websocket client. After the connection is successful, the camera is ready to send data to the server.

At this point, modifications of the data are required for shifting data transmission. The data type received from the camera module is in a special struct like "camera\_fb\_t". The "buf" parameter of this struct corresponds to the pixel data received from the camera. The raw form of the data taken from the camera is in "char" pointer type.

When a 32-bit left shift operation is applied to this data, the payload (i.e. real-time streaming data) coming from the camera becomes incomprehensible. After the shift operation, the client is in binary type; the shifted payload and the size of this payload are sent.

#### 4.2 Web Server Side

The Web Server side was developed on "Node.js". Some components were used in the development process. These components are: 'path' [21], 'express' [22] and 'ws' [23]. Port number 8888 was determined as a Web Server port. On the other hand, 8000 was determined as hypertext transfer protocol (HTTP) port. After the Web Server made the necessary connections, it started to listen to the data from the camera module. Here, the reverse shift operation was applied after the stream from the camera was handled. Then, the stream data ready for rendering were sent to the hypertext markup language (HTML) page by the client for display.

#### 4.3 Rendering Page Side

The rendered page is a HMTL page [24]. This page creates the connection to the Web Server and waits for the messages from there. It casts the data from the buffer type to the blob type and assigns it to the object created with "img" tags so, the image can be seen by this HTML page.

#### 4.4 Order of Operations

The process is in the following order:

1. The Arduino code is assigned to the ESP32-CAM module.
2. The file path containing the Node.js codes, created as a web server, is accessed from the "Node.js command prompt" screen.
3. In "Node.js command prompt" screen, the server is run using the "node <filename.js>" command.
4. The Chrome web browser runs on the computer where Web Server is running. Then, the "IPv4 address:8000/client" URL is accessed (IPv4 address is the address hosted on the web server).
5. Data flow is triggered by resetting the ESP32-CAM module.

#### 5. Shifted Encrypted Data Transfer and Render

Under this section, it is suggested to add a security layer that is not included in the system mentioned in the previous subsections. Now let's explain this model and how to add the security layer.

##### 5.1 ESP32-CAM Module Side

Some additional libraries have been used in the shifted encrypted data transfer and creation process for the ESP-32 Cam module side. These libraries can be listed as "AES.h", "base64.h", "iostream", "stdio.h" and "string.h". Everything is done as described in "shifted data" section (Section 4) until the data is taken from the camera module. After the data reaches, the processes differ.

Each of the received data is stored as "HEX" in "unsigned int" type. All of the stored data is too large to be encrypted. Therefore, the data are divided into 256- and 200-byte blocks.

Firstly, each divided block goes through base64 encoding operation by using the initial vector. The cipher text, secret key, and initial vector, encoded with base64, are subjected to 128-bit AES encryption. Parts of payload that are converted into encrypted form are sent to the Web Server one by one.

## 5.2 Web Server Side

In addition to the operations given in the "shifted data" section, "crypto-js" is used by the Web Server. On the server, the encryption key is shared with the ESP32-CAM module side.

Each block of the data coming from the camera module handles on the server side. Since the camera module sends the data in binary format, the incoming data is first converted to the "Base64" data type. The data converted to the appropriate format is decrypted with an initial vector and key. Since the streaming data comes piece by piece, it is brought together in accordance with order of arrival.

The type of incoming data must be in accordance with the JPEG data format. The header formats of the data, which are decoded and gathered, are checked to see if there is any interference between the data transmission. Finally, it is sent to the HTML page to be rendered.

The operations to be applied after this process is the same as the subsections "Rendering Page Side" and "Order of Operations" which are under the "Shifted Data Transfer and Render" section.

## 5.3 General Diagram

In Figure 1, you can see the process flowchart of the secure video transmission process with ESP32-CAM.

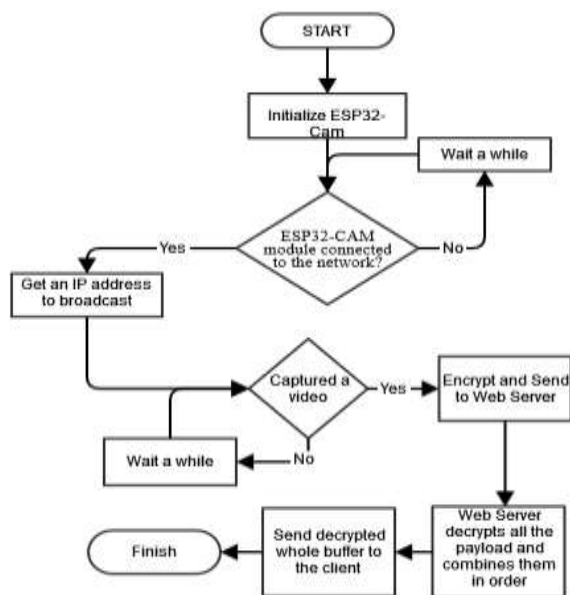


**Figure 1.** Flowchart of the secure video transmission process with ESP32-CAM.

Figure 2 gives an overview of all the process steps described in the previous sections.

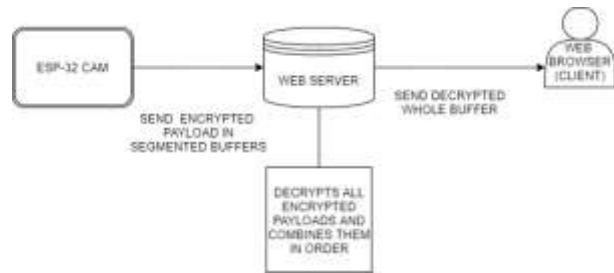


**Figure 2.** General diagram of the encrypted payload transfer.

The encrypted payload contained in the segmented buffer is sent to the Web server over the ESP-32 CAM. On a webserver, all encrypted payload is decrypted, and the webserver combines them in order. Finally, decrypted whole buffer is sent to the client (web browser).

## 6. Results and Discussion

You can find the general structure of the system and test results in the subsections below.

### 6.1 General Structure

In this study, the operations and experiments were carried out by using the ESP32-CAM IoT device.

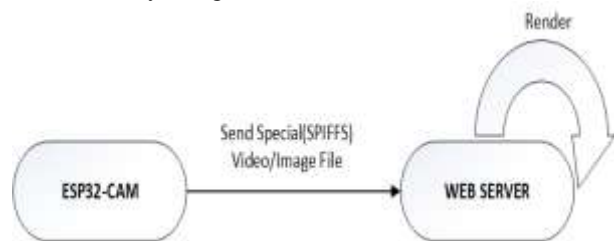


**Figure 3.** ESP32-CAM and web server transmission diagram.

On the system given in Figure 3, the ESP32-CAM module is acting on a server and the image was taken at the local host of the computer connected to the same network. In this state, the device sends received image to the web server and the browser renders the image. The structure established in this way has a security flaw. The image or video file is transmitted over the wireless network without a security layer. Since it does not have a security layer, it is vulnerable to malicious people. Another disadvantage of this structure is that only one client who wants to obtain the images or video from the camera can reach them. Another problem encountered in this structure is the format of the file sent from the ESP32-CAM module to the web server. It is not possible to encrypt and send the file and decrypt it by the web server. Because the IoT module and Web Server are programmed on the same device. Therefore, it is not possible to determine and apply a dividing line between them.



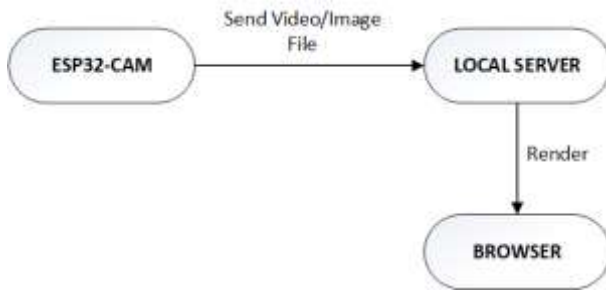


**Figure 4.** Separated ESP32-CAM and local server diagram.



**Figure 5.** ESP32-CAM and local server communication.

As shown in Figures 4 and 5, a different approach has been taken to address the previously mentioned flaw. Instead of keeping the server on ESP32-CAM, server was designed as a separated computer connected on the same network, so the only task of the camera module is sending the video or picture. This computer is acting as a server and took over the task of rendering in the browser. In this way, the camera module is able to send the encrypted file. On the computer, the server set up as Node.js is able to decrypt and render the incoming file. As a result of this design, an extra security layer has been added to the system for a critical process such as an image or video transfer. Moreover, this system enables more than one client to receive images at the same time.

## 6.2. Test Results

In Table 1, a comparison table was given. Response times are shown when encryption is performed for image transfer and when encryption is not performed.

Each tuple in Table 1 represents images that mean packages of the same size. Each of these tuples represents different images. The average Wi-Fi speed of the modem used is 30 MBits/s. Encrypted data has the same size as plain data to avoid growth in transferring data.

The time when data is sent from the ESP32-CAM module is determined at the start time for each calculated time. On the other hand, the end time is obtained when the server sends the data to the HTML page. Within this period when encryption is proceeded, there are processes such as encryption, transmission, decryption of the payload and combination of the buffers that come with coordination. The image that is

not encrypted has only the payload that is sent during the transfer and the server has to handle the incoming message.

**Table 1.** Comparison table for encrypted and non-encrypted image transfer durations.

Transferred Image Packages	Non-Encrypted Image Transfer and Render Durations (ms)	Encrypted Image Transfer, Decryption and Render Durations (ms)
Package_1	2169	4597
Package_2	203	5462
Package_3	512	5205
Package_4	756	4975
Package_5	650	4870
Package_6	924	5634
Package_7	712	4989
Package_8	618	4782
Package_9	569	5084
Package_10	878	4829

## 7. Conclusion

The number of IoT devices is increasing and their usage areas are expanding. These devices can capture images and videos. This image or video data obtained is transmitted over wireless networks. This situation brings along various security problems. There are many challenges in ensuring security, especially for live and streamed data. There are some studies in the literature to find a solution to this and to secure communication. In this context, this study has been put forward to ensure the secure transmission of video and images from IoT devices. ESP32-CAM was used in the study. ESP32-CAM has the ability to shoot video and images. It can also communicate by connecting to a network with a wireless connection. As the first approach, the image and video data obtained were shifted and transmitted in this way. There are problems in the structure of this model and in the security of the transmitted data. Therefore, a second model has been proposed. Structural changes have been made in this model and the transmitted data is encrypted with AES. In addition, the comparison of the transmission durations was given in order to compare the two models in the study.

As a result, with the structure established in the second model, a more secure system against attacks has been introduced. This model makes an important contribution to the security of IoT devices that are lightweight in terms of hardware resources.

## Author's Contributions

Pınar SAVAŞTÜRK: Wrote the draft manuscript, prepare the system, and made the experiments.  
 Ömer AYDIN: Assisted in analysis on the structure, supervised the experiment's progress, made result

interpretation, helped in manuscript preparation, made the manuscript ready for the journal, took part in the journal submission and following the journal process. Gökhan DALKILIÇ: Served as the consultant in the execution of the whole process. He supervised in the process of the preparation of the manuscript, revealed the main idea, made criticism, and made the proof reading in language.

## Ethics

There are no ethical issues after the publication of this manuscript.

## References

1. Urien, P. An Innovative Four-Quarter IoT Secure Architecture Based on Secure Element, In 2018 14th International Wireless Communications & Mobile Computing Conference (IWCMC), Limassol, 25-27 June, 2018, pp. 1074-1080. Doi: 10.1109/IWCMC.2018.8450435
2. Urien, P. An innovative security architecture for low cost low power IoT devices based on secure elements: A four quarters security architecture, In 2018 15th IEEE Annual Consumer Communications & Networking Conference (CCNC), Las Vegas, 12-15 January, 2018, pp. 1-2. Doi: 10.1109/CCNC.2018.8319309
3. Singh, M, Rajan, M, Shivraj, V, Balamuralidhar, P. Secure MQTT for Internet of Things (IoT), In 2015 Fifth International Conference on Communication Systems and Network Technologies, Gwalior, 746-751, 4-6 April, 2015. Doi: 10.1109/CSNT.2015.16
4. Yerlikaya, Ö, Dalkılıç, G. Authentication and authorization mechanism on message queue telemetry transport protocol. In 2018 3rd International conference on computer science and engineering (UBMK), 2018, pp. 145-150. IEEE.
5. Windley, PJ. 2015. API access control with OAuth: Coordinating interactions with the Internet of Things, *IEEE Consumer Electronics Magazine*, 4:52-58.
6. Fremantle, P, Aziz, B. OAuthing: Privacy-enhancing federation for the Internet of Things, In 2016 Cloudification of the Internet of Things (CIoT), 2016, pp. 1-6, doi: 10.1109/CIOT.2016.7872911.
7. Aydın, Ö, Erhan, İ. 2021. Video or Image Transmission Security for ESP-EYE IoT device used in Business Processes. *Yönetim Bilişim Sistemleri Dergisi*, 7(1): 1-9. Retrieved from <https://dergipark.org.tr/tr/pub/ybs/issue/63606/857203>
8. Radu, D, Cretu, A, Avram, C, Astilean, A, Parrein, B. Video content transmission in a public safety system model based on flying Ad-hoc networks. In 2018 IEEE International Conference on Automation, Quality and Testing, Robotics (AQTR), Cluj-Napoca, 24-26 May, 2018, pp. 1-4. doi: 10.1109/AQTR.2018.8402713
9. Miranda Pinto, LG, Mora-Camino, F, de Brito, PL, Brandão Ramos, AC, Castro Filho, HF. A SSD – OCR Approach for Real-Time Active Car Tracking on Quadrotors, In 16th International Conference on Information Technology-New Generations (ITNG 2019), Las Vegas, 1-3 April 2019, pp. 471-476. Doi: 10.1007/978-3-030-14070-0\_65
10. Maniccam, S, Nikolaos, G. 2004. Image and video encryption using SCAN patterns, *Pattern Recognition*, 37(4): 725-737. doi: 10.1109/30.920426
11. Yi, X, Tan, CH, Slew, CK, Syed, MR. 2001. Fast encryption for multimedia. *IEEE Transactions on Consumer Electronics*, 47(1): 101-107.
12. Tosun, AS, Feng, WC. Efficient multi-layer coding and encryption of MPEG video streams, In 2000 IEEE International Conference on Multimedia and Expo. ICME2000, New York, NY, 30 July-2 August, 2000, pp. 119-122. Doi: 10.1109/ICME.2000.869559
13. Choo, E, Lee, J, Lee, H, Nam, G. SRMT: A lightweight encryption scheme for secure real-time multimedia transmission, In 2007 International Conference on Multimedia and Ubiquitous Engineering (MUE'07), Seoul, 26-28 April, 2007, pp. 60-65. Doi: 10.1109/MUE.2007.194.
14. Qiao, L, Nahrstedt, K. A new algorithm for MPEG video encryption, In First International Conference on Imaging Science System and Technology, Las Vegas, Nevada, USA, 30 June- 3 July, 1997, pp. 21-29.
15. Tang, L. Methods for encrypting and decrypting MPEG video data efficiently. In Fourth ACM international conference on Multimedia, Boston Massachusetts USA, November, 1996, pp. 219-229.
16. Sikora, T. 1997. MPEG Digital Video Coding Standard. *IEEE Signal Processing Magazine*, 14(5): 82-100. Doi: 10.1109/79.618010
17. Shannon, CE. 1949. Communication Theory of Secrecy Systems, *The Bell System Technical Journal*, 28(4):656-715. Doi: 10.1002/j.1538-7305.1949.tb00928.x
18. Spanos, GA, Maples, T. B. Security for real-time MPEG compressed video in distributed multimedia applications, In 1996 IEEE Fifteenth Annual International Phoenix Conference on Computers and Communications, Scottsdale, AZ, USA, 27-29 March, 1996, pp. 72-78. Doi: 10.1109/PCCC.1996.493615
19. Adam, JA. 1992. Cryptography = privacy?. *IEEE Spectrum*, 29(8): 29-35. Doi: 10.1109/6.144533
20. Spanos, GA, Maples, TB. Performance Study of a Selective Encryption Scheme for the Security of Networked, Real-Time Video, In Fourth International Conference on Computer Communications and Networks - IC3N'95, Las Vegas, NV, USA, 20-23 September, 1995. DOI: 10.1109/ICCCN.1995.540095
21. Internet: Nodejs.org, <https://nodejs.org/api/path.html> (accessed at 17.09.2021).
22. Internet: Fast, unopinionated, minimalist web framework for Node.js, <https://expressjs.com/> (accessed at 17.09.2021).
23. Internet: ws: a Node.js WebSocket library, <https://github.com/websockets/ws> (accessed at 17.09.2021).
24. Graham, I. S. (1995). The HTML sourcebook. John Wiley & Sons, NY United States. ISBN: 978-0-471-11849-7